FABRICATION, INVESTIGATION AND OPTIMIZATION OF ELECTROMAGNETIC PARAMETERS OF FERRITE COMPOSITE BASED RF ABSORBER

Thesis Submitted for the Award of the Degree of

DOCTOR OF PHILOSOPHY

in

Electronics and Communication Engineering

By

Sayed Tathir Abbas Naqvi

Registration Number: 42000206

Supervised By

Dr. Charanjit Singh (21882)

Electronics and Communication Engineering (Professor)

Lovely Professional University, Punjab

Co-Supervised by

Dr. Sachin Kumar Godara

Apparel and Textile Technology (Assistant Professor)

Guru Nanak Dev University, Punjab

LOVELY PROFESSIONAL UNIVERSITY, PUNJAB

2024

DECLARATION

I, hereby declared that the presented work in the thesis entitled "**Fabrication, Investigation and Optimization of Electromagnetic Parameters of Ferrite Composite based RF Absorber**" in fulfilment of degree of **Doctor of Philosophy (Ph. D.)** is outcome of research work carried out by me under the supervision of Dr. Charanjit Singh, working as Professor, in the Electronics and Communication Engineering, School of Electronics and Electrical Engineering of Lovely Professional University, Punjab, India. In keeping with general practice of reporting scientific observations, due acknowledgements have been made whenever work described here has been based on findings of other investigator. This work has not been submitted in part or full to any other University or Institute for the award of any degree.

(Signature of Scholar)

Name of the scholar: Sayed Tathir Abbas Naqvi

Registration No.: 42000206

Department/School: Electronics and Communication Engineering, School of Electronics and Electrical Engineering

Lovely Professional University,

Punjab, India

CERTIFICATE

This is to certify that the work reported in the Ph. D. thesis entitled "**Fabrication, Investigation and Optimization of Electromagnetic Parameters of Ferrite Composite based RF Absorber**" submitted in fulfillment of the requirement for the award of degree of **Doctor of Philosophy (Ph.D.)** in the Electronics and Communication Engineering, is a research work carried out by Sayed Tathir Abbas Naqvi, 42000206, is bonafide record of his original work carried out under my supervision and that no part of thesis has been submitted for any other degree, diploma or equivalent course.

(Signature of Supervisor)

Name of supervisor: Dr. Charanjit Singh

Designation: Professor

Department: ECE

University: LPU, Phagwara, Punjab

(Signature of Co-Supervisor)

Name of Co-Supervisor: Dr. Sachin Kumar Godara

Designation: Assistant Professor

Department: Apparel and Textile Technology

University: GNDU, Amritsar, Punjab

Abstract

Electromagnetic pollution is posing a threat to human health and the operation of electronic/electrical devices. It refers to the unwanted electromagnetic waves/signals radiated from electronic devices/equipment. Microwave absorbers/absorbing materials have been developed to mitigate the problems associated with this kind of pollution. The radiated signals from the surroundings interact with the electronic devices and cause a malfunction in their operation termed electromagnetic interference (EMI). This radiation is not only affecting electronic equipment rather has a very adverse effect on human health too. Hence microwave absorbers are necessary to suppress or reduce the effect of these unwanted signals. They are the materials designed to attenuate the EMI either by absorbing microwave energy or converting it to heat. In this regard, researchers have reported that ferrites have emerged as a potential applicant for the use as absorbing materials. Several reports are available in the literature that signify the feasibility of ferrites in the field of microwave absorbers. Hence the present research is based on M-type hexaferrites. Since the pure M-type hexaferrites lag to match the required characteristics of an efficient absorber, dopants are included to enhance their absorption capabilities. So in the present work, doping of different metal ions is performed in the pure ferrites and their composites. Thus, synthesis using sol-gel technique and investigation of Zn^{2+} and Co^{2+} substituted $SrCo_xZn_xFe_{12-2x}O_{19}$, Ni^{2+} and Co^{2+} substituted $SrCo_xNi_xFe_{12-2x}O_{19}$, Zr^{4+} and Co^{2+} substituted $SrCo_xZr_xFe_{12-2x}O_{19}$ M-type hexaferrites and their composites using polyaniline (PANI) with a composition [$SrCo_xZn_xFe_{12-2x}O_{19}$ (80%) + PANI (20%)], [$SrCo_xNi_xFe_{12-2x}O_{19}$ (80%) + PANI (20%)] and [$SrCo_xZr_xFe_{12-2x}O_{19}$ (80%) + PANI (20%)] has been carried out.

The structural, morphological, dielectric/electric, magnetic, and microwave absorption characteristics of these prepared series were performed. The structural characterization is done using X-ray diffraction (XRD) analysis utilizing powder-x software. The morphological analysis was conducted using a scanning electron microscope. To investigate dielectric/electric properties LCR meter was utilized while a Vibrating Sample Magnetometer (VSM) was used for magnetic analysis. The electromagnetic parameters were obtained utilizing a Vector Network Analyzer (VNA).

M-type hexaferrites $SrCo_xZn_xFe_{12-2x}O_{19}$ have been synthesized using the sol-gel method. The structural, dielectric, and electrical characteristics of Zn^{2+} and Co^{2+} substituted strontium ferrites have been carried out. The dielectric and electric characteristics of prepared ferrites have been explored in the range of 100-2x10^6 Hz. Formation of the hexaferrite-phase has been confirmed using the X-ray diffraction analysis. Co^{2+} and Zn^{2+} substitution causes a reduction in crystallite size from 39.50 to 26.42 nm being the smallest in the case of x=1.0. Scanning electron microscopy (SEM) indicates the formation of honeycomb-like grain structures in composition x=1.0. The dielectric graphs show that the dielectric constant and tanδ vary in a non-monotonous way due to the inclusion of Co-Zn content. A non-Debye type relaxation is observed in the electric modulus of the developed compositions. There is a decrease in relaxation time with the increase in doping of Co-Zn. The impedance spectroscopy suggests the impact of grains and grain boundaries on the electrical characteristics. An impedance analysis has been performed by modeling the electrical behavior of the samples using electrical circuit modeling. The simulated results and measured results are in concurrence with each other. Composition x=1.0 owes a maximum RL= -41.72 dB for a 1.9 mm thickness. For the same sample, a broad BW of 2.02 GHz is obtained at the same thickness.

M-type hexaferrites $SrCo_xNi_xFe_{12-2x}O_{19}$ were prepared using the sol-gel technique. The phase was characterized by XRD, grain morphology was investigated from scanned electron micrographs, and dielectric/electric/impedance characteristics were analyzed from 100 Hz to 2 MHz. XRD revealed the formation of hexaferrites without any secondary phase. The grain size and distribution were significantly affected by Co-Ni dopants and there was an observation of cluster of grains, grain agglomerates, and improved inter-grain connectivity. The substitution of Co-Ni caused a reduction in crystallite size from 41.47 to 23.14 nm and the dielectric constant/loss varied non-monotonically. Electric modulus shows the non-Debye type behavior and the charge transport mechanism exhibited conductivity relaxation to be more dominant than dielectric relaxation. The correlation of simulated grain/grain boundary parameters with morphology, dielectric parameter, and electric modulus has been presented. The highest RL= -37.46 dB was achieved for a 8.0 mm thickness in

composition x=0.8 while the broad bandwidth of 1.35 GHz was obtained in composition x=1.0.

M-type hexaferrites $SrCo_xZr_xFe_{12-2x}O_{19}$ had been prepared using the sol-gel method. Zr^{4+} and Co^{2+} substitution effects on structural, dielectric, and electrical properties had been performed. The frequency range opted for the analysis of the prepared ferrites was 100 Hz to 2 MHz. XRD validated the development of a hexagonal structure and at the same time obtained patterns indicated no presence of a secondary phase. The inclusion of Co^{2+} and Zr^{4+} caused a decrement in the crystallite size from 41.47 to 29.77 nm. To investigate the morphology of prepared ferrites scanning electron microscopy (SEM) had been conducted, which indicated the development of needle-shaped platelet structures. Non-monotonically varied dielectric constant and loss were obtained by the inclusion of Co-Zr. The electric modulus showed the non-Debye-type behavior for all prepared compositions. The increase in doping of Co-Zr caused a reduction in relaxation time. The impedance spectroscopy illustrated the contribution of grains as well as grain boundaries on the electrical properties. The simulated electrical parameters are in good agreement with the measured ones. The composition x=1.0 has the maximum RL of -37.69 dB among all the compositions at a small 2.9 mm thickness. The highest bandwidth of 1.09 GHz was reported in composition x=0.0.

$SrCo_xZn_xFe_{12-2x}O_{19}$/PANI composites were prepared by adding polyaniline to the ferrite samples. The mixing ratio of these two materials is 80:20 which means 80 % of ferrite and 20 % of PANI. The morphology of the composites was investigated using SEM. It shows the formation of grain cluster in composition x=0.6 while the fused grain can be viewed in micrographs of composition x=1.0. The dielectric constant decreases with enhancing Co-Zn content in PANI composites. Electric modulus follows the non-Debye type nature with an increase in the relaxation time with the increment in Co-Zn doping content. The impedance spectroscopy indicates the presence of dielectric relaxation. The charge transport is affected by grain as well as grain boundaries. The highest RL= -18.53 dB at 8.4 mm thickness, however, 1.51 GHz bandwidth was obtained for the thickness of 9.2 mm for composition x=0.0.

$SrCo_xNi_xFe_{12-2x}O_{19}$/PANI composites were prepared by mixing polyaniline in the ferrite samples with a mixing ratio of 80:20. Scanning electron microscopy was

utilized to analyze the microstructural/morphological characteristics of ferrite composites. SEM images reveal that the inclusion of Co-Ni has affected the grain distribution and agglomeration of grains could be viewed. A considerable increase in grain sizes was noticed in composition x=1.0. The dielectric constant and loss varied inconsistently with an increase in the doping of Co^{2+} and Ni^{2+} in the PANI composites. Electric modulus follows a non-Debye type relaxation. Co-Ni doping in the composites caused a reduction in the relaxation time with the increment in doping content. The impedance spectroscopy suggested the impression of both grains and grain boundaries in conduction. Composition x=1.0 shows the RL=-41.39 dB at a 5.4 mm thickness. The broad bandwidth of 1.93 GHz was found for the band of 10.47-12.40 GHz in the same composition.

$SrCo_xZr_xFe_{12-2x}O_{19}$/PANI composites were prepared using polyaniline with the ferrite samples. Both these were mixed in a ratio of 80:20 with 80 % of ferrite and 20 % of PANI. The morphology of the prepared composites was investigated using a scanning electron microscope. The inclusion of Co^{2+}-Zr^{4+} caused a growth in the grain size. The formation of fused grains in composition x=0.2 while platelet-type grains were formed in composition x=0.6. The dielectric constant and tangent varied in a non-monotonical way due to the increase in the Co-Zr doping. The non-Debye type relaxation was noticed in the electric modulus with a reduction in the relaxation time as the Co-Zr doping increases. The relaxation peaks in the curves of impedance with frequencies suggested the presence of dielectric relaxation. The highest RL of -45.98 dB with 4.8 mm is in x=0.6. A bandwidth of 1.68 GHz was received at the thickness of 4.1 and 4.4 mm in x=0.6.

Acknowledgment

First of all, I show my gratitude and thanks to GOD for giving me the strength, zeal, and courage to complete my research work. It is he who always takes me out of difficult situations and shows me the correct path to face and overcome the challenges during this research journey.

I would like to present my gratitude to my supervisor **Dr. Charanjit Singh** (Professor), and Co-supervisor **Dr. Sachin Kumar Godara** (Ass. Professor) for their guidance, support, and motivation throughout the research work. They always stood as a guiding torch whenever I was in need during my research.

I am thankful to all the faculty members of the Electronics and Communication Engineering Department for their help and support. I sincerely thank Dr. R.B Jotania (Department of Physics, Gujarat University, Ahmedabad, India) and Dr. Suwarna Datar (Department of Applied Physics, Defence Institute of Advanced Technology, Pune, India) for providing various support in characterization.

Last but not least, a special thanks to my lovely parents (Shamim Abbas and Jamal Zahra), my wife (Sidra Sagir), my daughters (Arfia and Madiha), my dear sister (Sanay Zehra) and all my family members for their consistent support, motivation, and prayers throughout my research.

Sayed Tathir Abbas Naqvi
Registration No: 42000206
Date: 10-10-2024

TABLE OF CONTENTS

LIST OF TABLES

LIST OF FIGURES

CHAPTER 1

INTRODUCTION

Electromagnetic (EM) Pollution is a very serious concern nowadays. EM pollution refers to the effect of electromagnetic waves by which we are surrounded. Due to the advancement in wireless technology everywhere we all are surrounded by electromagnetic waves. Everywhere there are a large number of electromagnetic wave radiation sources. When we are at home we come under the influence of radiation produced by electronic devices such as laptops, mobile phones, cordless phones, Wi-Fi devices, microwave ovens, etc. while outside we are exposed to radiation produced by mobile towers, Wi-Fi routers, radio stations, satellites, radioactive devices like CT scanner, MRI, etc. Prolonged exposure to this radiation causes harm to human health [1]. Not only do humans suffer due to this radiation, but electronic devices also have an adverse effect on their performance. The impact of EM waves on electronic devices is termed electromagnetic interference (EMI). EMI is the disturbance produced due to the other nearby circuits or components in the circuit itself, which degrade the performance of the circuit. Nowadays size of printed circuit boards is so small that the tracks on them are very thin. When the width of these is approximated to $\lambda/4$ of the radiation frequency they start working like antenna and radiate electromagnetic energy. This energy radiation has an impact on the nearby components in the circuit or the other nearby devices [2].

As today's world is digital, all our data is stored digitally and all the financial transactions are done digitally which has a risk of unauthorized access to data. Data may be damaged or stolen through electromagnetic interference in devices. The hackers can transmit electromagnetic waves which can cause interference with electronic devices and stop or change the operation of that device. A person's confidential information like account number, password, user ID, or personal information can be tracked and misused. These issues can be handled with the help of a microwave absorber. The materials that can reduce the effect of unwanted radiation either by absorbing or attenuating the signal are called microwave absorbers. When the signal

passes through these materials either it is completely absorbed or there is an attenuation in the signal which makes it weak thus reducing the radiative effect of the signal.

Absorbers can be used externally or internally to maintain the required performance of the circuit or to protect it from outside radiation [3]. Microwave absorbers are also available to protect human beings from exposure to electromagnetic radiation. The researchers are continuously working to develop microwave absorbers according to different applications. Significant efforts were made to reduce the EMI effect on the devices as well as on the bodies of human beings. Microwave absorbers are available in different types as per the application [4]. They are available in the form of fabric, paint, foam as well as sheets. In this regard, researchers have reported that ferrites have emerged as a potential applicant for absorbing materials. Several reports are available in the literature that signify the feasibility of ferrites in the field of microwave absorbers [5].

1.1 Introduction to Ferrites

Ferrites are an important functional material because of their vast range of applications [6-8] and are used in various fields from microwaves to radio frequency. Ferrites are ceramic materials developed using oxides of iron with other elements like barium, strontium, manganese, nickel, and zinc. They are characterized based on their properties like permittivity, permeability, dielectric loss, magnetic loss, saturation magnetization and coercivity, etc. Ferrites possess the permanent type of magnetism termed ferrimagnetism. The term ferrimagnetism was coined by Neel to explain the magnetism in ferrite. It refers to the magnetism in which material possesses both the properties of ferromagnetism and anti-ferromagnetism. In ferrites, magnetic moments of some atoms aligned theirself in parallel directions while some were in antiparallel directions thus securing both ferromagnetism and anti-ferromagnetism. Thus the gross magnetic field is higher than anti ferromagnetic material but lower than the ferromagnetic materials. The synthesis method, chemical composition, grain size, and porosity largely affect the structural and electrical properties of the ferrites [9].

1.1.1 History of Ferrites

The history of ferrites started with the discovery of a stone that had the properties to attract iron. This mineral is named magnetite (Fe_3O_4) on behalf of the place Magnesia where its abundant accumulation was found. The initial application of ferrite by ancient people was to detect magnetic north. The name 'Ferrite' has been taken from the Latin language which means iron. In 1930 Dr. Taleshi Takie published a paper indicating that this material had high permeability and was well suited in high frequency applications. RADAR's invention motivated researchers to work on radar-absorbing material. In 1936 first quarter-wavelength resonant-type absorber was prepared in Nederland. After that during World War II Germany prepared radar-absorbing material. America developed an absorbing material called "HARP" Halpern Anti Radiation Paint. At the same time, a synthesis of the Salisbury Screen was done. In the postwar period (1945-1950) emphasis was on the development of broadband absorbers.

In 1956, a new class of ferrite material called garnet ferrite was developed by Neel and co-workers. Koops developed a formula to give phenomenological theory to explain conduction behavior in dielectric materials. The development of hexagonal ferrite in 1956 was a milestone in the field of ferrite. These are magnetic oxides with the formula $MeFe_{12}O_{19}$ with Me representing Barium, Strontium, or Lead. Around 1960 Phillips developed strontium hexaferrites ($SrO.6Fe_2O_3$). Since then barium and strontium ferrites are dominating the market due to their ease of synthesis and low cost. The optimization techniques in the 1980's promoted ferrites in the field of absorbers. The use of polymers with ferrites around 1990 led to the development of composite absorbers. Since then the ferrites have found a wide range of applications such as in satellite communication, microwave absorbers, storage media, cores of transformers, etc. They are gaining the attention of researchers and new explorations are coming out day by day.

1.1.2 Classification of Ferrite

Ferrites are categorized based on two parameters: the first is magnetic properties and the second is crystal structure. Based on magnetic properties, there are two kinds: soft ferrite and hard ferrite. The prime difference between them is the coercivity of these

ferrites. Soft ferrite possesses a lower value of coercivity while hard ferrites possess a large value of coercivity. Besides, soft ferrites are ferrimagnetic which means they don't hold their magnetism after being magnetized while hard ferrites have permanent magnetism means they hold their magnetism after magnetization. They have small and narrow hysteresis curves and have low eddy current losses while hard ferrites have broad and wide hysteresis curves and high retentivity and eddy current losses.

Based on crystal structure they are divided into four types: spinel, garnet, hexagonal, and ortho ferrites, among which the first two have cubic structure; the hexagonal ferrites have a hexagonal structure, while ortho ferrites have perovskite structure. Spinel ferrites are naturally occurring ferrites and so the name is derived from the mineral spinel ($MgAl_2O_4$). The spinel ferrites have the general formula of $MeFe_2O_4$ similar to the mineral spinel, here 'Me' represents the divalent atom like Ca, Zn, Co, etc. The cubic structure of spinel ferrites has two kinds of interstitial site one is tetrahedral (A) while the second is octahedral (B) site. Similar to mineral spinel Me^{2+} in spinel ferrites occupies A sites while Fe^{3+} fills B sites.

Garnet ferrites owe the structure of silicate mineral garnet. The formula of garnet ferrite is $Me_3Fe_5O_{12}$ where all the metal ions are trivalent. Mostly Me is yttrium or any other rare earth element. Ortho ferrites are the ferrites having the formula $RFeO_3$ where R is the rare earth element. These ferrites have an orthorhombic structure rather than the cubic as in the case of spinel. Hexagonal ferrites are also termed hexaferrites and are one of the most widely used ferrites. Due to their unique characteristics like high curie temperature, good microwave absorption, high electric resistivity, and low-cost hexagonal ferrites are gaining attention [9].

1.2 Hexagonal ferrites

Hexagonal or hexaferrites have hexagonal structures and are ferromagnetic in nature. The hexagonal ferrites have three sites which are octahedral, trigonal bi-pyramidal, and tetrahedral. These interstitial sites are occupied by metallic divalent and trivalent cations. There are six kinds: M, W, X, Y, Z, and U-type ferrites. M-type hexagonal ferrites are one of the most widely used types of hexagonal ferrites.

1.3 M-type hexaferrites

M-type hexaferrites have a magnetoplumbite structure named after a mineral of the same name. The M-type hexaferrites have a formula of $MFe_{12}O_{19}$ where M is either Ba, Sr, or Pb. Most of the M-type ferrites are ferromagnetic however some are anti-ferromagnetic. The most used compounds are $BaFe_{12}O_{19}$, $SrFe_{12}O_{19}$, and $PbFe_{12}O_{19}$. The most use of M-type ferrite is in microwave absorber applications.

1.4 Technological application of ferrites in various fields

The ferrites have a vast range of applications from microwave to radio frequency. Different technological applications of ferrites are discussed as follows.

1.4.1 Inductors

Ferrites are used as inductors in various electronic/electrical circuits like filters, amplifiers, switching circuits and ferrite beads, etc. The magnetic properties of ferrites make them suitable for the use of inductors. The most common use of ferrite as an inductor is the ferrite beads used in various electronic devices.

1.4.2 Microwave devices

The use of ferrite in the fabrication of a microwave device is one of the important applications. Microwave devices like circulators, isolators, phase shifters, etc. are examples of microwave devices made of ferrite material.

1.4.3 Sensor

Ferrites are also used in the area of sensors. The ferrite nanoparticles show high sensitivity and hence are of prime importance in the area of sensors. The use of nickel ferrite for chlorine, zinc ferrite for ethanol, and magnesium ferrite for liquid petroleum gas is well evident.

1.4.4 Microwave absorbing material

The use of ferrites as microwave-absorbing material is the most widely used application of ferrites. The ferrites have the capability to absorb the microwave radiation. Electronic pollution caused by EM radiation is a very major threat not only to electronic

devices but also to human beings. The effect of these radiations is suppressed or reduced by the microwave-absorbing material. The ferrites due to their ferromagnetic behavior are promising candidates in the development of microwave absorbers.

1.4.5 Wastewater treatment

Ferrites are also used in the treatment of water and wastewater due to their adsorption capabilities. The hazardous element mixed with water can be removed with the use of ferrites. For example, mercury in water can be removed by precipitating it into a magnetic resultant using ferrite.

1.5 Microwave absorption mechanism

The materials that absorb microwave radiation are termed microwave-absorbing materials (MAMs). These are materials designed to reduce the EMI either by absorbing energy or converting it to heat. MAMs were first commercialized during World War II to enhance radar performances [10]. Since then extensive research has been done in the field of absorbing materials, which has produced a variety of absorbing materials in different shapes and sizes. Since electromagnetic waves have electric and magnetic fields, the performance of a microwave absorber depends on its dielectric and magnetic loss capabilities. The materials based on magnetic loss are magnetic metals, magnetic metal oxides, and ferrites, while on the other hand, conductive polymers and carbon-based materials depend on dielectric loss [11]. A good absorber has characteristic features viz-a-viz lightweight, low density, excellent chemical stability, and thin thickness as shown in Fig.1.1 [12]. The absorption phenomenon is based on the Quarter-wavelength [13] and impedance-matching mechanism [14].

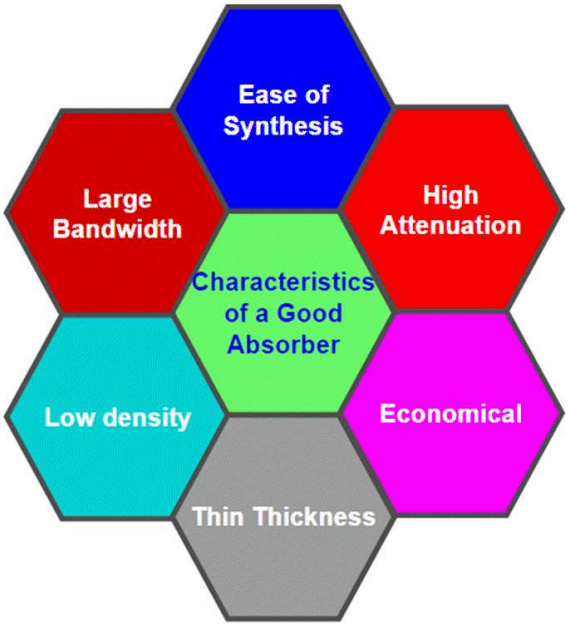

Fig. 1.1 Characteristics of a good absorber.

1.5.1 Quarter Wavelength Mechanism

The mechanism indicates that if the width of ferrite material is one-fourth of the wavelength of an incident signal, it will either attenuate the signal or absorb it as shown in Fig. 1.2.

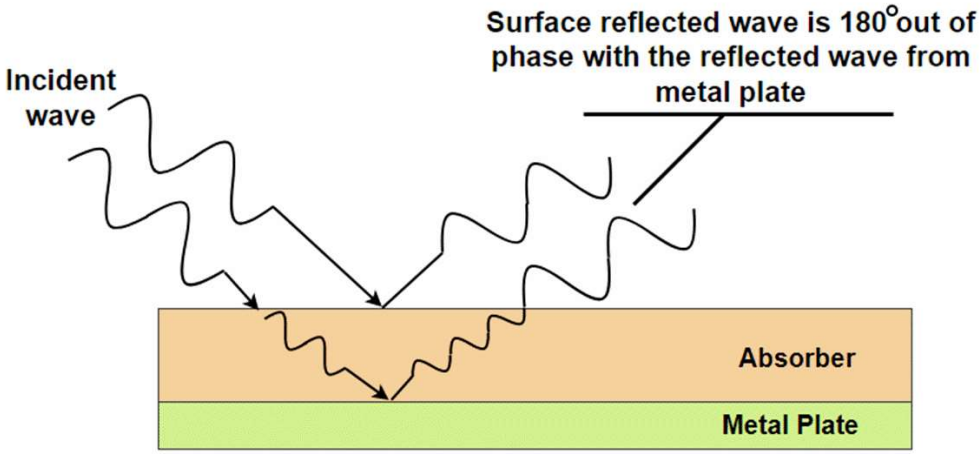

Fig. 1.2 Schematic representation of quarter-wavelength mechanism.

The absorption characteristics of a material are understood by a parameter called reflection loss. Reflection loss tells how much the material is effective as an absorber.

The higher the reflection loss better the absorption characteristics in a material. This is denoted by RL with dB as a unit, and determined with the help of the material's input impedance Z_{in} and the impedance of free space Z_0.

1.5.2 Impedance Matching Mechanism

The phenomenon states that the reflection loss in any material will become infinite as the impedance of the material matches the impedance of air which is calculated as 377 Ω. Hence by matching the Z_{in} of the material with Z_0 the reflection loss can be increased and with the increase in RL, the absorption characteristics of the ferrite can be increased. Filler materials are used to manipulate the characteristics of the material to achieve desired outcomes. The use of filler material helps to match the input impedance of the material to that of the characteristic impedance and increases the machineability to give desired shape. The schematic diagram of the impedance matching mechanism is demonstrated in Fig. 1.3.

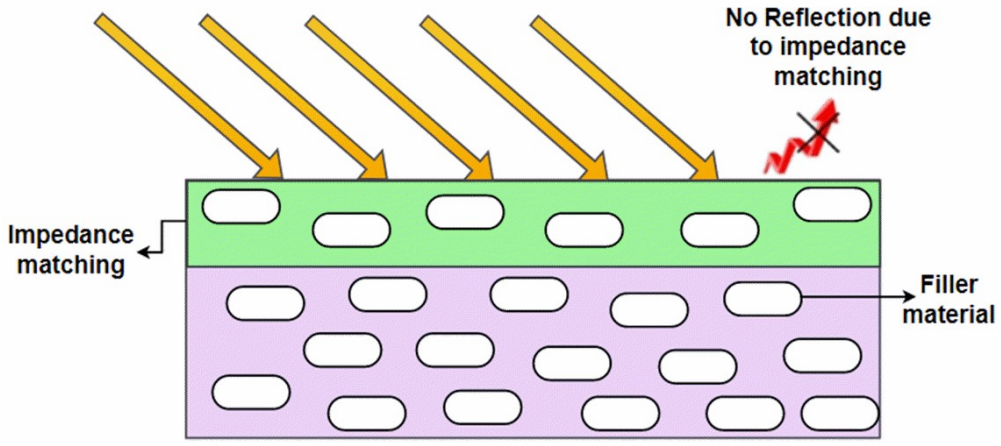

Fig. 1.3 Schematic representation of Impedance matching mechanism.

1.6 Polyaniline (PANI)

A polymer is a material having large molecules called macromolecules pertaining large number of repeating units. A polymer may be conductive or non-conductive. Polyaniline (PANI) is a conductive polymer that allows conductivity to an electric field. It is one of the most widely used polymers due to its unique physiochemical properties. PANI has good thermal stability, low synthesis cost, good corrosion resistance, and

enhanced conductivity. PANI is used in the field of microwave absorption due to its inherent property as it can improve microwave absorption through conduction loss. PANI shows Eddy current loss which is beneficial in the design of an absorber. Besides this, PANI has a high dielectric constant which supports polarization. The use of PANI with different metallic and ferromagnetic materials has increased in recent years as these materials have sufficient mechanical and EMI shielding properties but suffer from being heavy and corrosive. The conductive nature of PANI can enhance absorption qualities by enhancing dielectric loss. PANI has three forms namely leucoemeraldine, pernigraniline, and emeraldine among which emeraldine is the most conductive. Hence in microwave absorption application emeraldine form among the three is mostly used.

In the present research work, microwave-absorbing materials have been developed using ferrite. Ferrites are suitable in the field of microwave absorbers due to their unprecedented characteristics such as high Curie temperature, good microwave absorption, high electric resistivity, and low cost. The structural and electrical characteristics of the ferrites rely on the synthesis method, composition, grain size, and porosity. Thus by varying such parameters, their characteristics can be tuned as per the requirement. Hence the utilization of ferrite for the preparation of radio frequency absorber is a good choice. There are many methods to prepare the ferrite which are the sol-gel technique, hydrothermal synthesis, ceramic, and co-precipitation method. Among these, a sol-gel method is cost-effective method of ferrite development. Besides this, the sol-gel method has reproducibility in that the samples can be prepared many times with the same characteristics. Hence sol-gel method has been chosen to develop the ferrite samples.

1.7 Chapter Outline

Chapter 1: Introduction about the investigated work along with the role and need of microwave absorbing material is discussed. A discussion about the structure, types, and use of ferrite as an absorber is also explained. The microwave absorbing mechanism is discussed based on the impedance matching mechanism and quarter wavelength mechanism.

Chapter 2: This chapter presents the literature review carried out in the field of microwave absorbers to understand the various strategies followed by the researchers to synthesize and analyze the various electrical and magnetic properties of different microwave absorbing materials.

Chapter 3: The chapter elucidates the experimental procedure used in the preparation of ferrite compositions. It also explains the experimental procedure involved in the measurement of different electric/dielectric parameters of the prepared compositions. The procedure used to determine microwave absorption characteristics of the prepared ferrites and their composites is also explained in detail.

Chapter 4: This chapter presents the results and discussions regarding the investigated research work. The obtained results of ferrites and composites doped with Zn, Ni, and Zr are discussed and analyzed in detail. The structural analysis using XRD and morphological investigation using SEM has been explained. The electric/dielectric characteristics like dielectric constant, loss, electric modulus, ac conductivity, and impedance of the developed compositions have been explained in detail. This chapter also discusses the microwave absorption analysis of the prepared compositions based on Quarter wavelength and impedance matching mechanisms.

Chapter 5: This chapter presents the summary and conclusion of the investigated research work. The outcomes of the research performed are discussed in this chapter. This chapter also discussed the future aspects of the investigation performed.

CHAPTER 2

LITERATURE REVIEW

2.1 Review of Literature

The literature review is an important part of any research. An extensive literature survey is performed to achieve the desired objectives of the research work. This section presents a review of the literature.

Jing et al. (2024) developed praseodymium (Pr) and dysprosium (Dy) doped strontium ferrites by deploying the sol-gel method. The structure, magnetic, and absorption characteristics were investigated with different calcination temperatures and doping levels. XRD indicated that the ferrites had both an M-type phase and heterophase caused due to the doping of Pr and Dy. Micrographs indicated that the grain size had reduced with the higher doping level. It was observed that saturation magnetization reduced, however, coercivity increased with the increase in Pr-Dy doping amount. They reported RL= -52.51 dB with an effective absorption bandwidth of 4.81 GHz [15].

Jin et al. (2024) utilized the sol-gel method to develop the chromium-doped M-type hexaferrites with the chemical composition of $BaCe_xFe_{12-2x}O_{19}$. The investigation of microstructural, morphological, and absorption characteristics has been carried out. It was observed that the doping level of Ce did not affect the crystal structure, however, the electromagnetic and absorption properties had been improved with the doping. The composition x=0.2 gave the highest absorption performance with a -58 dB reflection loss. The bandwidth obtained is 9.44 GHz at a thickness of 2.3 mm [16].

Wei et al. (2024) prepared M-type hexaferrites with the Nd-Nb and Nd-Ta substitution. The authors employed the solid-state reaction method for the preparation of the samples. Investigation from different aspects such as structural, magnetic, and absorption had been performed. The increased doping level of Nd-Nb and Nd-Ta ions caused an increase in saturation magnetization from 63.76- 65.39 emu/g and coercivity first increased and then decreased for high doping level. The Nd-Nb substitution improved RL from -11.39 dB to -47.08 dB and Nd-Ta enhanced RL to -34.81 dB [17].

Panwar et al. (2024) used Bi and Co for the substitution of Ca and Fe ions in an M-type ferrite. The sol-gel technique was utilized to fabricate the compositions. The

studied structural, dielectric, and magnetic behavior of the prepared composition. The crystallite size of the developed composition ranges between 42-49 nm. The doping of Co-Bi caused an increase in the saturation magnetization and coercivity. The Ms ranges between 15.51-38.27 emu/gm while Hc ranges from 207.93-1359.69 Oe [18].

Yang et al. (2024) synthesized Ce-doped M-type strontium ferrite by deploying the sol-gel technique. The effect of doping on different structures and magnetic properties was investigated. They reported that the addition of dopant had reduced the size of grain and saturation magnetization from 76.16- 62.60 emu/gm. It was observed that the coercivity has increased from 4361 to 4638 Oe with the increment in doping level [19].

Chen et al. (2024) prepared an M-type strontium ferrite with Holmium (Ho) as a dopant. The technique used to develop the composition was the sol-gel method. The analysis was done to determine the effect of Ho inclusion on the characteristics of the hexaferrite. The addition of Ho content caused a decrease in saturation magnetization from 76.73-73.28 emu/gm. The coercivity was also reduced with a high doping concentration of Ho from 5.26-4.78 kOe [20].

Kayalvizhi et al. (2024) prepared ferrite composites using strontium ferrite with reduced graphene oxide (rGo). They developed strontium ferrite ($SrFe_{12}O_{19}$) first and then used rGo to prepare ferrite composite $SrFe_{12}O_{19}$/rGo. The hydrothermal method was adopted for the fabrication of required compositions. The microwave absorption analysis was performed for a frequency band of 2-18 GHz. The structural analysis confirmed the reduction in the particle size from 55.60- 41.55 nm with the inclusion of rGo. Furthermore, the inclusion of non-magnetic rGo also reduced the magnetic parameters of the ferrite. The saturation magnetization decreased from 53.3 to 35.89 emu/gm. The coercivity showed an increasing trend (from 2679-3606 Oe) with the addition of rGo. The respective values of reflection loss for ferrite and rGO composites were -28.49 dB and -23.78 dB respectively [21].

Yang et al. (2024) investigated band gap, magnetic, and absorption characteristics of Zn^{2+} and Sn^{4+} doped barium hexaferrites. The auto-combustion method was employed to synthesize the hexaferrite. They reported that the band gap increased (1.80-1.97 eV) with the increment in the Zn-Sn doping content. The doping also reduces the magnetic saturation, coercivity, and anisotropy field. The ferrite showed an absorption bandwidth of 6 GHz with an absorption band of 11.4-17.4 GHz. The authors also prepared ferrite

composites using carbon nano-tube (CNT). To develop composite material hydrothermal method was adopted. It is reported that the composites with CNT have improved microwave absorption with a bandwidth of 7.1 GHz for approximately the same thickness [22].

Wei et al. (2024) prepared epoxy resin-based CNT/barium ferrite composites. The absorption performance was investigated on a frequency band of 2-18 GHz. The wt % to prepare composites were 20, 30, 40, and 50 %. The highest absorption performance was obtained with 40 wt% with an RL of -57.30 dB and bandwidth of 5.68 GHz. The RL ranges between -26.56 to -50.32 dB for the rest of the samples [23].

Shu et al. (2024) fabricated the three-dimensional (3D) composite with nitrogen-doped reduced graphene (NRGO), magnesium ferrite ($MgFe_2O_4$), and polyaniline (PANI). A comparative analysis among pure NRGO, NRGO/$MgFe_2O_4$, and 3D composite had been carried out. It was reported that the developed 3D composite showed better microwave performance in comparison to the other two. The prepared 3D composite showed the highest performance with RL=-42.9 dB at 3.57 mm with a bandwidth of 7 GHz [24].

Mudasar et al. (2024) prepared M-type hexaferrite-based composites using $Ti_3C_2T_x$-MXene. The used Co-Zn doped barium-strontium ferrite was prepared using the solid-state reaction method. The developed composite showed good absorption capabilities with an RL of -49 dB 15.2 GHz. The obtained highest absorption bandwidth below -10 dB was 8.3 GHz while below -15 dB it was 6.4 GHz [25].

Bala et al. (2024) developed nickel ferrite-based composites with carbon derived from cotton. The mechanical alloy method was used to develop the composites. The absorption performance was evaluated for a frequency band of 8.2-12.4 GHz. It was noted that the saturation magnetization had decreased from 51.59-0.75 emu/gm due to the inclusion of a non-magnetic compound. The maximum absorption of -26.46 dB at 10.01 GHz was obtained [26].

Yunasfi et al. (2024) used the co-precipitation method for the fabrication of La^{3+} doped nickel ferrite. The investigation on structural, magnetic, and absorption was performed. The particle size of the prepared composition ranges from 100 to 800 nm. It was observed that with the addition of La^{3+}, the saturation magnetization reduces from 35.89 to 21.54 emu/g due to the non-magnetic nature of La^{3+}, however, the coercivity

increased from 249 to 416 Oe. The absorption analysis was performed for a frequency band from 8 to 12 GHz. The maximum reflection loss of -15.41 dB at 10.60 GHz was obtained [27].

Kaur et al. (2024) synthesized Ni-Zr substituted Zinc-cobalt ferrites for the application as a microwave absorber for Ka-band. They utilized the sol-gel technique for the development of ferrite compositions and investigated structural, optical, magnetic, and microwave absorption characteristics. The saturation magnetization values are found to be decreased with the inclusion of Ni-Zr. The composition x=0.1 provided the RL of -50.34 dB at 29.2 GHz with a thickness of 1.3 mm [28].

Siddique et al. (2024) prepared Co-Cd ferrites and investigated the influence of Zn inclusion on the structural, electrical, and absorbance performance of the prepared compositions. The chemical composition used is $Cd_{0.5-x}Zn_xCo_{0.5}Fe_2O_4$. The authors used the sol-gel technique for the development of ferrites and reported crystalline sizes ranging from 43-50 nm. The substitution of Zn^{2+} causes a decrement in coercivity from 246.47 to 192.10 Oe while an increment in saturation magnetization 58.92-106.41 emu/g is observed. Authors obtained the highest RL of -26.85 dB for composition x=0.3 at 3.9 GHz [29].

Akhtar et al. (2024) reported Zr-In substituted Ni-Zn nano ferrites having a chemical formula of $Ni_{0.7}Zn_{0.3}(ZrIn)_xFe_{2-2x}O_4$ (x=0.0-0.2). The structural, dielectric, and magnetic characteristics were analyzed by FESEM, XRD, and VSM. The composition x=0.2 provided the highest RL values of -61.5 dB with a frequency of 2.43 GHz, while an RL=-57.3 dB with frequency of 1.93 GHz was obtained in composition x=0.15 [30].

Tian et al. (2023) examined the role of Mn substitution on structural, magnetic, and absorption characteristics of hexagonal ferrites. The dielectric constant of the prepared ferrites was found to be decreased with the increase in doping while the permeability was found to be increased. Reflection loss of -64.39 dB at a 1.85 nm thickness was reported. The authors observed an increase in effective bandwidth from 5.5 to 9.1 GHz due to the increase in Mn doping concentration [31].

Verma et al. (2023) prepared M-type hexaferrites using the solid-state reaction method and investigated structural and magnetic parameters with the doping of Zn-Zr. The authors observed a decrement in crystallite size (149-69 nm) with the increment in

doping of Zn-Zr. The highest saturation magnetization of 72.77 emu/g for composition x=0.1 was achieved. The coercivity decreased from 4118 Oe to 319 Oe [32].

Sahu et al. (2023) performed the synthesis of Sr^{2+} doped Ni-Co ferrites with a ball milling process. The chemical composition used in the study was $Ni_{0.5}Co_{0.5-x}Sr_xFe_2O_4$ (x=0.0-0.1, step size 0.025). The authors investigated the magnetic and absorption characteristics of the developed ferrite and reported the influence of Sr doping on the characteristics of the prepared compositions. They observed a decrease in saturation magnetization by the use of Sr. The highest M_s of 60 emu/g was achieved in composition x=0.05. They achieved a high RL of -35.59 dB at 17.74 GHz with the thickness of 3 mm [33].

Gulbadan et al. (2023) synthesized Yb-Co doped barium-strontium hexaferrites using the sol-gel method. The authors observed a decay in dielectric constants while an increment in loss tangent with the increase in Yb-Co doping. A band gap of 1.961 to 1.875 eV was obtained by the UV-Vis spectroscopy. The authors reported the enhancement of ac conductivity with the inclusion of Yb-Co content [34].

Gui et al. (2023) prepared W-type hexaferrites using the sol-gel technique with a chemical composition of $Ba_{1-x}La_xCo_2Fe_{16-y}Al_yO_{27}$. The authors measured absorption parameters in the frequency range of 2-18 GHz. They noted a high RL peak of -50.13 dB at 11.9 GHz for the thickness of 7 mm. They also obtained a -20 dB absorption bandwidth from 11.6-12.2 GHz [35].

Zhang et al. (2022) investigated structural, optical, and magnetic characteristics of M-type ferrites with the chemical formula of $Sr_{0.7}La_{0.3}Zn_{0.3}Fe_{11.7-x}Al_xO_{19}$. The dielectric constant had decreased while the loss tangent had increased with the doping. Saturation magnetization M_s was found to be decreasing, while coercivity H_c was increased with the increase in doping level. There was a large increment of 2246.6 Oe in Hc as it varied from 2330.2 Oe to 4576.8 Oe [36].

Akthar et al. (2022) prepared rare earth element doped graphene-based $NiFe_2O_4$ nanocomposites and investigated structural, optical, and magnetic properties. The authors used a rare earth element: Yb, Gd, and Sm for the preparation process and selected the sol-gel method for synthesizing the ferrites. The authors reported an optical band gap in the range of 1.65 to 2.66 eV. They observed an increment in saturation magnetization from 11.552 to 46.243 emu/g [37].

Agarwal et al. (2022) synthesized nickel zinc ferrites with Mg and Zr as dopants. The synthesized ferrites have the chemical composition of $Ni_{0.6}Zn_{0.4}(MgZr)_xFe_{2-2x}O_4$. It was noted that complex permittivity and permeability were increased with an increase in doping which enhances the absorption ability of ferrite. The best RL value of -33.4 dB was achieved for the composition x=0.15 [38].

Hassan et al. (2022) developed cerium-substituted hexagonal ferrites using the sol-gel route and analyzed the electrical and magnetic performance. Authors reported an increment in the dielectric loss by the increment in doping of Ce content, while the dielectric constant was reduced by the dopants. The ac conductivity illustrates an increasing trend and dc resistivity decreased by an increment in doping [39].

Singh et al. (2022) investigated M-type ferrites $Ba_{0.5}Sr_{0.5}Co_xY_xFe_{12-2x}O_{19}$ with doping of Co and Y. Substitution of Co and Y causes an increment in the absorption. The highest RL=-28.72 dB was achieved for x=0.2 at 11.64 GHz with 1.5 mm thickness. They explained the bandwidth-thickness ratio concept and reported that x=0.8 possesses a 3.6 bandwidth-thickness ratio at 10.55 GHz [40].

Dilshad et al. (2022) investigated the structural, optical, and dielectric characteristics of M-type Sr ferrite with Al^{3+} doping. They explained the change in dielectric parameters using space charge polarization. Variation in conductivity was explained with the help of Maxwell-Wagner model [41].

Basha et al. (2022) synthesized M-type strontium hexaferrite with doping of La via hydrothermal technique and investigated structural, electrical, and magnetic properties. Dielectric modulus was used to investigate the space charge mechanism, while Cole-Cole plots were discussed to explain the electric conduction mechanism [42].

Yousaf et al. (2022) reported Nd-Cr substituted Bismuth ferrites opted by the sol-gel. The chemical composition used in the investigation was $BiNd_xC_xF_{1-2x}O_3$ (x=0, 0.05, 0.1, 0.15). The reflection loss of -37.7dB with a thickness of 3 mm was achieved with doping of Nd and Cr [43].

Zahid et al. (2022) synthesized Cr^{3+} doped strontium hexaferrites with composition $Sr_{1-x}Cr_xFe_{12}O_{19}$ applying the sol-gel technique. An increase in Lattice parameters and a fall in grain size were reported with the inclusion of dopants. The authors concluded that this change was due to the large ionic size of Cr^{+}. The dielectric constant and ac

conductivity increased with the doping of Cr. The coercivity values obtained are in the range of 6.64-6.72 KOe [44].

Purnama et al. (2022) used the co-precipitation method for developing strontium-doped cobalt ferrites. The analysis was done with different annealing temperatures. The XRD analysis indicated that the crystallite size of the prepared ferrites increased by enhancing the annealing temperature. They reported that saturation magnetization falls with higher temperatures. The highest H_c of 2.76 kOe was reported at a 1000 °C temperature [45].

Habib et al. (2021) prepared a microwave absorber using waste toner. The ferrite used was MnNiZn ferrite in the preparation of the composite ferrite absorber. The analysis was done on the basis of structural, magnetic, and absorption characteristics of the ferrite composite. The investigation was performed for a wide frequency from 2 GHz to 8 GHz. The obtained results were compared with ferrite composite using paraffin. It is evident from the RL curves of paraffin and waste toner that the performance of ferrite with waste toner is better as compared to paraffin. The authors claimed an RL=-22.5 dB with a BW of 3.5 GHz at a 5mm thickness [46].

Lim et al. (2021) fabricated M-type cobalt strontium ferrites using La and Ti as dopants. The chemical composition used was $Sr_{0.906}\ La_{0.094}Fe_{11-2x}Co_xTi_xO_{19}$. Epoxy was used with a weight percent of 10wt%. The doping of Co-Ti caused a decrement in saturation magnetization and coercivity. It was reported that the increase in doping composition enhanced the absorption performance of the composite. The characteristics of composition 0.8 were the worst among all the compositions. In all the compositions x=1.4 had the highest reflection loss of -40 dB [47].

Singh et al. (2021) developed an M-type barium strontium ferrite using the doping of Co^{2+} and Sn^{4+}. The composition used was $Ba_{0.5}Sr_{0.5}Co_xSn_xFe_{12-2x}O_{19}$. X-ray diffraction and vector network analyzer were used for the structural and absorption characterization. The doping of Co and Sn had a significant role in the performance parameters of the ferrite. The outcomes indicate that the doping of Co and Sn increases the electromagnetic parameters of the samples. There was a large increment of 35.89 dB in the reflection loss, as the RL value without doping was found to be -15.2 dB while with doping it becomes -51.09 dB for composition x=0.6 [48].

Kumar et al. (2021) fabricated Zinc-Cobalt ferrite with polyaniline. The composite prepared was $Co_{1-x}Zn_xFe_2O_4$ with x varying from 0.1 to 0.4. The prepared ferrites were developed using the sol-gel method. The polyaniline was added with the ferrites via in situ polymerization. The authors studied the EMI shielding performance of the composite. The study was done from 8-12 GHz. The composition x=0.3 provided the highest shielding effectiveness (SE) of 106 dB. The authors reported an increase in the shielding effectiveness with an increment in the thickness [49].

Singh et al. (2021) developed Ba-Sr hexagonal ferrites and structural characteristics, absorption peaks, and electromagnetic parameters were studied. Doping of Co and Cr was performed and the effect of doping on parameters was investigated. The result showed a significant effect of quarter wavelength and impedance matching criterion on the reflection loss. A large reflection loss of -52.09 dB was reported for 8.78 GHz with 5.6 mm thickness for composition 0.8. The composition 0.6 provided a broad BW of 3.28 GHz. The analysis shows that the composite prepared is well-suitable for absorber applications [50].

Chakradhary et al. (2021) prepared cobalt-doped nickel ferrite with carbon nanofiber. First cobalt nickel ferrite had been developed and investigated. Initially, the prepared ferrite provided very low absorption characteristics. A low bandwidth of 1.45 GHz was achieved with the large thickness of 10.3 mm. When carbon nanofiber was added, this addition enhanced the absorption properties. An increment in bandwidth was obtained, which became 3.23 GHz with a reduced 1.6 mm thickness. Thus it can be reported that carbon nanofiber enhances the absorption characteristics [51].

Zhang et al. (2021) prepared Cobalt ferrite composites with Carbon nanofibers. The composites are prepared with 5wt%, 10wt%, and 15wt%. The authors termed the composites CFO-5, CFO-10, and CFO-15. Then C/CFO composite samples were prepared and named C/CFO-5, C/CFO-10, and C/CFO-15. The C/CFO composite with 10wt% i.e. C/CFO-10 produced a large RL peak of -137 dB with a BW of 11.44 GHz at 2.6 mm thickness. In comparison composite pure Carbon nanofibers and Cobalt ferrite composite provide reflection loss of -48.6 and -28.6 dB respectively [52].

Agarwal et al. (2021) presented a study on the doping of cobalt and zirconium in nickel-zinc ferrite. The synthesis of ferrites was performed using the sol-gel method. The chemical composition used was $Ni_{0.6}Zn_{0.4}(CoZr)_xFe_{2-2x}O_4$ with x from 0.05 to 0.25.

From the graph of reflection loss versus frequency, it is evident that a large RL of -44.92 dB was achieved at 9.29 GHz for composition x=0.20 while a reflection peak was obtained at 8.70 GHz with an RL of -40.43 dB for x = 0.25. Thus substitution of Co and Zr increased the absorption characteristics of Ni Zn ferrite [53].

Chang et al. (2020) prepared the W-type hexagonal ferrites with doping of co and Zr. The composition of ferrite prepared was $BaCo_2Fe_{16-x}(Co_{0.5}Zr_{0.5})_xO_{27}$. The synthesis of ferrite was performed using sol-gel method and the analysis was done for a frequency range of 1 to 18 GHz. The undoped hexaferrite possesses -21.03 dB reflection loss for a frequency of 13.15 GHz. The performance of the ferrite in terms of absorption properties was improved with the doping of Co and Zr. The reflection loss was improved from -21.03 dB to -37.84 dB for the composition x=0.4. The peak of reflection loss was obtained at a frequency of 16.3 GHz when the corresponding thickness was 5.0 mm [54].

Tao Ma et al. (2020) synthesized reduced graphene oxide/MnZn ferrite. The authors studied the effect of graphene on the performance of ferrites. They pointed out that the dielectric/magnetic properties of the ferrite composite were enhanced and a Rl=-60.9 dB was received for an applied frequency of 12.4 GHz with 2.75 mm. A 5.6 GHz bandwidth was achieved if the thickness was 2.38 mm [55].

Zhang et al. (2020) synthesized Zr-NiCo doped barium ferrites using the sol-gel process. The study was performed for a frequency range of 2 to 8 GHz. Composition x=0.6 in all the compositions was best in terms of reflection loss as a large reflection loss of -53.9 dB was achieved for a frequency of 11.0 GHz. It can be noted that they also obtained a broad BW of 6.9 GHz [56].

Jiao et al. (2020) studied Ni-Zn ferrite with polyaniline as a matrix material. The composition of the ferrite composite was $Ni_{0.5}Zn_{0.5}Nd_{0.04}Fe_{1.96}O_4$. They performed an investigation on the electromagnetic parameters of ferrite. The results show that the substitution of PANI enhances the absorption characteristics of the ferrite. The permittivity improved with the mixing of PANI in the ferrite sample. It was reported that the absorbing characteristics of the prepared sample can be tuned by the amount of aniline added to the samples. The -37.4 dB reflection loss was gained for 8.4 GHz for 4.0 mm [57].

Tang et al. (2020) presented a composite of Zinc ferrite with MWCNTs. It can be noted from the graph between reflection loss and frequency that for pure $ZnSO_4$, the RL peak was above -10 dB from 01 to 3 GHz. This shows that pure $ZnSO_4$ was not suitable for absorption application. When the ferrite nanoparticles were covered by a thin carbon layer, there was an improvement in reflection loss. $ZnFe_2O_4$@C had a reflection loss of -20.6 dB at 2.19 GHz for a thickness of 5 mm. The addition of the nanotube caused an enhancement in RL values and reflection loss ability had increased to -40.65 dB at 0.81 GHz if the thickness is 2.5 mm [58].

Shu et al. (2020) developed NRGO/nickel zinc ferrite composite. The authors investigated the filler loading effect on the composite's absorption properties. The filler loading studies were done with 30, 35, 40, 50 and 60 wt%. Among all of these, loading of 40 wt% provided the highest reflection loss of -63.2 dB at 2.9 mm. A 5.4 GHz effective absorption bandwidth was obtained for the same filler loading with a small thickness of 2.0 mm. The result showed that reduced graphene had improved the performance of the ferrite, as pure ferrites have lower absorption characteristics as compared to doped composite [59].

Khadour et al. (2020) prepared a flexible microwave absorber using MnNiZn ferrite. The filler matrix used was polyurethane. The study was performed to cover both the S and C bands. The loading of 70, 75, and 80 wt% of MnNiZn ferrite was performed in the fabrication of polyurethane nanocomposites. The filler loading of 80 wt% had come out as the best among the three, as at this loading percentage RL of -29.7 dB was achieved with 5 mm thickness. The authors reported that the absorption characteristics of nanocomposites were improved with the use of polyurethane in comparison to Paraffin Wax [60].

Bhongale et al. (2020) synthesized Mg-Cd Spinel ferrites with substitution of Nd. The chemical composition used was $Mg_xCd_{1-x}Nd_{0.03}Fe_{1.97}O_4$. The analysis was done from 8.2 to 12.4 GHz. All the compositions except x=0 and 0.8 had an RL peak in the range of the X band. The composition x=0.2 had the highest reflection loss of -18.38 dB at 12.32 GHz, however, x=1 had an RL of -18.33 dB with a bandwidth of 2.12 GHz. The thickness used for the ferrite sample was 4.2 mm [61].

Moradnia et al. (2020) fabricated and performed a comparative study of $BaFe_{12}O_{19}$, $Ba_4MnZnFe_{36}O_{60}$, and $NiFe_{12}O_4$ ferrites. A comparative graph of RL versus frequency

was presented for the three ferrites. From the graph, it can be noted that the $NiFe_2O_4$ ferrite had the highest reflection loss of -35 dB, while $BaFe_{12}O_{19}$ and $Ba_4MnZnFe_{36}O_{60}$ had -15 dB and -22 dB respectively. It can be concluded that $NiFe_2O_4$ had better absorption properties as compared to the other two [62].

Yu He et al. (2020) prepared a Co_2Y ferrite and investigated the performance parameters. The process used in the development of ferrite was the sol-gel method. The analysis was first done on simple Y ferrite. The results revealed that in pure Y ferrite, the absorption characteristics were very poor. The RL peaks below -10 dB were obtained at large thickness as a RL of -24.82 dB was obtained at 8.0 mm. Since the thickness below 6.0 mm provides very low reflection loss hence authors mixed Ni with Y ferrite and studied the effect on the performance of the ferrite. The results imply that the addition of Ni had improved the characteristics of ferrite since higher reflection peaks were present at low thickness. The analysis was done for a thickness of 2.0 mm with Ni wt % of 20, 40, 50 and 60%. There was an increase in the RL values as compared to pure ferrite. Among the different wt%, Ni with 40 wt% has an RL peak of -18.76 at a frequency of 6.24 GHz [63].

Rani et al. (2020) synthesized Ba-Sr hexagonal ferrite and performed an analysis on the effect of Co and Ga doping. The chemical composition used in the investigation was $Ba_{0.5}Sr_{0.5}Co_xGa_xFe_{12-2x}O_{19}$ where x had values from 0 to 1 with a step of 0.2 each. The analysis was done using impedance matching criteria as well as the $\lambda/4$ mechanism. They reported a reflection loss value of -33.36 dB when x=0.4 with a thickness of 2.0 mm for a frequency of 9.62 GHz [64].

Arora et al. (2019) presented a study on La and Na barium hexagonal ferrites to be used in Ka-band. The two chemical compositions used were $Ba_{1-2x}La_xNa_xFe_{10}CoTiO_{19}$ and $Ba_{1-2x}La_xNa_xFe_{10}Co_{0.5}TiMn_{0.5}O_{19}$. The authors claimed that the substitution of Mn caused higher electromagnetic properties. The first composite had a -31.68 dB reflection loss value for composition x=0.2 while the second composite had a -55.33 dB reflection loss. Thus it can be stated that the use of Mn enhanced the absorption of ferrite [65].

Luo et al. (2019) designed a hybrid material with reduced graphene, barium ferrite, and PANI. The ferrite composition was $BaTb_{0.2}Eu_{0.2}Fe_{11.6}O_{19}$. The authors presented an investigation of the effect of graphene on the absorption properties of the composite.

They achieved a good -60.9 dB loss with a small thickness of 1.95 mm. The frequency of the RL peak was found to be 16.4 GHz. The result indicates that the composite is very suitable as an absorption material due to its wide bandwidth of 4.2 GHz [66].

Wang et al. (2019) synthesized a $BaFe_{12}O_{19}$@ PANI composite for microwave absorption applications. The amount of aniline under investigation is 200, 400, and 600 ul. The analysis of barium ferrite, pure PANI particles, and barium ferrite/PANI composite was performed. The reflection loss obtained with $BaFe_{12}O_{19}$ was -14.15 dB while the pure PANI particles provide -35.8 dB. The $BaF_{12}O_{19}$@400PANI provided a -48.6 dB RL which shows that the PANI enhanced the characteristics of the composite [67].

Shu et al. (2018) prepared RGO/$ZnFe_2O_4$ nanocomposites. The electromagnetic parameters were determined with the help of a VNA. The frequency range used in the determination of the parameter was 2 to 18 GHz. The samples were prepared with a weight percentage of 25, 50, and 75 % with a paraffin matrix. The results showed that the increase in the filler content increases the absorption characteristics. The 75 wt% provided the highest RL with a value of -41.1 dB at 2.5 mm [68].

Li et al. (2018) investigated Co-doped barium ferrite with a composition of $Ba(CoZr)_xFe_{12-2x}O_{19}$. In all the composition x=0.4 had performed best in terms of higher loss and large bandwidth. A reflection loss of -28.7 dB with a thickness of 1.6 mm was obtained in this composition. -10 dB bandwidth of 5.36 GHz was obtained at a 1.7 mm thickness. All the compositions had reflection loss higher than the -10 dB mark. Thus the composite material may be stated as a prominant material for radio absorption [69].

Song et al. (2018) synthesized M-type barium ferrite using the sol-gel technique and investigated the role of Co and Ti substitution on the performance of barium ferrite. The chemical formula for the composite was $Ba(CoTi)_xFe_{12-2x}O_{19}$ with x = 0.2, 0.4 and 0.6. The analysis was done for a wide frequency band of 2 to 18 GHz. All three compositions had reflection peaks below the -10 dB. The reflection loss achieved for composition 0.2, 0.4, and 0.6 were -14.79 dB, -36.37dB, and -29.51 dB respectively. Hence it can be said that composition x=0.4 was better as compared to others in terms of absorption characteristics. The corresponding thicknesses for these compositions were 4.7, 4.5, and 3.6 mm respectively [70].

Joshi et al. (2017) worked on M-type Ba-Sr hexaferrites doped with Co and Gd. An investigation was done for the chemical formula of $Ba_{0.5}Sr_{0.5}Co_xGd_xFe_{12-2x}O_{19}$ at x=0, 0.2, 0.4, 0.6, 0.8. The authors used the ceramic method for the fabrication of required ferrites. The composition at x=0.0 provides 96.23% absorption at a frequency of 11.22 GHz with a thickness of 3.0 mm. The maximum absorption of 96.90% was achieved with composition x=0.8 for a thickness of 2.9 mm at an 8.3 GHz frequency. From the results, it is evident that variation in frequency, thickness, and doping causes tunable absorption [71].

Singh et al. (2017) prepared an M-type hexaferrite using doping of Co and Al ions. The composition used in the analysis was $Ba_{0.5}Sr_{0.5}Co_xAl_xFe_{12-2x}O_{19}$. The analysis was carried out for a frequency range of 8.3 GHz to 12.4 GHz. Obtained results indicated that the absorption performance of ferrite had increased with the doping of Co and Al ions. The authors claimed a percentage absorption of 96.94 with a reflection loss of -16.4 dB with 2.9 mm thickness at 11.22 GHz. Absorption bandwidths of 500, 670, and 800 MHz were achieved for x=0.0, 0.2, and 0.8 respectively [72].

Malana et al. (2016) prepared molybdenum-doped strontium calcium hexagonal ferrites. The coercivity of all the prepared compositions increased with an increment in Mo doping concentration. The coercivity of the samples increases from 681.81 Oe (x=0.0) to 808 Oe (x=0.4). The reason behind this is that the replacement of Fe^{3+} (magnetic) by Mo^{6+} (less magnetic) causes a reduction in iron ions which in turn increases the coercivity [73].

Z. Mosleh et al. (2016) synthesized Ce-substituted barium hexaferrite with the chemical composition of $Ba_{1-x}Ce_xFe_{12}O_{19}$. A non-uniform variation in saturation magnetization and coercivity was observed with the inclusion of Ce content. The maximum values for these two were 53 emu/g and 5088 Oe in the case of sample x=0.1. They reported the highest reflection loss of -20.40 dB with 16.1 GHz for x=0.2 [74].

Aminreza Baniasadi et al. (2016) analyzed the microwave absorption properties of Ti–Zn doped strontium ferrites with a chemical composition of $SrFe_{12-x}Ti_{x/2}Zn_{x/2}O_{19}$. Authors reported a decrement in coercivity from 5640 to 1486 Oe with the inclusion of Ti-Zn content. The maximum saturation magnetization of 63 emu/g was obtained in the case of composition x=0.5. The maximum reflection loss of -36.58 dB was achieved for composition x=2.5 [75].

Zheng He et al. (2015) prepared a PANI/Ag/$SrFe_{12}O_{19}$ composite and analyzed the electrical, optical, and magnetic parameters of the developed composites. An inclusion of Ag caused a decrement in the saturation magnetization from 117.22 to 70.54 emu/g. The PANI/Ag/$SrFe_{12}O_{19}$ composite had the highest RL peak of -14.86 dB at 9.98 GHz [76].

2.2 Research Gap and Problem Formation

The literature survey is carried out on microwave-absorbing materials using ferrite. The literature survey indicates that the absorber using ferrite is a very growing field of research. It has been noted from the study of literature that most of the work is done to obtain high reflection loss and wide bandwidth. However, for a good absorber, it is necessary that it should also be feasible in terms of size and should be cost-effective.

For an absorber if it is providing higher reflection loss but its size is big then it cannot be used with the electronic circuits which are very small in size. Hence thickness of the material becomes a very important parameter in this situation. So to meet this requirement, the bandwidth-to-thickness ratio of an absorber becomes a very critical parameter for an absorber. In the literature survey, this concept looks missing. Thus research in this regard is extensively required to deal with this restrain.

From the survey it can also be noted that most work has been done on spinel ferrites and microwave absorption studies have not been conducted much on M-type strontium ferrites. An investigation of the doping effect on the performance of the strontium-cobalt ferrite composite is also required. Hence to deal with these restrains the following M-type ferrite series and their composites are prepared and investigated.

Series I: $SrCo_xZn_xFe_{12-2x}O_{19}$ (x=0.0-1.0, step size 0.2)

Series II: $SrCo_xNi_xFe_{12-2x}O_{19}$ (x=0.0-1.0, step size 0.2)

Series III: $SrCo_xZr_xFe_{12-2x}O_{19}$ (x=0.0-1.0, step size 0.2)

2.3 Title of the Research Work

“Fabrication, Investigation and Optimization of Electromagnetic Parameters of Ferrite Composite based RF Absorber”

2.4 Objectives of Proposed Work

1. Fabrication of ferrite composites and study of their band gap characteristics.
2. Measurement, evaluation and analysis of electromagnetic parameters of ferrite composite; complex permittivity and complex permeability
3. Optimization of performance parameters; reflection loss, -10 dB bandwidth and bandwidth to thickness ratio.

CHAPTER 3

RESEARCH METHODOLOGY

3.1 Fabrication process of Hexaferrite

The first objective of the research work is the fabrication of M-type hexagonal ferrite samples. There are many methods to prepare ferrite samples which are the sol-gel, hydrothermal synthesis, co-precipitation, and ceramic methods. Among these, a sol-gel method is the simple and cost-effective method of ferrite synthesis. Hence this method has been used to develop the ferrite samples. This method is best suited as it provides good purity and uniform structure. Three series have been prepared with a general chemical formula of $SrCo_xM_xFe_{12-2x}O_{19}$, where M is Zn, Ni, and Zr and x=0.0, 0.2, 0.4, 0.6, 0.8, and 1.0. Thus the chemical compositions for these series can be written as $SrCo_xZn_xFe_{12-2x}O_{19}$, $SrCo_xNi_xFe_{12-2x}O_{19}$, and $SrCo_xZr_xFe_{12-2x}O_{19}$.

3.1.1 Preparation of Ferrite sample using sol-gel

The sol-gel process contains multiple steps which are hydrolysis, polymerization, gelation, condensation, and drying. The fabrication process is divided into twelve steps which are shown in the form of a flow chart in Fig. 3.1 and are explained below.

1. The first step is to weigh the stoichiometric amount of chemicals using a weighing machine.
2. The second step is to prepare a nitrate solution. AR-grade nitrates of all the elements have been mixed in distilled water while stirring the solution on a magnetic stirrer.
3. The next step is to prepare a citric acid solution. For it, citric acid powder is mixed with distilled water while stirring it on a magnetic stirrer.
4. This solution is added to the nitrate solution.
5. Now this solution is cooled to room temperature.
6. A solution of ammonia with water is prepared. This ammonia solution is added dropwise to the prepared solution.
7. The PH level is checked during the mixing of ammonia solution. Ammonia is added till a PH of 7 is achieved.

8. When the PH level of the solution becomes 7 it is called Sol.
9. This sol is heated at 80^0 C on a hot plate till it turns into Gel.
10. An auto combustion starts which makes this gel into ash.
11. This ash is converted into fine powder.
12. This powder is heated for 8 h at 900^0 C to get the final sample.

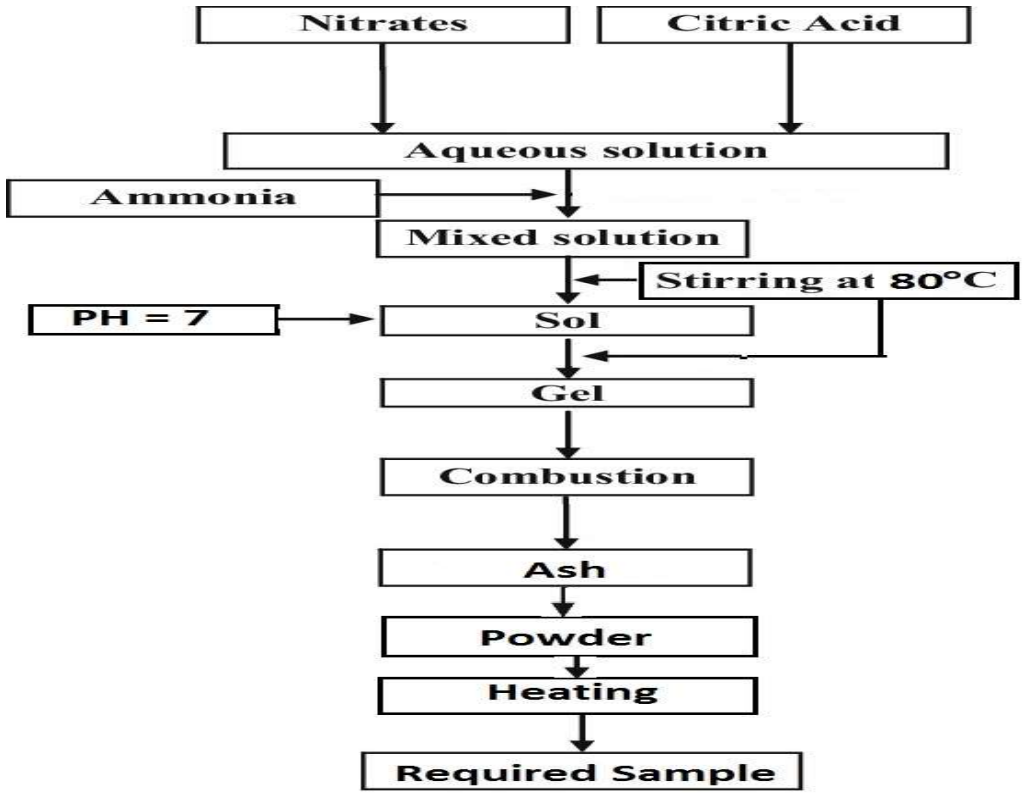

Fig. 3.1 Flow chart of the fabrication process of ferrite samples

Fig. 3.2 Sample prepared using sol-gel method

3.1.2 Preparation of ferrite composites

With the process discussed in the previous section ferrite samples were prepared. As the ferrites are hard in nature they should be made soft by mixing filler materials to get the desired shape. The mixing of these filler materials also improves the electric and magnetic parameters of ferrite samples. To prepare ferrite composites polyaniline (PANI) was added to the ferrite samples. PANI is a conductive polymer that enhances the electromagnetic properties of the ferrites. First PANI was prepared using a chemical polymerization method in which ammonium persulfate as an oxidizing agent is used. Ammonium persulfate was used to polymerize the aniline by maintaining a temperature of 0 to 5 °C. After drying the solution required powder form of PANI was obtained. The PANI powder was mixed with the ferrite powder in a ratio of 20 % (PANI) to 80 % (ferrite) to form the ferrite composites.

3.2 Pellet formation and sintering

The prepared samples as discussed in the previous section were used to prepare pellets. The pellets of these samples were prepared using a hydraulic press. The shape of the

pellets should be rectangular as the waveguide used for the measurement of EM parameters using Vector Network Analyzer (VNA) is rectangular. First, a die set was prepared in a rectangular shape for the formation of pellets. The synthesized powder was put in the rectangular die and placed under the hydraulic press. A uniaxial pressure of 2-3 tons/cm^2 with a holding time of 2 minutes was applied by a hydraulic press to convert fine powder into pellet.

The pellets formed using the above-said procedure are sintered to make them hard so that the measurement of parameters through VNA can be performed. The pellets were sintered at 900 ºC for 2 h. After that, they were cooled to room temperature to obtain hexagonal ferrite compositions.

Fig. 3.3 Rectangular pellets prepared for VNA measurement

3.3 Microstructural/Morphological Characterization

3.3.1 X-ray diffraction analysis

This analysis has been performed to determine the structural parameters and phase identification. Rigaku Miniflex-II diffractometer of 15 mA current and 30 kV voltage with a step size of 0.005 was used to acquire the XRD pattern. The analysis was performed with Cu Kα radiation (λ=1.5405 Å) for the angle of 20°-80°. The analysis has been carried out using Powder-X software to determine Miller indices. The patterns were indexed using the standardized patterns of Strontium ferrite-$SrFe_{12}O_{19}$ having space group P63/mmc (ICDD file no.84-1531).

The d-spacing (d_{hkl}) and the cell volume (V) of the developed compositions have been calculated by lattice parameters $(a = b, c)$ and miller indices (h, k, l) using equations 3.1 and 3.2 [77].

$$\frac{1}{d_{hkl}^2} = \frac{4}{3}\left(\frac{h^2}{a^2} + \frac{hk}{a^2} + \frac{k^2}{a^2}\right) + \frac{l^2}{c^2} \quad (3.1)$$

$$V = \frac{\sqrt{3}}{2}a^2c \quad (3.2)$$

The Debye-Scherer equation is used to determine the average crystallite size (D_{xrd}) as shown in equation 3.3.

$$D_{xrd} = 0.94\ \frac{\lambda}{\beta Cos\theta} \quad (3.3)$$

Where D_{xrd} is an average crystallite size at Bragg angle θ with wavelength $\lambda = 1.5406$ Å and β is FWHM of the major intensity peak.

3.3.2 Scanning electron microscopy

An SEM is used to investigate the microstructure/morphology of the prepared compositions. The grain size and grain distribution for the prepared compositions are analyzed using SEM images. The scanning electron microscopy was performed with an accelerating field of 5 to 10 kV handled at a 5 mm working distance. The microscope (FESEM, Jeol, JSM-7100, Japan) was used to obtain the microstructures of the prepared compositions.

3.4 UV-Vis spectroscopy

For optical characterization, UV-Vis spectroscopy has been performed using a spectrophotometer (Jasco V-770). The band gap characteristics are determined using UV-Vis spectroscopy. In this technique, the analysis is done on the basis of light absorbed or transmitted by the material. The sample is placed under UV rays and absorbance has been determined. This absorbance data is further used to acquire the band gap of the material. The formula used to calculate the band gap is given in equation 3.4.

$$(\alpha h\nu)^2 = A^2\ (h\nu - E_g) \quad (3.4)$$

Here α is the absorbance coefficient, hν represents photon energy and E_g denotes band gap. According to equation 3.4 at $\alpha h\upsilon = 0$, E_g=hν. Hence a plot between $(\alpha h\upsilon)^2$ and hν was plotted and an intercept was found on the hν axis.

3.5 Measurement and analysis of electromagnetic parameters

3.5.1 Electrical characterization

Electrical characterization of the prepared composition has been done to determine various electrical parameters. Disk-shaped pellets were made of a diameter of around 5 mm and a thickness between 1.5 and 3.1 mm. The silver paste was coated on the pellets to make contact points for the measurement of electrical parameters. Agilent LCR meter (Model-E4980A) was used to determine the capacitance and resistance values in a 20 Hz to 2 MHz frequency band. The measured values were used to calculate the impedance (Z′= R and Z″= 1/ωC) of the prepared compositions. These impedance values were further used to determine different dielectric/electric parameters which are as follows.

Fig. 3.4 LCR meter used for electrical characterization

3.5.1.1 Dielectric constant

Dielectric constant of ferrite is of complex nature with its real part (ε') indicating the degree of polarization in the ferrite material and imaginary term (ε'') representing the

dielectric loss. The formula to calculate the real part of the dielectric constant is presented in equation (3.5).

$$\varepsilon' = \frac{L}{\omega A \varepsilon_o} \cdot \frac{Z''}{Z'^2 + Z''^2} \quad (3.5)$$

Where L, ω, A, and ε_o are thickness, angular frequency, area, and free space permittivity respectively, while Z' and Z'' represent the real and imaginary values of impedance respectively.

The imaginary part of the dielectric constant (ε'') is calculated using the formula mentioned in equation (3.6). From the values of ε' and ε'' the required loss tangent ($tan\delta$) could be obtained as given in equation (3.7).

$$\varepsilon'' = \frac{L}{\omega A \varepsilon_o} \frac{Z'}{Z'^2 + Z''^2} \quad (3.6)$$

$$tan\delta = \frac{\varepsilon''}{\varepsilon'} \quad (3.7)$$

3.5.1.2 Electric Modulus

The electric modulus (M) provides the electrical relaxation of ionic solids. This is used to investigate a frequency dependence of the conductivity of materials. The study of complex electric modulus formalism guides to understand electrical conduction as well as the space charge polarization influence. The electric modulus is given by M= M′ + j M″ where real and imaginary parts are calculated as

$$M' = \frac{\varepsilon'}{\varepsilon'^2 + \varepsilon''^2} \quad (3.8)$$

$$M'' = \frac{\varepsilon'\prime}{\varepsilon'^2 + \varepsilon''^2} \quad (3.9)$$

3.5.1.3 AC conductivity

Hopping of the electrons between Fe^{2+} and Fe^{3+} for (Octahedral) B-sites has the leading role in the conduction process in ferrites. The increase in frequency causes a relative increment in the hopping frequency of charge carriers which enhances the conductivity. The ac conductivity ($\boldsymbol{\sigma_{ac}}$) is related to the dielectric relaxation which follows the empirical power law [78]

$$\sigma(\omega) = A\omega^n \quad (3.10)$$

A and n are constants that depend on the composition of the sample.

The term $A\omega^n$ denotes the dispersion in ($\boldsymbol{\sigma_{ac}}$). As per Funke [79], $n < 1$ represents a translational motion with sudden hopping, whereas $n > 1$ indicates localized hopping between neighbor sites. The values of n for prepared compositions were acquired by fitting plots.

3.5.2 Magnetic Characterization

For the magnetic characterization of the prepared compositions magnetic parameters are determined. These magnetic parameters which are coercivity (H_c), saturation magnetization (M_s) and remanence (M_r) of the samples were determined utilizing VSM (vibrating sample magnetometer) measurement. Magnetization (M) v/s magnetic field (H) graphs of all the compositions are plotted to analyze the magnetic characteristics. Besides the $M\ v/s\ H$ loops graphs of M v/s $1/H^2$ are plotted and linear fitting is performed to calculate the respective value of saturation magnetization (M_s) and anisotropy field (H_a).

3.5.3 Microwave absorption characteristics

The microwave absorption characterization of the prepared compositions has been performed by measuring different electromagnetic parameters. A Vector Network analyzer (VNA) is employed to determine these parameters. VNA is a device that measures different scattering parameters (S-parameters) of the signal passed through the sample under test. The measurement representation of parameters using VNA is shown in Fig. 3.5.

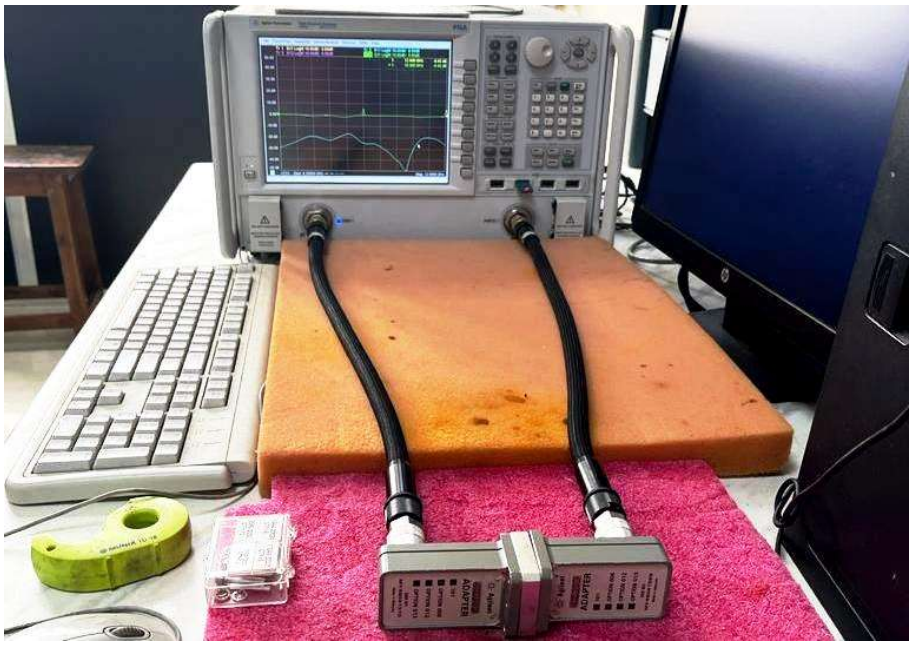

Fig. 3.5 Measurement of parameters using VNA

The model used in the measurement was Agilent N5222A. The rectangular pellets of the prepared compositions are put in the rectangular waveguide attached to the VNA. The measurement of the parameter using a vector network analyzer is performed for the 8.2 to 12.4 GHz frequency band.

3.5.3.1 Complex permittivity and complex permeability

The parameters required to observe the absorption performance of the samples are complex permittivity ε and complex permeability μ. The VNA measures S-parameters which are utilized to determine respective complex permittivity and permeability by the Nicholson-Ross-Weir method. A complex permittivity is written as

$$\varepsilon = \varepsilon' - j\varepsilon'' \qquad (3.11)$$

ε′ represents the dielectric constant and ε″ is the respective loss (attenuation) caused in the material. The loss tangent can be determined as $\tan\delta_\varepsilon = \varepsilon''/\varepsilon'$. In the same way, the permeability is given as

$$\mu = \mu' - j\mu'' \qquad (3.12)$$

Here μ′ is permeability, however, μ″ is magnetic loss respectively. The magnetic loss tangent can be calculated by tan $\delta_\mu = \mu''/\mu'$. These losses in an electric or magnetic field or both caused attenuation in the incident waves.

3.5.3.2 Reflection Loss and BTR

Reflection loss denotes the absorption characteristics of a material. Transmission line theory is deployed to determine the reflection loss (RL) for a material. The RL of the developed compositions was determined from the equation 3.13 given as [13]

$$\boldsymbol{RL = 20log\left|\frac{(Z_{in}-Z_o)}{(Z_{in}+Z_o)}\right|} \qquad (3.13)$$

Since Z_0 is the characteristic impedance of free space its value is predetermined which is 377Ω, however, the input impedance of material Z_{in} can be acquired using the formula given as [13]

$$\boldsymbol{Z_{in} = Z_o\sqrt{\frac{\mu_r}{\varepsilon_r}}tanh\left[j(\frac{2\pi ft}{c})\sqrt{(\mu_r.\varepsilon_r)}\right]} \qquad (3.14)$$

Here μ_r and ε_r are complex permeability and complex permittivity of the material while c denotes speed of light and t represents thickness respectively.

The -10 dB reflection loss denotes 90% absorption while -20 dB of RL denotes the 99% absorption. From the values of RL, determined as discussed above, the bandwidth to thickness ratios (BTR) of the developed compositions were determined. First, bandwidth was calculated from the frequency band having RL above -10 dB. Onward, the BTR was determined as the absorption bandwidth divided by the respective thickness of the sample.

3.6 Optimization of electromagnetic parameters

The observations received in the above steps will be optimized to provide better performance of the sample prepared. The absorption characteristics of the absorber will be optimized using the impedance matching phenomenon and λ/4 mechanism.

3.6.1 Impedance matching mechanism

From equation (3.13) it is clear that as the input impedance Z_{in} becomes equal to the characteristic impedance Z_0 the reflection loss will get infinite value. Thus, by matching

the input impedance of the material with Z_0, reflection loss can be increased. The obtained sample parameters will be varied according to the criteria so that the performance of the sample can be enhanced. Further, from equation (3.14) it can be noted that Z_{in} is a complex value that has both real as well as imaginary parts, hence to satisfy the impedance matching criteria the input impedance's real part should be equal to Z_0 (377 Ω) and imaginary term must be zero. Hence input impedance Z_{in} along with real and imaginary parts for all the prepared compositions is investigated to analyze the occurrence of impedance matching mechanism in the prepared compositions. The graphs of $|Z_{in}|$ and RL with frequency are plotted for the prepared composition to investigate impedance matching. The graphs of Z_{real}, $Z_{imag,}$ and RL against frequency are also analyzed.

3.6.2 Quarter wavelength mechanism

Quarter wavelength (λ/4) mechanism is used to optimize the thickness of the sample. On the basis of the λ/4 mechanism the thickness is a function of wavelength and is given as [14]

$$t_m = \frac{n\ \lambda}{4\sqrt{|\mu_r.\varepsilon_r|}} \qquad (3.15)$$

Where t_m is the thickness, λ is the wavelength and n is an odd integer. μ_r represents the permeability and ε_r is the permittivity of the material.

Various thicknesses and wavelengths are used to satisfy the λ/4 mechanism to achieve optimum results from the prepared compositions. The calculated thickness (t_m^{cal}) of each composition for different values of n=1, 3, and 5 are determined using equation 3.15. The graphs of reflection loss against frequency for various simulated thicknesses (t_m^{sim}) are plotted to establish the relation between RL peaks and λ/4 mechanism. The investigation is done by comparing the t_m^{sim} with t_m^{cal}. The respective graph of t_m^{cal} versus frequency is plotted in association with the RL versus frequency graph of various simulated thicknesses. The lines from the RL peaks are stretched to the calculated thickness versus frequency graph. These lines cut exactly or nearly at the same calculated thickness on the n λ/4 curve which shows the accomplishment of the quarter wavelength mechanism.

Chapter 4

RESULTS AND DISCUSSION

4.1 $SrCo_xZn_xFe_{12-2x}O_{19}$ series

4.1.1 Microstructural/Morphological characteristics

XRD graphs of the prepared hexagonal ferrites are shown in Fig. 4.1. The analysis has been carried out using Powder-X software to determine Miller indices. The patterns were indexed with a standard pattern of Strontium ferrite-$SrFe_{12}O_{19}$ with space group P63/mmc (JCPDS card no.84-1531). From the diffractograms, it can be seen that there is no secondary phase present and all the peaks of prepared compositions matched with the pure phase of strontium ferrite. Table 4.1 enlists different structural parameters of prepared compositions. It can be observed that the lower level causes a meager change in the crystallite size, however, it decreases substantially at the high doping level. The crystallite size ranges between 40.66 to 26.42 nm and the composition x=1.0 has the lowest crystallite size of 26.42 nm.

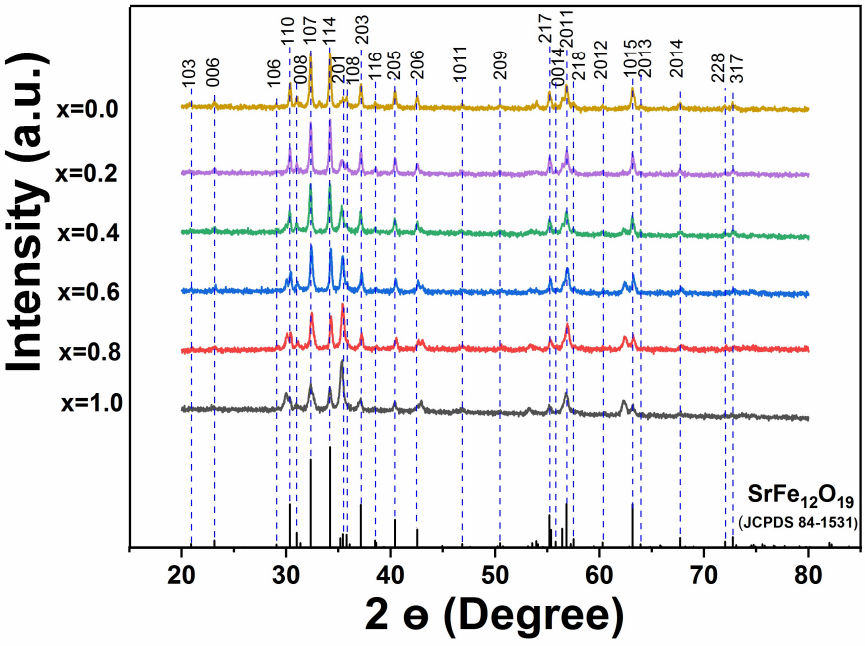

Fig. 4.1 XRD pattern of $SrCo_xZn_xFe_{12-2x}O_{19}$.

Table 4.1. Structural parameters of $SrCo_xZn_xFe_{12-2x}O_{19}$.

Co-Zn Content (x)	a (Å)	c (Å)	c/a	V(Å)^3	D_{xrd}(nm)	d-spacing (Å)
0.0	5.8869	23.0500	3.9154	691.7707	39.50	2.77
0.2	5.8869	23.0400	3.9137	691.4705	40.66	2.62
0.4	5.8915	23.0500	3.9124	692.8522	38.77	2.62
0.6	5.8778	23.0350	3.9189	689.1848	38.77	2.62
0.8	5.8717	23.0150	3.9196	687.1580	32.16	2.53
1.0	5.8874	23.0500	3.9151	691.8882	26.42	2.53

For analyzing the morphology of the developed compositions scanning electron microscopy was done. These micrographs of compositions of $SrCo_xZn_xFe_{12-2x}O_{19}$ are displayed in Fig. 4.2. The large grains have been formed due to the fusion and agglomeration of grains in the composition x=0.0 and composition 0.2. The doping of Co-Zn has affected the grain distribution with the decrease in grain size, improved inter-grain connectivity, and grain agglomerates as observed in Fig. 4.2 (b), (c), and (d). A honeycomb with a needle-shaped structure is formed with the increment in doping as demonstrated in Fig. 4.2 (f).

The SEM shows that there are visible voids in the arrangement of grains that provide a hindrance to the flow of the charges that accumulated at the grain boundary. This causes polarization and modifies the electrical properties. The small size of grains will cause an increase in the number of grain boundaries. Hence more boundaries will provide high resistivity to the applied field.

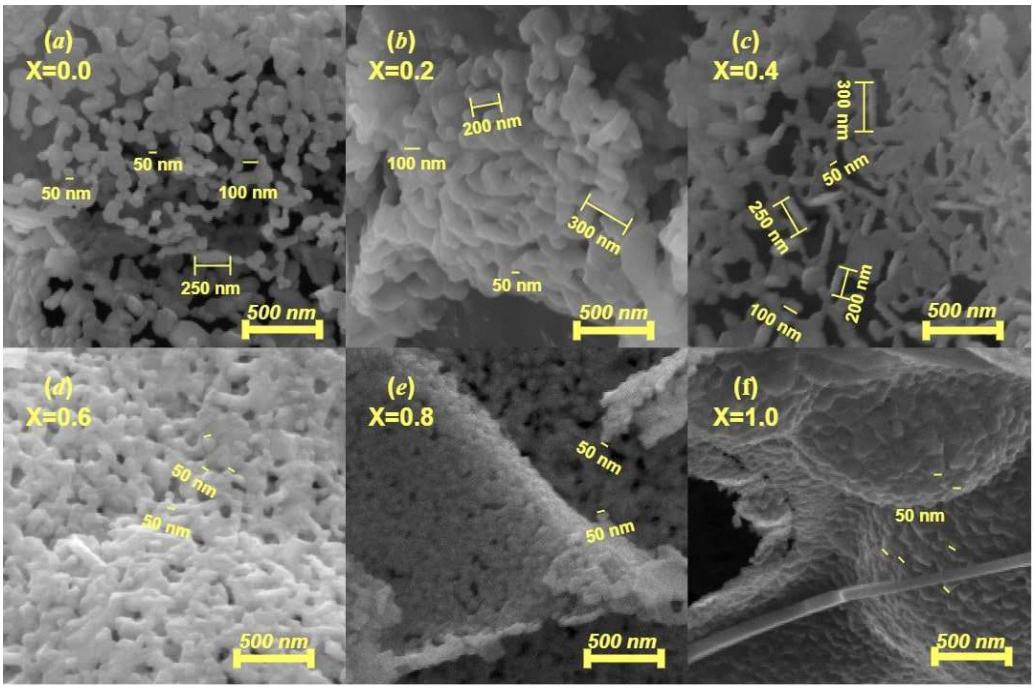

Fig. 4.2 SEM micrographs of $SrCo_xZn_xFe_{12-2x}O_{19}$

4.1.2 Electrical Characteristics

4.1.2.1 Dielectric Constant

Dielectric constant of ferrite is of complex nature with its real part (ε') indicating the degree of polarization in the material and imaginary part (ε'') representing the dielectric loss. The formula to determine the real part is shown in equation (3.5). Dielectric loss ε'' is calculated using equation (3.6), while the loss tangent ($tan\delta$) can be determined by equation (3.7) as given in chapter 3.

The variations in ε' and ε'' versus frequency are displayed in Fig. 4.3. ε' increases non-linearly with dopants and owes high values in the low-frequency area, while in the high-frequency regime, it first decreases and then attains a constant value. This dispersion is due to the interfacial polarization and complies with the Maxwell-Wagner model with Koop's phenomenon [36, 80]. For a low frequency, grain boundary is more prominent while grains are for high frequencies. The high resistance of grain boundaries causes charge careers to gather at the boundaries causing space charge polarization which contributes to the permittivity at low frequency. However, for high frequencies grains assist the conduction, and electron's hopping in Fe^{2+} and Fe^{3+} can not accompany the

change in frequency, and lag behind the field. It reduces the gathering of charges at boundaries and leads to a decrement in the dielectric constant.

It is noteworthy that composition x=0.2 carries with maximum ε' in the low-frequency region among doped compositions. The polarization is dependent on Fe^{3+}/Fe^{2+} in ferrites and such charge carriers are higher in x=0.2 than the other doped compositions, causing ε' scale to the maximum value. However, ε' for composition x=0.0 is lower than x=0.2 in spite highest Fe^{3+}/Fe^{2+} in the former. This is related to grain morphology in Fig. 4.2: undoped x=0.0 constitutes small grains with large porosity, while x=0.2 owes less porosity with relatively better inter-grain connectivity than x=0.0. Thus, the applied signal encounters more impediment in x=0.0 resulting in high porosity induced low polarization which lowers down ε'.

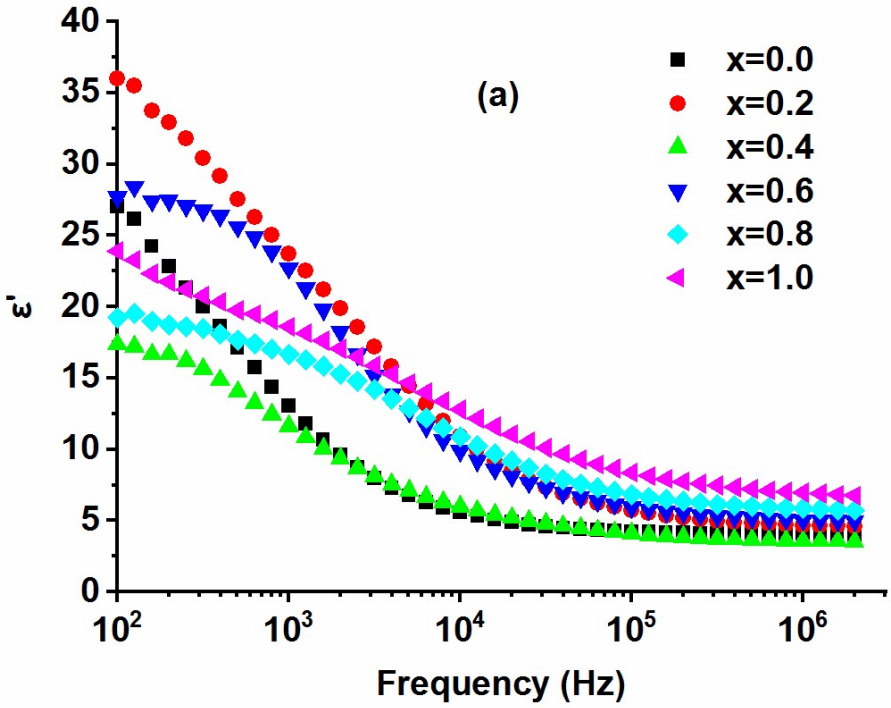

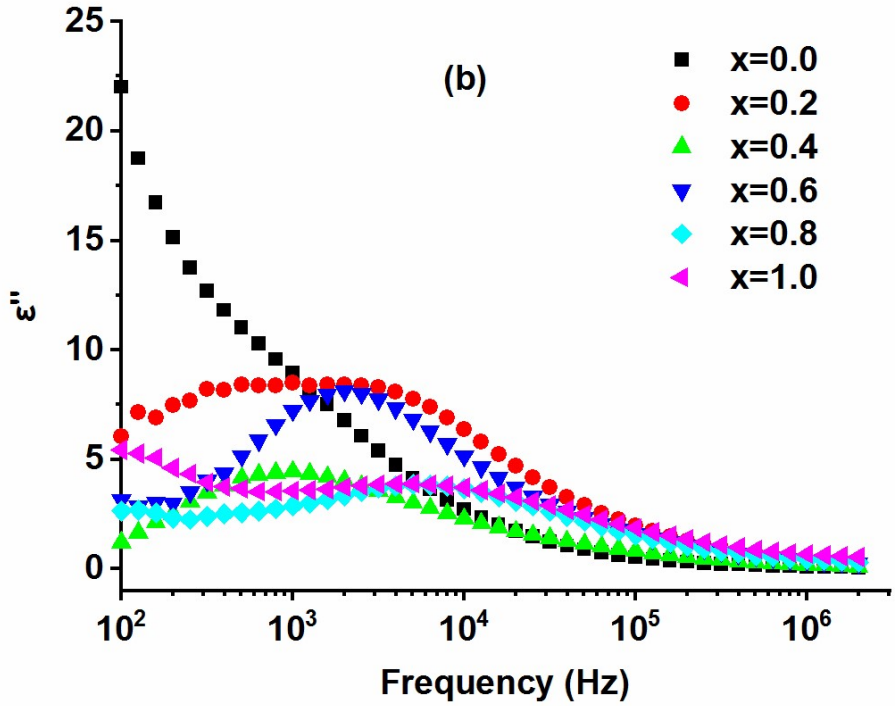

Fig. 4.3. Plot of dielectric constant (a) real term (b) imaginary term for $SrCo_xZn_xFe_{12-2x}O_{19}$.

The plots for loss tangent (tanδ) with frequency are demonstrated in Fig. 4.4 which shows a decrease in tanδ with the frequency increment. The decrement in the loss tangent is according to Koop's phenomenological theory of dielectrics [80]. Since for low frequency, grain boundaries are active and impede electron hopping which causes a high value of loss tangent. At high frequencies grains are active and render the electron hopping, thus owing small values of loss.

The loss tangent varies in a non-monotonical way with Co-Zn doping and relaxation peaks are observed for all the compositions. This nature is associated with the Rezlescu model [81] according to which this peaking nature is obtained when the charge hopping frequencies match the frequency of the applied fields. Composition x=0.0 has the largest tanδ among all at the low-frequency region: The stored energy may be easily dissipated through the visible pores around the grains (Fig. 4.2) in comparison to doped compositions. The relaxation peaks become broad with dopants due to an increase in heterogeneity accompanied by an increase in the number of interfaces that require more

time for relaxation. It is noticed from the figure that the peak shifting towards the high-frequency regime due to the doping of Co-Zn is noticed.

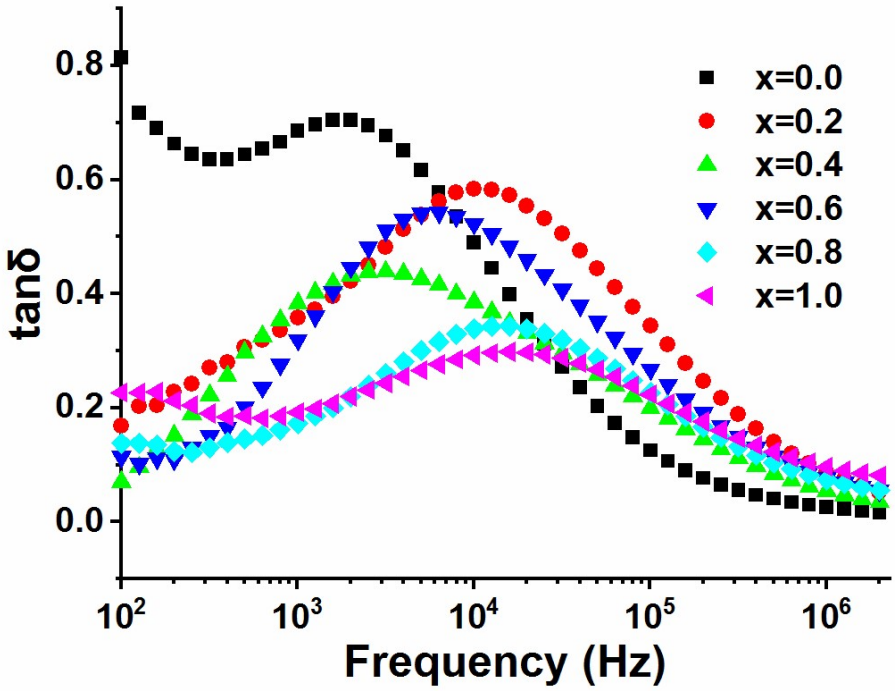

Fig. 4.4. Loss tangent versus frequency graph of $SrCo_xZn_xFe_{12-2x}O_{19}$.

4.1.2.2 Electric Modulus

A sigmoidal step in M′ and a broad asymmetric peak in M″ are the basic features of M concerning frequency [82, 83]. The graphs of M′ and M″ with frequency are given in Fig. 4.5 (a) and (b) respectively. It is noted that a similar trend has been reported in earlier reports [84]. M′ has a low value in a low-frequency regime and increases up to a certain value with the frequency increment. After that it tends to saturate at high frequencies, being the highest for composition x=0.4. The insufficiency of restoring force that governs the charge carriers' mobility may be a reason behind these observations. These observations assist to the long-range mobility of charges. A sigmoidal increase with an increase in frequency corresponds to the charge carrier's short-range mobility.

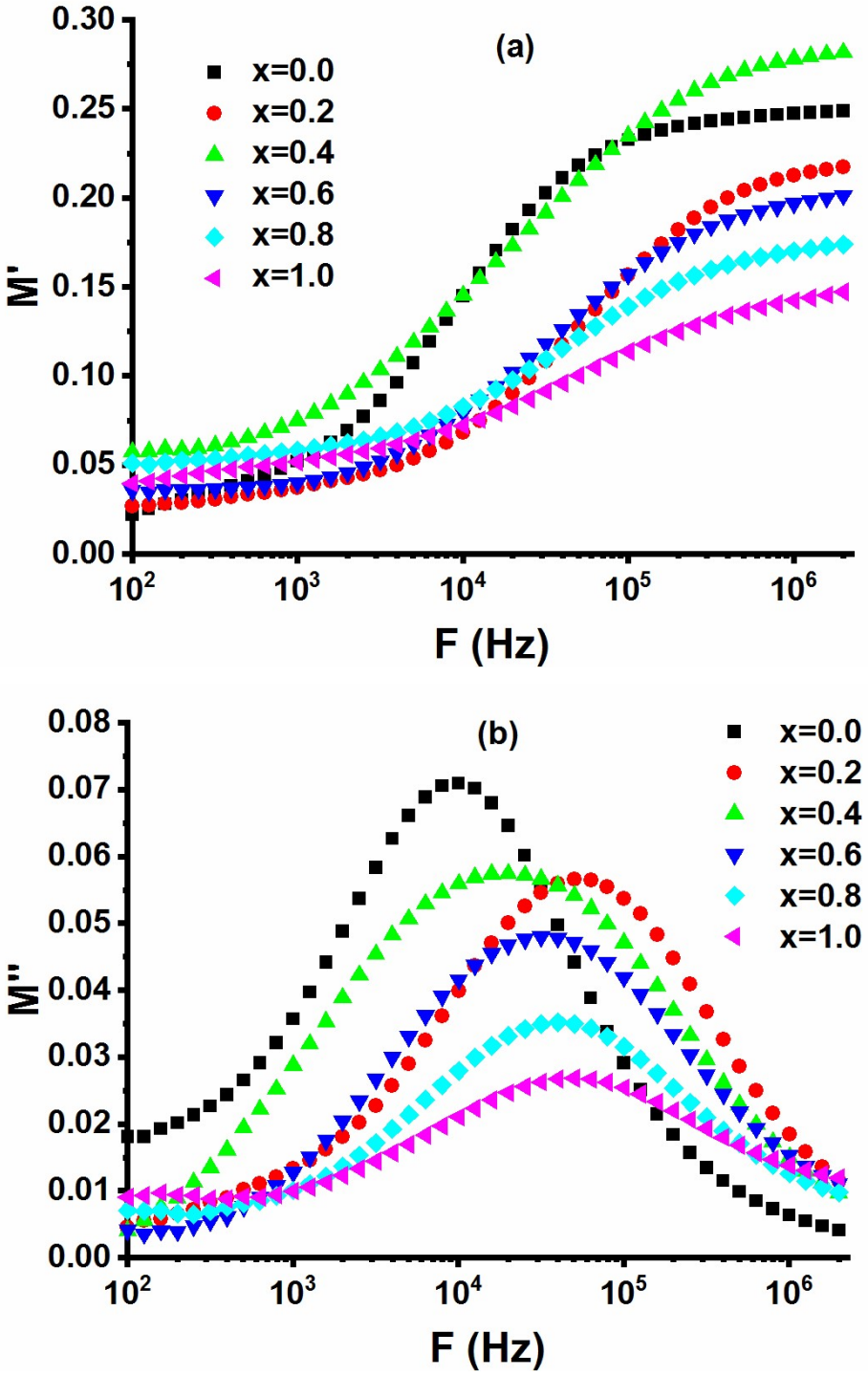

Fig. 4.5. (a), (b) Electric Modulus v/s frequency for $SrCo_xZn_xFe_{12-2x}O_{19}$.

The M″ versus frequency curve provides information about the charge relaxation mechanisms. It can be seen from the graph that all the prepared compositions show

asymmetric peaks. The low-frequency area of the peak is related to the long-distance movement of ions while for the high-frequencies they can do localized motion only and are confined to their potential well. The conduction relaxation time can be estimated from the peak frequency. The height of M″ reduces with the increase in doping due to a decrease in Fe^{3+} ions which causes a reduction in the number of charge careers. The doping also causes a broad nature of relaxation peaks associated with an increase in the heterogeneity of interfaces and dipoles. There is a shift in peaks toward the high frequency value with the increase in doping of Co-Zn which indicates the localized motion of ions. This shifting with doping of Co-Zn toward a high-frequency area indicates a reduction in relaxation time.

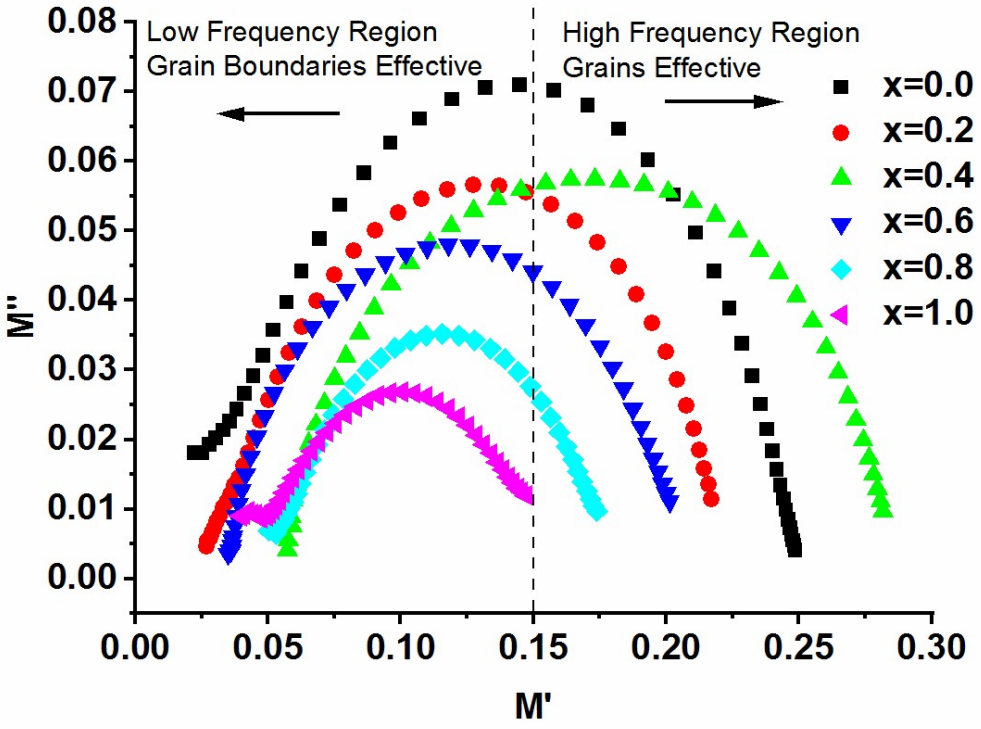

Fig. 4.6. Cole-Cole plots of $SrCo_xZn_xFe_{12-2x}O_{19}$

Fig. 4.6 shows the Cole-Cole plot ($M'vs\,M''$) of $SrCo_xZn_xFe_{12-2x}O_{19}$ (x = 0.0, 0.2, 0.4, 0.6, 0.8, and 1.0). An asymmetric deformed semicircle can be seen for all the prepared compositions with the center deviating from the x-axis which implies a non-Debye nature. The semicircle in undoped composition x=0.0 lies almost equally along high as well as low-frequency regions, hence both grain and grain boundaries are responsible

for charge transport. The doping of Co-Zn (x=0.2, 0.6, 0.8, and 1.0) shifts the arc towards a low-frequency regime while for x=0.4 it is toward high-frequency. This trend indicates that grains contribute more in composition x=0.4 while grain boundaries are dominant in the rest of the compositions.

4.1.2.3 Impedance Spectroscopy

Fig. 4.7 (a) indicates the change in Z′ with frequency. Z′ continuously decreases with frequency for a short period and becomes constant thereafter. The reason behind this variation can be due to the Maxwell-Wagner model accompanied by the effectiveness of grain boundary and grain respectively at low-frequency and high-frequency areas. A decrement in a maximum value of Z′with the increase in doping of Co-Zn as compared to the undoped (pure) composition. Micrographs depict improvement in inter-grain connectivity which reduces the resistance of individual grain boundaries. Further, for the high-frequencies, all plots coalesced with the lowest values.

The plot of Z'' concerning frequency is given in Fig. 4.7 (b). It increases with an increase in doping of Co-Zn and reveals the rise in the reactance of a material. This type of behavior is because of the decrement in space charge polarization with the increase in Co-Zn content: reactance is related in opposite to the capacitance (X or $Z' \leftrightarrows 1/\omega C$) and polarization varies in proportion to capacitance. Further, at high-frequency coalescing of all the curves indicates the fall in space charge polarization with increasing frequency.

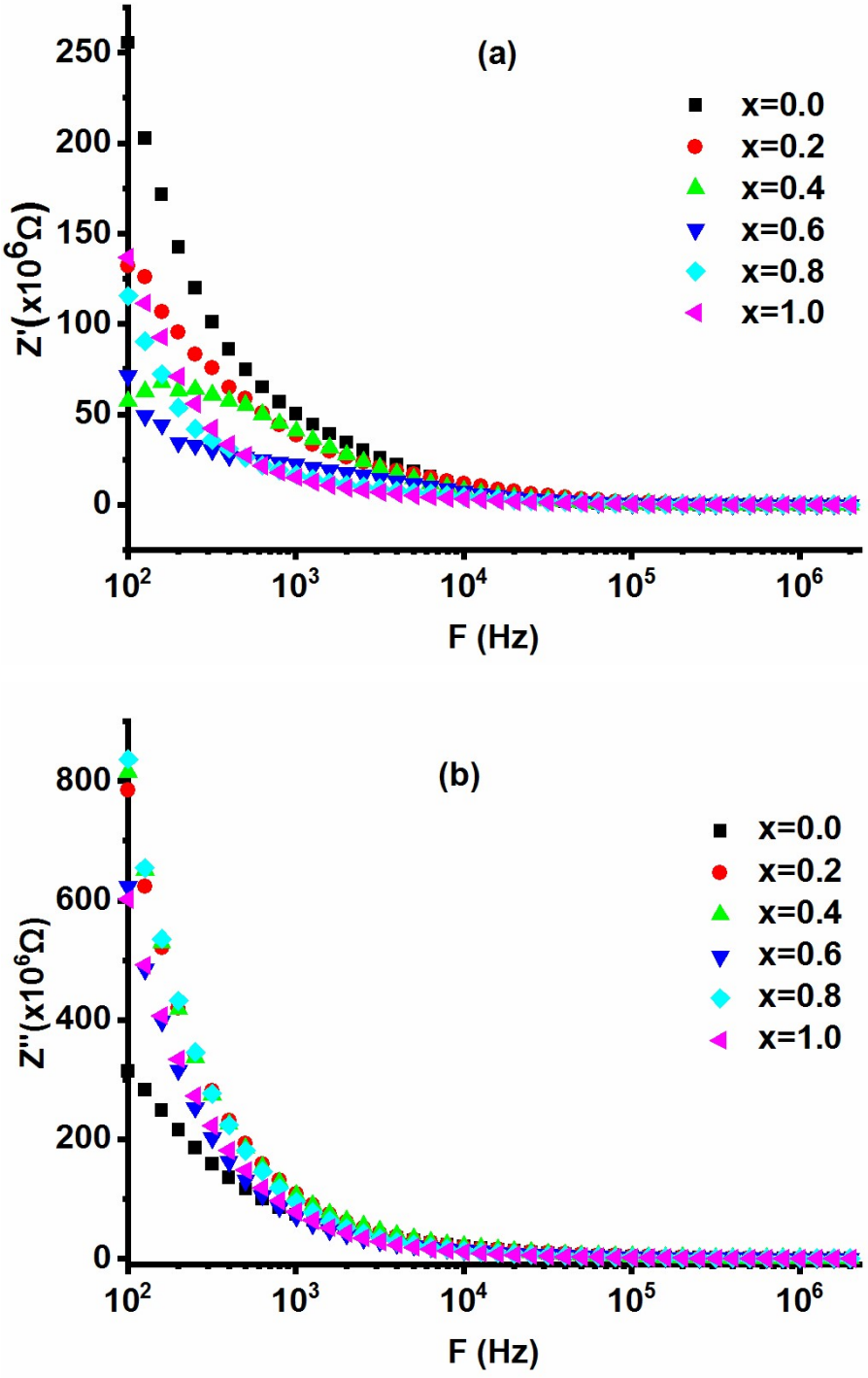

Fig. 4.7. (a), (b) Variation of Impedance of $SrCo_xZn_xFe_{12-2x}O_{19}$.

Cole-Cole plots ($Z''versus\ Z'$) of prepared compositions are demonstrated in Fig. 4.8. The plots show a semi-circular arc for each composition. The plots for x=0.0, 0.2, and

0.4, lie in the mid-region of the frequency which signifies that both grains and grain boundaries are contributing. The composition x=0.6 shows the bending of the curve toward the high-frequency side showing the fusing of grains as depicted in micrograph Fig. 4.2 (d). The curves of compositions x=0.8, 1.0 are indicating the dominance of grains as they lie on the high side.

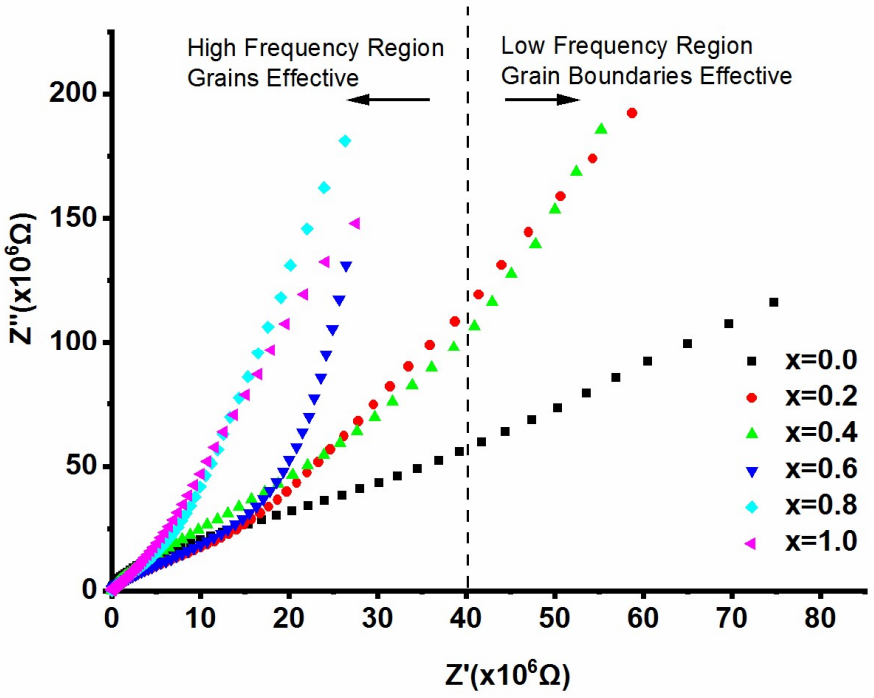

Fig. 4.8. Cole-Cole plot of Impedance for ferrite $SrCo_xZn_xFe_{12-2x}O_{19}$.

4.1.2.4 AC conductivity

The plot of ac conductivity **(σ_{ac})** of prepared compositions is plotted in Fig. 4.9. It tends to increase after a particular frequency called hopping frequency. This hopping frequency indicates the transition from the flat plateau region of dc conductivity **(σ_{dc})** to the dispersive region of ac conductivity **(σ_{ac})**. All the compositions show frequency-independent behavior below this. The inclusion of Zn^{2+} and Co^{2+} ions causes a decrease in conductivity in the low-frequency range but there is an increase in conductivity for doped compositions in comparison to the undoped composition in the high-frequency region. It can also be noted from the figure that the hopping frequency shifted to a low frequency with the increment in Co-Zn content. The reason for low values of dc conductivity is linked to the prevalence of interfacial polarization in dielectric constant

parameters as shown in Fig. 4.3 and diffusion of charge carriers is responsible for σ_{dc} [85].

For the high-frequency region with grain dominance, both x=0.0 and 0.4 have significantly low conductivity $\boldsymbol{\sigma_{ac}}$**.** It is due to the morphology: composition x=0.0 has large porosity around grains (Fig. 4.2), while the area of cross-section to the charge carriers of needle-shaped grains is very small in x=0.4, thereby reducing $\boldsymbol{\sigma_{ac}}$. Similarly, grain connectivity is good in x=1.0 which gives rise to the highest $\boldsymbol{\sigma_{ac}}$. The fitting of curves using Jonscher law has been done and the value of parameter n for prepared compositions (x=0.0 to x=1.0) was calculated. The respective values of n are 0.310, 0.367, 0.409, 0.430, 0.494, and 0.604. Thus, less than $n < 1$ values suggest, that the ac conductivity follows the hopping of charge carriers.

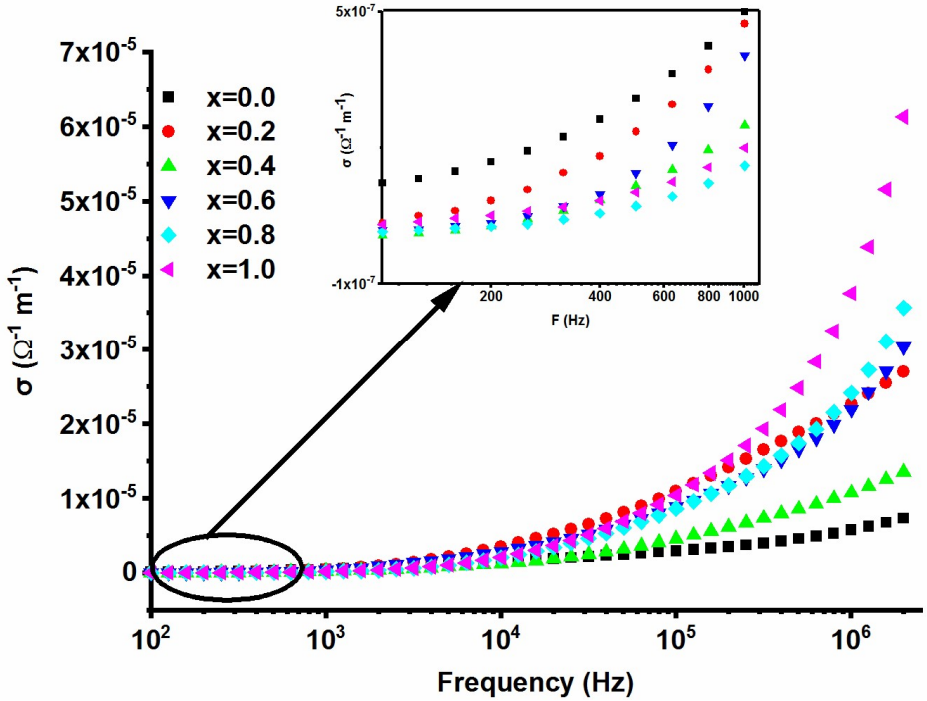

Fig. 4.9. AC conductivity v/s frequency for ferrite $SrCo_xZn_xFe_{12-2x}O_{19}$.

4.1.2.5 Software-based Impedance Simulation

Electrochemical impedance spectroscopy (EIS) software [86] is used to explore complex impedance data using circuit modeling as shown in Fig. 4.10. It has two parallel RC networks connected in series. One RC combination signifies resistance and capacitance

of grains (R_g, C_g), while the other is for grain boundary (R_{gb}, C_{gb}). Due to the non-Debye-type nature of compositions, a constant phase element (CPE) is employed. The capacitance of CPE was obtained using the relation [87]:

$$C_{CPE} = (AR^{-(n-1)})^{1/n} \qquad (4.1)$$

Here *A* and *n* are fitted parameters of CPE and R is the resistive value obtained from the equivalent circuit.

Fig. 4.10 shows the simulation results with the equivalent circuit obtained using EIS software. It can be seen that measured plots and simulated/fitted graphs agree with each other. The determined values of resistances and capacitances for grains/grain boundaries are enlisted in Table 4.2.

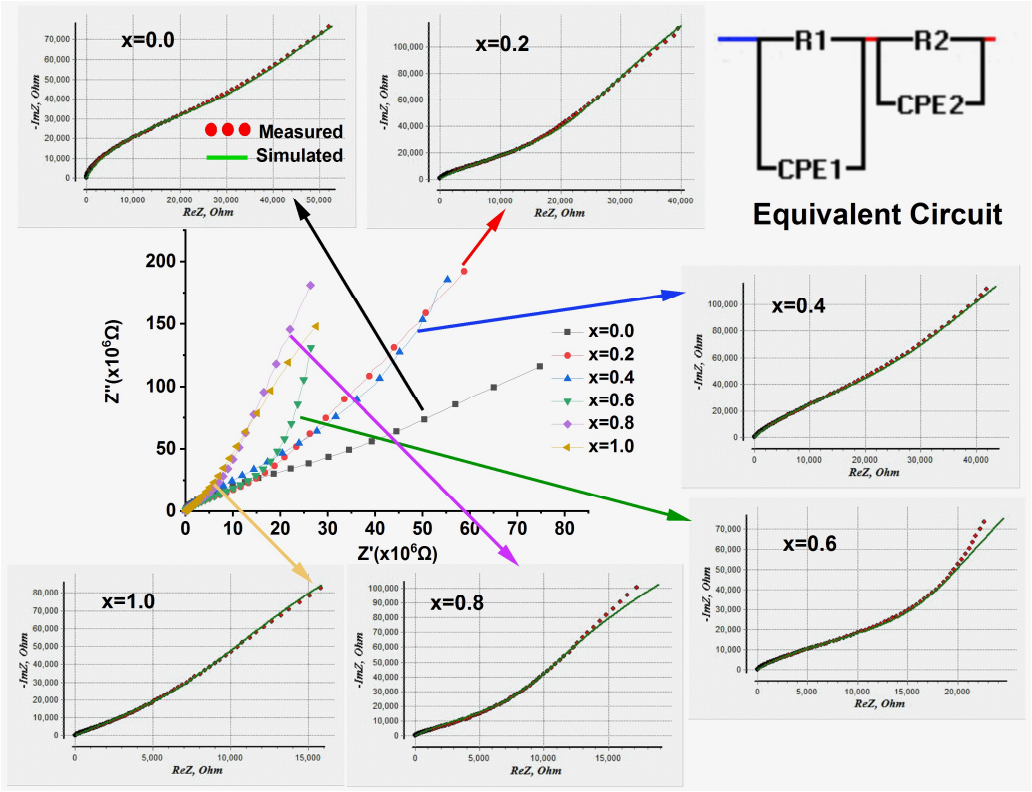

Fig. 4.10. Fitting of impedance curves for $SrCo_xZn_xFe_{12-2x}O_{19}$.

Table 4.2. Parameters of prepared compositions derived using EIS software of $SrCo_xZn_xFe_{12-2x}O_{19}$.

x	R_g (MΩ)	R_{gb}(MΩ)	C_g (μF)	C_{gb} (μF)
0.0	622.10	30.08	31.60	7.02
0.2	1180.00	26.89	2.33	119.17
0.4	1000.00	41.00	1.62	34.48
0.6	923.04	21.15	2.38	38.76
0.8	1000.00	10.27	1.65	39.46
1.0	1115.00	12.30	2.09	471.82

Simulated Grain/Grain boundary parameters and Morphology

Composition x=0.0 has two layers of large as well as small grains as depicted in the micrographs in Fig. 4.2; small grains on the top layer and large grains on the bottom layer. Besides this, large porosity is seen among small grains due to which there will be weak polarization. This results in a low value of grain boundary capacitance C_{gb} which is in agreement with the lowest simulated C_{gb}=7.02 μF (Table 4.2). The portion of micrographs also shows large grains in the form of fused/agglomerated/clustered grains, this promotes polarization in grains causing the highest simulated C_g=31.60 μF and lowest R_g=622.10 MΩ. For composition x=0.4, numerous needle-shaped grains can be seen, and a large number of grain boundaries with large circumference/perimeter contribute to maximal simulated R_{gb}=41 MΩ among the compositions.

Composition x=1.0 shows the honeycomb-like structure of grains as depicted in Fig. 4.2 and evidently, inter-grain connectivity is relatively better in this composition. The closeness of grain boundaries gives rise to strong polarization causing enhancement of C_{gb}, matching with the highest simulated C_{gb}=471.82 μF in Table 4.2. All doped compositions have small grains and constitute pores between grains. The small size of

grains reduces the polarization (C_g) inside the grains and this causes a low value of C_g in doped compositions as listed in Table 4.2.

Simulated Grain/Grain boundary parameter and Dielectric Parameter

Compositions x=0.2 and 0.4 owe the highest and least value of ε' (Fig. 4.3) for low-frequency regions respectively: $\varepsilon'$is inversely related to resistivity. As discussed before grain boundary is active at the low-frequencies, however, grains at high frequencies according to the Maxwell-Wagner model. Table 4.2 shows that x=0.4 has the maximum simulated value of R_{gb}=41 MΩ among all compositions and owes lowest ε'=17.35 at 100 Hz. Composition x=0.2 has large R_{gb}=26.89 MΩ in comparison to x=0.6 (21.15 MΩ), x=0.8 (10.27 MΩ) and x=1.0 (12.30 MΩ), thus x=0.2 should have low ε'in the low-frequency region. However, it has the maximum Fe^{3+}/Fe^{2+} available for hopping/polarization than x=0.6, 0.8, and 1.0. Competition between the two factors causes x=0.2 to have large ε'=35.97 at 100 Hz among doped compositions. While comparing composition x=0.2, considerable porosity can be observed in composition x=0.0, particularly around small grain boundaries (Fig. 4.2). It causes an impediment to the applied filed flow and polarization diminution in the latter despite the maximum Fe^{3+}/Fe^{2+} available for hopping, hence x=0.0 has a lower ε′ than x=0.2 at 100 Hz. Similarly, x=0.0 has the highest ε'' and tanδ (Fig. 4.4) attributing to the same reason.

Simulated Grain/Grain boundary parameters and Electric Modulus

Composition x=0.0 (Fig. 4.6) demonstrated a prominent role of grain boundaries than grains with relaxation in the form of a semi-circle with its area lying more towards the low-frequency region. The doping caused composition x=0.4 to have the role of grains due to the movement of semicircle towards the high-frequency and further doping enhanced the contribution of grain boundaries with the shift of semi-circles towards the low-frequency area and reduced the diameter of semi-circles in x=0.2, 0.6, 0.8 and 1.0 as well. This behavior can be well explained in conjunction with Table 4.2: conductivity relaxation is prominent in grain boundaries for composition x=0.0 with the lowest simulated C_{gb}=7.02 μF, causing more contribution of grain boundaries for conductivity relaxation. The simulated lowest C_g=1.62 μF in x=0.4 is responsible for the profound role of needle-shaped grains for conductivity relaxation; needle shape significantly reduced polarization inside the grains with less cross-section area. The good grain

connectivity in x=1.0, with Rg=1115.0 MΩ and Cg=2.09 μF, renders an effective role of grain boundaries with strong polarization.

4.1.3 Band gap Characteristics

Band gap characteristics of the prepared ferrite compositions are analyzed with the help of UV-Vis spectroscopy. UV-Vis spectroscopy is the method to analyze the band gap characteristics of the material. As discussed in Chapter 3 absorbance data is first determined using a UV-Vis spectrometer. Tauc plots are obtained from this measured data from which the band gap has been obtained. Fig 4.11 shows the Tauc plots drawn for the prepared composition. Equation 3.4 as given in the experimental section in Chapter 3 is used to calculate the required values of band gap. The interception on the x-axis is found from the linear area of the Tauc plot to obtain the band gap. The band gaps of the prepared compositions x=0.0 to 1.0 are 2.68, 2.82, 2.56, 2.86, 2.71, and 2.58 eV respectively. The ferrites generally have a band gap in the range of 2 to 3 eV hence the obtained values are in the prescribed range.

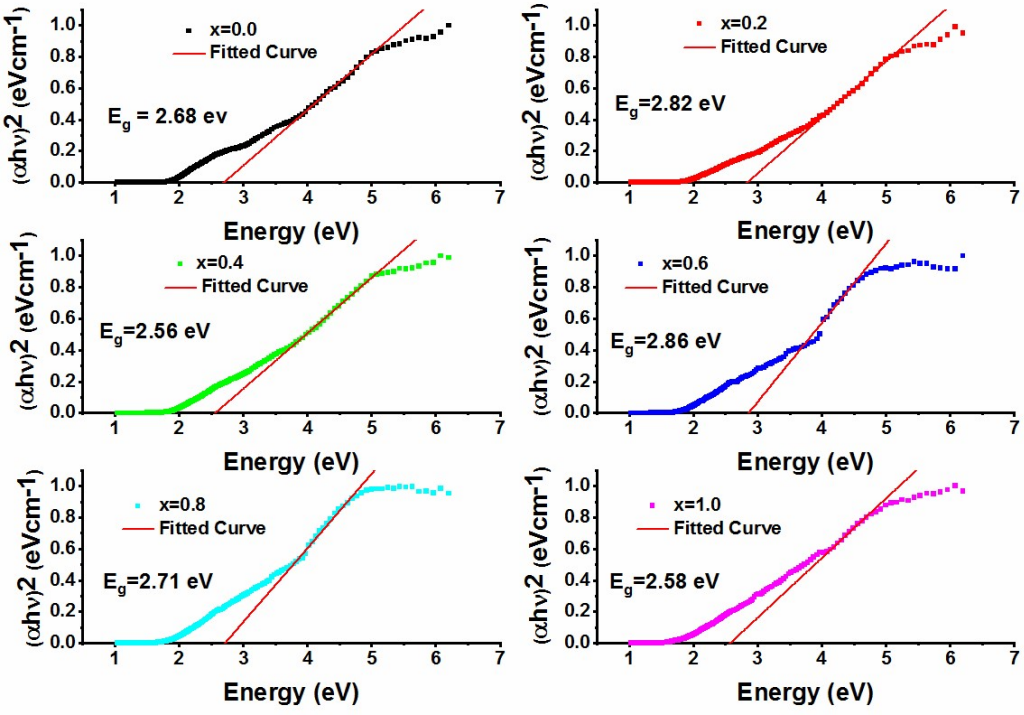

Fig 4.11 Tauc plots of $SrCo_xZn_xFe_{12-2x}O_{19}$.

4.1.4 Magnetic Characteristics

Magnetization (M) v/s magnetic field (H) graphs of $SrCo_xZn_xFe_{12-2x}O_{19}$ hexaferrites are plotted to investigate the magnetic characteristics of the prepared hexaferrites. Fig 4.12 (a) shows the hysteresis loops for the prepared compositions. The site occupancy of the ions is related to their electronegativity. The ion having high electronegativity mostly tries to hold an octahedral site rather than a tetrahedral [88]. The electronegativity of Zn^{2+}(1.65) ions are less than that of Co^{2+}(1.88), hence the former will try to acquire the tetrahedral site $4f_1(\downarrow)$ [89]. As per the ligand field theory, Zn^{2+} have no preference due to all filled d locations ($3d^{10}$) while Co^{2+} with $3d^7$prefer octahedral sites 12k ($\uparrow$), $2a(\uparrow), 4f_2(\downarrow)$ [90]. Phor et al. [91] reported that Zn^{2+}prefer tetrahedral $4f_1$ sites while Singh et al. [90] reported that Co^{2+} prefer to occupy an octahedral.

The law of saturation is employed to determine the saturation magnetization (M_s) and anisotropy field (H_a) using a formula [92].

$$M = M_s \left(1 - {}^{A}/_{H} - {}^{B}/_{H^2}\right) + \chi_P H \qquad (4.2)$$

M_s represents saturation magnetization, A, χ_P, and B represent inhomogeneity parameter, susceptibility, and anisotropy respectively.

In hexaferrites B is given as $B = H_a^2/15$ with (H_a) representing the anisotropy field. M-H loops displayed in Fig. 4.12 (a) show a steep rise in magnetization at the low applied field which declined at the high field. The undoped composition x=0.0 possesses a large slope at high fields indicating an unsaturated state which reduces with the substitution of Zn^{2+} and Co^{2+}. The reduction in the anisotropy field is the reason behind it. Since a linear relationship is observed at high values from 10 KOe to 15 KOe terms A/H and χ_P maybe removed and B could be obtained from the relation $M = M_s\ (1 - B/H^2\ )$. With the help of B anisotropy field (H_a) is determined by applying a relation $H_a^2 = 15\ B$. Thus M v/s $1/H^2$ graph is plotted and linear fit is used to calculate the respective values as displayed in Fig. 4.12 (b). The magnetic parameters determined from M-H loops and M v/s $1/H^2$ plots are listed in Table 4.3.

For hexagonal crystal structure, the magnetic moment relation with spin-up and down sites is as [93]

$$M_s = M_a(2a + 12k + 2b)(\uparrow) - M_b\,(4f_1 + 4f_2)\,(\downarrow) \qquad (4.3)$$

M_a denotes magnetization due to spin-up sites, while M_b is for spin-down sites. Thus, it should be noted that the occupation of a weak/non-magnetic ion on spin-down sites ($4f_1 \downarrow + 4f_2 \downarrow$) enhances saturation magnetization while more occupancy at spin-up sites (2a↑ + 12k↑ + 2b↑) reduces it. There is a non-monotonous variation in M_s of the prepared compositions. It increases by 14% with the substitution of Zn^{2+} and Co^{2+} from x=0.0 (88.32 emu/g) to x=0.4 (101.9 emu/g). The reason behind this is the substitution of Fe^{3+} by Zn^{2+} and Co^{2+} at the spin-down sites. From the relationship among M_s, M_a, and M_b as given in the equation we can say that the occupancy of diamagnetic Zn^{2+} and weak magnetic Co^{2+} at the spin-down sites ($4f_1\downarrow + 4f_2\downarrow$) causes a decrease in the value of M_b which in turn, increases the M_s. Thereafter, x=0.4 onwards M_s starts decreasing and there is a 25% decrease in the value of M_s from x=0.4 to x=1.0. This is due to the low magnetic moment of Co^{2+} (3μB) and diamagnetic Zn^{2+} (0 μB). The replacement of Fe^{3+} at spin-up sites creates an imbalance in electrical neutrality, hence to maintain it Fe^{3+} is converted into Fe^{2+} due to this the superexchange interactions weaken and cause a decrease in magnetization. Beside this, substitution at spin-up sites (2a↑ + 12k↑ + 2b↑) reduces the net value of M_a in response to which M_s decreases.

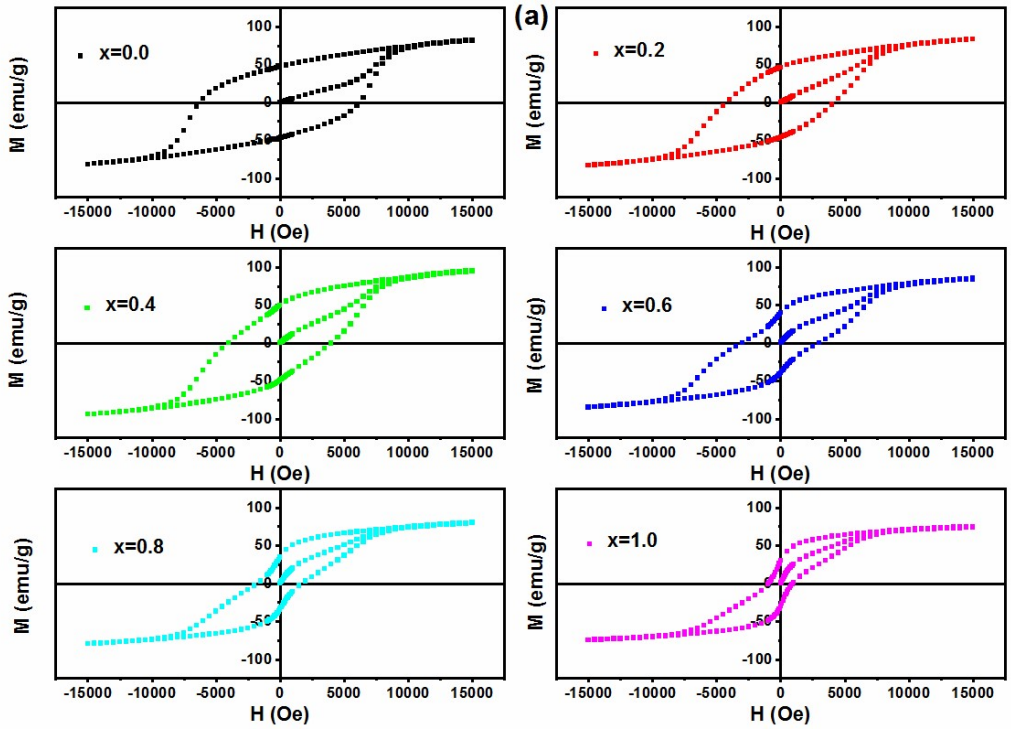

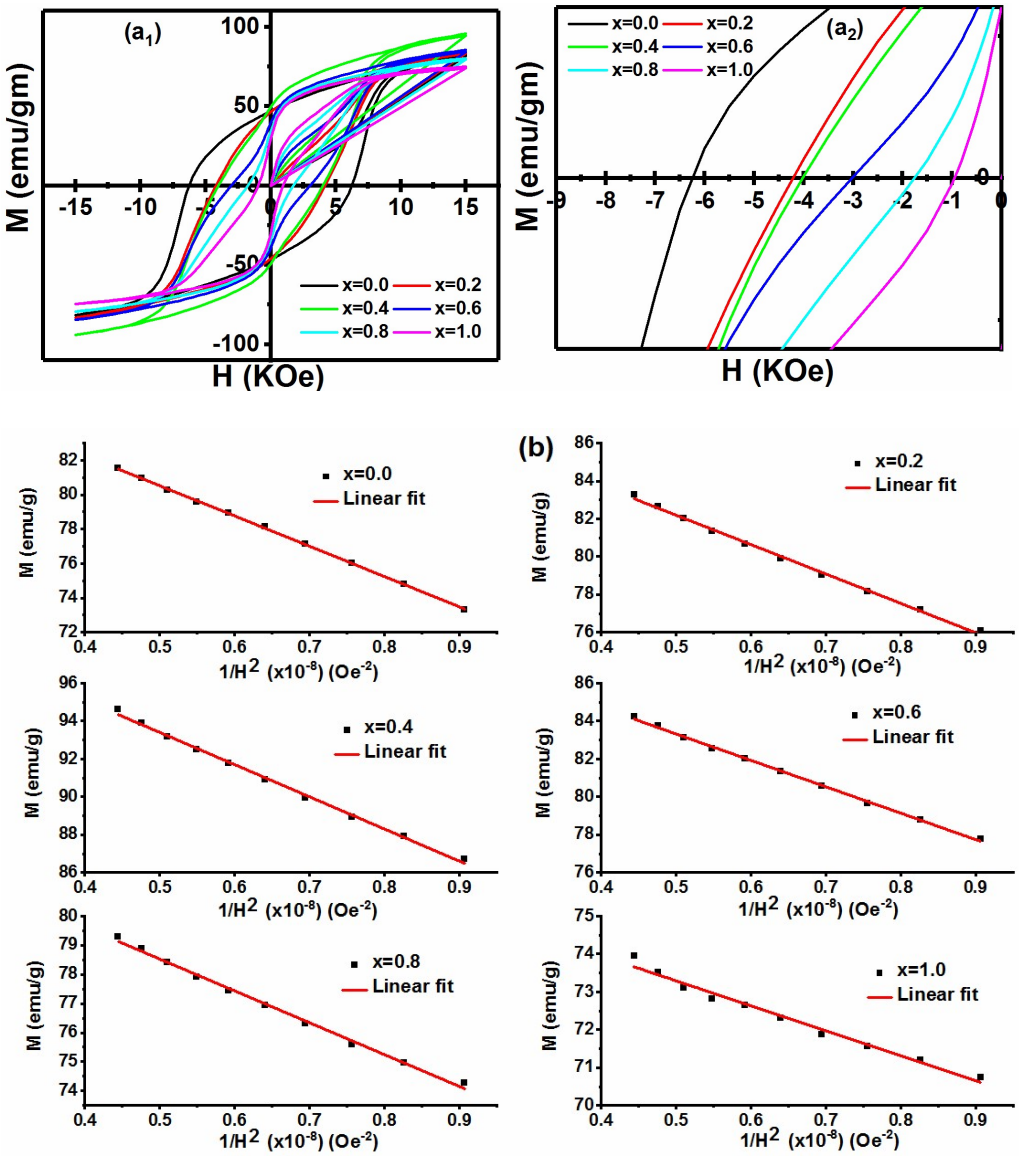

Fig. 4.12 (a) M-H loops (a_1 and a_2) combined and enlarged view (b) M_s v/s $1/H^2$ plots of $SrCo_xZn_xFe_{12-2x}O_{19}$

The low value of coercivity H_c is the prime requirement in the design of a microwave absorber. Table 4.3 illustrates that the doping of Co-Zn causes a reduction in the value of H_c. The H_c decreases from a high value of 6263 Oe (x=0.0) to a small value of 948 Oe (x=1.0). The 85 % drop in H_c is due to the fact that the substitution of non-magnetic Zn^{2+} and weak magnetic Co^{2+} dopants converted them into magnetically soft ferrites. There are two factors affecting the values of H_c one is the intrinsic factor involving the

anisotropy field H_a and second, is an extrinsic factor related to morphology. Table 4.3 reveals that there is a decrease in the value of H_a which has a direct relation with H_c. The consistent decrease in the anisotropy field H_a causes a decrement in H_c. There is around a 33 % decrease in the value of H_a from x=0.0 to x=1.0 which is due to the substitution of Fe^{3+} at $4f_2$ and $2b$ sites, as these sites commit large anisotropy field and the replacement of Fe^{3+} at these sites causing the reduction in H_a. There is a 33% decrease in H_a while H_c decreases by 85 % so another reason for the large reduction in H_c is the large ionic radius of Zn^{2+} (0.74 Å) and Co^{2+}(0.745 Å) in comparison to Fe^{3+} (0.645 Å). Secondly from the SEM images, it is evident that there are pores in the composition x=0.0 which reduces with the inclusion of Co-Zn, and composition x=1.0 possesses good grain connectivity thus reducing coercivity(H_c).

Table 4.3. Magnetic parameters determined for $SrCo_xZn_xFe_{12-2x}O_{19}$

x	M_s (emu/g)	M_r (emu/g)	H_a (kOe)	H_c (Oe)	M_r/M_s
0.0	89.32	47.11	17.20	6263	0.53
0.2	89.94	46.36	16.09	4220	0.52
0.4	101.9	49.57	15.82	4027	0.49
0.6	90.29	39.70	15.22	3026	0.44
0.8	83.99	34.54	13.97	1747	0.41
1.0	76.59	30.04	11.44	948	0.39

The M_r/M_s ratio explains the retention of magnetization after the removal of the applied field. This ratio varies between 0 and 1 and a value less than 0.5 represents randomly oriented multi-domain particles while values greater than 0.5 indicates a single domain. The composition x=0.0 and 0.2 have M_r/M_s ratio more than 0.5 shows multi-domain while this ratio for x=0.4 to 1.0 shows single domain.

4.1.5 Electromagnetic Characteristics

4.1.5.1 Complex permeability and complex permittivity

The graphs of (ε'), (ε″), (μ′), and (μ″) against frequency are depicted in Fig 4.13. Both the dielectric constant and loss vary non-uniformly with the doping of Co-Zn. There is a decrement in the value of the ε' while an increment in ε″ is observed as compared to the undoped composition. In compositions x=0.0, 0.2, 0.4, and 1.0 no significant change is observed in the dielectric constant with the frequency increment. The compositions x=0.6 and 0.8 depict a reduction in ε' with the increment in frequency being lowest in the case of x=0.6. The composition x=0.2 and x=0.6 have relaxation peaks in ε″ around 11 GHz and 10 GHz respectively.

The permeability of the compositions varies non-uniformly with the doping of Co-Zn. At the low frequencies, 8 GHz to 9 GHz doped composition has high values of μ′ as compared to undoped composition. The composition x=0.8 has a relaxation peak around 9.5 GHz, however, all the compositions except x=0.6 have a relaxation peak near about 11 GHz. There is an increment in the value of μ′ with the increment in frequency for all the compositions being highest in x=0.6. All the compositions except x=0.6 possess dual relaxation peaks one at low frequencies (8 to 9 GHz) and another at high (11 to 12 GHz). At low frequencies, the composition 0.4 has the maximal value of μ" while x=1.0 obtains higher value among all in the high frequency range.

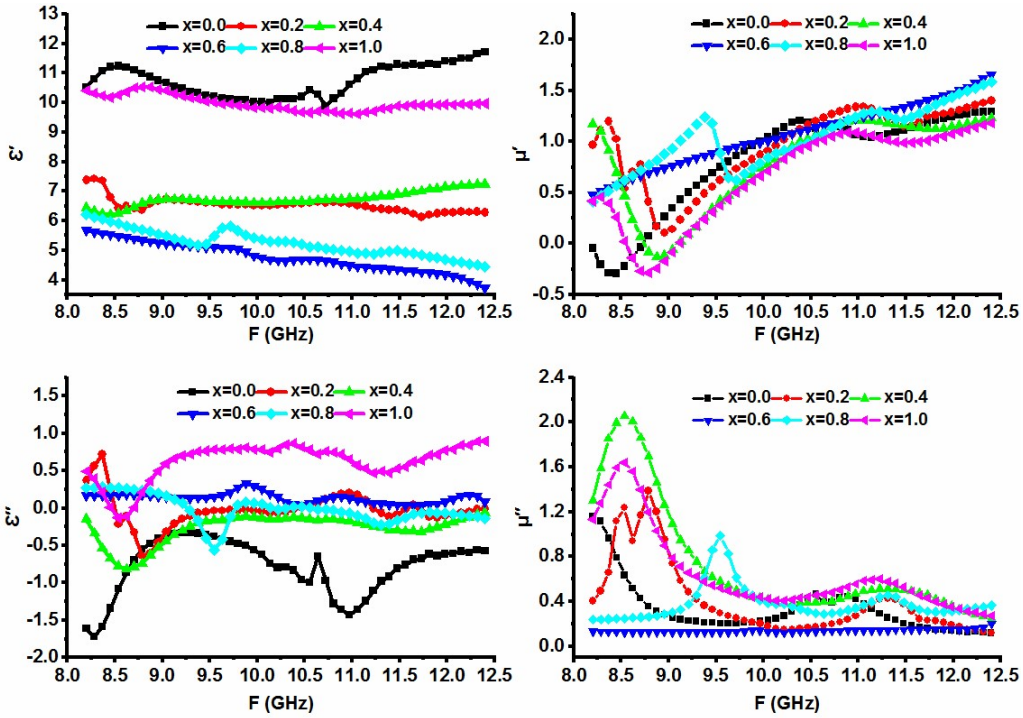

Fig 4.13 Complex permittivity and permeability versus frequency plot of $SrCo_xZn_xFe_{12-2x}O_{19}$

In the microwave regime, there is a dependence of complex permittivity/permeability on grains, porosity, grain size distribution, electron spin, and dipole polarization [94]. Besides that, dielectric polarization occurs because of the electron hopping in Fe^{2+}/Fe^{3+} [95]. The porosity depresses polarization and restrains the field flow. The exchange resonance among Fe^{3+}/Fe^{2+} and ferromagnetic resonance govern the complex permeability [96, 97]. The decrement in the number of Fe^{3+} ions with doping of Co-Zn affects the polarization and resonance. There are pores in the micrographs of the prepared compositions that act as non-magnetic voids and affect magnetization related to complex permittivity/permeability. The size of grain and grain boundaries vary non-linearly as can be seen in micrographs (Fig. 4.2) which modifies the permittivity/permeability.

Grain having large size supports electron hopping, however, grain boundaries discourage the field flow. The accumulation of charge at grain boundaries causes polarization while large grains enhance electron spin that increases permeability. Meanwhile, there is a reduction in exchange resonance due to porosity and small grains

which is the cause of magnetic loss between Fe^{3+} and Fe^{2+}. The peaking nature in complex permittivity/permeability in all compositions is related to the dielectric relaxation and ferromagnetic resonance.

4.1.5.2 Microwave absorption in $SrCo_xZn_xFe_{12-2x}O_{19}$

The absorption characteristics of a material are determined by the parameter called reflection loss. The higher the reflection loss the better is absorption. It is calculated from the material's input impedance Z_{in} and impedance of air Z_0 using equations 3.13 and 3.14. The microwave absorption characteristics are explored on the basis of the λ/4, impedance matching, and dielectric/magnetic losses as explained in the following sections.

4.1.5.3 Quarter Wavelength Mechanism

The graphs of reflection loss (RL) with frequency for various simulated thicknesses have been used to explain the concept of absorption in the prepared compositions. Fig. 4.14 (a, c, e), 4.15 (a, c, e), 4.16 (a, c, e), 4.17 (a, c, e), 4.18 (a, c, e, g) and 4.19 (a) depict RL plots of prepared $SrCo_xZn_xFe_{12-2x}O_{19}$ ferrites. These figures are used to determine different parameters such as matching frequencies, bandwidths, and frequency bands of RL below -10/-20 dB. The summarized values of these are given in Table 4.4.

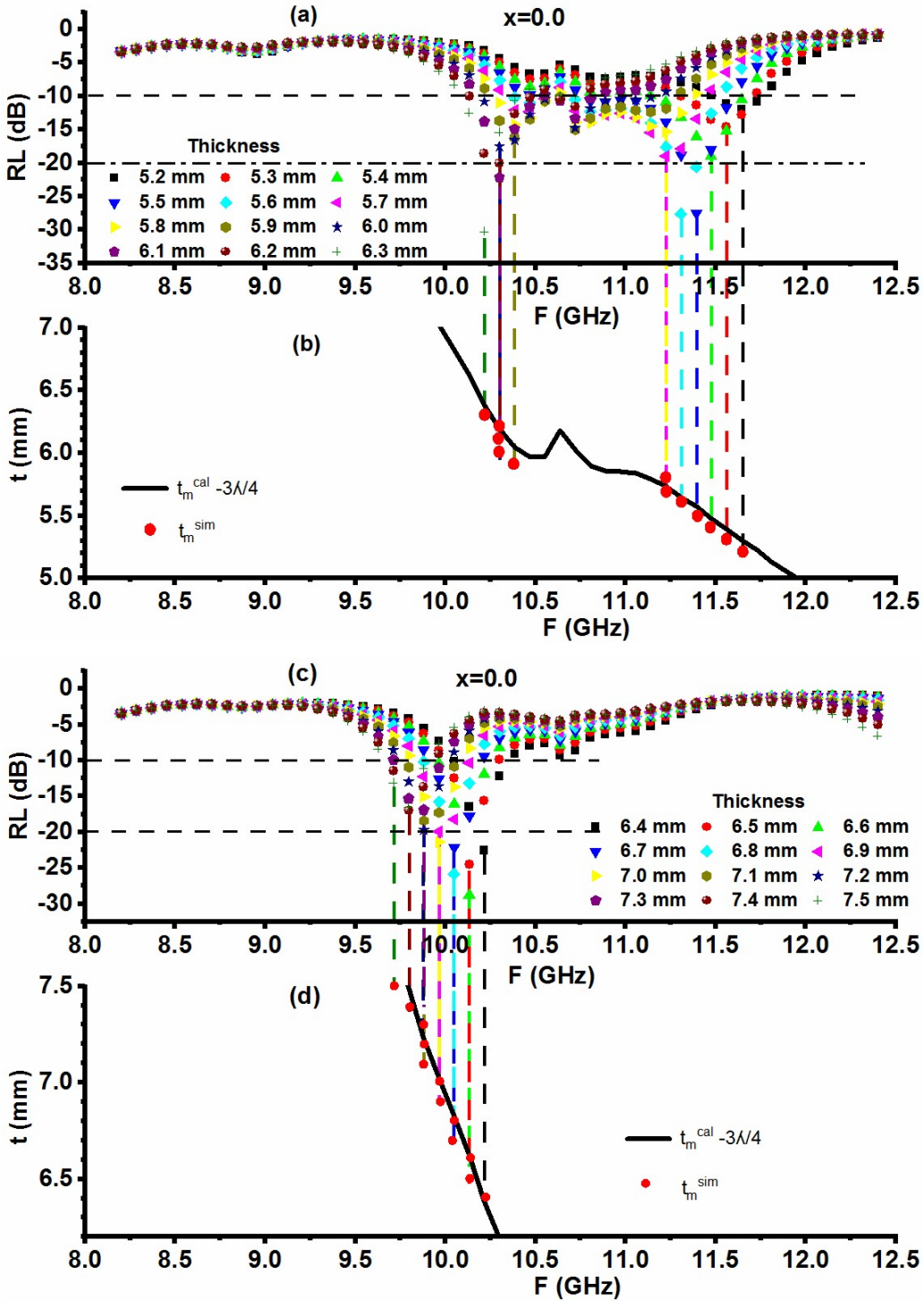
(a)
x=0.0
RL (dB)
Thickness
5.2 mm
5.3 mm
5.4 mm
5.5 mm
5.6 mm
5.7 mm
5.8 mm
5.9 mm
6.0 mm
6.1 mm
6.2 mm
6.3 mm
F (GHz)
(b)
t (mm)
t_m^{cal} -3λ/4
t_m^{sim}
F (GHz)
(c)
x=0.0
RL (dB)
Thickness
6.4 mm
6.5 mm
6.6 mm
6.7 mm
6.8 mm
6.9 mm
7.0 mm
7.1 mm
7.2 mm
7.3 mm
7.4 mm
7.5 mm
F (GHz)
(d)
t (mm)
t_m^{cal} -3λ/4
t_m^{sim}
F (GHz)

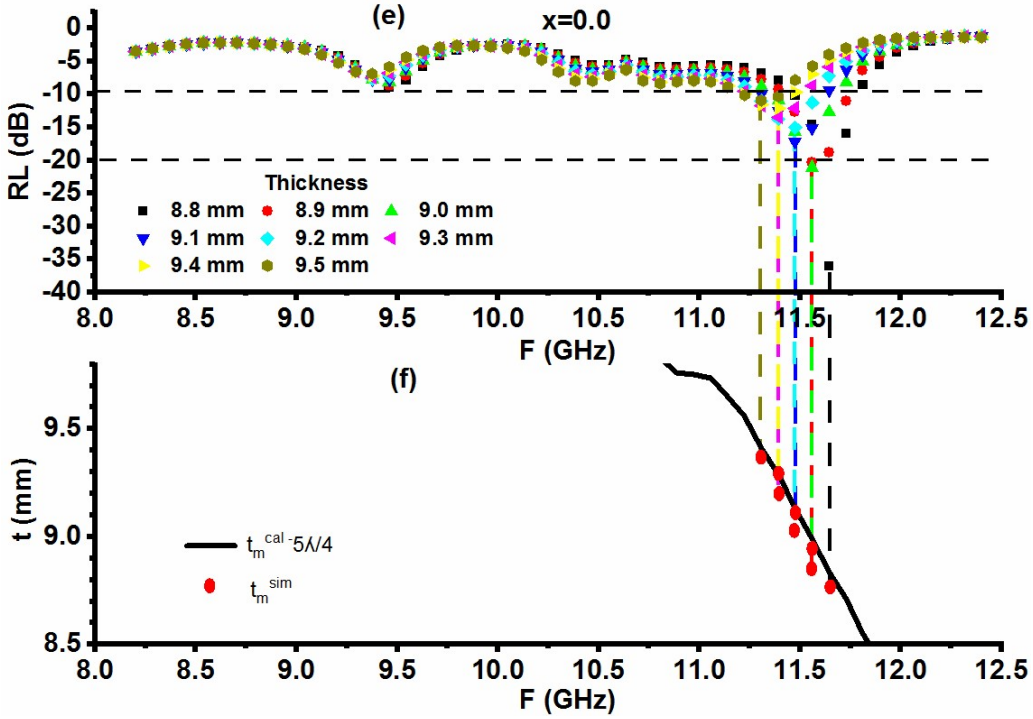

Fig. 4.14 (a, c, e) RL versus frequency, (b, d, f) thickness versus frequency in x=0.0 for $SrCo_xZn_xFe_{12-2x}O_{19}$.

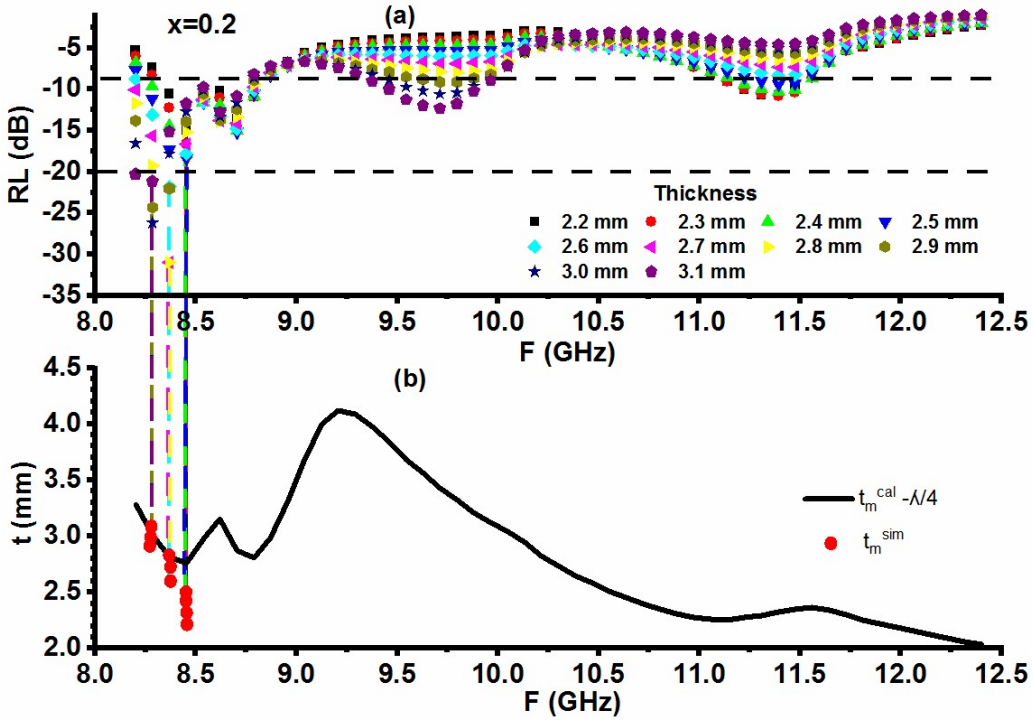

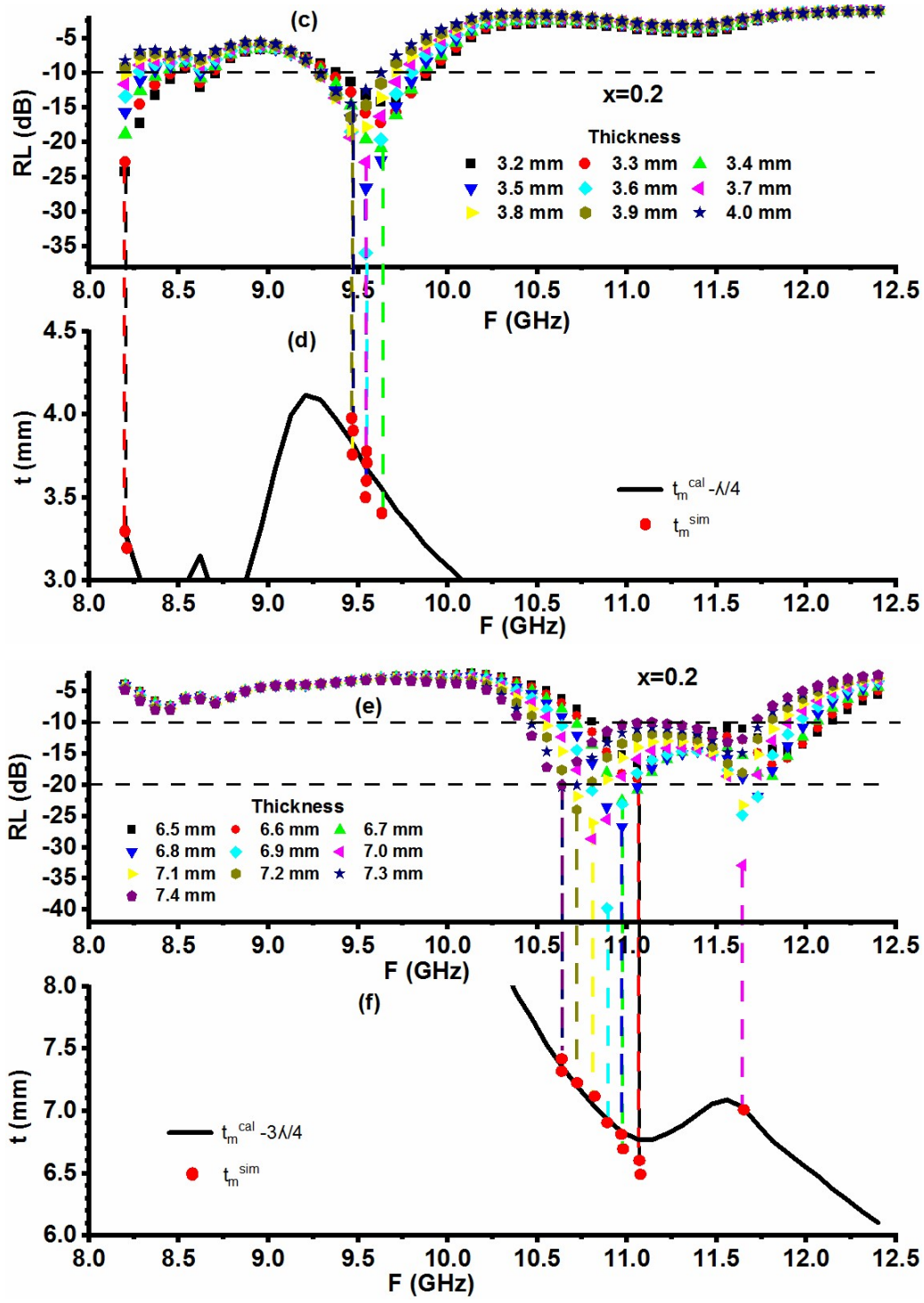

Fig. 4.15 (a, c, e) RL versus frequency (b, d, f) thickness versus frequency in x=0.2 for $SrCo_xZn_xFe_{12-2x}O_{19}$.

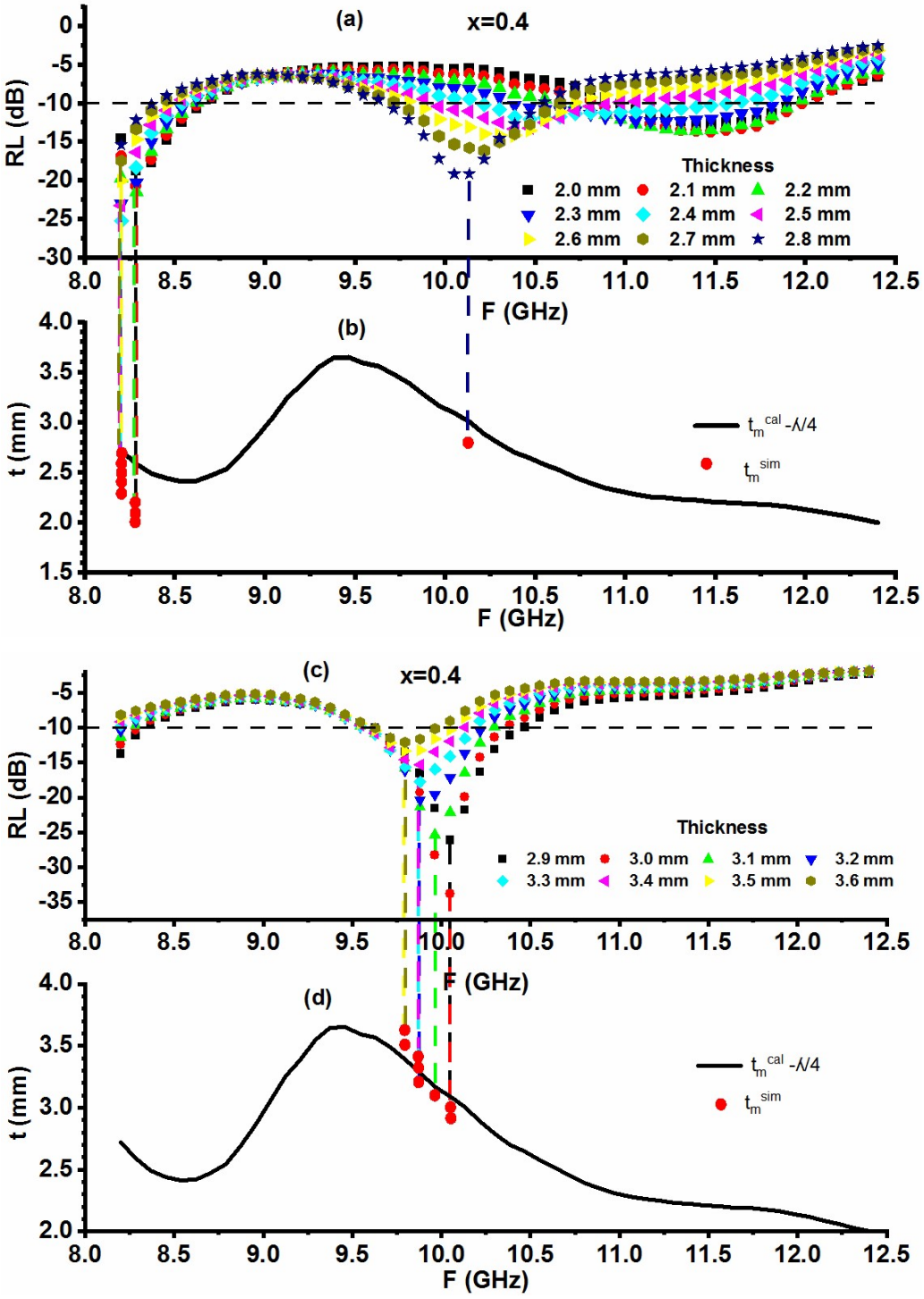
(a)
x=0.4
RL (dB)
Thickness
2.0 mm
2.1 mm
2.2 mm
2.3 mm
2.4 mm
2.5 mm
2.6 mm
2.7 mm
2.8 mm
F (GHz)
(b)
t (mm)
t_m^{cal} -λ/4
t_m^{sim}
F (GHz)
(c)
x=0.4
RL (dB)
Thickness
2.9 mm
3.0 mm
3.1 mm
3.2 mm
3.3 mm
3.4 mm
3.5 mm
3.6 mm
F (GHz)
(d)
t (mm)
t_m^{cal} -λ/4
t_m^{sim}
F (GHz)

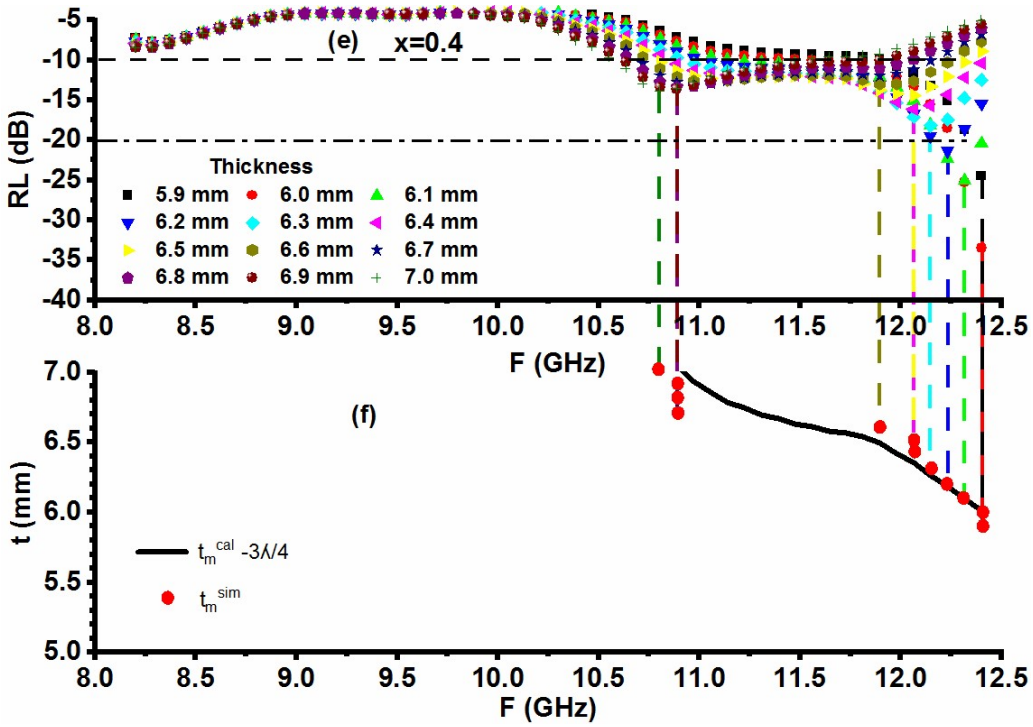

Fig. 4.16 (a, c, e) RL versus frequency (b, d, f) thickness versus frequency in x=0.4 for $SrCo_xZn_xFe_{12-2x}O_{19}$.

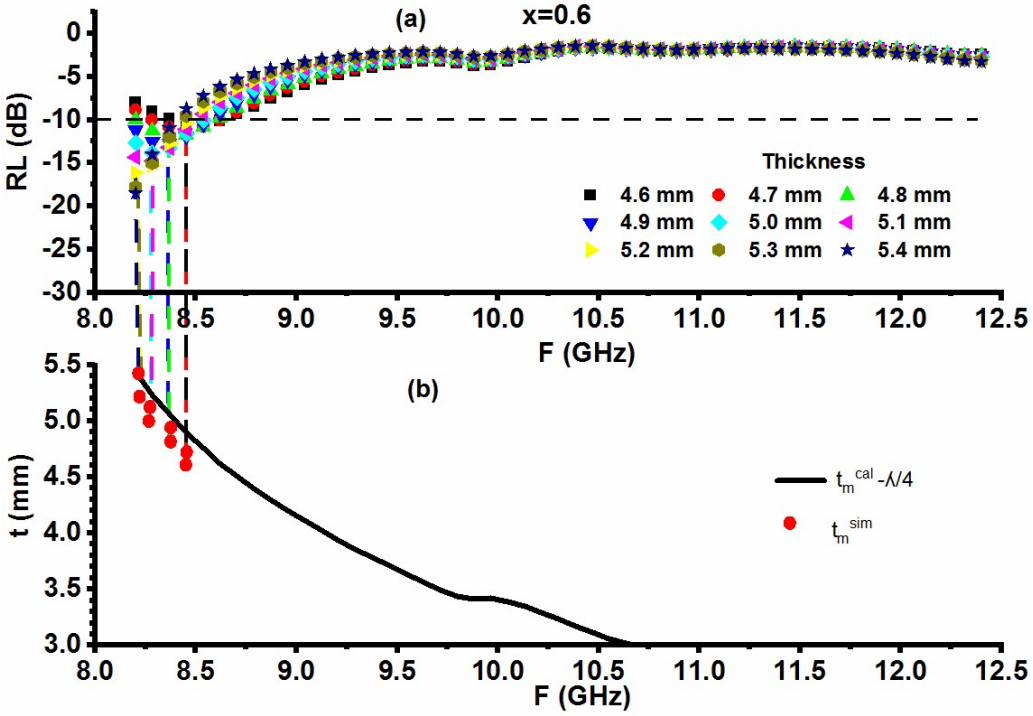

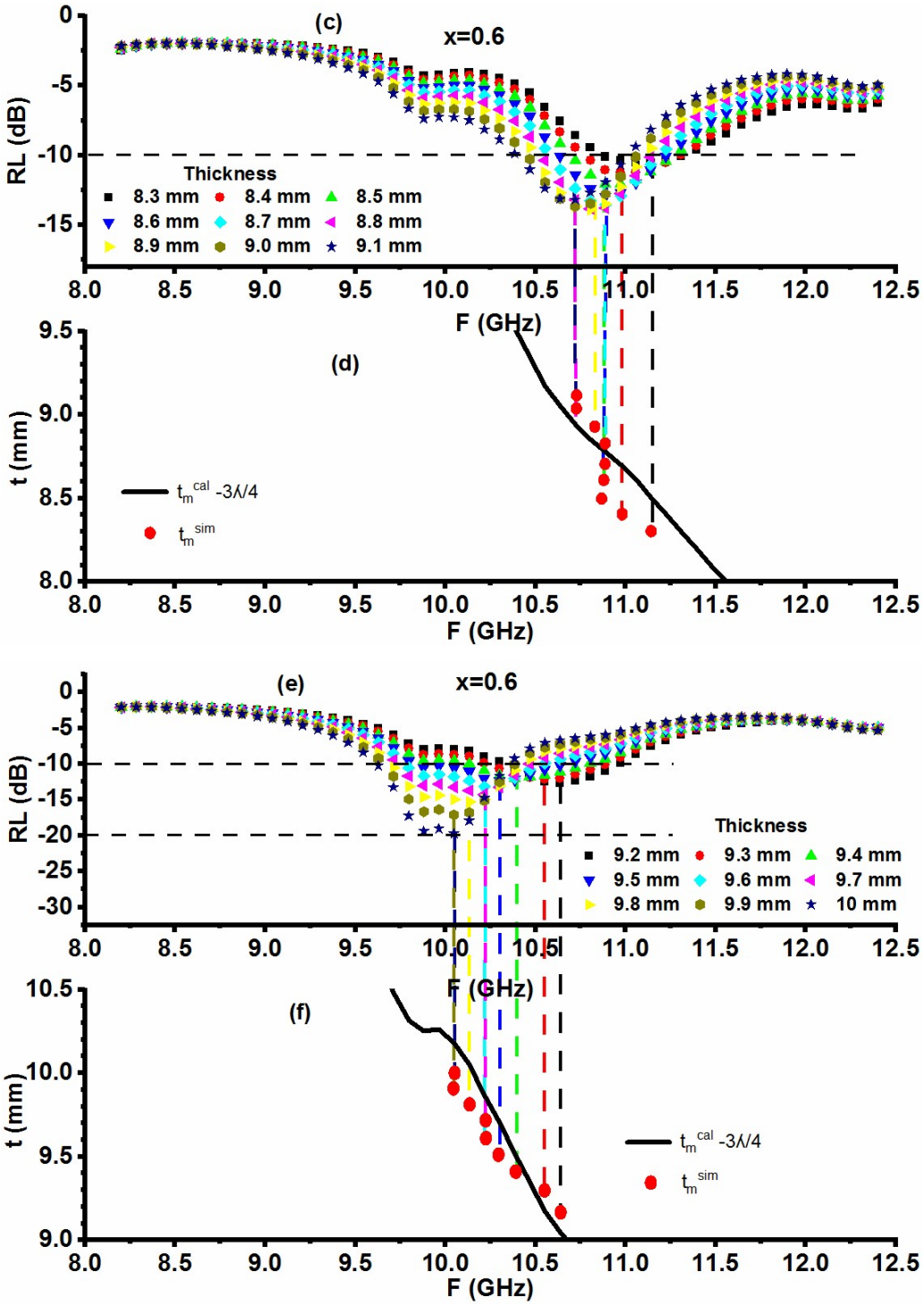

Fig. 4.17 (a, c, e) RL versus frequency (b, d, f) thickness versus frequency in x=0.6 for $SrCo_xZn_xFe_{12-2x}O_{19}$.

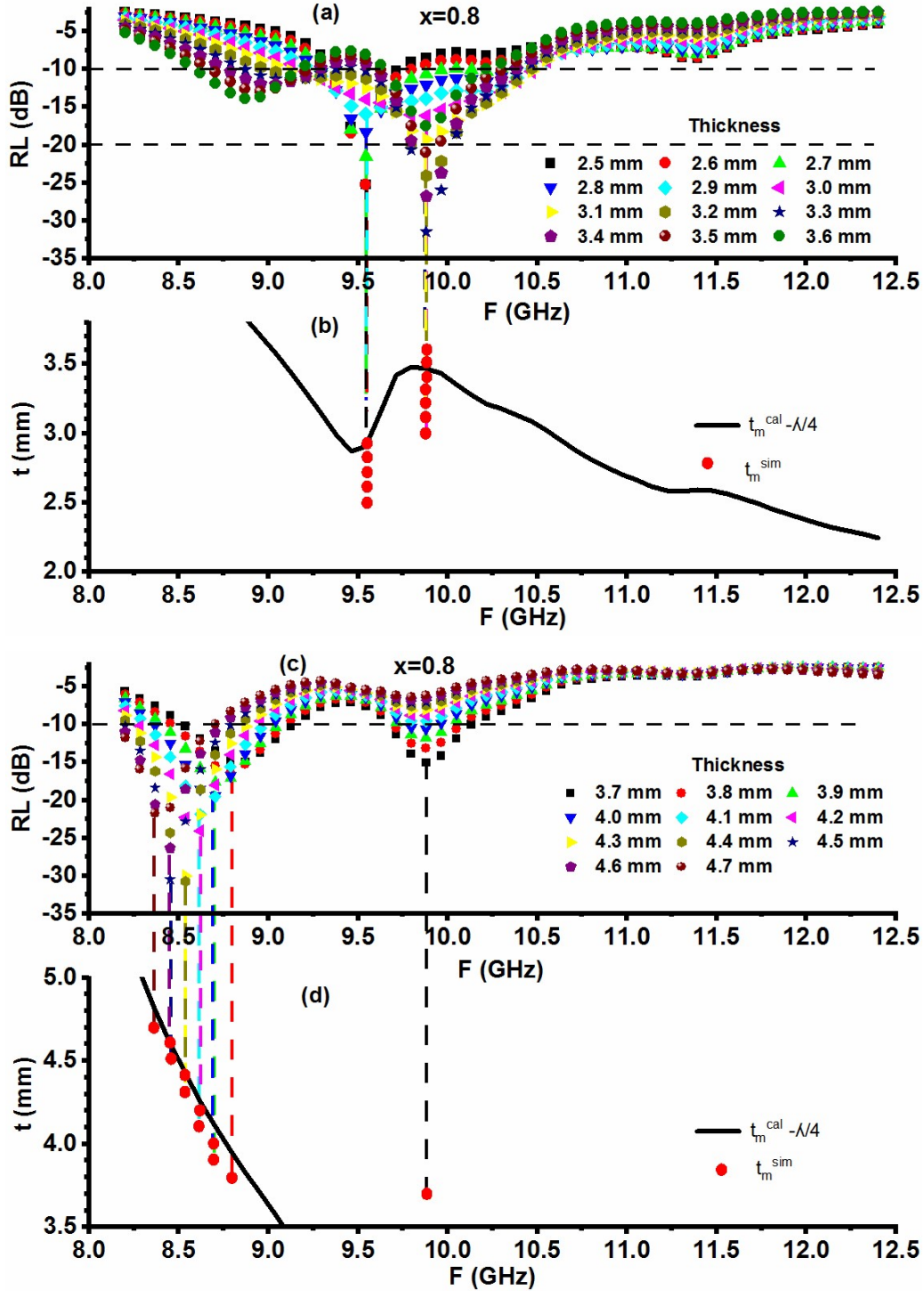
(a)
x=0.8
RL (dB)
F (GHz)
Thickness
2.5 mm
2.6 mm
2.7 mm
2.8 mm
2.9 mm
3.0 mm
3.1 mm
3.2 mm
3.3 mm
3.4 mm
3.5 mm
3.6 mm
(b)
t (mm)
F (GHz)
t_m^{cal} -λ/4
t_m^{sim}
(c)
x=0.8
RL (dB)
F (GHz)
Thickness
3.7 mm
3.8 mm
3.9 mm
4.0 mm
4.1 mm
4.2 mm
4.3 mm
4.4 mm
4.5 mm
4.6 mm
4.7 mm
(d)
t (mm)
F (GHz)
t_m^{cal} -λ/4
t_m^{sim}

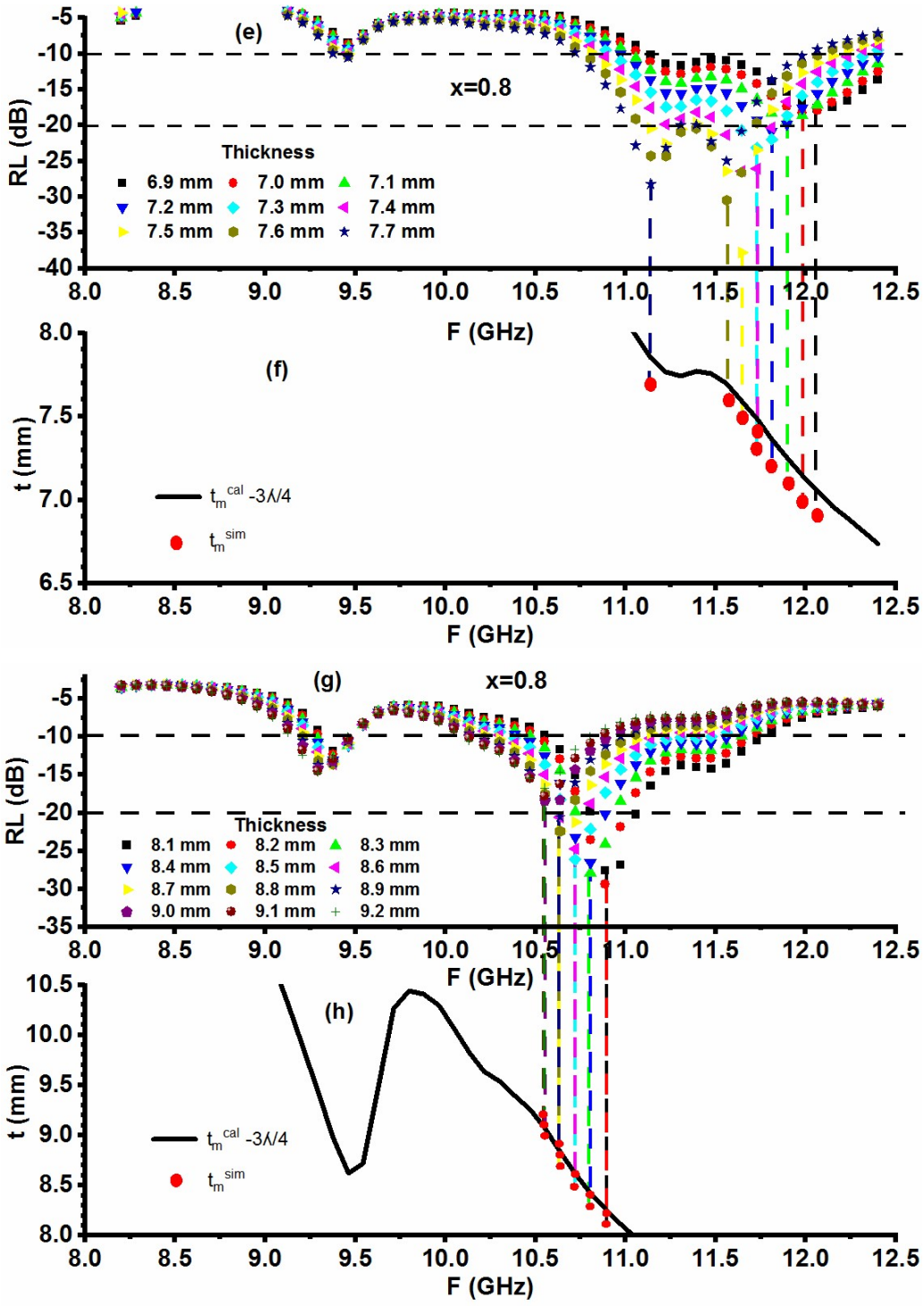

Fig. 4.18 (a, c, e, g) RL versus frequency (b, d, f, h) thickness versus frequency in x=0.8 for $SrCo_xZn_xFe_{12-2x}O_{19}$.

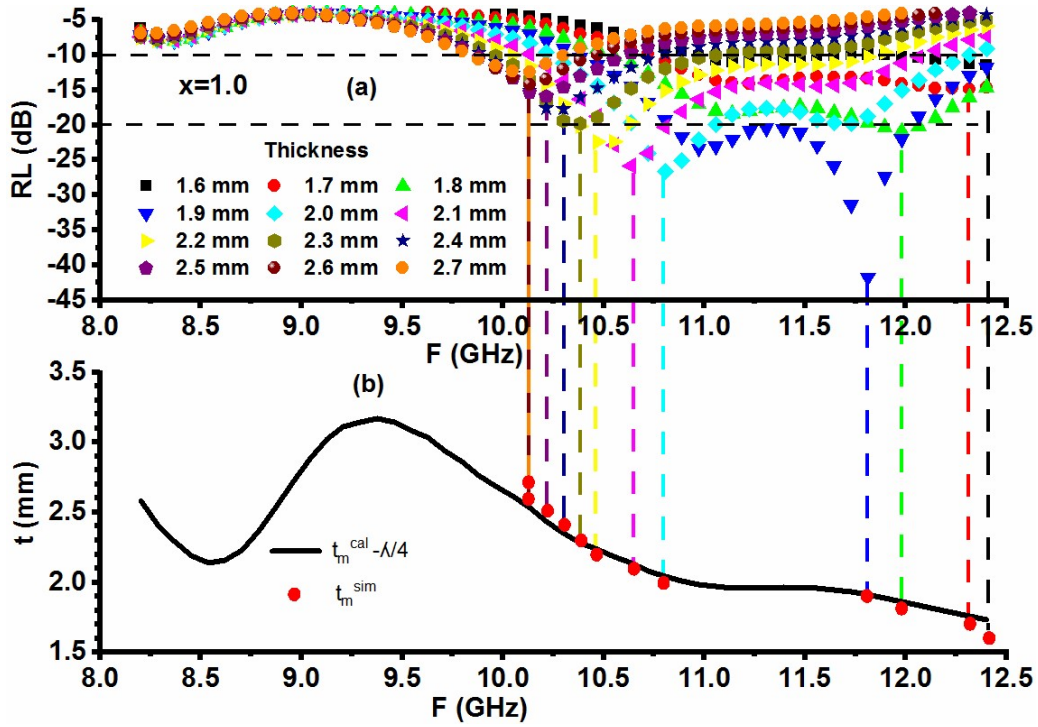

Fig. 4.19 (a) RL versus frequency (b) thickness versus frequency in x=1.0 for $SrCo_xZn_xFe_{12-2x}O_{19}$.

The highest RL=-41.72 dB is obtained in composition x=1.0 at an 11.81 GHz frequency with a small thickness of 1.9 mm. The RL ranges between -12.42 dB and -39.74 dB for 10.30 and 10.89 GHz for 9.5 and 6.9 mm respectively. There is a non-monotonous variation in the RL peak with the increment in thickness. Fig. 4.14 (a, c, e) demonstrates the absorption characteristics of composition x=0.0. It displays that the thickness from 5.5 to 6.0 mm has an RL≥ -10 dB for the frequency ranging from 10.80-11.14 GHz. The RL peak shifted toward low frequency with the increment in thickness. The frequency band of reflection loss ≥ -20 dB from 11.30-11.39 GHz is obtained at the thickness of 5.6 mm.

The maximum RL of -39.74 dB at 10.89 GHz in composition x=0.2 is obtained. The respective RL has been obtained at 6.9 mm. In this composition thickness from 2.2 to 3.0 mm for a frequency band ranging from 8.37-8.70 GHz and thickness of 6.5 to 7.3 mm for a band of 10.89 to 11.73 GHz show RL ≥ -10 dB Fig. 4.15 (a, c, e). The thicknesses 2.9, 3.5, 6.8, 6.9, 7.1, and 7.3 mm possess RL ≥ -20 dB.

Composition x=0.4 possesses an RL= -33.82 at 3.0 mm at the frequency of 10.05 GHz. The thicknesses 2.3, 2.9, 3.0, 6.0, and 6.1 mm show *RL* ≥ -20 dB Fig. 4.16 (a, c, e). For

x=0.6 the maximum RL of -19.74 at 10.0 mm is obtained for a frequency of 10.05 GHz Fig. 4.17 (a, c, e). The composition x=0.8 has peaks corresponding to *RL* ≥ -10/-20 dB from 2.5 to 4.7 mm and 6.0 to 9.2 mm Fig. 4.18 (a, c, e, g). The composition x=1.0 shows an *RL* ≥ -10 dB for the thickness of 1.6 mm to 2.7 mm. In x=1.0 a large frequency spectrum of RL ≥ -20 dB ranging from 10.89-11.98 GHz is observed (Fig. 4.19 (a)).

A relation between RL peaks and the λ/4 mechanism has been explored by comparing the simulated thickness (t_m^{sim}) and the calculated thickness (t_m^{cal}). Fig. 4.14 (b, d, f), 4.15 (b, d, f), 4.16 (b, d, f), 4.17 (b, d, f), 4.18 (b, d, f, h) and 4.19 (b) show the graphs of calculated thickness (nλ/4) against the frequency. For comparison between simulated and calculated thickness lines from RL peaks are brought to the thickness-frequency graphs. It is worth noting that the λ/4 mechanism is fulfilled in compositions x=0.2, 0.4, 0.6, and 0.8 for n=1 and 3, while in x=0.0 it exists at n=3 and 5. The composition x=1.0 is matched only for λ/4. The presence of this mechanism in composition x=0.0 contributed -10 dB bandwidth ranging from 0.25 to 1.09 GHz for 5.6 to 8.8 mm as given in Table 4.4. Composition x=0.2 possesses *RL* ≥-10 dB for a frequency region of 8.28 to 10.97 GHz. A broad bandwidth of 1.26 GHz associated with a -10 dB band is observed at thicknesses of 6.8, 6.9, 7.1, and 7.3 mm, while a -20 dB bandwidth of 170 MHz is obtained for 6.8 and 6.9 mm.

The composition x=0.4 possesses RL values for both -10/-20 dB at low thicknesses from 2.3 to 6.7 mm. This composition has the highest BW of 1.52 GHz at 6.5 mm thickness. This broad bandwidth is obtained for the frequency band of 10.80-12.32 GHz. The -20 dB bandwidth ranging from 80 MHz to 170 MHz is also obtained at thickness 2.9 and 6.1 mm. A -10 dB bandwidth of 0.76 GHz from 9.88-10.64 GHz is reported in composition x=0.6. The broad bandwidths associated with -10 dB/-20 dB bands are observed in x=0.8. A 1.43 GHz absorption bandwidth at 7.2 mm for the -10 dB band and 0.50 GHz at 7.6 mm associated with -20 dB respectively are observed for this composition. The composition x=1.0 possesses the highest RL of -41.72 dB along the highest bandwidth of 2.02 GHz at a very low 1.9 mm thickness. Further, the same composition also has the highest -20 dB absorption bandwidth i.e. 1.09 GHz with a band of 10.89-11.98 GHz.

Table 4.4. RL with matching thickness/frequency, BW, and PBW for $SrCo_xZn_xFe_{12-2x}O_{19}$.

x	Max. RL (dB)	Matching Thickness (mm)	Matching Frequency (GHz)	-10 dB band (GHz)	-10 dB BW (GHz)	-20 dB band (GHz)	-20 dB BW (GHz)	BTR	PBW (%)
0.0	-27.60	5.6	11.31	10.72-11.48	0.76	11.31-11.39	0.08	0.331	6.720
	-16.25	5.9	10.38	10.30-11.22	0.92	-	-	0.405	8.863
	-17.58	6.0	10.30	10.22-11.14	0.92	-	-	0.404	8.932
	-30.29	6.3	10.22	10.13-11.22	1.09	-	-	0.457	10.665
	-36.03	8.8	11.64	11.48-11.73	0.25	-	-	0.063	2.148
0.2	-30.97	2.7	8.37	08.20-08.70	0.5	-	-	0.779	5.974
	-24.31	2.9	8.28	08.20-08.70	0.5	8.28-08.37	0.09	0.725	6.039
	-26.57	3.5	9.54	9.38-9.80	0.42	9.54-9.63	0.09	0.392	4.403
	-26.65	6.8	10.97	10.72-11.98	1.26	10.89-11.06	0.17	0.433	11.486
	-39.74	6.9	10.89	10.64-11.90	1.26	10.80-10.97	0.17	0.4323	11.570
	-26.05	7.1	10.80	10.55-11.81	1.26	10.72-10.80	0.08	0.427	11.667
	-20.35	7.3	10.64	10.47-11.73	1.26	10.64-10.72	0.08	0.422	11.842
0.4	-23.0	2.3	8.20	10.38-11.81	1.43	08.20-8.28	0.08	1.522	17.439
	-25.28	2.4	8.20	10.22-11.48	1.26	-	-	1.342	15.366
	-26.23	2.9	10.05	9.63-10.38	0.75	9.96-10.13	0.17	0.776	7.463
	-33.82	3.0	10.05	9.63-10.30	0.67	9.96-10.05	0.09	0.676	6.667
	-33.50	6.0	12.40	11.56-12.40	0.84	12.32-12.40	0.08	0.293	6.774
	-25.06	6.1	12.32	11.22-12.40	1.18	12.23-12.40	0.08	0.417	9.578
	-16.11	6.4	12.06	10.89-12.40	1.51	-	-	0.524	12.521
	-14.41	6.5	12.06	10.80-12.32	1.52	-	-	0.527	12.604
	-13.11	6.7	10.97	10.72-12.15	1.43	-	-	0.492	13.036
0.6	-12.75	4.9	8.37	08.20-8.54	0.34	-	-	0.297	4.062
	-16.12	5.2	8.20	08.20-8.45	0.25	-	-	0.208	3.049
	-12.90	8.6	10.89	10.64-11.22	0.58	-	-	0.170	5.326
	-13.67	9.0	10.72	10.47-11.06	0.59	-	-	0.170	5.504
	-12.42	9.5	10.3	09.88-10.64	0.76	-	-	0.228	7.379
	-17.09	9.9	10.05	09.71-10.38	0.67	-	-	0.201	6.667
	-19.74	10	10.05	09.63-10.30	0.67	-	-	0.203	6.667
0.8	-18.13	2.8	9.54	9.28-10.38	1.09	-	-	1.224	11.426
	-16.14	3.0	9.88	9.21-10.47	1.26	-	-	1.307	12.753
	-19.27	3.1	9.88	9.12-10.47	1.34	-	-	1.368	13.664
	-24.05	3.2	9.88	9.04-10.38	1.35	9.80-9.96	0.16	1.339	13.563
	-20.87	7.2	11.81	10.97-12.40	1.43	-	-	0.438	12.108
	-37.75	7.5	11.64	10.89-12.15	1.26	11.48-11.73	0.25	0.381	10.825
	-30.46	7.6	11.56	10.80-12.06	1.26	11.14-11.64	0.50	0.382	10.900

	-28.26	7.8	11.06	10.72-11.90	1.18	10.97-11.22	0.25	0.356	10.669
	-30.97	8	10.97	10.64-11.73	1.09	10.89-11.06	0.17	0.328	9.936
	-26.55	8.4	10.80	10.47-11.56	1.09	10.72-10.89	0.17	0.322	10.093
1.0	-14.90	1.7	12.32	10.80-12.40	1.60	-	-	2.108	12.987
	-20.91	1.8	11.98	10.55-12.40	1.85	11.90-12.06	0.16	2.357	15.442
	-41.72	1.9	11.81	10.38-12.40	2.02	10.89-11.98	1.09	2.478	17.104
	-26.67	2.0	10.8	10.30-12.23	1.93	10.72-10.97	0.25	2.298	17.870
	-25.83	2.1	10.64	10.22-12.06	1.84	10.55-10.81	0.25	2.133	17.293
	-22.40	2.2	10.47	10.05-11.81	1.76	10.38-10.55	0.17	2.022	16.810
	-19.78	2.3	10.38	9.96-11.06	1.1	-	-	1.303	10.597
	-17.74	2.4	10.3	9.96-10.72	0.76	-	-	0.890	7.379

4.1.5.4 Impedance matching mechanism

The absorber has an impedance different from that of the free space as their permittivity/permeability differs from each other. The difference between these two affects the absorption characteristics of the absorber. The mismatch in these two impedances causes reflection of the major part of the incident signal from the surface of the material and less portion of the signal enters the material. On the other hand, if they match major portion of the signal travels into the signal and is absorbed by the material. Hence it becomes necessary to analyze the impedance matching mechanism for the development of an effective absorber.

Fig. 4.20 displays the plots of reflection loss and impedance i.e. $|Z_{in}|$ against frequency for all the compositions. Table 4.5 enlists the values of Z_{in} corresponding to the maximum reflection loss of the various compositions. All the compositions (x=0.0 to 1.0) follow the impedance matching mechanism with their highest RL peaks, however, deviation at a few frequencies in x=0.2, 0.6, and x=0.8 occurs. The composition x=0.0 has an RL $= -36.03$ dB for 8.8 mm with a corresponding value of Z_{in}=366.74 Ω which is near to Z_o=377 Ω. Similarly, the compositions x=0.4 and x=1.0 have RL=-33.82 dB at 10.05 GHz with Z_{in}=388.20 Ω and RL=-41.72 dB at 11.81 with Z_{in}=379.55 Ω respectively, which are in agreement with the value of Z_o=377 Ω. In composition x=0.2 there is a problem with $|Z_{in}|$ as there is a RL peak of -24.78 at 11.64 GHz with Z_{in}=356.34 Ω while there is no RL peak RL=-5.86 dB at 12.15 GHz with a Z_{in}=366.17 Ω which is more close to Z_o=377 Ω than Z_{in}=356.34 Ω. A similar situation occurs in x=0.6 and x=0.8 at 10.47 GHz (Z_{in}=410.11 Ω, RL=-7.83 dB) and 12.15 GHz

(Z_{in}=379.07 Ω, RL=-10.28 dB) respectively in comparison to Z_{in}=420.34 Ω at 10.05 GHz with RL=-19.37 dB in x=0.6 and Z_{in}=386.80 Ω at 11.64 with RL=-37.75 dB in x=0.8.

This type of behavior is linked to the complex nature of $|Z_{in}|$ containing real and imaginary parts (Z_{real} & Z_{img}). Hence, Z_{real} and Z_{img} are determined and graphs of Z_{real} and Z_{img} are plotted as shown in Fig. 4.21. The values of Z_{real} and Z_{img} are obtained and enlisted in Table 4.5. Table 4.5 illustrates that the maximum *RL* value of -41.72 dB with 11.81 GHz obtained in x=1.0 follows Z_{real}=377 Ω and/or Z_{img}=0 condition. Since, for it $Z_{real} = 379.50$ Ω and Z_{img}=-5.68 Ω, which are approximately 377 Ω and 0. In the case of x=0.2 low RL=-5.86 dB at 12.15 GHz with Z_{in}=366.17 Ω is due to Z_{real}=215.57 Ω and Z_{img}=-295.99 Ω which are far away from Z_{real}=377 Ω and/or Z_{img}=0. The values of Z_{real} and Z_{img} associated with RL_{max} for compositions x=0.0, 0.2, 0.6, 0.8, and 1.0 are given in Table 4.5.

Thus it can be noted that the discrepancies observed in x= 0.2, 0.6, and 0.8 are because Z_{real} and Z_{img} values in those cases deviate more from 377 Ω and/or zero and the combined effect of these two causes low values of RL. There is a non-monotonical variation in input impedance Z_{in} with the Co-Zn doping. Thus both the λ/4 and impedance mechanism are followed in all compositions.

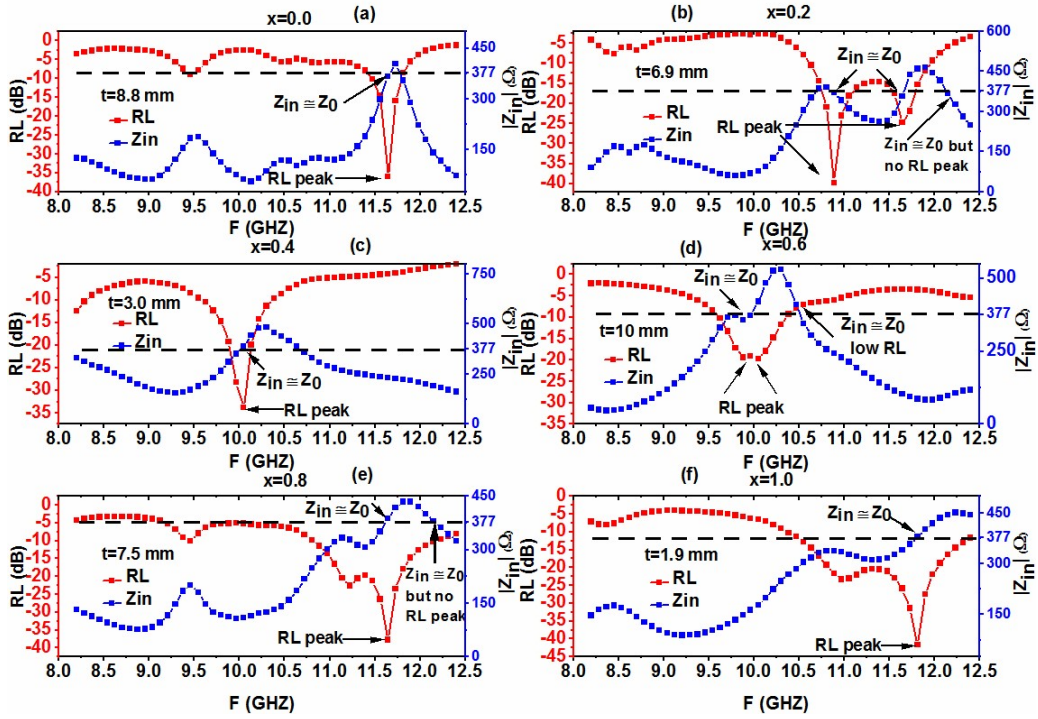

Fig. 4.20 Z_{in} and RL curve against frequency for $SrCo_xZn_xFe_{12-2x}O_{19}$.

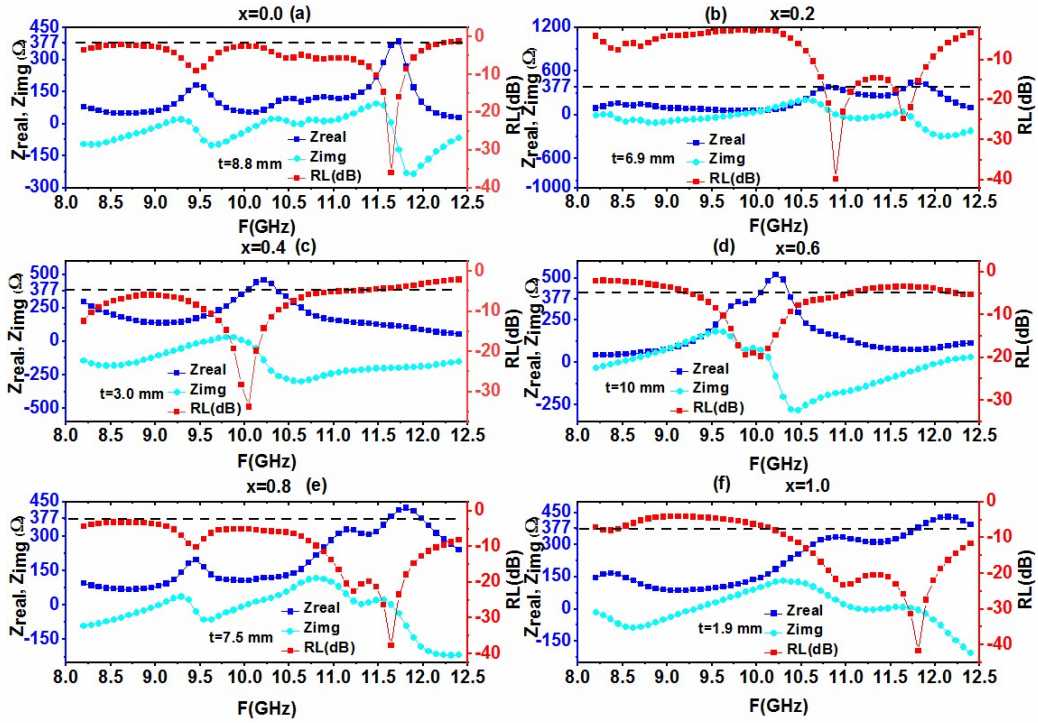

Fig. 4.21 Z_{real}, Z_{imag}, and RL v/s frequency graphs of $SrCo_xZn_xFe_{12-2x}O_{19}$.

Table 4.5. Z_{in}, Z_{real}, and Z_{imag} values corresponding to maximum RL of $SrCo_xZn_xFe_{12-2x}O_{19}$.

x	RL (dB)	Matching Thickness (mm)	Matching Frequency (GHz)	$\|Z_{in}\|$ (Ω)	Z_{real} (Ω)	Z_{img} (Ω)
0.0	-36.03	8.8	11.64	366.74	344.70	5.65
0.2	-39.74	6.9	10.89	370.92	370.89	4.70
0.4	-33.82	3.0	10.05	388.20	388.04	-11.0
0.6	-19.74	10	10.05	420.34	413.95	73.03
0.8	-37.75	7.5	11.64	386.80	386.80	1.34
1.0	-41.72	1.9	11.81	379.55	379.50	-5.68

4.1.5.5 Role of Electromagnetic/Material Parameters

The peaking nature in ε″ and μ" also has their contribution in the absorption which should also be taken care of. The peaks perceived in ε″ and μ" in the prepared compositions are contributing to absorption in the compositions: in composition x=0.2, *RL*=-39.74 dB at 10.89 GHz with the thickness of 6.9 mm correspond to ε″ peak at 10.89 GHz; similarly in x=0.8 ε″ peak at 9.88 GHz is in accordance to *RL*=-24.05 dB at 3.2 mm, and *RL*=-18.13 at 2.8 to μ" peak at 9.54 GHz. Thus dielectric and magnetic losses also participate in microwave absorption.

4.1.5.6 Eddy Current Loss

In ferrites, Eddy current loss contributes in the form of magnetic loss. The formula to determine eddy current loss is given as [98]:

$$C_0 = (\mu''(\mu')^{-2})/f \qquad (4.4)$$

Where C_0 is a constant and the rest of the parameters are the same as discussed earlier. It is worth noting that if C_0 has a constant value with the increment in frequency, there is a contribution of the eddy current loss. C_0 versus frequency plot of all the compositions is given in Fig. 4.22. It is evident that after 9.20 GHz plots of all the

compositions are constant which shows that eddy current loss is contributing to the absorption of ferrite compositions.

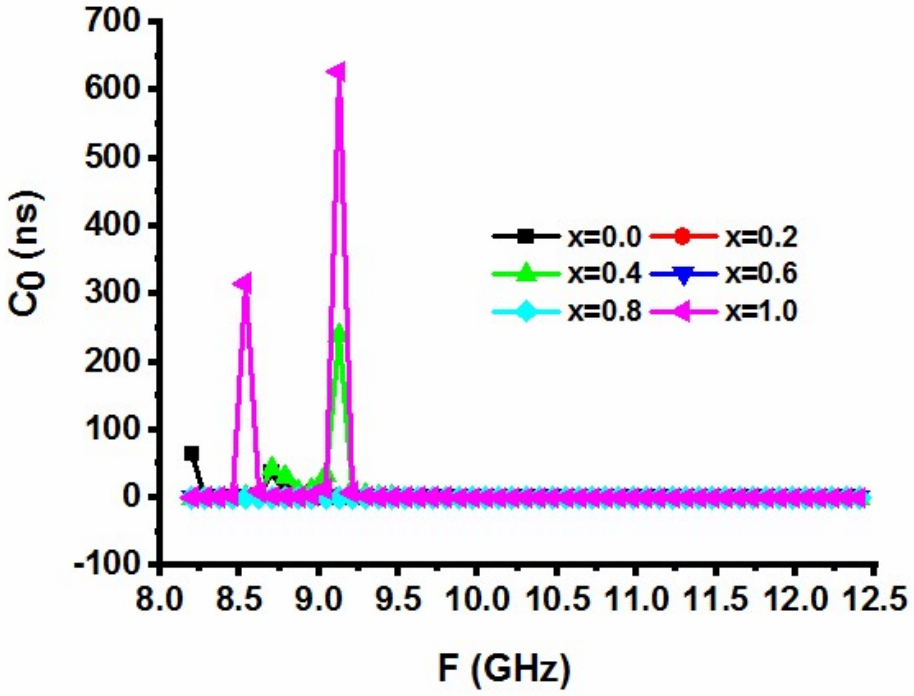

Fig. 4.22 C_0 versus frequency curve for $SrCo_xZn_xFe_{12-2x}O_{19}$.

4.1.5.7 Bandwidth to Thickness Ratio

Except for the RL≥-10 dB the broad bandwidth with less thickness is an important criterion in the design and characterization of an absorber. After achieving the desired RL≥-10 dB mark, one should aim at achieving low thickness, rather than increasing RL only. Due to this factor bandwidth-to-thickness-ratio (BTR) and percentage bandwidth (PBW) are determined as [99-101]:

$$BTR = \frac{BW}{t} \qquad (4.5)$$

$$PBW = \frac{f_2 - f_1}{f_0} \qquad (4.6)$$

Where BW is the bandwidth, f_2, f_1, and f_0 denote the high, low, and center frequencies of a frequency band, while t denotes the thickness corresponding to the RL peak.

From Table 4.4, it can be noted that doping has increased BTR. Composition x=1.0 owes the highest BTR=2.478 at 11.81 GHz and RL=-41.72 dB. Besides it, x=1.0 also possesses a high BTR=2.357 at 11.98 GHz with RL=-20.91 dB and 2.298 at 10.80 GHz

with RL of -26.67 dB. After that, the composition x=0.4 has significant BTR=1.522 and 1.342 at *f*=8.2 GHz for RL= -23.0 dB and -25.28 dB respectively. There is an increment in percentage bandwidth with the doping. The composition x=1.0 has the highest PBW=17.87 at 2.0 mm. PBW ranges from 7.38 to 17.87 % in sample x=1.0. The undoped composition x=0.0 shows PBW in the range of 2.15 to 10.67.

4.2 $SrCo_xNi_xFe_{12-2x}O_{19}$ series

4.2.1 Microstructural/Morphological characteristics

Fig. 4.23 depicts the X-ray diffraction pattern for $SrCo_xNi_xFe_{12-2x}O_{19}$ hexagonal ferrites, prepared using the sol-gel method. It is evident from the diffractograms that no secondary phase (additional peak) is present in any composition and all the peaks are indexed with the standard peaks of strontium ferrite. The compositions x=0.0, 0.2, and 0.4 have a major intensity peak with hkl (114), while compositions x=0.8, and 0.4 have a peak of 201 as a major intensity peak. The structural variables of prepared compositions are given in Table 4.6. It illustrates that the crystallite size decreased with the doping level of Co-Ni. The crystallite size ranges between 41.48 to 23.24 nm with the lowest one for the composition x=0.8.

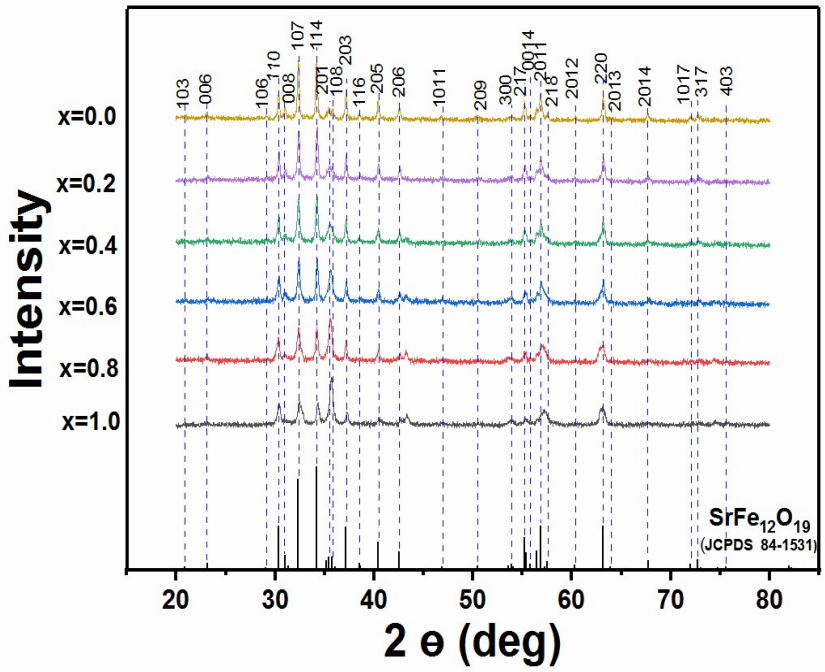

Fig. 4.23 XRD pattern of $SrCo_xNi_xFe_{12-2x}O_{19}$.

Table 4.6. Structural parameters of $SrCo_xNi_xFe_{12-2x}O_{19}$.

Co-Ni Content	a (Å)	b (Å)	c/a	V $(Å)^3$	D_{xrd} (nm)	d-spacing (Å)
0.0	5.88569	23.07226	3.920	692.17	41.47	2.77
0.2	5.88135	23.04695	3.919	690.39	37.89	2.62
0.4	5.88485	23.05776	3.918	691.54	36.24	2.62
0.6	5.88169	23.02567	3.915	689.83	41.48	2.76
0.8	5.89049	23.01370	3.907	691.54	23.24	2.54
1.0	5.87620	23.01867	3.917	688.34	25.59	2.53

The micrographs of ferrite composition $SrCo_xNi_xFe_{12-2x}O_{19}$ are presented in Fig. 4.24. The grain distribution has been affected by the doping of Co-Ni in terms of grain size, improved inter-grain connectivity, and grain agglomeration as depicted in Fig. 4.24. Composition x=0.0 has a greater number of small grains with high porosity and compositions x=0.4 and x=0.6 show the development of needle-shaped grains as given in Fig. 4.24 (c) and (d); x=0.4 has fused grains as depicted in Fig. 4.24 (c). The increase in doping causes the development of grain clusters as well as a decrement in grain size as shown in Fig. 4.24 (e) and (f) for the compositions x=0.8 and x=1.0 respectively.

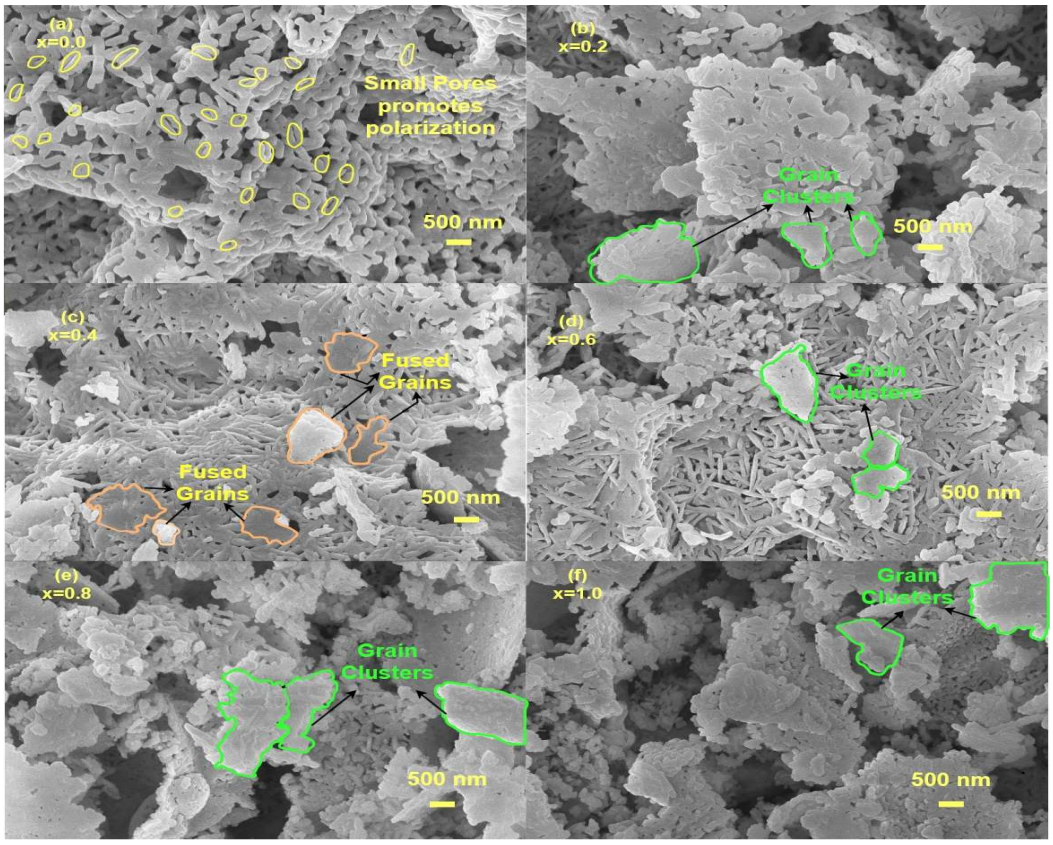

Fig. 4.24. SEM micrographs of $SrCo_xNi_xFe_{12-2x}O_{19}$.

4.2.2. Electrical characteristics

4.2.2.1 Dielectric Constant

The dielectric constant (ε) of ferrite is found to be a complex value with its real part (ε') indicating the degree of polarization and imaginary part (ε'') representing the dielectric losses. The formula to determine the real part is shown in equation (3.5). Dielectric loss ε'' is calculated using equation (3.6), while the loss tangent ($tan\delta$) can be determined by equation (3.7) as given in chapter 3. Fig. 4.25 shows the change in ε' and ε'' with the frequency for the developed ferrites. ε' possesses high values at the low frequencies while it first decreases and then acquires a constant value in the high-frequency regime. The dispersion is due to the interfacial polarization and complies with the Maxwell-Wagner model with Koop's phenomenon [80]. Since grain boundaries act most at low frequencies, their high resistance causes space charge polarization. This is the cause that the dielectric constant has higher values for low frequency. However, hopping

between Fe^{2+} and Fe^{3+} can't match up with the applied field at high frequency, which leads to a decay in space charge polarization. Due to this first ε' decreases and thereafter, it becomes constant.

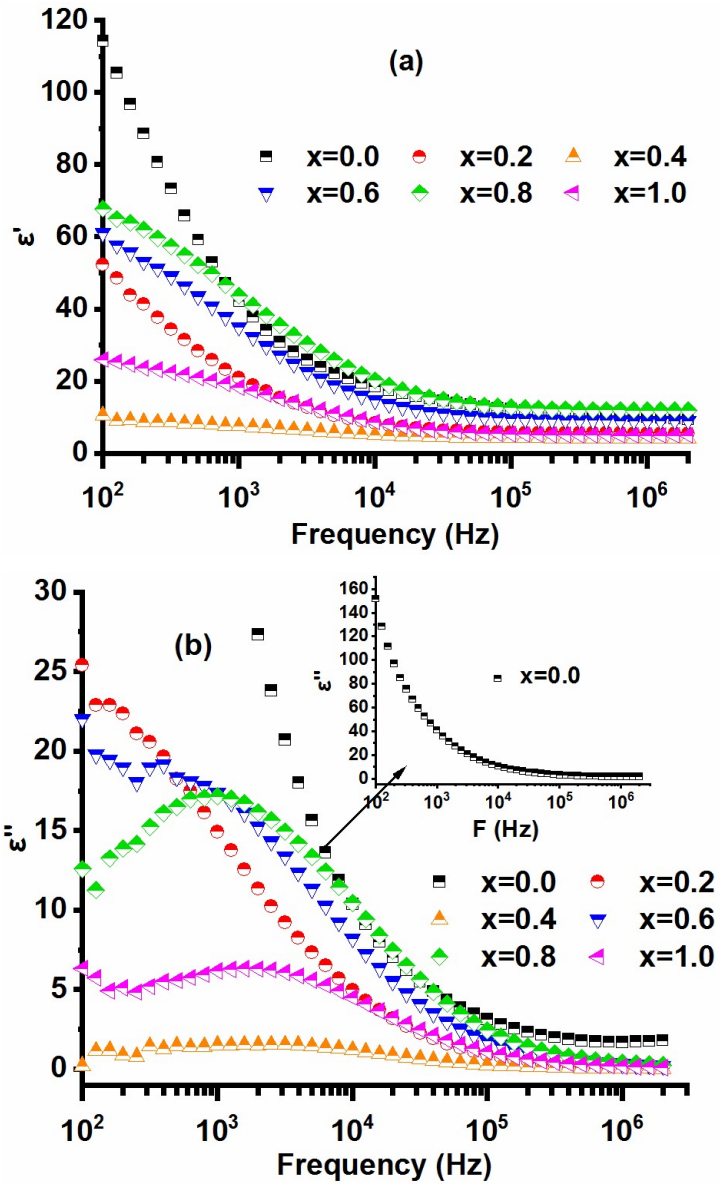

Fig. 4.25 Plot of dielectric constant for $SrCo_xNi_xFe_{12-2x}O_{19}$ (a) real (b) imaginary.

The value of ε' decreases inconsistently with the doping of Co^{2+} and Ni^{2+} caused by the decrement in the number of Fe^{3+} due to doping. The composition x=0.4 has ε'=10.5 being the lowest among all the compositions at 100 Hz.

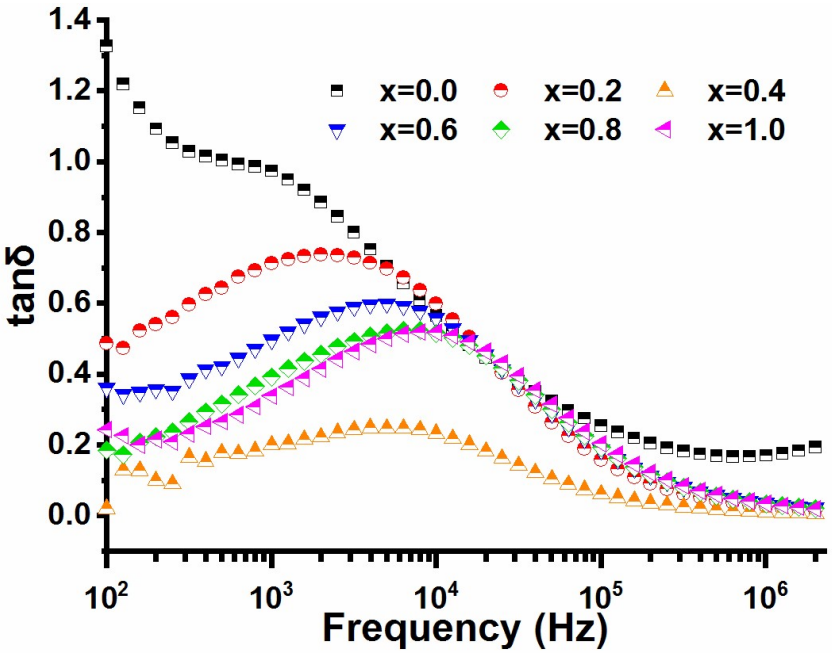

Fig. 4.26. Loss tangent v/s frequency of prepared compositions for $SrCo_xNi_xFe_{12-2x}O_{19}$.

Fig. 4.26 demonstrates the plots of loss tangent (tanδ) v/s frequency. A decrement in the value of tanδ with frequency increment can be noted, which follows Koop's dielectric theory [80]. The doping of Co-Ni causes a decrease in the value of tanδ and the relaxation peaks can be seen for all the prepared compositions. According to the Rezlescu model, this peaking nature is obtained if the electron hopping frequency of Fe^{2+} and Fe^{3+} matches the applied field frequency [81]. The doping of Co^{2+} and Ni^{2+} causes the shifting of the peak towards the high-frequency regime. As energy requirement for electron exchange is more at low frequencies causing high loss tangent while it is less at high frequencies leading to low loss values.

4.2.2.2 Electric modulus

Fig. 4.27 (a) and (b) describe the graphs of M′ and M″ respectively. M has two basic features, the first sigmoidal step in M′ and the second broad asymmetric peak in M″ [82, 83]. It can be noted that a similar trend has been reported in earlier reports [102]. The value of M′ is low at low frequencies, however, it first increases, and after that saturated at high frequencies being the highest for x=0.4. The reason behind these observations may be the weakness of restoring force that governs charge carriers's

mobility [102]. A sigmoidal increase is associated with the charge carrier's short-range mobility; however, saturation assists the long-range mobility. The plot between M″ and frequency describes the charge transport mechanisms where asymmetric peaks can be seen for all the compositions. The low-frequency area of the peak denotes long-distance movement, while the high-frequency range denotes the localized motion. The peak frequency is used to determine the conduction relaxation time. The value of M″ varies non-monotonically with the enhanced doping content of Co-Ni. The height of the peak increases with the doping of Co-Ni, attributed to an increase in charge storage and dissipation. The doping narrows down the peak width and they shifted towards the high frequency with the doping of Co-Ni, which signifies a reduction in relaxation time: the product of hopping frequency and relaxation at a particular peak is equal to unity ($\omega\tau=1$) and hence $\tau=1/\omega$.

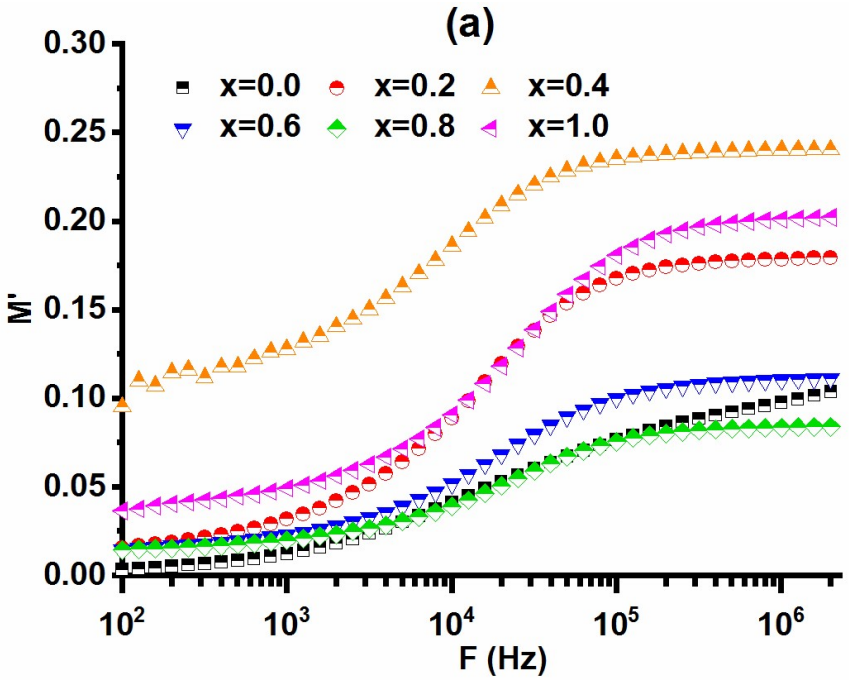

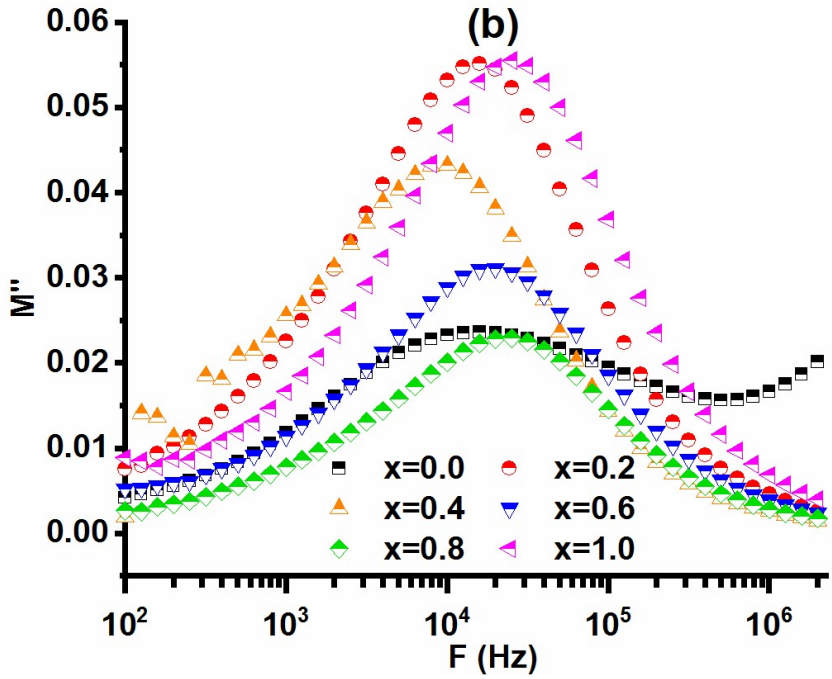

Fig. 4.27. (a), (b) Variation of Electric Modulus of $SrCo_xNi_xFe_{12-2x}O_{19}$.

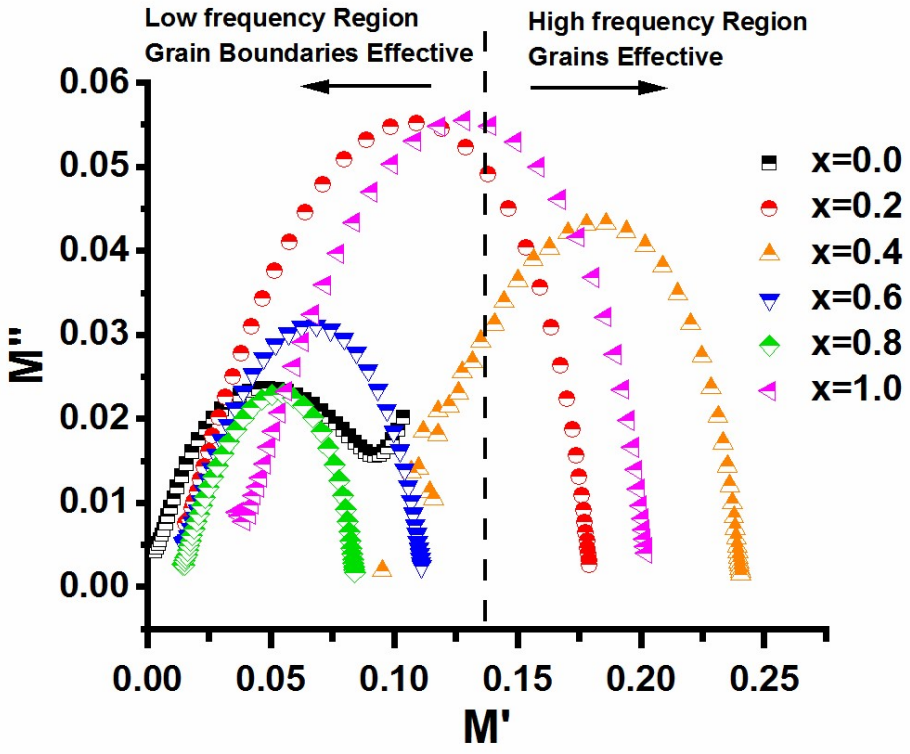

Fig. 4.28 Cole-Cole plot of $SrCo_xNi_xFe_{12-2x}O_{19}$.

A Cole-Cole plot ($M''v/s\ M'$) for $SrCo_xNi_xFe_{12-2x}O_{19}$ is shown in Fig. 4.28. It depicts asymmetric deformed semicircles for all the compositions. The centers of semicircles lie below the x-axis, implying a non-Debye behavior. The composition x=0.4 has a semicircle in the high-frequency range indicating the dominance of grains which is in correlation with micrographs (Fig. 4.24c) with the presence of colossal fused grains. The compositions (0.0, 0.2, 0.6, and 0.8) have semicircles in the low-frequency area, indicating that the grain boundaries are more prevalent. Composition x=0.0 has a larger number of small grains with lots of grain boundaries can be noticed (Fig. 4.24a). Composition x=0.2 has considerably connected grains besides the grain clusters (Fig. 4.24b), thus, relaxation is relatively more towards low frequencies, wherein grain boundaries are more active than grain clusters. Composition x=0.6 has a larger number of needle-shaped grains (Fig. 4.24d), causing an increase in grain boundaries, thus relaxation towards the low-frequency. The plot for x=1.0 is found to be in the middle of the frequency band, showing the effect of grains and grain boundaries. This composition has grain clusters causing the grain effect, as well as a large number of small grains contributing to the grain boundary effect (Fig. 4.24f). Composition x=0.8 has shown abnormal behavior of showing relaxation in the low-frequency region despite grain clusters. The exact reason for this behavior cannot be determined and needs further investigation.

4.2.2.3 Complex impedance spectra

Fig. 4.29 depicts the plot of impedances versus frequency of the prepared ferrite compositions. Z' and Z'' indicate the impedance's real and imaginary terms for the prepared ferrites. Z' gradually falls first with an increase in frequency and thereafter, it attains a constant value. This variation corresponds to the frequency-dependent resistance in grain boundary and grain which complies with the Maxwell-Wagner model. Z' increases non-monotonically with an increment in the doping content of Co^{2+}, Ni^{2+}. The coalescing of plots occurs for the high-frequency regime, which indicates the reduction of resistance of grain boundaries at high-frequencies [103].

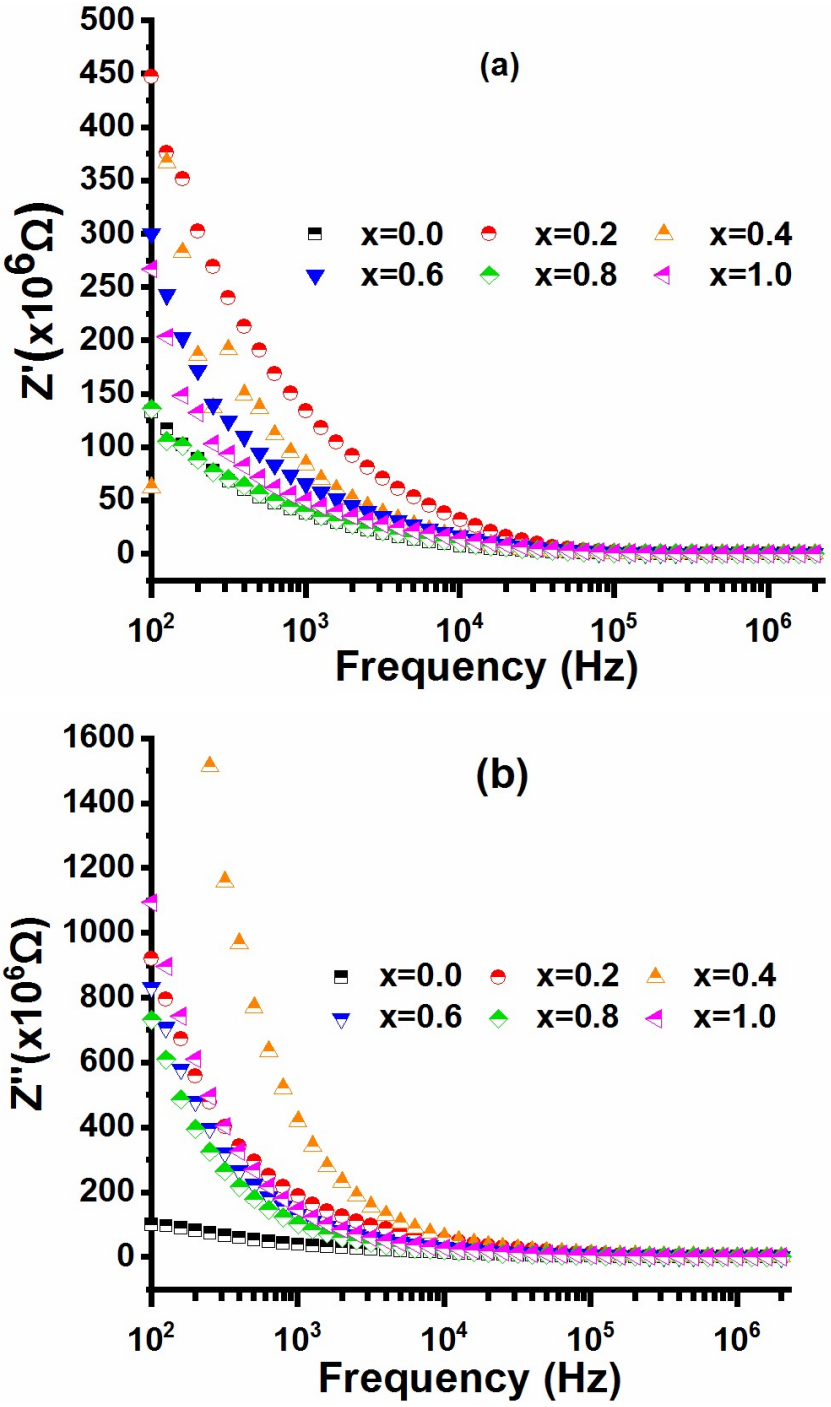

Fig. 4.29. Variation of Impedance of $SrCo_xNi_xFe_{12-2x}O_{19}$.

The doping of Co-Ni causes an increment in Z'' in the low frequencies. This signifies the increment in the reactance, which is inversely proportional to capacitance (Z''≒1/ωC), and polarization varies in proportion to capacitance. Hence the decrement

in space charge polarization may be the reason behind this increment in $Z''$with doping of Co-Ni. Further, the coalescing of all the curves at high frequency illustrates the reduction in space charge polarization with a frequency increment [103].

Cole-Cole plots of impedance Z''versus Z' are shown in Fig. 4.30 which shows a semi-circular arc for each composition. The semi-circular arcs are due to the weak dielectric relaxation [104]. Co-Ni doping shifts the arc towards the high-frequency region, which indicates that the role of grains is dominant as compared to grain boundaries. This is in agreement with the morphology (Fig. 24) as the formation of grain clusters can be seen in micrographs. As compositions 0.2 and 0.4 have their plots in the mid-frequency area, both the grains and grain boundary have a role in charge transport. However, the rest of the compositions have plots in the high-frequency area attributing to the dominance of grain in comparison to the grain boundaries.

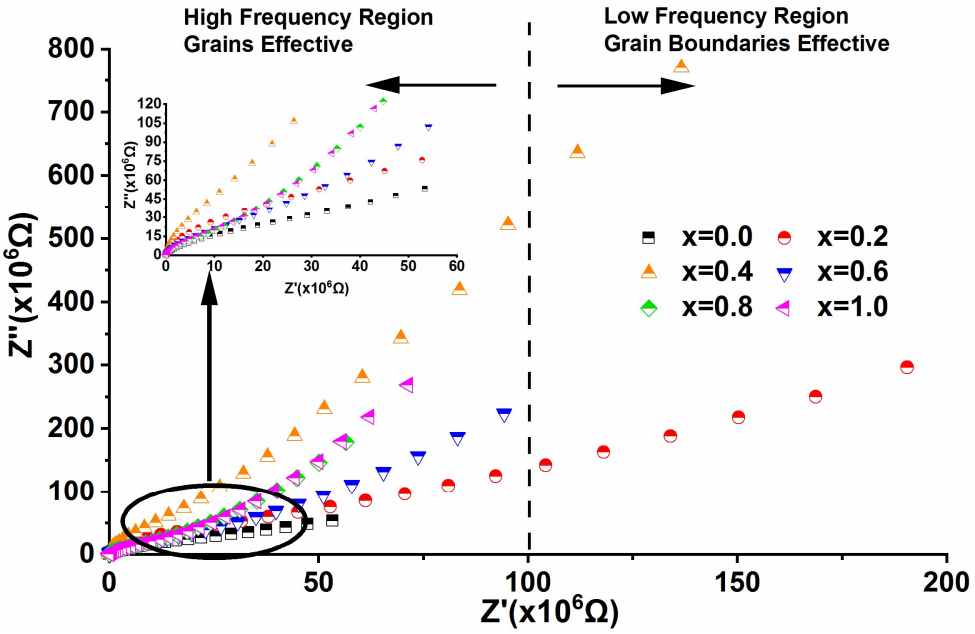

Fig. 4.30. Cole- Cole plot of Impedance for ferrite $SrCo_xNi_xFe_{12-2x}O_{19}$.

4.2.2.4 AC Conductivity

Fig. 4.31 demonstrates a plot of ac conductivity (σ_{ac}) with respect to frequency that shows a gradual increase in σ_{ac}. This increment is caused by the enhancement in the hopping of electrons for Fe^{2+} and Fe^{3+}. The conductivity increases after a frequency

called hopping frequency which indicates the transition from the flat plateau region of dc conductivity **(σ_{dc})** to the dispersive region of ac conductivity **(σ_{ac})**. Before this hopping frequency, nearly a frequency-independent behavior is shown by all the compositions. The addition of Ni^{2+} and Co^{2+} ions causes a decrease in conductivity as compared to the undoped composition. This decrement is due to the reduction in the hopping of electrons as doping reduces the Fe^{3+} ions.

The reason for low values of DC conductivity is linked to the prevalence of interfacial polarization in dielectric constant parameters as shown in Figure 4.25 attributing to the diffusion of charge carriers [85], while minimum space charge polarization causes a growth in AC conductivity at high frequency. The composition x=0.0 has the highest values of σ_{ac} which is due to the morphology: composition x=0.0 has good inter-grain connectivity (Fig. 4.24). The composition x=0.4 has the lowest values of ac conductivity, which is due to the less cross-sectional area of needle-shaped grains as depicted in micrograph fig. 4.24 (c). By fitting the plots, values of parameter n were calculated for the prepared compositions. The obtained values of n are 0.504, 0.394, 0.614, 0.503, 0.567, and 0.587. All the values are found to be less than 1 which indicates that ac conductivity follows the hopping mechanism.

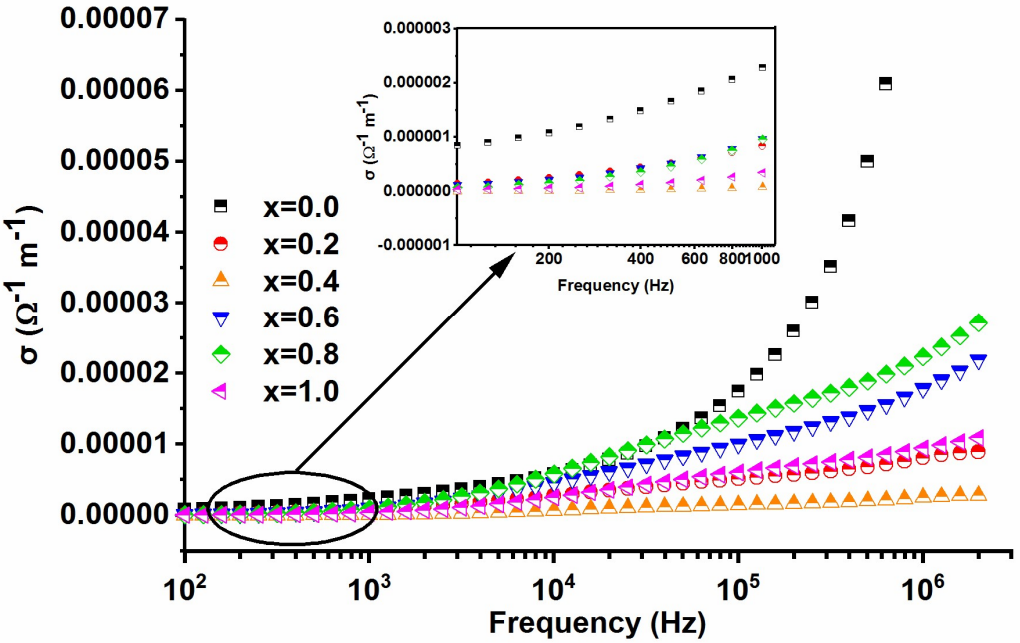

Fig.4.31 AC conductivity v/s frequency for ferrite $SrCo_xNi_xFe_{12-2x}O_{19}$.

4.2.2.5 Software-based Impedance Simulation

EIS software is employed to analyze impedance data. An equivalent circuit comprising two parallel RC circuits is proposed as given in Figure 4.32. These RC circuits represent the resistances and capacitances of grain (R_g, C_g) and grain boundaries (R_{gb}, C_{gb}). The constant phase element (CPE) is employed against the capacitor in regard non-Debye-type behavior of ferrite.

The capacitance of CPE is obtained from the relation given in equation 4.1.

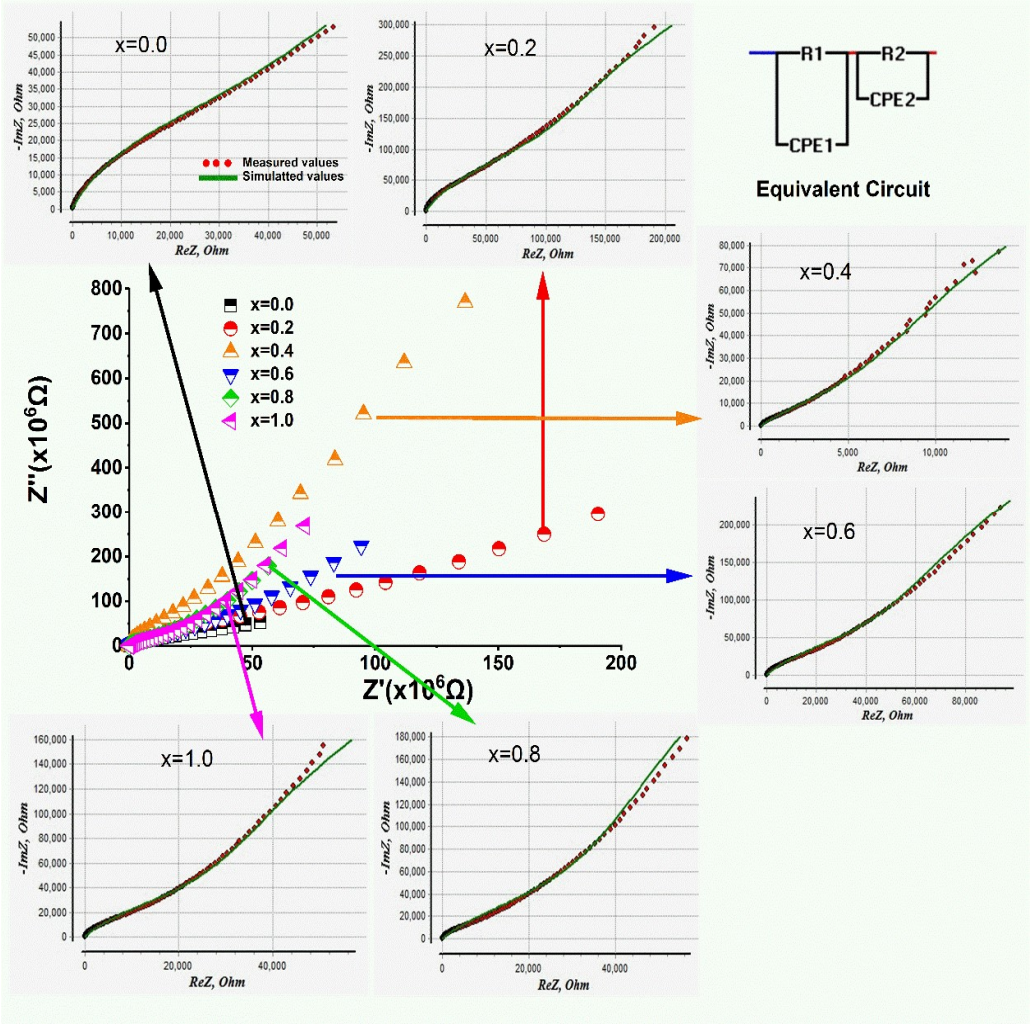

Fig. 4.32 Fitting of impedance curves using EIS software for $SrCo_xNi_xFe_{12-2x}O_{19}$.

The simulated/fitted curves showed harmony with the measured ones. Simulated parameters are reported in Table 4.7.

Table 4.7. Simulated parameters derived from EIS for $SrCo_xNi_xFe_{12-2x}O_{19}$.

x	R_g (MΩ)	R_{gb} (MΩ)	C_g (μF)	C_{gb} (μF)
0.0	29.75	409.5	57.43	95.03
0.2	140.56	1000	18.03	0.11
0.4	91.84	9921.5	604.13	41.39
0.6	62.96	1425	35.25	0.18
0.8	46.51	1980	71.50	0.18
1.0	38.14	1060	19.91	0.11

Correlation of simulated parameters with Morphology

The composition x=0.0 has a large number of small grains among all the compositions, causing the maximum number of grain boundaries as depicted in micrograph Fig. 4.24 (a). Many small pores can also be seen among the grains, which support the polarization at grain boundaries. It causes high grain boundary capacitance that is in agreement with the highest simulated C_{gb}=95.03 μF (Table 4.7). The poor connectivity of grain boundaries due to porosity renders the lowest grain boundary resistance of R_{gb}=409.5 MΩ among all the compositions. The composition x=0.2 has grain clusters with reasonable connectivity of small grains (micrograph Fig. 4.24), causing the highest grain resistance R_g=140.56 MΩ. The composition x=0.4 has a uniform distribution of needle-shaped grains (with good connectivity) as well as fused grains (Fig. 4.24) that promote polarization inside the grains resulting in the highest simulated C_g=604.13 μF (Table 4.7). A large number of small needle-shaped grains contribute to more grain boundaries giving the highest simulated R_{gb}=9921.5 MΩ. The composition x=0.6 has higher C_g=35.25 μF as compared to the grain boundary capacitance C_{gb}=0.18 μF due

to the polarized needle-shaped grains. The large porosity between grains causes hindrance to polarization at grain boundaries. The micrographs of compositions x=0.8 and x=1.0 show the formation of large grains/grain clusters due to fusion/agglomeration, which promotes polarization in grains causing higher C_g than C_{gb} matching with the simulated values as listed in Table 4.7.

Correlation of simulated parameters with Dielectric Parameters

Composition x=0.0 has the highest while x=0.4 owes the lowest value of dielectric constant for the low-frequency regime (Fig. 4.25). As per the Maxwell-Wagner model, a grain boundary is active in the low-frequency area, while the grain is in the high-frequency area. Table 4.7 shows that x=0.4 has the highest simulated R_{gb}=9921.5 MΩ, instead of owing lowest ε'=10.5 at 100 Hz that validates inverse relation of ε' with resistivity. Composition x=0.0 has the smallest R_{gb}=409.5 MΩ among all the compositions resulting highest value of ε'=114.27. Likewise, x=0.0 has the highest ε'' and tanδ (Fig. 4.26) attributing to the same reason.

Correlation of simulated parameters with Electric Modulus

The composition x=0.0 shows semicircles towards the low-frequencies (Fig. 4.28) attributing to the dominance of grain boundaries. The plots of x=0.2 are in mid of the frequency region with an inclination towards the low-frequency side. The composition x=0.4 has more role of grains due to the shifting of semicircle towards the high-frequency (Fig. 4.28). The semi-circles of x=0.6 and 0.8 lie in the low-frequency area, showing dominance of grain boundaries. Composition x=1.0 shows a similar behavior as the composition x=0.2 with a slight shift of peak towards high frequency. This behavior can be described in conjunction with Table 4.7: The impact of grain boundaries for composition x=0.0 can be validated by the highest values of simulated C_{gb}=95.03 μF. The contribution of grain boundaries for charge transport mechanism in composition x=0.2 can be validated by the high value of grain boundary resistance R_{gb}=1000 MΩ as compared to grain resistance R_g=140.56 MΩ. Composition x=0.4 owes the highest grain capacitance C_g=604.13 μF attributing to the role of grains. The shift of peak towards the grain side in composition x=1.0 as compared to x=0.2 can be validated by the increase in grain capacitance C_g from 18.02 μF (x=0.2) to 19.91 μF (x=1.0).

4.2.3. Band gap Characteristics

Fig 4.33 shows the Tauc plots drawn for the prepared $SrCo_xNi_xFe_{12-2x}O_{19}$ hexaferrites. Equation 3.4 as given in the experimental section in Chapter 3 is employed to find the required values of band gap. From the linear region of the Tauc plot an intercept on the x-axis is found to obtain the band gap. The band gaps of the prepared compositions x=0.0 to 1.0 are 2.68, 2.54, 2.92, 2.90, 2.89, and 3.01 eV respectively. The ferrites generally have a band gap in the range of 2 to 3 eV hence the obtained values are in the prescribed range.

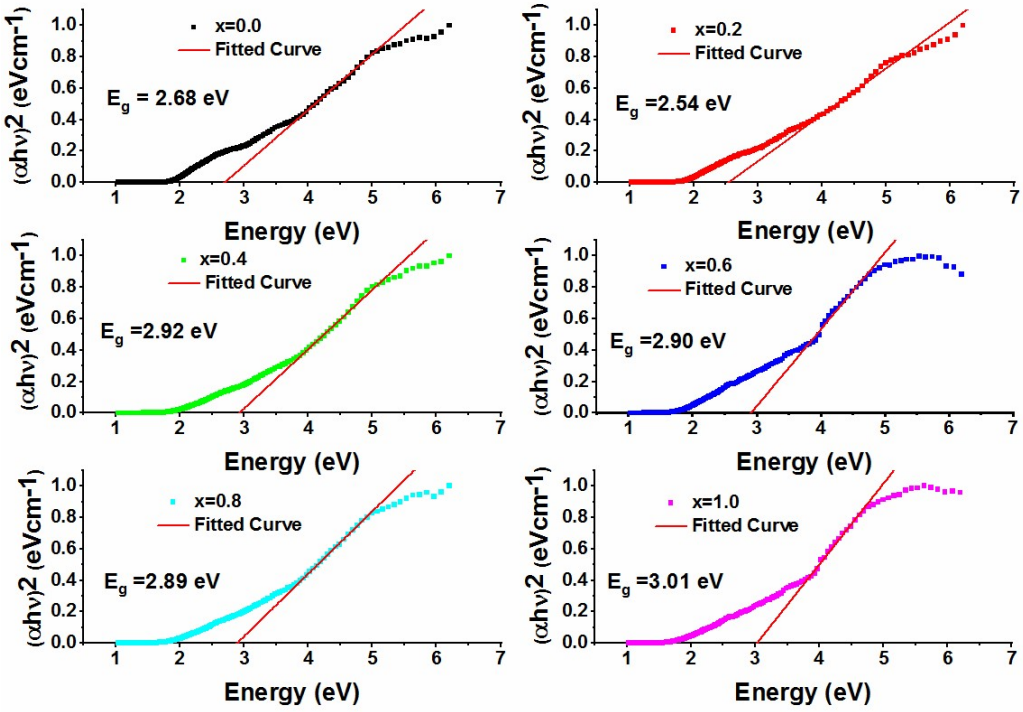

Fig. 4.33 Tauc plots of $SrCo_xNi_xFe_{12-2x}O_{19}$.

4.2.4. Magnetic Characteristics

For the analysis of magnetic characteristics of $SrCo_xNi_xFe_{12-2x}O_{19}$ hexaferrites magnetization (M) versus magnetic field (H) plots are drawn. The respective hysteresis loops are displayed in Fig. 4.34 (a). The site occupancy of the ions is related to their electronegativity. The ions having higher electronegativity mostly try to acquire octahedral rather than tetrahedral sites [88]. The electronegativity of Ni^{2+}(1.91) is

higher than that of Co^{2+}(1.88) hence they will tend to occupy the octahedral sites 4f2(↓) [89]. As per the ligand field theory, Ni^{2+}due to $3d^8$ configuration and Co^{2+} with $3d^7$preferably choose octahedral sites 12k (↑), $2a(\uparrow), 4f_2(\downarrow)$ [90]. Karim et al. [105] reported that Ni^{2+}prefer octahedral $4f_2$sites while Singh et al. [90] reported that Co^{2+} prefer to occupy octahedral sites.

Saturation magnetization (M_s) and anisotropy field (H_a) are determined by the law of saturation [92] using equation 4.2.

In hexaferrites, B is related to H_a as $B = H_a^2/15$ with H_a representing the anisotropy field. Fig. 4.34 (a) shows a steep rise in magnetization at the low field that declined at the high fields. The undoped composition x=0.0 possesses a large slope at high fields indicating an unsaturated state which reduces with the substitution of Ni^{2+} and Co^{2+}. The reason behind this is the reduction in anisotropy field. From the plots, it can be noted that there is a linear relationship for the values from 10 KOe to 15 KOe hence A/H and χ_P maybe removed in equation 4.2. Thus the value of B can be obtained from the relation $M=M_s\ (1-B/H^2)$. With the help of B, the values of H_a can be obtained by applying the relation $H_a^2 = 15\,B$. Hence to find out M_s, plots of M v/s $1/H^2$ for all the compositions have been plotted, and linear fitting is performed to acquire the respective values as shown in Fig. 4.34 (b). Table 4.8 enlists the values of different parameters obtained from M-H loops and M v/s $1/H^2$ plots.

For hexaferrites, the magnetic moment related to spin-up and down sites is given as in equation 4.3 which is utilized to explain the effect of substitution of ions. From the relation given in equation 4.3, it can be noted that the substitution of weaker/non-magnetic ions on spin-down sites Mb $(4f_1\downarrow + 4f_2\downarrow)$ enhances saturation magnetization while more occupancy at spin-up sites Ma $(2a\uparrow + 12k\uparrow + 2b\uparrow)$ reduces it. There is a non-monotonous variation in M_s for the prepared compositions. It increases 46 % with the substitution of Ni^{2+} and Co^{2+} from 57.18 to 105.77 emu/g for x=0.0 to 0.6. This is due to the replacement of Fe^{3+} by Ni^{2+} and Co^{2+} at spin-down sites.

The relation among M_s, M_a, and M_b indicates that the substitution of weak magnetic Ni^{2+} and Co^{2+} at the octahedral spin-down sites $4f_2(\downarrow)$ results in a decrease in the value of M_b which in turn enhances the M_s. The large increase in M_s is attributed to the

morphology: formation of needle-shaped grains (micrographs Fig. 4.24) causes an increase in surface-to-volume ratio which enhances M_s. After x=0.6 M_s starts decreasing and there is a 37% decrease in M_s from x=0.6 to x=1.0. The low magnetic moment of Co^{2+} (3μB) and Ni^{2+} (2 μB) is the reason behind it. The replacement of Fe^{3+} at octahedral spin-up sites 2a↑ and 12k↑ causes an imbalance in electrical neutrality and to maintain it Fe^{3+} is converted into Fe^{2+} which diminishes the strength of superexchange interactions due to which magnetic moment decreases. Also the substitution at spin-up sites $(2a\uparrow + 12k\uparrow + 2b\uparrow)$ reduces the net value of M_a in response to which M_s decreases.

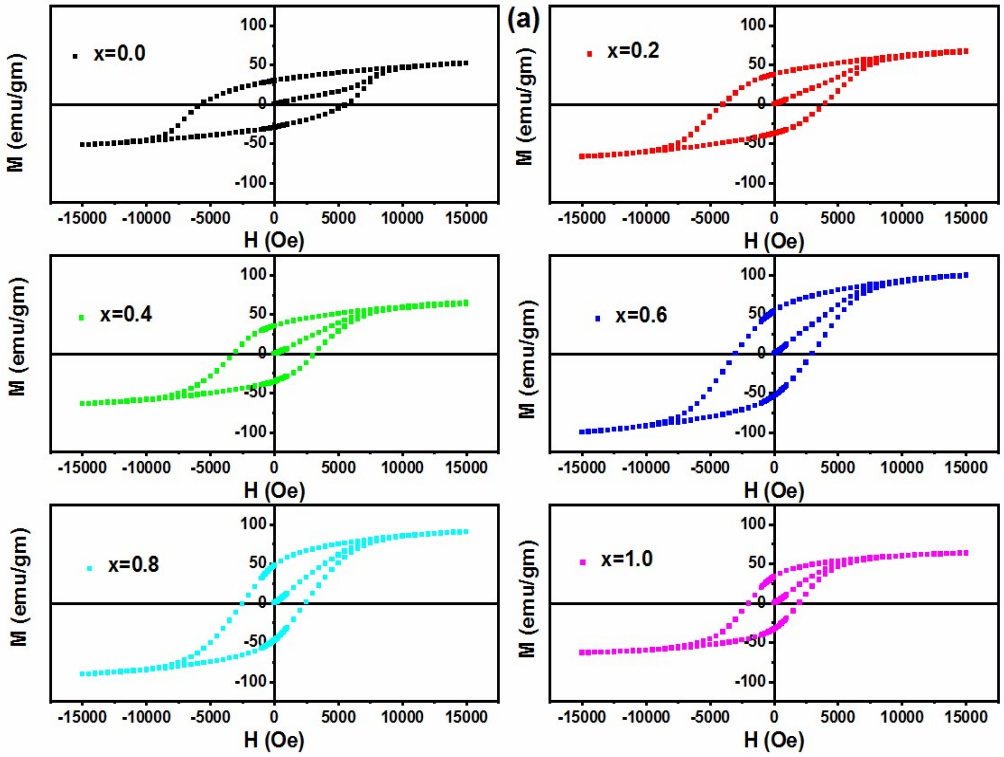

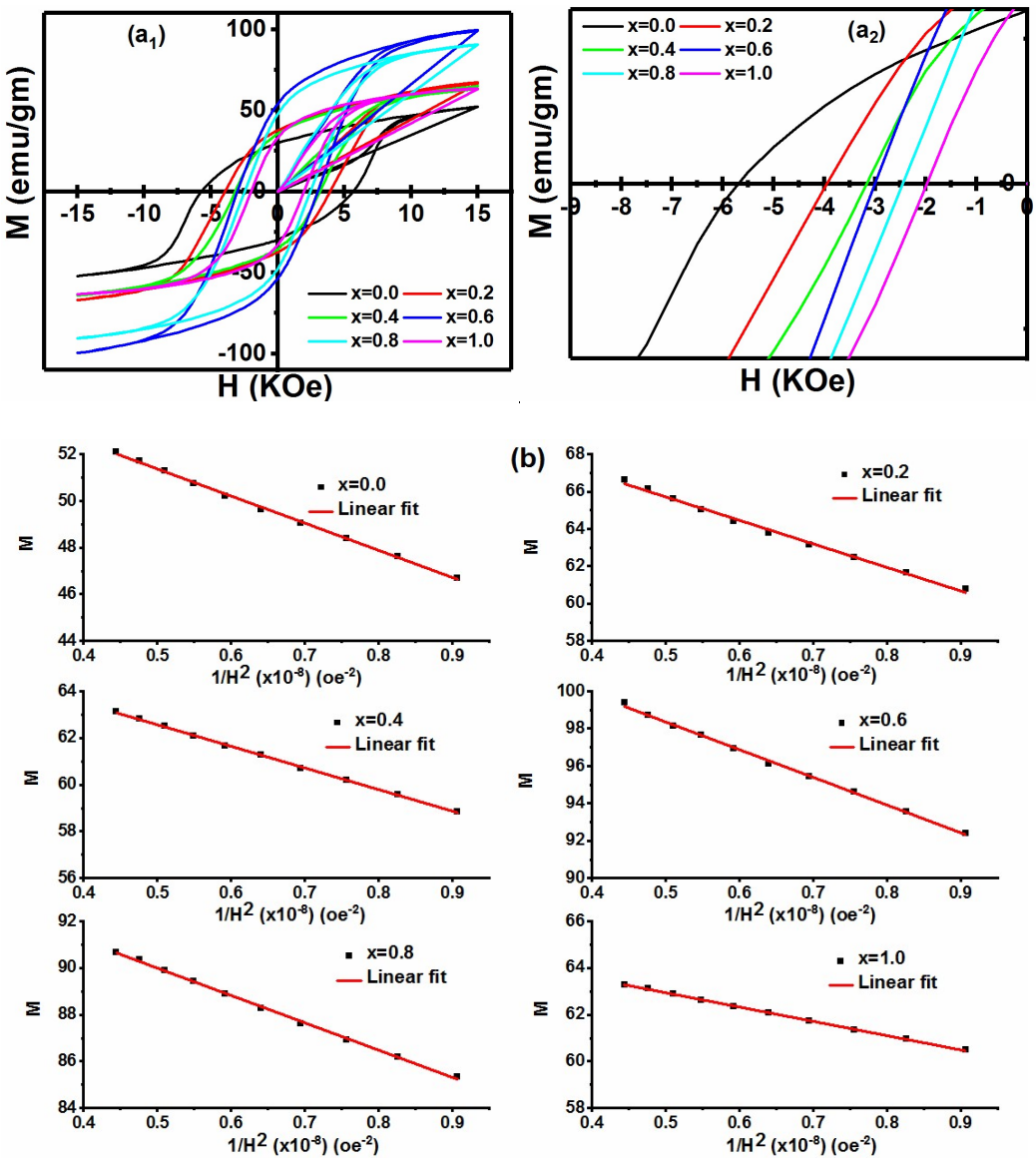

Fig. 4.34 (a) M-H loops (a_1, a_2) combined and enlarged view (b) Ms v/s $1/H^2$ plots of $SrCo_xNi_xFe_{12-2x}O_{19}$.

Table 4.8 Magnetic parameters determined from M-H loops of $SrCo_xNi_xFe_{12-2x}O_{19}$.

x	M_s (emu/g)	M_r (emu/g)	H_a(kOe)	H_c (Oe)	M_r/M_s
0.0	57.18	29.84	17.47	5710	0.52
0.2	72.01	37.71	16.20	3955	0.52

0.4	67.18	35.55	14.37	3169	0.53
0.6	105.77	53.92	14.50	3007	0.51
0.8	95.84	47.72	13.53	2448	0.50
1.0	65.99	33.15	11.79	1974	0.50

The lower values of coercivity (H_c) is the prime requirement in the design of an efficient absorber. Table 4.8 reveals that the doping of Co-Ni has reduced the value of H_c. The highest H_c=5710 Oe is obtained in composition x=0.0 while the smallest value of H_c=1974 Oe is achieved in composition x=1.0. There is a 65 % decrease in the value of H_c, which is due to the substitution of weak-magnetic Ni^{2+} and Co^{2+} which converted the ferrites to magnetically soft ferrites. There are two factors affecting the values of H_c one is the intrinsic factor involving anisotropy field H_a and the second is extrinsic related to morphology. From Table 4.8 it is evident that there is a reduction in the value of H_a which has a direct relation with H_c. The consistent decrease in the values of H_a produces a decrement in H_c. H_a decreases around 32 % (x=0.0 to 1.0) which is due to the substitution of Fe^{3+} at octahedral sites $4f_2$, as this site contributes to a large anisotropy field. Replacement of Fe^{3+} at this site causes a reduction in H_a. H_c decreases by 65 %, while a 33 % decrease in H_a, so another reason for a large reduction in H_c is the large ionic radius of Ni^{2+} (0.69 Å) and Co^{2+} (0.745 Å) in comparison to Fe^{3+} (0.645 Å). Secondly, the SEM images reveal that there are pores in the composition x=0.0 which reduces with the inclusion of Co-Ni, and composition x=1.0 possesses large grain clusters causing good grain connectivity and reducing coercivity H_c as grain size and H_c have inverse relation.

M_r/M_s ratio describes the retention of magnetization after the removal of the applied field. This ratio ranges from 0 to 1 and a value less than 0.5 represents randomly oriented multi-domain particles while values higher than 0.5 indicates a single domain. All the compositions have M_r/M_s ratio more than 0.5 representing single domain structure.

4.2.5 Electromagnetic Characteristics

4.2.5.1 Complex permeability and complex permittivity

Graphs for dielectric constant/loss ($\varepsilon', \varepsilon''$), and permeability/magnetic loss (μ', μ'') against frequency are depicted in Fig 4.35. Both the dielectric constant and loss vary in a non-monotonous way with the inclusion of Co-Ni. A decrement in the value of the ε' while an increment in ε'' is observed in doped compositions as compared to the undoped composition. There is a decrement in the value of ε' with the frequency increment in compositions x=0.2, 0.4, 0.6, and 1.0 while it increases for x=0.0. The composition x=0.2 has the least ε' with the increment in frequency among all doped compositions. Compositions x=0.2 and x=0.6 have a relaxation peak in ε'' around 11.5 GHz. The composition x=1.0 shows dual relaxation peaks one large peak at 9.5 GHz while a comparatively small peak around 11.5 GHz. Besides that, this composition has the highest dielectric loss among all the compositions.

The permeability of the compositions varies non-linearly with the addition of Co-Ni. The doped composition has high values of μ' as compared to the undoped composition. The compositions x=0.2 and 0.4 have relaxation peaks around 9.5 GHz, however the x=0.0 has a relaxation peak near about 10.5 GHz. There is an enhancement in the value of μ' with the increment in frequency for all compositions being highest in x=1.0. The compositions x=0.2 and 0.4 possess dual relaxation peaks in μ'' one at low frequencies (9 to 10 GHz) and another at high (11.5-12.4 GHz). The composition x=0.0 possesses a relaxation peak near about 10.5 GHz. For low frequencies, composition x=0.0 has the maximal value of μ'' while x=0.4 obtains the maxima in the high frequency region.

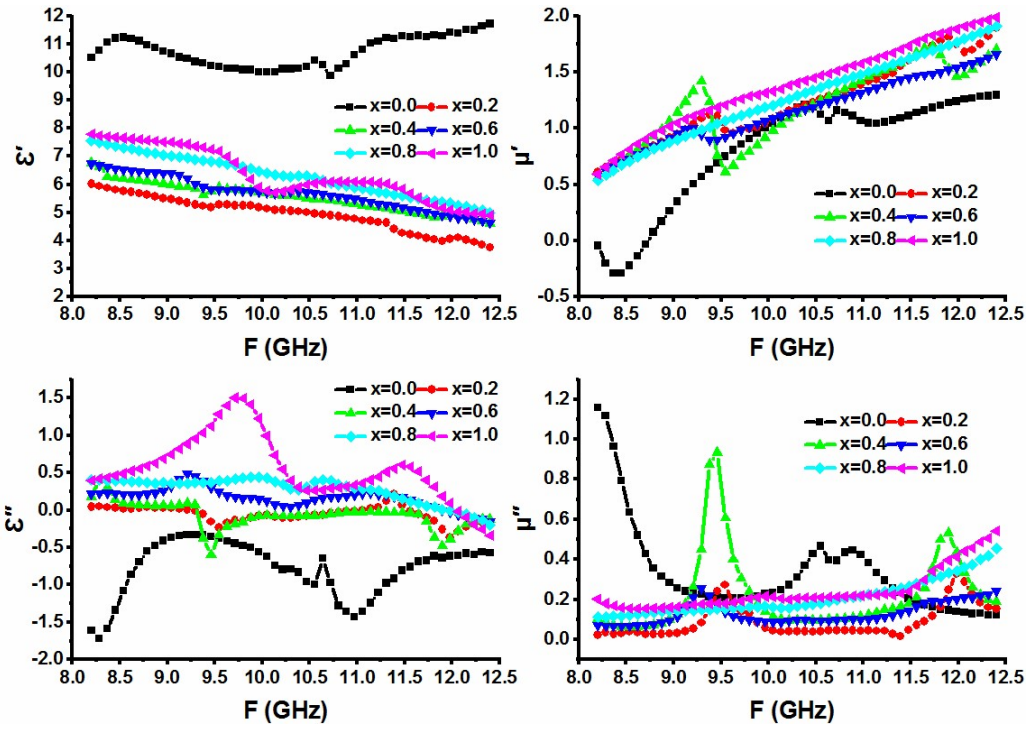

Fig. 4.35 Complex permittivity and permeability versus frequency plots for $SrCo_xNi_xFe_{12-2x}O_{19}$.

The complex permittivity/permeability depends on grains, porosity, grain distribution, electron spin, and polarization at the microwave region [94]. Electron hopping in Fe^{2+}/Fe^{3+} causes dielectric polarization [95]. The large porosity depresses polarization as well as restrains field flow. Exchange resonance among Fe^{3+}/Fe^{2+} and ferromagnetic resonance govern the complex permeability [96, 97]. The doping of Co-Ni decreases the number of Fe^{3+} which affects polarization and resonance. Pores in the SEM images can be seen which are non-magnetic vacancies affecting magnetization related to permeability. There is an inconsistent variation for grain size as well as grain boundary as can be viewed in micrographs (Fig. 4.24) which modifies the permittivity/permeability.

Large-size grain supports electron hopping, however, grain boundaries discourage the field flow. The permeability increases as the large grains enhance electron spin while the accumulation of charge at grain boundary promotes polarization. Further, the reduction in exchange resonance due to porosity and small grains is responsible for magnetic loss between Fe^{3+} and Fe^{2+}. The peaking nature in complex

permittivity/permeability observed in the prepared compositions is attributed to the dielectric relaxation and ferromagnetic resonance respectively.

4.2.5.2 Microwave absorption in $SrCo_xNi_xFe_{12-2x}O_{19}$

The absorption characteristics of any material are understood on the basis of reflection loss: the higher the reflection loss better the absorption. It is calculated utilizing equations 3.13 and 3.14 using the material's impedance Z_{in} and impedance of air Z_0. The microwave absorption characteristics are explored on the basis of the $\lambda/4$ and impedance matching mechanism as well as dielectric/magnetic losses as explained in the following sections.

4.2.5.3 Quarter Wavelength Mechanism

Graphs of reflection loss (RL) against frequency at different simulated thicknesses have been used to explain the phenomenon of microwave absorption in the prepared compositions. Fig. 4.36 (a, c, e), 4.37 (a), 4.38 (a, c), 4.39 (a, c, e), 4.40 (a, c, e, g, i) and 4.41 (a, c, e, g) depict RL plots of $SrCo_xNi_xFe_{12-2x}O_{19}$ ferrites. These are used to determine different parameters such as matching frequency, bandwidths, and frequency bands of RL below -10/-20 dB. The summarized values of the parameters are provided in Table 4.9.

Highest RL=-37.46 dB is obtained in composition x=0.8 at the frequency of 10.05 GHz with 8.0 mm. The RL of other compositions ranges between -12.59 dB and -37.10 dB at 9.88 and 12.40 GHz at the thicknesses of 3.0 and 9.3 mm respectively. There is a non-monotonous variation in the RL peaks with the increment in thickness. Fig. 4.36 (a, c, e) demonstrates the absorption characteristics of composition x=0.0. The thicknesses from 5.5 to 6.0 mm have a RL ≥ -10 dB for the frequency band of 10.80-11.14 GHz. The RL peak shifted toward low frequencies with the increment in thickness. The frequency band of reflection loss ≥ -20 dB from 11.30-11.39 GHz is obtained for the thickness of 5.6 mm.

The x=0.2 has an RL=-24.94 dB with 9.54 GHz for 10.0 mm thickness. In this composition thickness from 9.0 to 10.0 mm for a frequency band ranging from 9.46-9.54 GHz show RL ≥ -10 dB Fig. 4.37 (a).

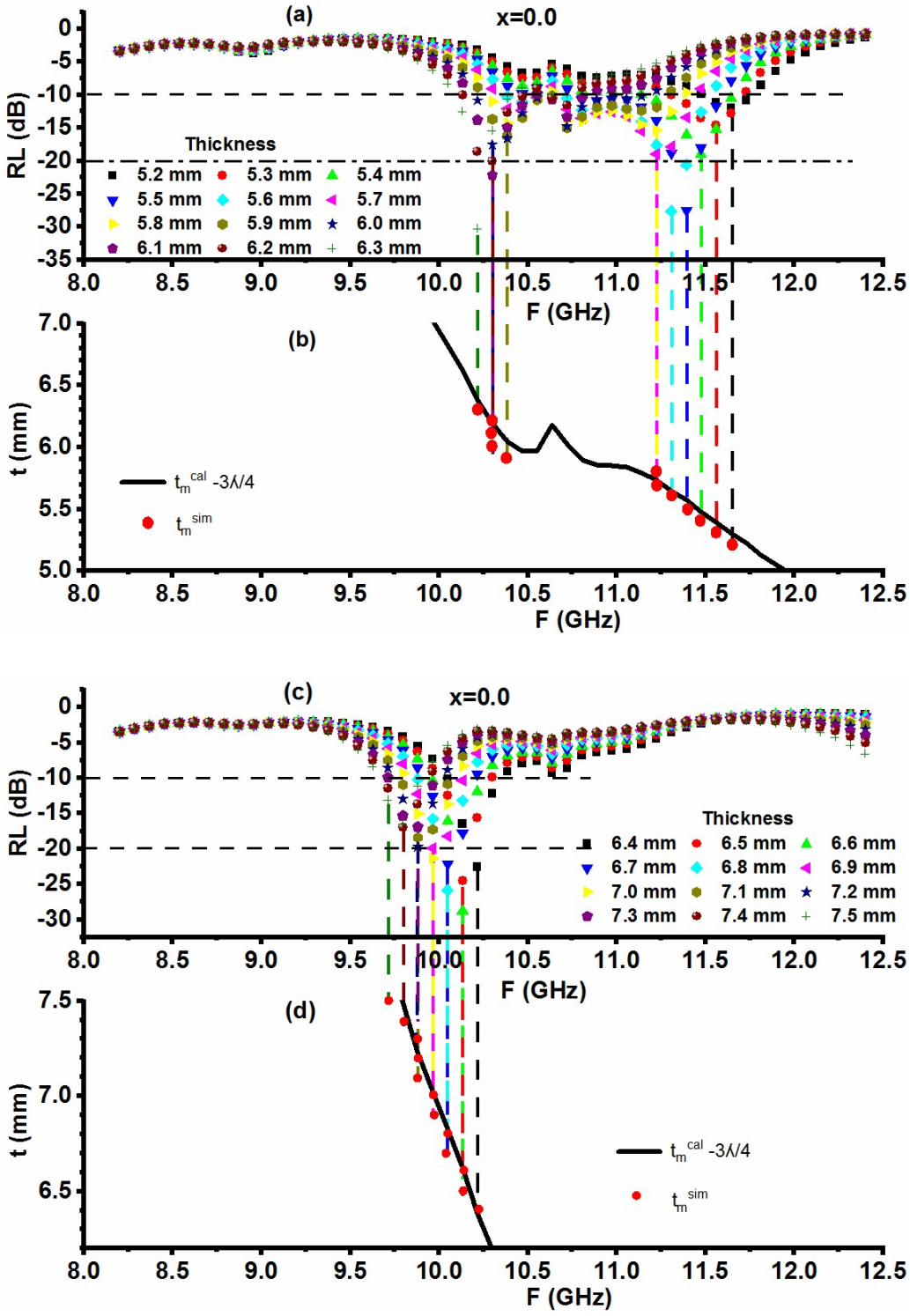
(a)
x=0.0
RL (dB)
Thickness
5.2 mm
5.3 mm
5.4 mm
5.5 mm
5.6 mm
5.7 mm
5.8 mm
5.9 mm
6.0 mm
6.1 mm
6.2 mm
6.3 mm
F (GHz)
(b)
t (mm)
t_m^{cal} -3λ/4
t_m^{sim}
F (GHz)
(c)
x=0.0
RL (dB)
Thickness
6.4 mm
6.5 mm
6.6 mm
6.7 mm
6.8 mm
6.9 mm
7.0 mm
7.1 mm
7.2 mm
7.3 mm
7.4 mm
7.5 mm
F (GHz)
(d)
t (mm)
t_m^{cal} -3λ/4
t_m^{sim}
F (GHz)

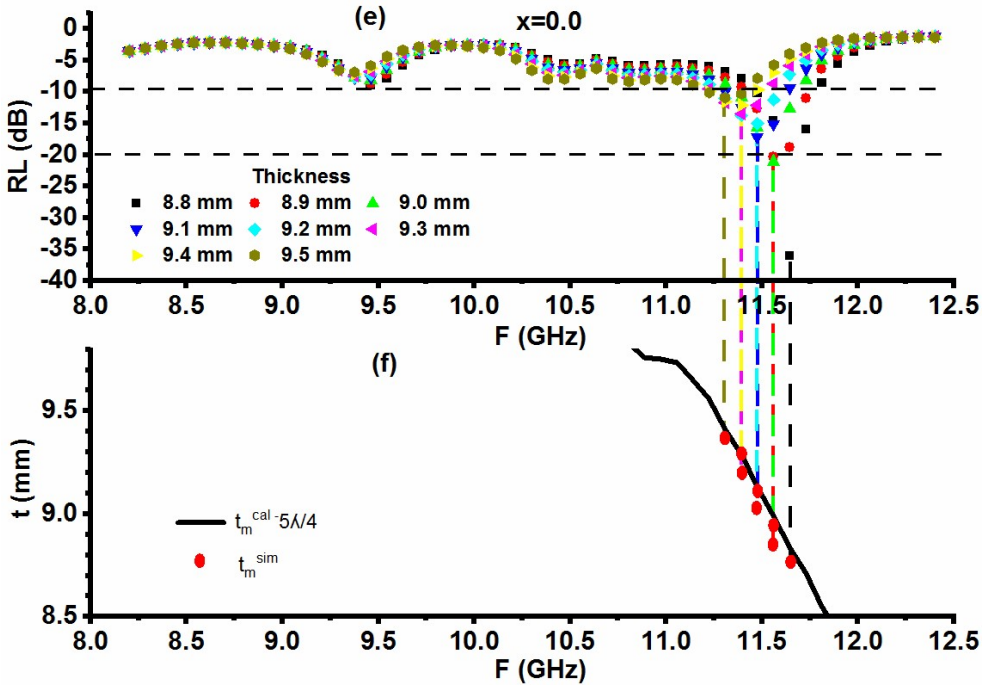

Fig. 4.36 (a, c, e) RL versus frequency (b, d, f) thickness versus frequency in x=0.0 for $SrCo_xNi_xFe_{12-2x}O_{19}$.

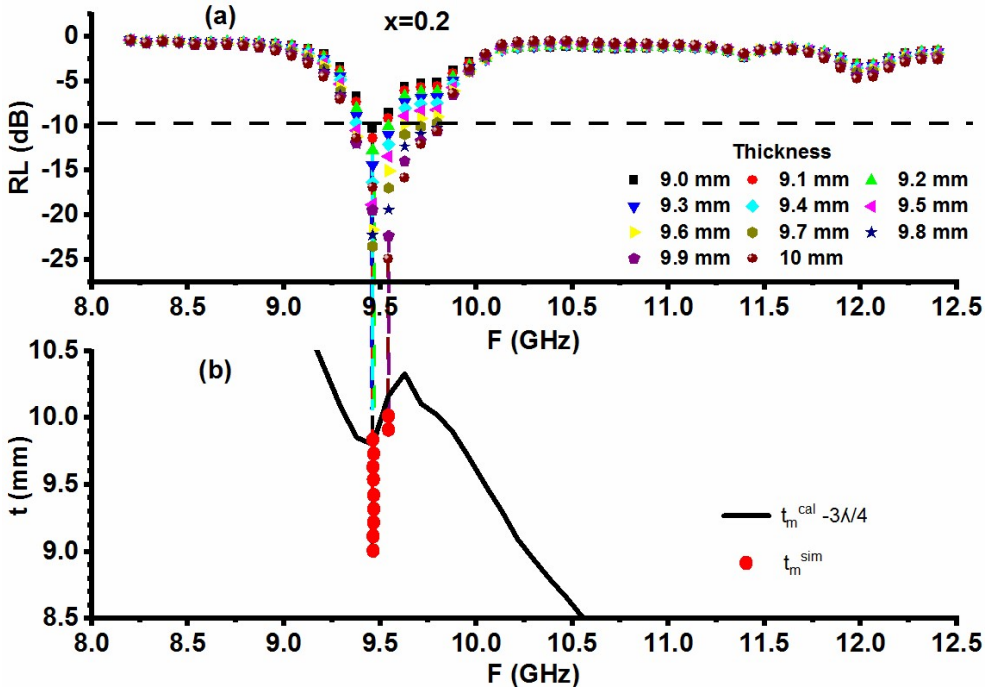

Fig. 4.37 (a) RL versus frequency (b) thickness versus frequency in x=0.2 for $SrCo_xNi_xFe_{12-2x}O_{19}$.

Composition x=0.4 possesses an RL=-34.49 dB at 3.5 mm for a frequency of 9.63 GHz. The 6.6 mm thickness shows *RL*≥-20dB for a frequency band of 11.90-11.98 GHz (Fig. 4.38 (a, c)). In x=0.6 a maximum RL=-30.43 dB with a frequency of 9.04 GHz at 10.0 mm is obtained (Fig. 4.39 (a, c, e)). The composition x=0.8 has peaks attributing reflection loss ≥-10/-20 dB from 5.4 to 10.0 mm (Fig. 4.40 (a, c, e, g, i)). This composition possesses the maximum RL=-37.46 dB among all the compositions. Composition x=1.0 shows RL peaks starting from a low thickness of 2.5 mm. An RL ≥ -20 dB is observed at thicknesses of 5.9, 6.1, 7.6, 9.3, 9.5, and 10.0 mm (Fig. 4.41 (a, c, e, g).

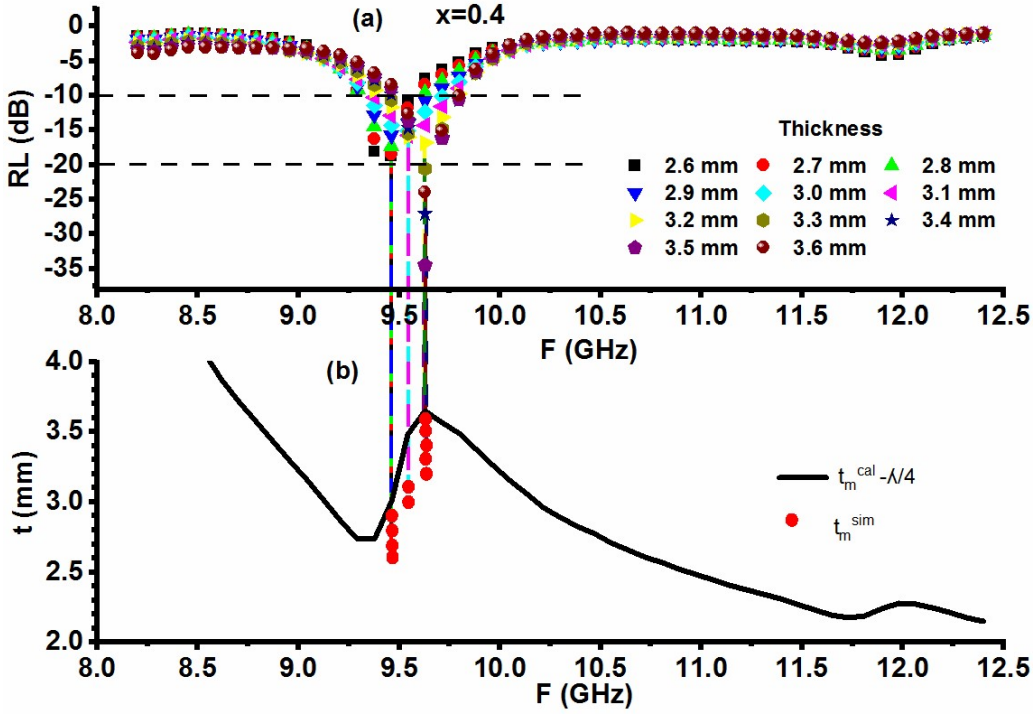

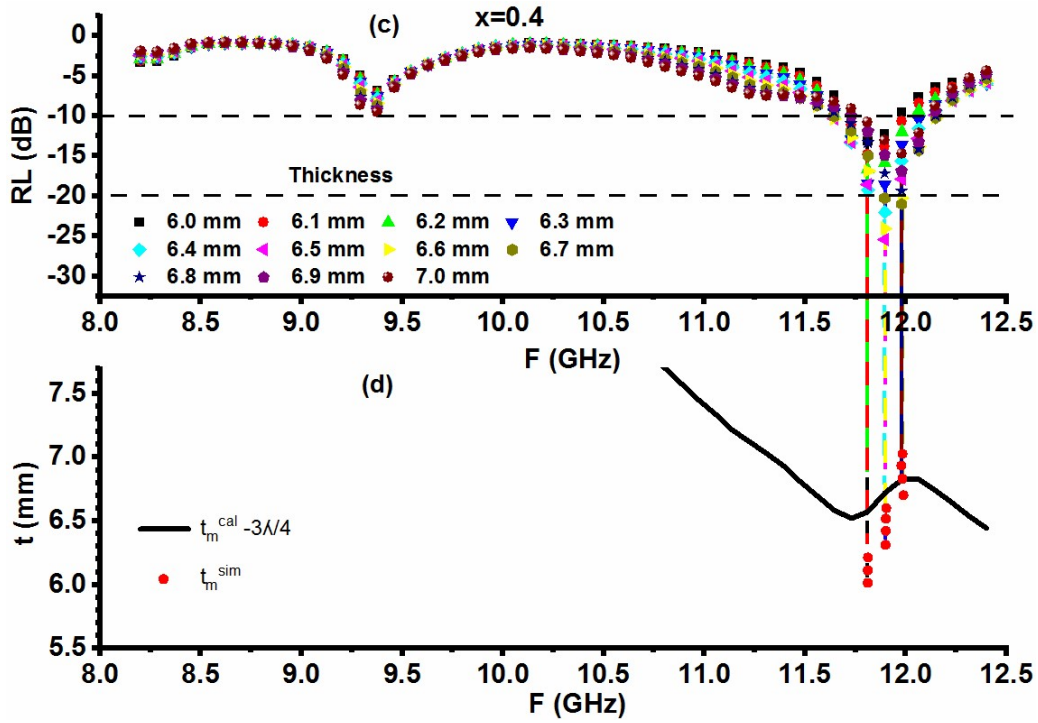

Fig. 4.38 (a, c) RL versus frequency (b, d) thickness versus frequency in x=0.4 for $SrCo_xNi_xFe_{12-2x}O_{19}$.

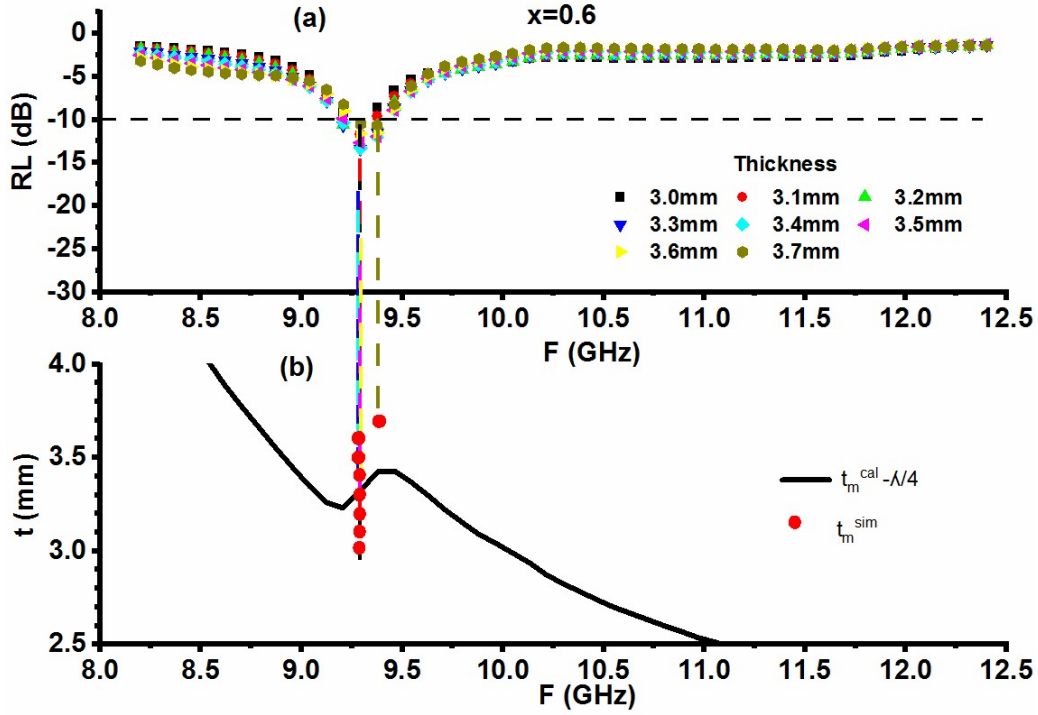

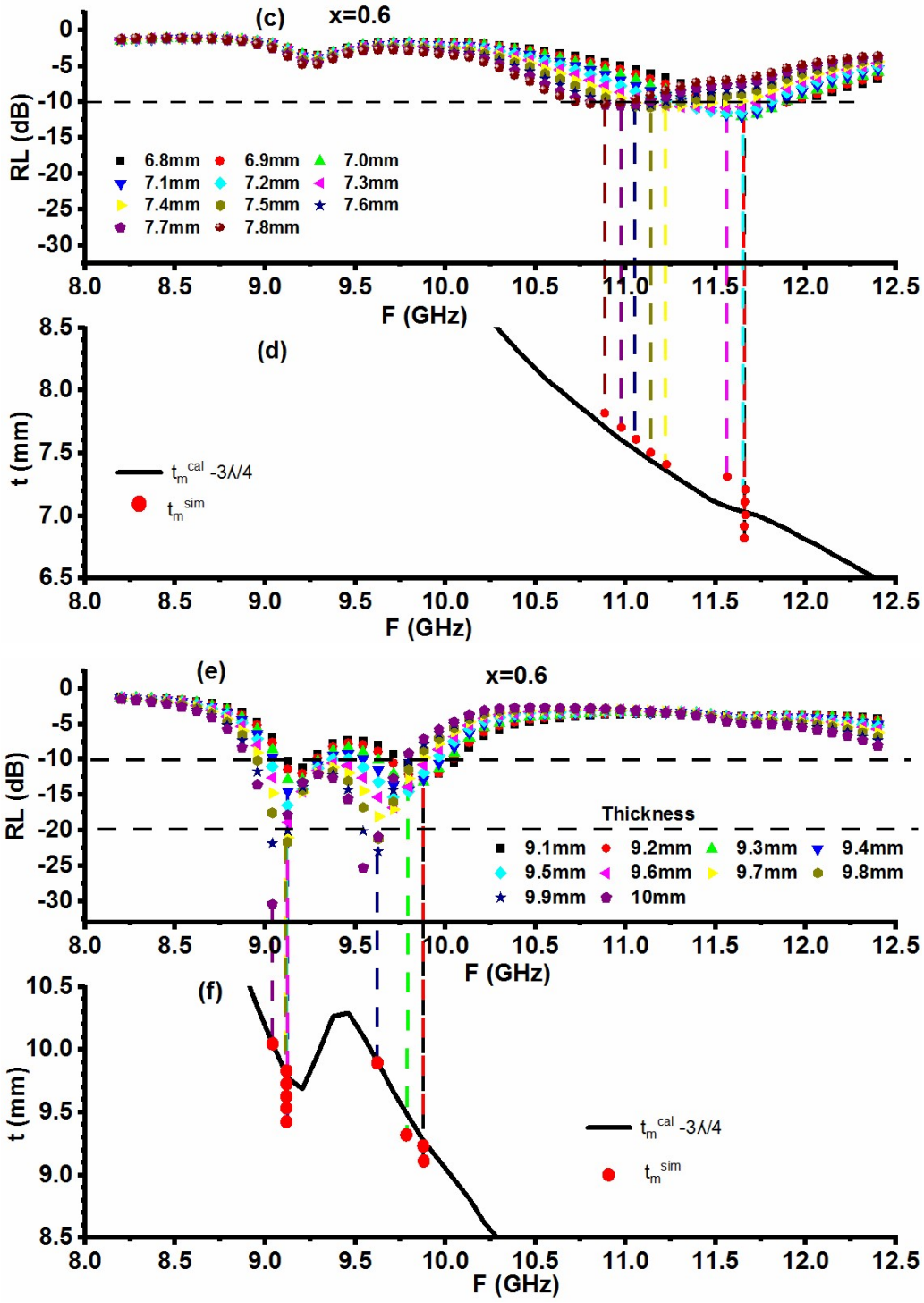

Fig. 4.39 (a, c, e) RL versus frequency (b, d, f) thickness versus frequency in x=0.6 for $SrCo_xNi_xFe_{12-2x}O_{19}$.

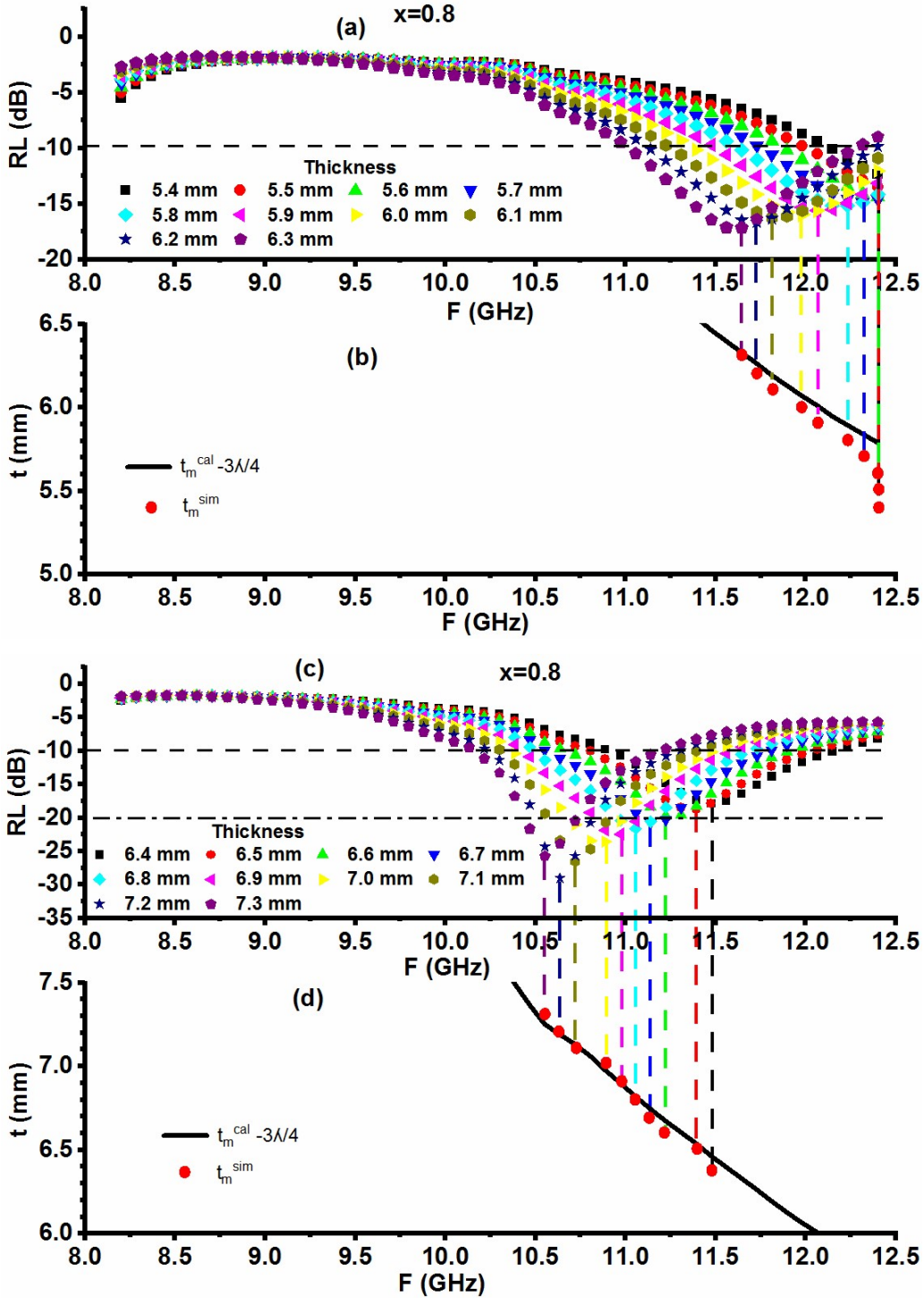
(a)
x=0.8
RL (dB)
F (GHz)
Thickness
5.4 mm
5.5 mm
5.6 mm
5.7 mm
5.8 mm
5.9 mm
6.0 mm
6.1 mm
6.2 mm
6.3 mm
(b)
t (mm)
F (GHz)
t_m^{cal} -3λ/4
t_m^{sim}
(c)
x=0.8
RL (dB)
F (GHz)
Thickness
6.4 mm
6.5 mm
6.6 mm
6.7 mm
6.8 mm
6.9 mm
7.0 mm
7.1 mm
7.2 mm
7.3 mm
(d)
t (mm)
F (GHz)
t_m^{cal} -3λ/4
t_m^{sim}

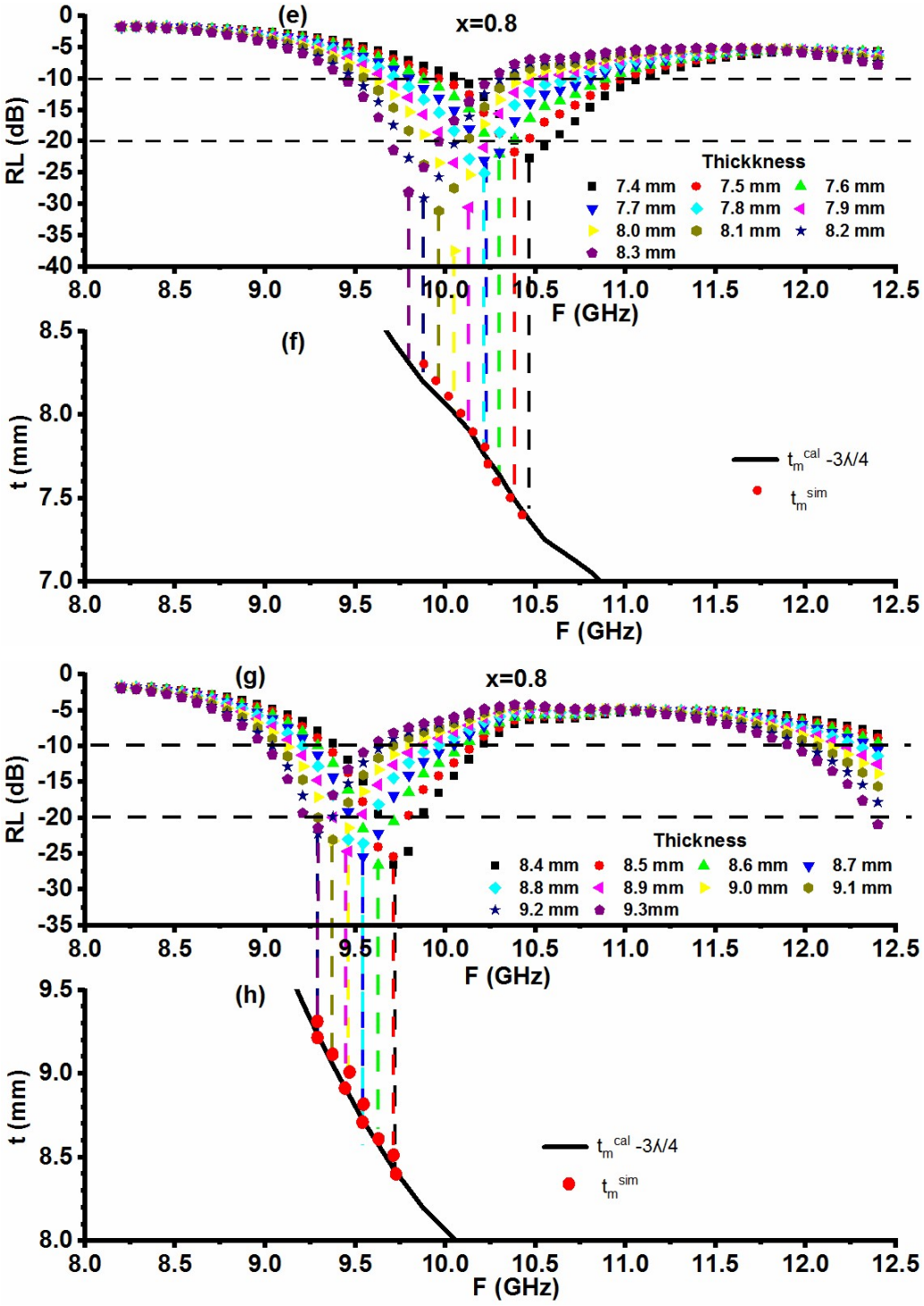
(e)
x=0.8
RL (dB)
F (GHz)
Thickness
7.4 mm
7.5 mm
7.6 mm
7.7 mm
7.8 mm
7.9 mm
8.0 mm
8.1 mm
8.2 mm
8.3 mm
(f)
t (mm)
F (GHz)
t_m^{cal} -3λ/4
t_m^{sim}
(g)
x=0.8
RL (dB)
F (GHz)
Thickness
8.4 mm
8.5 mm
8.6 mm
8.7 mm
8.8 mm
8.9 mm
9.0 mm
9.1 mm
9.2 mm
9.3mm
(h)
t (mm)
F (GHz)
t_m^{cal} -3λ/4
t_m^{sim}

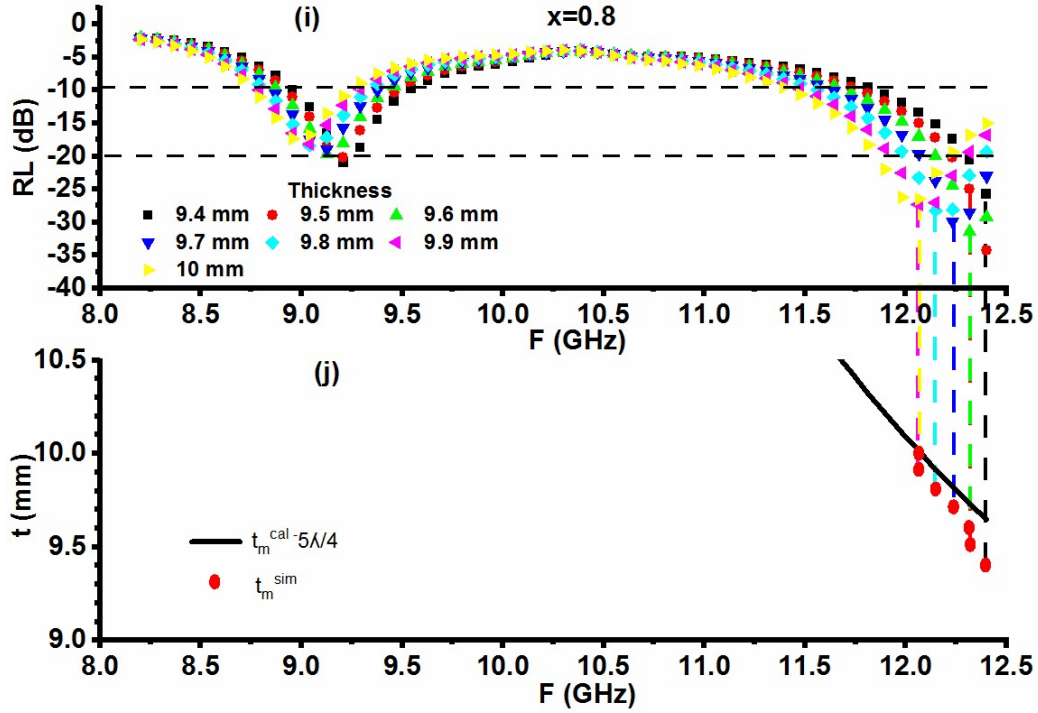

Fig. 4.40 (a, c, e, g, i) RL versus frequency (b, d, f, h, j) thickness versus frequency in x=0.8 for $SrCo_xNi_xFe_{12-2x}O_{19}$.

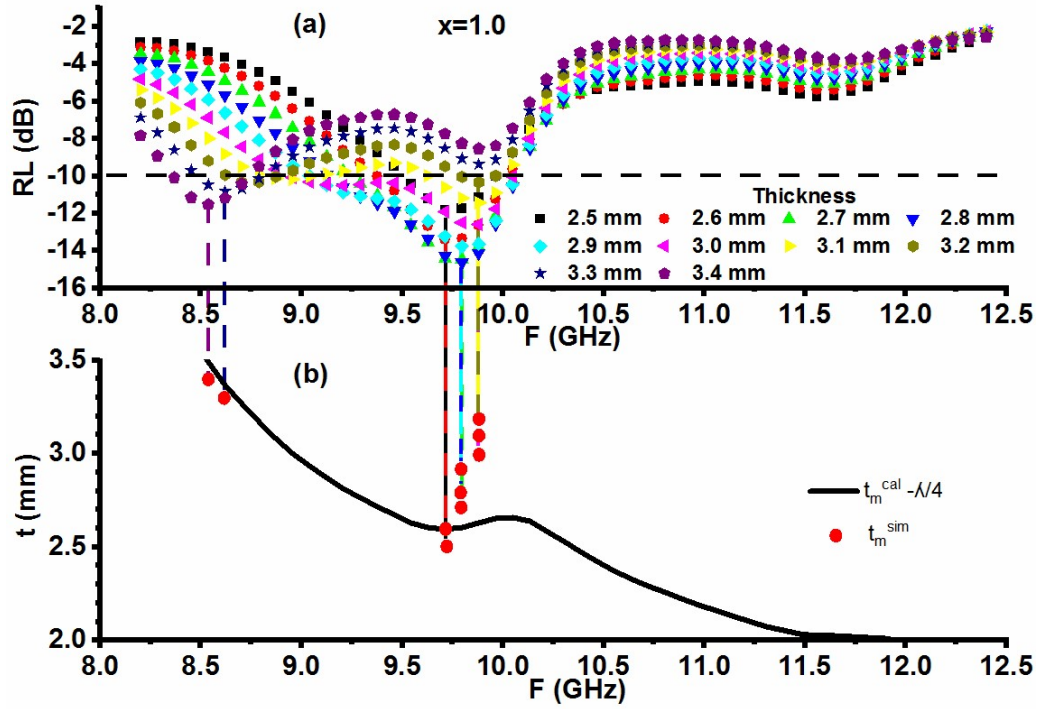

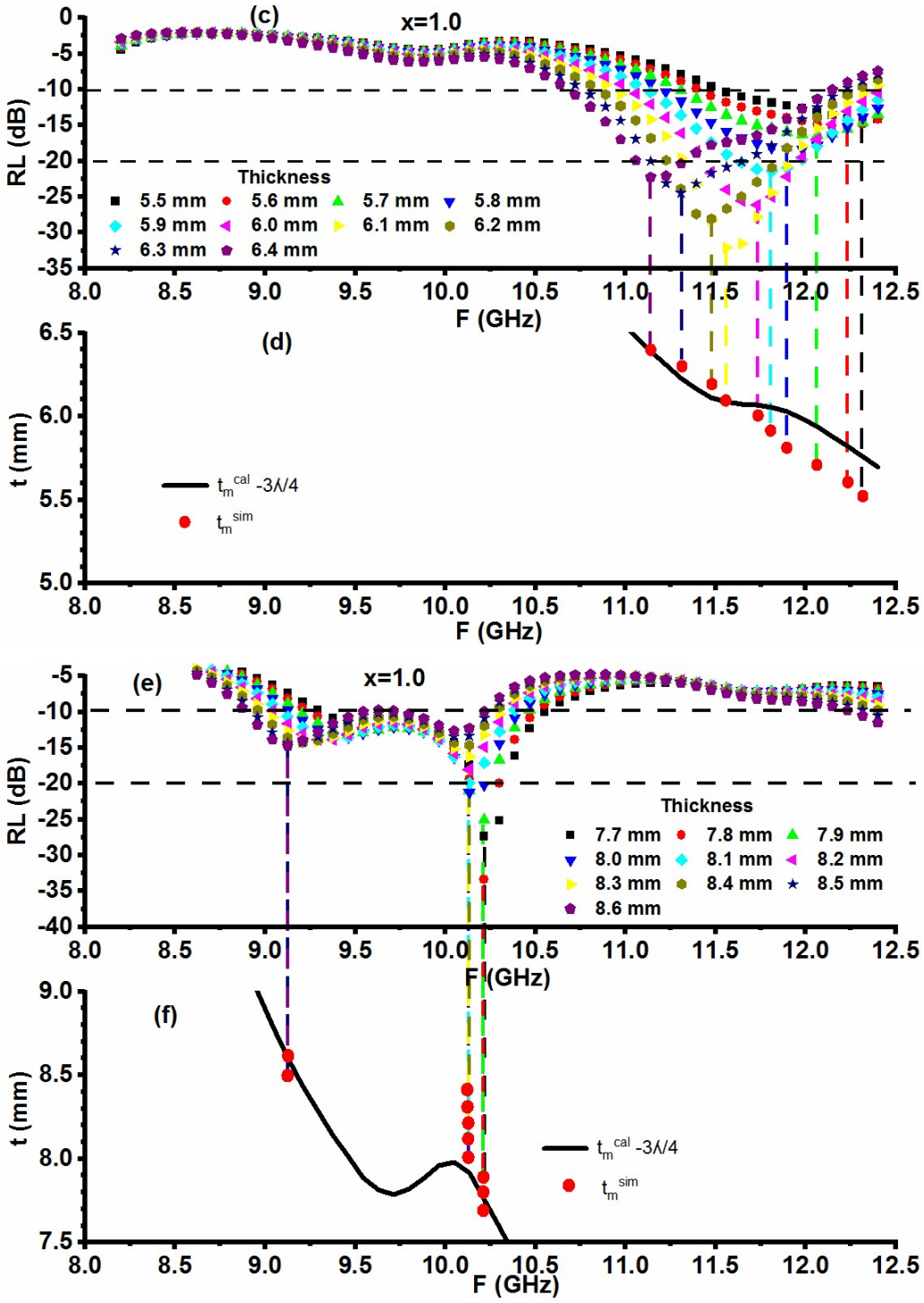
(c)
x=1.0
RL (dB)
F (GHz)
Thickness
5.5 mm
5.6 mm
5.7 mm
5.8 mm
5.9 mm
6.0 mm
6.1 mm
6.2 mm
6.3 mm
6.4 mm
(d)
t (mm)
t_m^{cal} -3λ/4
t_m^{sim}
(e)
x=1.0
Thickness
7.7 mm
7.8 mm
7.9 mm
8.0 mm
8.1 mm
8.2 mm
8.3 mm
8.4 mm
8.5 mm
8.6 mm
(f)

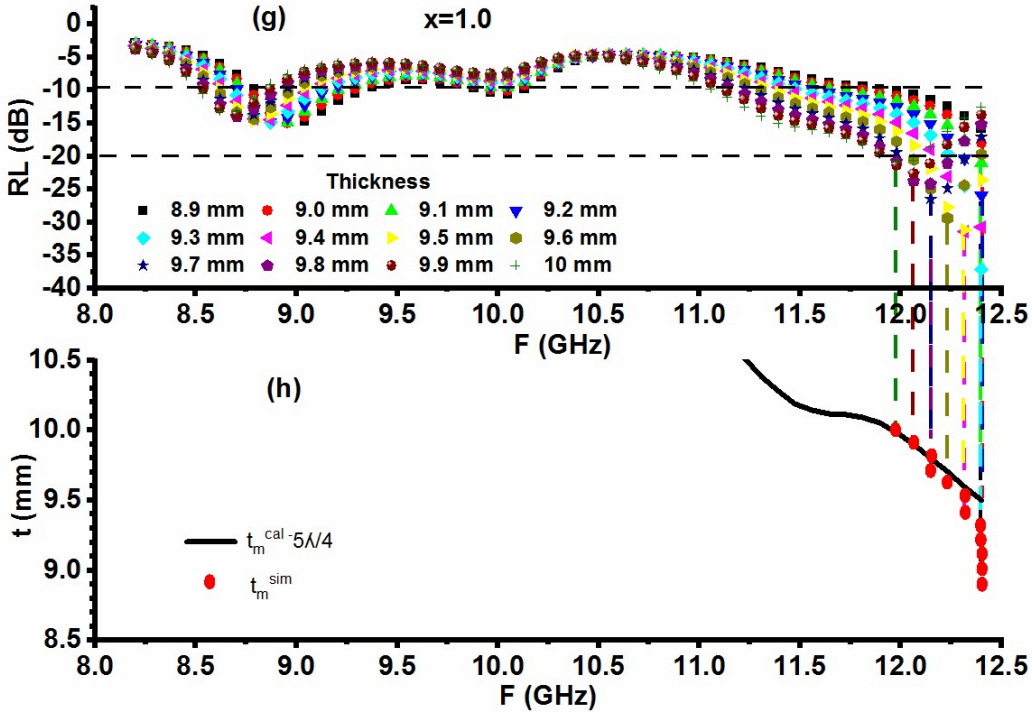

Fig. 4.41 (a, c, e, g) RL versus frequency (b, d, f, h) thickness versus frequency in x=1.0 for $SrCo_xNi_xFe_{12-2x}O_{19}$.

A comparison between simulated thickness (t_m^{sim}) and calculated thickness (t_m^{cal}) has been carried out to explore the relation between RL peaks and the λ/4 mechanism. Graphs of the calculated thickness (nλ/4) in the observed frequency range are given in Fig. 4.36 (b, d, f), 4.37 (b), 4.38 (b, d), 4.39 (b, d, f), 4.40 (b, d, f, h, j) and 4.41 (b, d, f, h). The comparison is performed by plotting lines from RL peaks to the thickness v/s frequency graphs. It is worth noting that the nλ/4 mechanism is fulfilled by composition x=0.2 for n=1 only, x= 0.4 and 0.6 for n=1 and 3, and in x=0.0 and 0.8 it exists at n=3 and 5. The composition x=1.0 is matched for n=1, 3, and 5. The presence of this mechanism in composition x=0.0 contributed -10 dB bandwidth having a range from 0.25 to 1.09 GHz at thicknesses from 5.6 to 8.8 mm as given in Table 4.9.

The composition x=0.2 shows *RL*≥-10 dB for the frequency ranging from 9.38 to 9.80 GHz. The bandwidth in this composition ranges between 0.16 and 0.42 GHz. The composition x=0.4 has RL values at low thicknesses from 2.6 to 7.0 mm. This composition has a bandwidth of 0.51 GHz at the thickness of 6.6 and 6.7 mm at a matching frequency of 11.90 and 11.98 GHz respectively. The -20 dB bandwidth of 80

MHz is also obtained at the thickness of 6.6 mm with the frequency band 11.90-11.98 GHz.

In composition x=0.6 bandwidth of 0.84 GHz at 9.6, 9.8, and 9.9 mm while a bandwidth of 0.75 GHz at 10.0 mm thickness associated with -10 dB are observed. Meanwhile, a -20 dB bandwidth of 90 MHz at 9.9 and 10.0 mm with the frequency band 9.54-9.63 GHz is obtained. The x=0.8 has -10 dB broad bandwidths of 1.17 GHz and 1.01 GHz at 6.3 and 7.6 mm. Besides it, -20 dB bandwidths of 0.25 GHz at 7.2 and 8.3 mm and 0.17 GHz at 8.0 mm are also obtained. The composition x=1.0 shows the highest 1.35 GHz BW on a 6.1 mm thickness with a frequency band of 10.97-12.32 GHz among all the compositions. The broad bandwidth of 1.26 GHz at 5.9, 8.3, and 10.0 mm while bandwidths of 1.17, 1.09, and 1.01 GHz at 7.6, 3.0, and 9.5 mm are also achieved in this composition. Further, the highest -20 dB bandwidth of 0.51 GHz with an 11.39-11.90 GHz band is also observed in x=1.0.

Table. 4.9 RL with matching thickness/frequency, BW, and PBW for $SrCo_xNi_xFe_{12-2x}O_{19}$.

x	Max. RL (dB)	Matching Thickness (mm)	Matching Frequency (GHz)	-10 dB band (GHz)	-10 dB BW (GHz)	-20 dB band (GHz)	-20 dB BW (GHz)	BTR	PBW (%)
0.0	-27.60	5.6	11.31	10.72-11.48	0.76	11.31-11.39	0.08	0.331	6.720
	-16.25	5.9	10.38	10.30-11.22	0.92	-	-	0.405	8.863
	-17.58	6.0	10.30	10.22-11.14	0.92	-	-	0.404	8.932
	-30.29	6.3	10.22	10.13-11.22	1.09	-	-	0.457	10.665
	-36.03	8.8	11.64	11.48-11.73	0.25	-	-	0.063	2.148
0.2	-21.61	9.6	9.46	09.38-9.54	0.16	-	-	0.056	1.691
	-23.49	9.7	9.46	09.38-9.71	0.33	-	-	0.112	3.488
	-22.22	9.8	9.46	09.38-9.80	0.42	-	-	0.140	4.440
	-22.35	9.9	9.54	09.38-9.80	0.42	-	-	0.139	4.403
	-24.94	10.0	9.54	09.38-9.80	0.42	-	-	0.137	4.403
0.4	-15.78	2.9	9.46	09.38-9.63	0.25	-	-	0.286	2.643
	-15.10	3.0	9.54	09.38-9.71	0.33	-	-	0.362	3.459
	-20.54	3.3	9.63	09.46-9.80	0.34	-	-	0.333	3.531
	-34.49	3.5	9.63	09.54-9.80	0.26	-	-	0.238	2.700
	-22.04	6.4	11.90	11.64-12.06	0.42	-	-	0.140	3.529
	-24.02	6.6	11.90	11.64-12.15	0.51	11.90-11.98	0.08	0.164	4.286

	-21.00	6.7	11.98	11.64-12.15	0.51	-	-	0.162	4.257
0.6	-12.78	3.2	9.29	09.21-9.38	0.17	-	-	0.185	1.830
	-18.82	9.6	9.12	09.04-9.88	0.84	-	-	0.294	9.211
	-21.63	9.8	9.12	08.96-9.80	0.84	-	-	0.293	9.211
	-23.03	9.9	9.63	08.96-9.80	0.84	09.54-9.63	0.09	0.290	8.723
	-30.43	10.0	9.04	08.96-9.71	0.75	09.54-9.63	0.09	0.259	8.296
0.8	-17.14	6.3	11.64	11.06-12.23	1.17	-	-	0.412	10.052
	-29.06	7.2	10.64	10.30-11.22	0.92	10.55-10.80	0.25	0.332	8.647
	-21.99	7.6	10.30	09.88-10.89	1.01	-	-	0.371	9.806
	-37.46	8.0	10.05	09.63-10.38	0.75	09.96-10.13	0.17	0.281	7.463
	-28.06	8.3	9.80	09.46-10.22	0.76	09.71-9.96	0.25	0.284	7.755
	-18.93	9.7	9.12	08.87-9.38	0.51	-	-	0.190	5.592
1.0	-12.59	3.0	9.88	08.96-10.05	1.09	-	-	1.211	11.032
	-21.43	5.9	11.81	11.14-12.40	1.26	11.64-11.90	0.26	0.464	10.669
	-32.09	6.1	11.56	10.97-12.32	1.35	11.39-11.90	0.51	0.491	11.678
	-30.71	7.6	10.30	09.38-10.55	1.17	10.22-10.30	0.08	0.467	11.359
	-16.22	8.3	10.13	09.04-10.30	1.26	-	-	0.489	12.438
	-37.10	9.3	12.40	11.56-12.40	0.84	12.32-12.40	0.08	0.189	6.774
	-31.13	9.5	12.32	11.39-12.40	1.01	12.15-12.40	0.25	0.226	8.198
	-20.67	10.0	11.98	11.14-12.40	1.26	11.98-12.06	0.08	0.274	10.518

4.2.5.4 Impedance matching mechanism

The input impedance of the material is different from that of the open field as permittivity/permeability differs. The difference between these two affects the absorption characteristics of the material. The majority of the incident signal gets opposed from the surface because of the mismatch between these two and fewer parts enter the material. However, if they match major portion of the signal travels into the material and gets absorbed by the material. Hence it becomes important to analyze the impedance matching mechanism for the development of an effective absorber.

The plots of reflection loss and impedance $|Z_{in}|$ v/s frequency of all the compositions are displayed in Fig. 4.42. The values of Z_{in} for the maximum reflection loss of various compositions are given in Table 4.10. The highest RL peaks in all the compositions (x=0.0 to 1.0) follow the impedance matching mechanism, however, there are some discrepancies at a few frequencies in x=0.2, 0.4, and x=0.8.

The composition x=0.0 has an RL of -36.03 dB with 11.64 GHz for 8.8 mm with a corresponding value of Z_{in}=366.74 Ω which is near 377 Ω. Composition x=0.6 possesses dual RL peaks with RL=-30.43 dB at 9.04 GHz with Z_{in}=386.61 Ω and RL=-

25.32 dB at 9.54 GHz with Z_{in}=357.88 Ω, which are in agreement with the value of Z_o=377 Ω. For composition x=1.0 RL peak of RL=-37.10 at 12.40 GHz with Z_{in}=368.36 Ω is observed. There is a discrimination with $|Z_{in}|$ in composition x=0.2 as there is a RL peak of -24.94 at 9.54 GHz with Z_{in}=336.78 Ω while there is no RL peak at 10.22 GHz with a Z_{in}=356.38 Ω which is more close to Z_o=377 Ω than Z_{in}=336.78 Ω. A similar problem occurs in x=0.4 and x=0.8 at 10.55 GHz (Z_{in}=366.10 Ω, RL=-1.07 dB) and 10.30 GHz (Z_{in}=377.57 Ω, RL=-13.34 dB) respectively in comparison to Z_{in}=366.07 Ω at 9.63 GHz with RL=-34.49 dB in x=0.4 and Z_{in}=373.30 Ω at 10.05 GHz with RL=-37.46 dB in x=0.8.

This kind of behavior is related to the complex form of $|Z_{in}|$ having real and imaginary parts (Z_{real} & Z_{img}). That's why, Z_{real} and Z_{img} are determined and graphs of Z_{real} and Z_{img} are plotted as shown in Fig. 4.43. Table 4.10 enlists the respective values of Z_{real} and Z_{img} related to the RL peaks. For the successful implementation of the impedance matching the impedances of the material should follow exactly/nearly the criteria of 377 Ω and/or 0. The highest *RL* of -37.46 dB with 10.05 GHz obtained for x=0.8 follows this condition as Z_{real}=373.18 Ω and Z_{img}=9.30 Ω. In the case of x=0.2 low RL at 10.22 GHz with Z_{in}=356.38 Ω is due to Z_{real}=24.39 Ω and Z_{img}=-355.44 Ω those are far away from 377 Ω and/or 0 condition. Similarly in x=0.8 less RL=-13.34 dB at Z_{in}=377.57 Ω in comparison to RL=-37.46 dB at Z_{in}=373.30 Ω is due to the fact that in the first case Z_{real}=344.14 Ω and Z_{img}=-155.34 Ω while in second Z_{real}=373.18 Ω and Z_{img}=9.30 Ω. Thus it can be summarized that the discrepancies observed in x= 0.2, 0.4, and 0.8 are due to the deviation in Z_{real} and Z_{img} from 377 Ω and/or zero which causes low values of RL. The doping of Co-Ni has a non-monotonous variation in Z_{in}, Z_{real}, and Z_{img}. Hence both the the λ/4 and impedance mechanisms are followed in all compositions having their role in the absorption characteristics of all compositions.

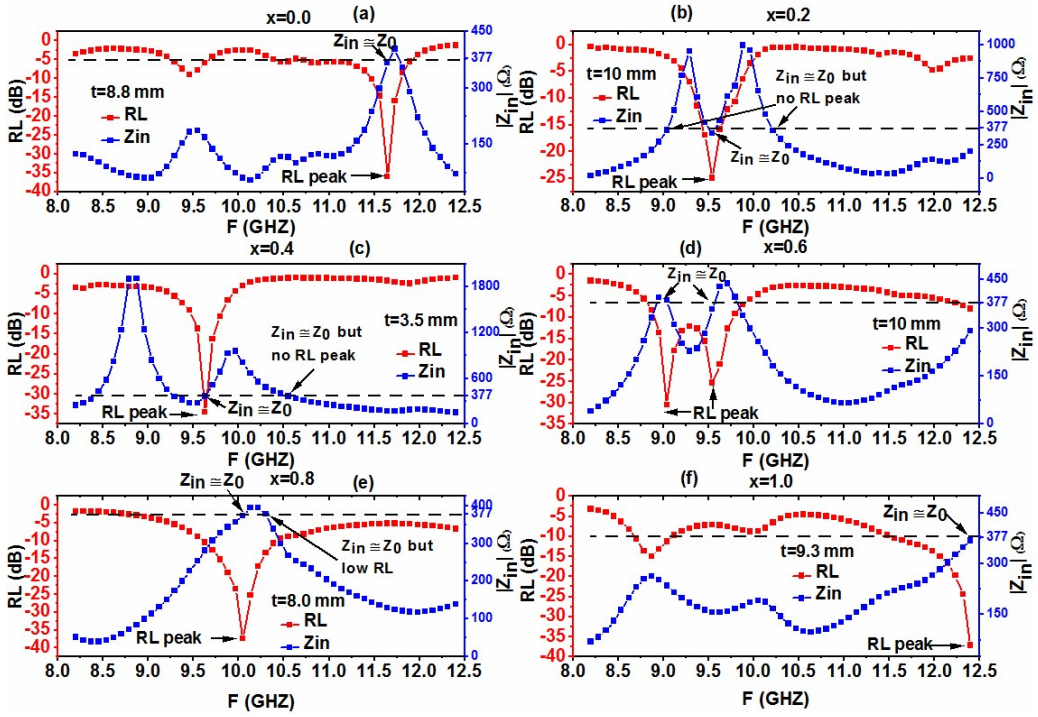

Fig. 4.42 Zin and RL curve against frequency for $SrCo_xNi_xFe_{12-2x}O_{19}$.

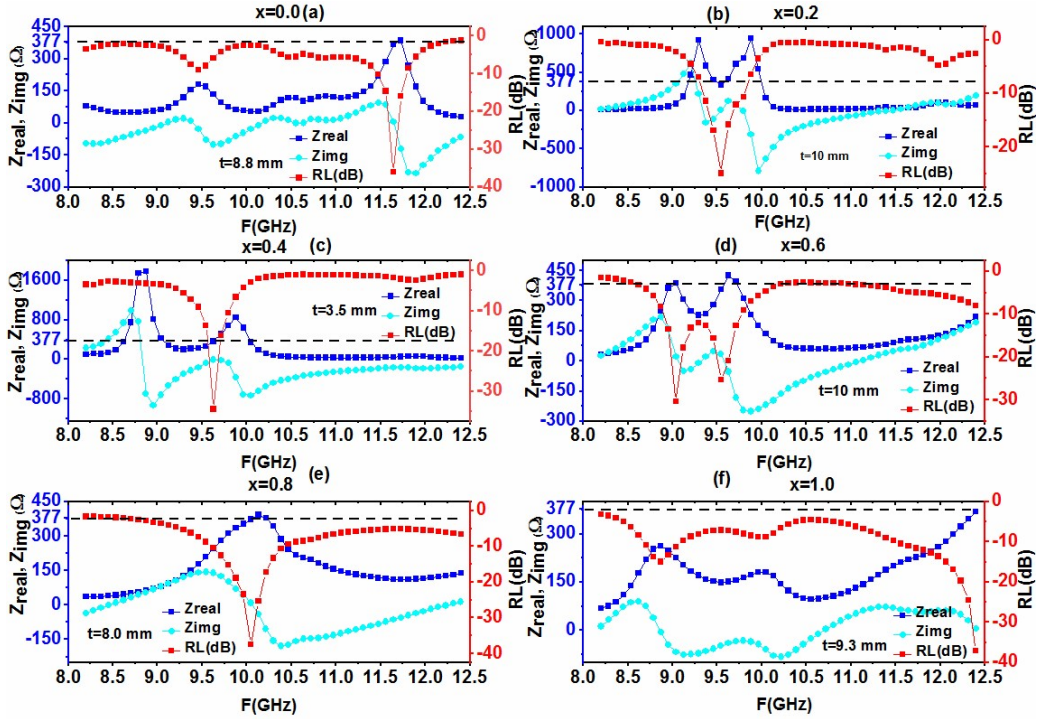

Fig. 4.43 Z_{real}, Z_{imag}, and RL v/s frequency for $SrCo_xNi_xFe_{12-2x}O_{19}$.

Table. 4.10 Z_{in}, Z_{real}, Z_{imag} values corresponding to RL_{max} for $SrCo_xNi_xFe_{12-2x}O_{19}$.

x	RL (dB)	Matching Thickness (mm)	Matching Frequency (GHz)	$\|Z_{in}\|$ (Ω)	Z_{real} (Ω)	Z_{img} (Ω)
0.0	-36.03	8.8	11.64	366.74	366.70	5.66
0.2	-24.94	10.0	9.54	336.78	336.76	3.81
0.4	-34.49	3.5	9.63	366.07	365.97	-8.65
0.6	-30.43	10.0	9.04	386.61	386.04	21.12
0.8	-37.46	8.0	10.05	373.30	373.18	9.30
1.0	-37.10	9.3	12.40	368.36	368.31	5.73

4.2.5.5 Role of Electromagnetic/Material Parameters

The relaxation peaks ε″ and μ" also have their contribution in the absorption which should also be taken care of. The peaks observed in ε″ and μ" in the prepared compositions are contributing to absorption in the compositions: in composition x=1.0, *RL*=-32.09 dB at the thickness of 6.1 mm correspond to ε″ peak at 11.56 GHz; the RL=-15.10 dB validate μ" peak at 9.54 GHz, similarly RL=-24.02 at 11.90 GHz attribute to the second peak of μ" peak at 11.90 GHz for composition x=0.4. In x=0.2 μ" peak at 9.54 GHz is attributed to the RL peak -24.94 dB at 9.54. In x=1.0 the highest RL= 37.10 dB at 12.40 GHz validate the maximum μ" at 12.40 GHz. Hence it can be said that dielectric and magnetic losses are also contributing to microwave absorption in the prepared compositions.

4.2.5.6 Eddy Current Loss

In ferrites, the eddy current loss also affects the absorption characteristics of ferrites. The formula to determine the eddy current loss is given as in equation 4.4 [98].

It should be noted that the constant value of C_0 with the increment in frequency indicates its contribution to the magnetic loss. The plot of C_0 against the frequency is plotted for all the compositions as given in Fig. 4.44. The plots indicate that doped compositions have constant values at the complete frequencies, while x=0.0 becomes constant after

8.87 GHz. This behavior indicates that eddy current loss is contributing to the absorption of ferrite compositions.

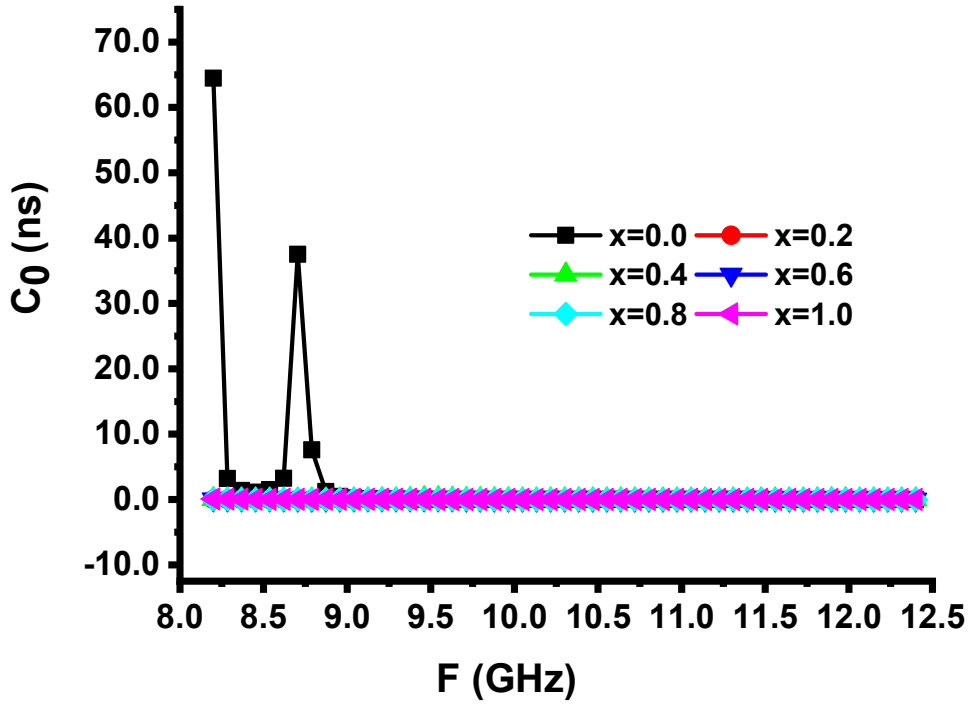

Fig. 4.44 C_0 versus frequency curve for $SrCo_xNi_xFe_{12-2x}O_{19}$.

4.2.5.7 Bandwidth to Thickness Ratio

The broad bandwidths with fewer thicknesses are very important in the design and characterization of an absorber. After achieving the RL≥-10 dB, one should aim at getting the low thicknesses, rather than increasing RL values only. Due to this factor bandwidth to thickness ratio (BTR) and percentage bandwidth (PBW) becomes important to determine. These two parameters are evaluated from equation 4.5 and 4.6.

The determined values for BTR and PBW for the prepared compositions are enlisted in Table 4.9. The table suggests that doping has increased BTR. The composition x=1.0 possesses the highest BTR of 1.211 with RL=-12.59 dB at 9.88 GHz among all the compositions. Besides this, this composition also possesses a high BTR=0.491 with RL=-32.09 dB and 0.489 with RL=-16.22 dB. After that, the composition x=0.8 has significant BTR=0.412 at 11.64 GHz for RL= -17.14 dB. There is an increase in

percentage bandwidth with the doping. The composition x=1.0 owes the highest PBW=12.44 at 8.3 mm. PBW ranges from 6.77 to 12.44 % for x=1.0. The undoped composition shows PBW in the range of 2.15 to 10.67.

4.3 $SrCo_xZr_xFe_{12-2x}O_{19}$ series

4.3.1 Microstructural/Morphologic Characteristics

The analysis of $SrCo_xZr_xFe_{12-2x}O_{19}$ hexaferrites, developed using the sol-gel method has been done utilizing Powder X software. The XRD diffractograms obtained are shown in Fig. 4.45 and the standard pattern of $SrFe_{12}O_{19}$ (JCPDS card no. 84-1531) is used to evaluate the phase purity of the prepared ferrites. No secondary peak is present, meanwhile, all were matched with the pure phase of strontium ferrite. The major intensity peak is 107 for all the compositions except x=0.8, where 114 has become a major intensity peak. There is a shift of the major intensity peak (107) toward the lower diffraction angle with the increment in doping concentration.

There is an increment in the values of the lattice parameter (a, c) as the doping content increases. The reason for this increment is the ionic radius difference among Zr^{4+} (0.720 Å), Co^{2+} (0.745 Å), and Fe^{3+} (0.645 Å). From Table 4.11, it can be noted that there is a decrement in crystallite size with the increment in Co-Zr doping. The crystallite size ranges between 41.474 to 29.778 nm. The lowest crystallite size of 29.778 nm is obtained for composition x=1.0.

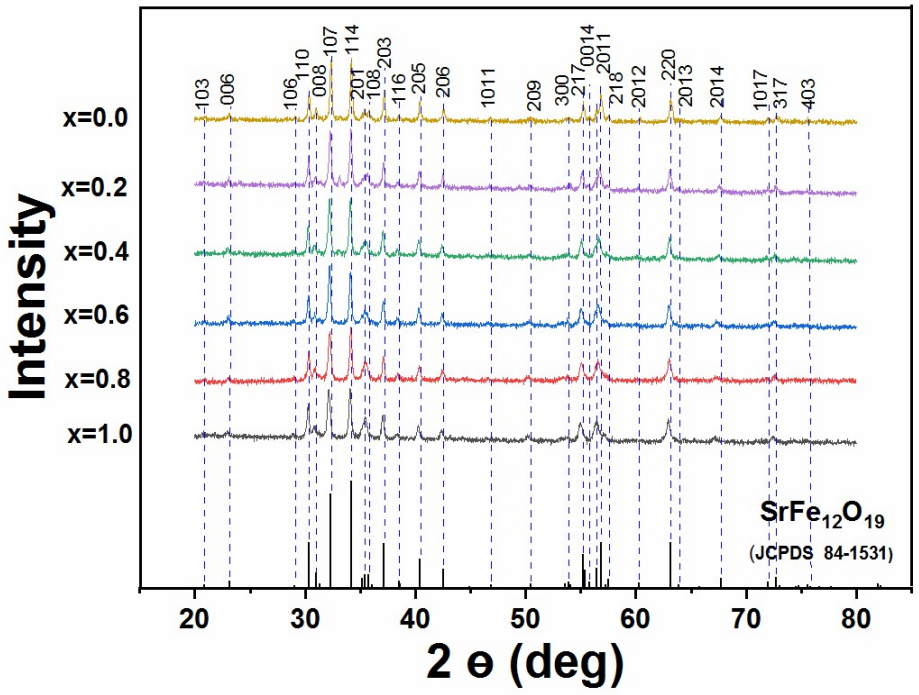

Fig. 4.45 XRD pattern of $SrCo_xZr_xFe_{12-2x}O_{19}$.

Table 4.11. Structural parameters of $SrCo_xZr_xFe_{12-2x}O_{19}$.

x	a=b (Å)	c (Å)	c/a	V(Å^3)	D_{xrd}	d-
0.0	5.8844	23.0499	3.917	691.18	41.474	2.77
0.2	5.8875	23.0865	3.921	693.01	37.697	2.77
0.4	5.8910	23.1395	3.928	695.42	33.845	2.77
0.6	5.8985	23.1500	3.925	697.51	34.550	2.78
0.8	5.8930	23.1780	3.933	697.05	38.404	2.63
1.0	5.9020	23.2400	3.938	701.06	29.778	2.78

Fig. 4.46 displays the micrographs of different compositions of $SrCo_xZr_xFe_{12-2x}O_{19}$. The grain fusion and agglomeration can be seen throughout the compositions. Compositions x=0.0 and 0.2 show the development of fused grains, however, there is a considerable decay in grain size in the composition x=0.4 as compared to the earlier ones. The grain distribution has been affected by the doping of Co-Zr with a decay in grain size. The Co-Zr doping has improved the inter-grain connectivity and grain agglomerates with

the increase in doping. The development of large grain clusters can be seen in the micrographs of x=0.6. The micrograph of composition x=0.8 contains both the large as well as tinny size grains. Composition x=1.0 shows good grain connectivity with a large decrease in grain size.

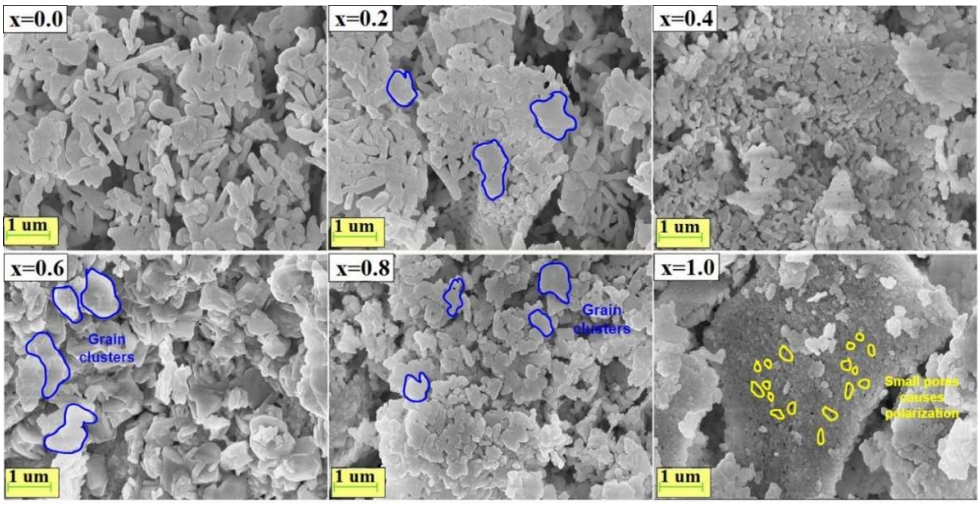

Fig. 4.46. SEM micrographs of ferrite $SrCo_xZr_xFe_{12-2x}O_{19}$.

4.3.2 Electrical characteristics

4.3.2.1 Dielectric Characterization

Ferrites have permittivity in a complex number where its real part (ε') indicates its charge storage capacity, while the imaginary part (ε'') shows the loss capabilities. The formula to determine the real part is shown in equation (3.5). Dielectric loss ε'' is calculated using equation (3.6), while the loss tangent ($tan\delta$) can be determined by equation (3.7) as given in chapter 3.

Fig. 4.47 displays the plots of ε' and ε'' versus the frequency of the prepared compositions. The doping of Co and Zr caused a non-linear increment in the dielectric constant. The graphs of ε' decreases gradually in the low-frequencies and attains constant values in high-frequencies. This decrease is caused by the interfacial polarization and complies with the Maxwell-Wagner model with the Koop phenomenon [80]. The dielectric materials are considered to have conductive grains separated by resistive grain boundaries. The grain boundaries have a prominent role at low frequencies, while at high frequencies grains are more dominant. The charge

careers gather at the boundaries due to the high resistivity of the grain boundary. This promotes space charge polarization that in turn enhances the dielectric constant for low frequency. However, the charges can't follow the applied field at high frequency, which reduces the charge carrier's accumulation at the boundary and causes a downfall in the dielectric constant.

The composition x=1.0 has the maximum ε'=113.2 at 100 Hz among all the compositions. Since polarization in the ferrites depends on Fe^{3+}/Fe^{2+} ions and these are minimum in x=1.0, the dielectric constant should be minimum in x=1.0. However, despite the highest number of Fe^{3+}/Fe^{2+}, the composition x=0.0 has less dielectric constant than x=1.0. The reason behind it is the grain morphology (Fig. 4.46): composition x=0.0 possesses large porosity, however, composition x=1.0 has the highest inter-grain connectivity among all compositions. Although the porosity is related to the sample preparation process if present, it influences the properties of the sample. Here composition x=1.0 has the highest dielectric constant despite fewer Fe^{3+}/Fe^{2+} ions, while the dielectric constant should be highest in x=0.0 due to the highest Fe^{3+}/Fe^{2+} ions. Hence we tried to explain that in view of SEM images, this may be due to the considerable inter-grain connectivity in x=1.0 and the high porosity in x=0.0. Since the signal faces more hindrance due to this high porosity and causing low polarization, which makes ε' lesser in composition x=0.0.

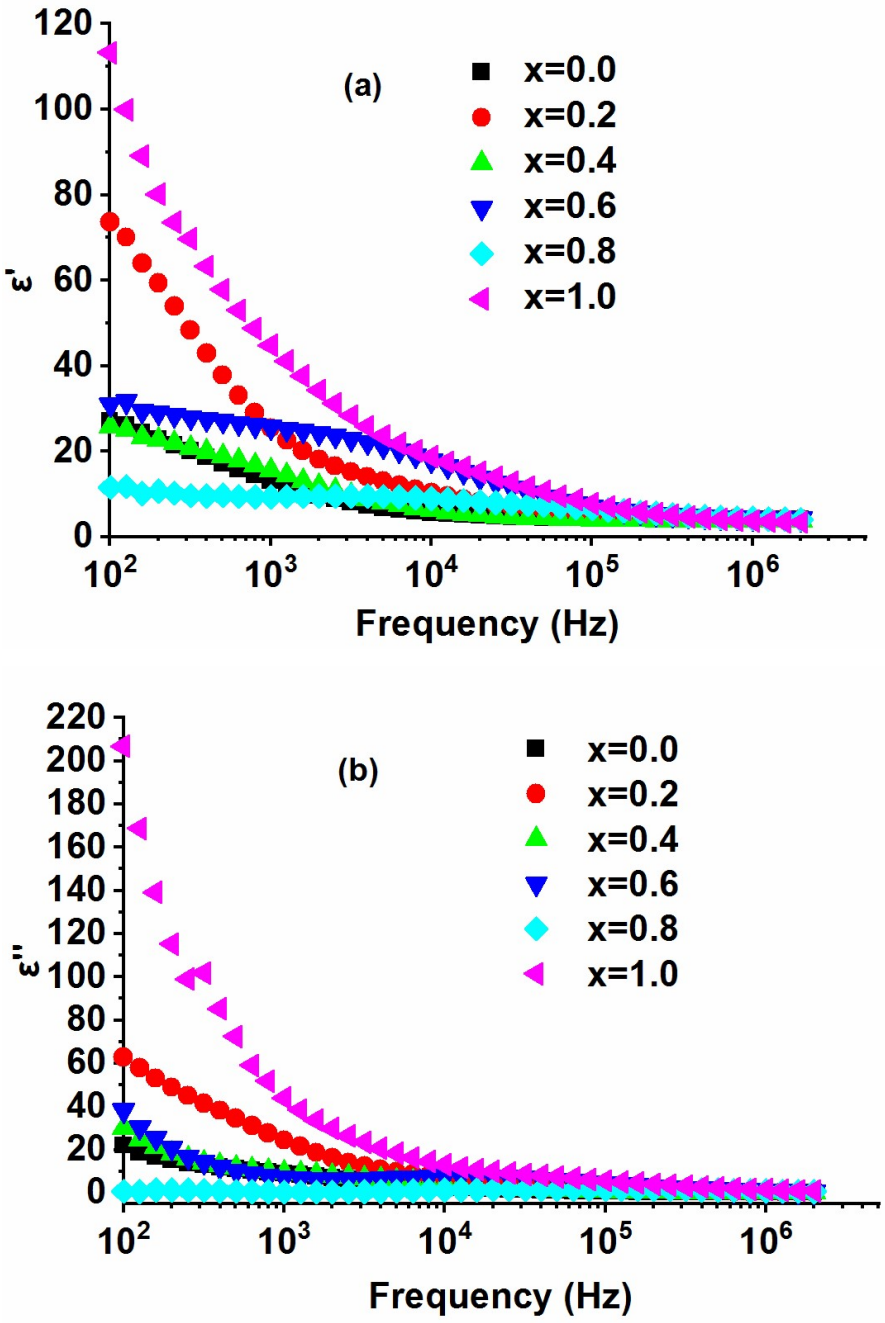

Fig. 4.47 Dielectric constant (a) real (b) imaginary versus frequency for $SrCo_xZr_xFe_{12-2x}O_{19}$.

Fig. 4.48 demonstrates the graph of loss tangent (tanδ) versus frequency for $SrCo_xZr_xFe_{12-2x}O_{19}$. There is a reduction in loss tangent with the increase in frequency. This decrement complies with Koop's phenomenological theory of dielectrics [80]. A

non-monotonical variation in loss tangent is obtained with the inclusion of Co-Zr, as well as multiple relaxation peaks are also obtained. This peaking nature is associated with the Rezlescu model [81] according to which it is obtained when the charge hopping frequency for Fe^{2+} and Fe^{3+} matches with the applied field's frequency. The highest tanδ is obtained in composition x=1.0: The small size of grains (Fig. 4.46) results in higher grain boundaries causing more polarization at grain boundaries. There is a broadening of relaxation peaks with the doping due to an increase in heterogeneity, which increases the number of interfaces that take more time for relaxation.

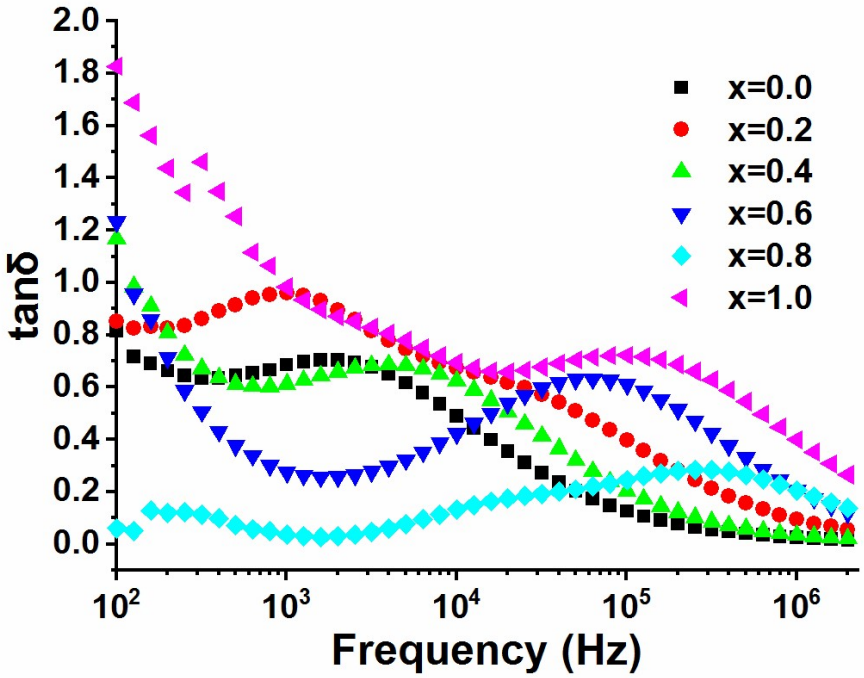

Fig. 4.48 Dielectric loss tangent versus frequency curves for $SrCo_xZr_xFe_{12-2x}O_{19}$.

It is worth noting that the peaks shifted to a high frequency with the inclusion of Co-Zr. Higher values of loss tangent at low frequency are signified by the role of grain boundary which impedes the electron hopping at low frequency. In a high-frequency regime, grains are prominent and offer electron hopping thus causing low values of loss.

4.3.2.2. Electric modulus

The electrical relaxation of ionic solids is described by the parameter called electric modulus (*M*). It explains the frequency dependence behavior of the conductivity of the

material. It is a complex quantity represented as $M = M' + jM''$, here $M' = \frac{\varepsilon'}{\varepsilon'^2+\varepsilon''^2}$ while $M'' = \frac{\varepsilon''}{\varepsilon'^2+\varepsilon''^2}$. Electric modulus not only elaborates the electric conduction rather also describes the space charge polarization effect. A sigmoidal step in M' and a broad asymmetric peak in M'' with frequency are the basic features of M [83]. Fig. 4.49 (a) and (b) display the variation of M' and M'' against frequency. It can be noted that a similar trend has been reported in earlier reports [106, 107]. At low frequency, M' possesses a low value while it increases at high frequency before attaining a constant value. The reason behind this type of nature may be the inadequate restoring force that controls the mobility of charge carriers. A sigmoidal step in M' is associated with the charge carrier's short-range mobility, while saturation behavior assists the long-range mobility.

The charge transport mechanism is described utilizing M'' versus frequency curve. Fig. 4.49 (b) shows asymmetric peaks in all the compositions. The peak's low-frequency side is linked to long-distance movement and the high-frequency side corresponds to short-range movement. The peak frequency can be used to determine the conduction relaxation time using the formula $\tau = \frac{1}{2\pi f_{max}}$. Where τ represents the relaxation time, while f_{max} denotes the relaxation frequency of the peak value of M''. The relaxation times determined for compositions x=0.0, 0.2, 0.4, 0.6, 0.8, and 1.0 are 1.58×10^{-5} s, 2.51×10^{-6} s, 7.96×10^{-6} s, 6.32×10^{-7} s, 3.16×10^{-7} s and 2.51×10^{-7} s respectively. It can be observed that the height of M'' varies non-monotonically with the increment in doping level. This is because of a change in the number of Fe^{3+} caused by doping, which in turn changes the number of charge careers. The inclusion of Co-Zr produces a shift in peaks toward the high-frequency regime referring localized motion of ions. The shifting in the direction of high frequency shows a reduction in relaxation time with the doping.

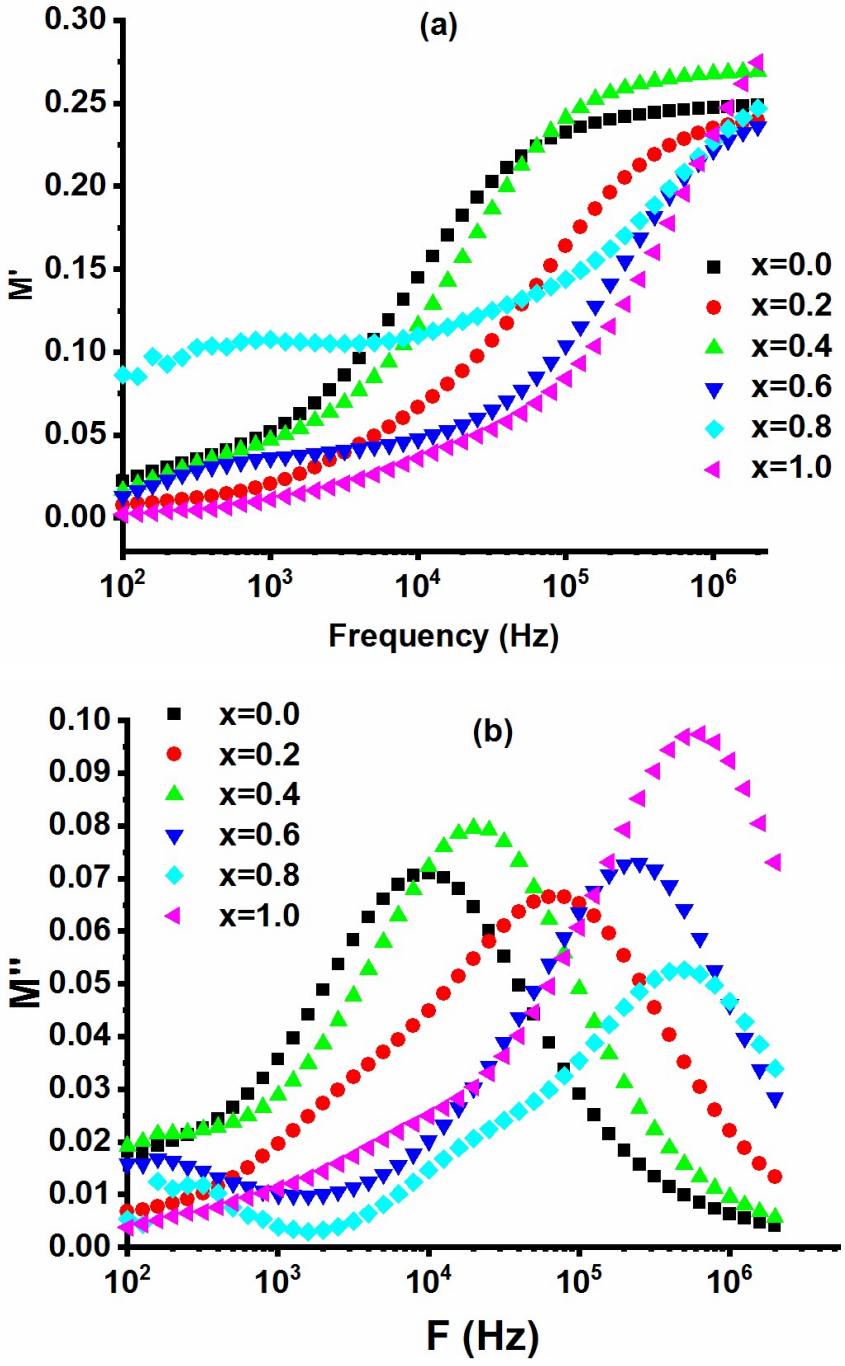

Fig. 4.49 (a), (b) Electric Modulus versus frequency curves for $SrCo_xZr_xFe_{12-2x}O_{19}$.

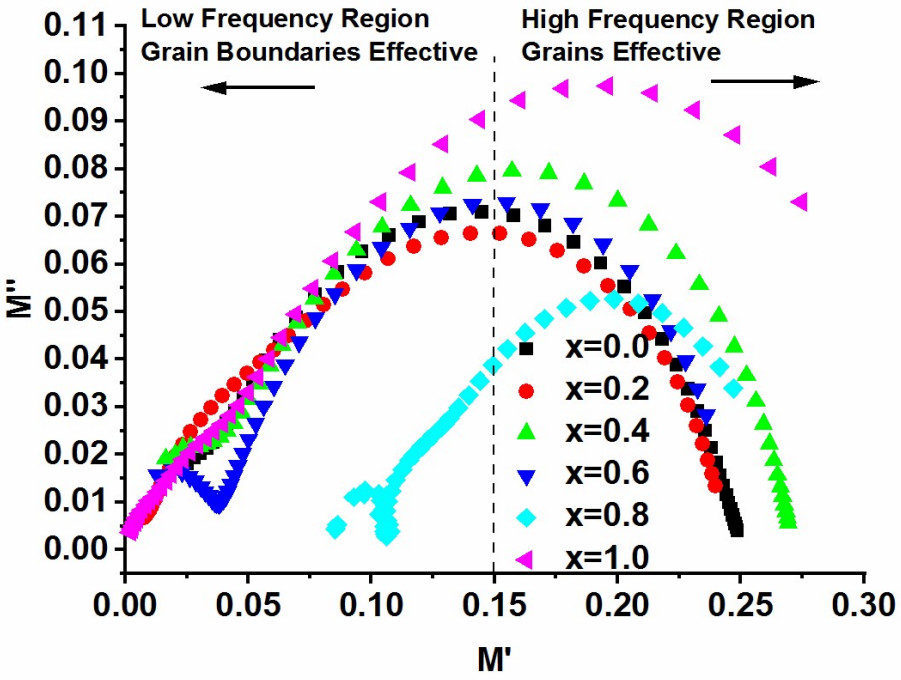

Fig. 4.50 Cole-Cole plot of ferrite $SrCo_xZr_xFe_{12-2x}O_{19}$

Cole-Cole plots ($M'v/s\ M''$) for $SrCo_xZn_xFe_{12-2x}O_{19}$ are depicted in Fig. 4.50. All the prepared compositions show asymmetric deformed semicircles implying a non-Debye relaxation. Since in x=0.0, semicircle exists almost equally in high and low frequencies grains and grain boundaries both have their role in charge transport. For x=0.2, 0.6, and 1.0 the semicircle shifted to low frequencies, however, in x=0.4 and 0.8 it moved to high frequencies. It shows that grains are dominant for x=0.4 and 0.8, while grain boundaries are prominent in others. Compositions x=0.6 and 0.8 show two semicircles depicting two types of relaxations one at low frequencies and another at high frequencies.

4.3.2.3. Complex impedance

The electrical response of dielectric materials is investigated with the help of Impedance spectroscopy. The impedance is $Z= Z' + j\ Z''$, here Z' implies to resistance and Z'' to reactance. The variation of Z' versus frequency is depicted in Fig. 4.51 (a). Z' is high at low frequency and continuously decreases till a certain point and becomes constant thereafter. This behavior follows the Maxwell-Wagner model. A non-

monotonical variation in the values of Z' is observed with the doping of Co-Zr. However, all the curves get coalesced in the high-frequency area.

The curves for Z'' versus f are displayed in Fig. 4.51 (b). The doping of Co-Zr causes a non-monotonical variation in the value of Z'' at low-frequency regions. However, at high frequency, all the curves coalesced which specify the decrement in space charge polarization with increasing frequency.

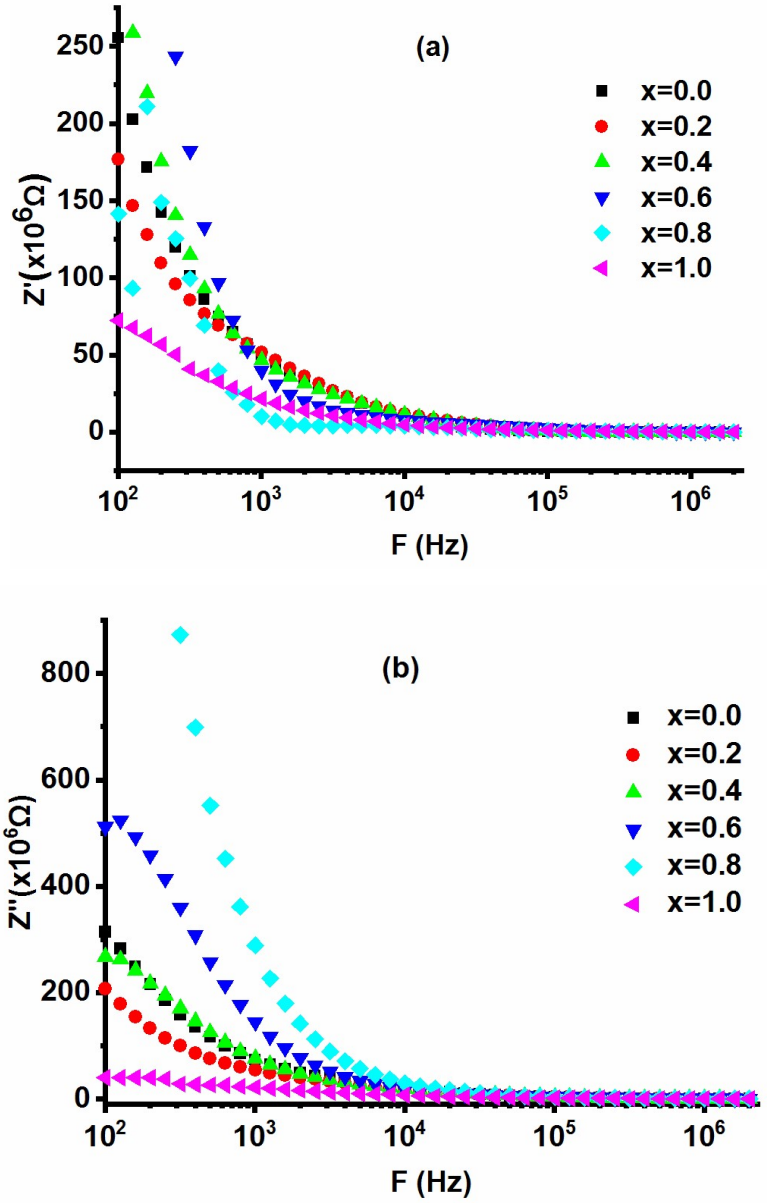

Fig. 4.51 (a), (b) Variation of Impedance of $SrCo_xZr_xFe_{12-2x}O_{19}$

Fig. 4.52 shows the Cole-Cole plots ($Z'versus\ Z''$) for the prepared compositions. All the compositions have a semi-circular arc as can be seen in Fig. 4.52. Both grains and grain boundaries have their effect in compositions x=0.0, 0.2, 0.4, and 0.6 as the curves of these compositions lie in the middle region. However, in composition x=0.6 the curve is shifted upward due to the morphology (Fig. 4.46): Large grain clusters with platelet structure enhance grain size as well as the number of grain boundaries as compared to x=0.0, 0.2, and 0.4. The dominance of grains can be noted in compositions x=0.8 and 1.0 due to the presence of curves completely in the high-frequency area.

The semicircles are not completing themselves in Fig. 4.52, instead, only semicircular arcs are present as the range of analysis was 100 Hz to 2 MHz. The size and shape of the curve depend on various factors such as morphology and electric/dielectric properties. The complete semicircles are not formed as they have some degree of decentralization and depression angle instead of being centered at the x-axis. Based on the scenario seen in the figure, it can be concluded that they will complete themselves at a low-frequency range.

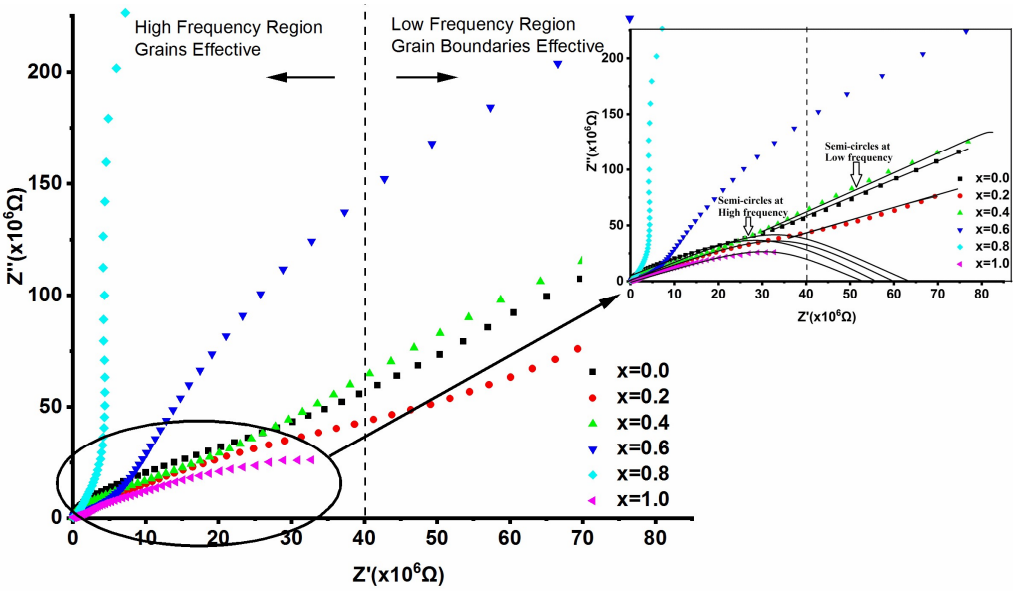

Fig. 4.52 Cole-Cole plot of Impedance for ferrite $SrCo_xZr_xFe_{12-2x}O_{19}$

The compositions x=0.0, 0.2, and 0.4 show two semicircles one at high frequency and another on the low-frequency side attributing two types of relaxation, while x=1.0 has a single semicircle which is completely in the high-frequency area as depicted in the

insite diagram of Fig. 4.52. Single semicircle in composition x=1.0 is due to the small size of grains and good grain connectivity in composition x=1.0 (Fig. 4.46). Fig. 4.52 indicates that the dielectric relaxation is weak as the plots for impedance have semicircular arcs instead of complete semicircles as in the case of electric modulus. Hence, from Cole-Cole plots of impedance (Fig. 4.52) and Electric modulus (Fig. 4.50), it can be concluded that loss relaxation peaks obtained in Fig. 4.48 were basically due to conductivity relaxation.

4.3.2.4. AC Conductivity

In ferrites, the conduction process has a considerable effect of electron hopping between Fe^{2+} and Fe^{3+}. It is worth noting that there is an increment in the hoping frequency of charge carriers due to the increment in frequency, which increases the conductivity. The polaron hopping model as described in [108] is used to describe this frequency-dependent conduction process. This model suggests an increase in conductivity for short-range polaron hopping, while a decrease is because of long-range polaron hopping.

Fig. 4.53 elucidates the curve of ac conductivity **(σ_{ac})** against the applied frequency for all the prepared compositions which shows that conductivity gradually increases with frequency increment. The conductivity curves start an increase above a particular frequency called hopping frequency. It shows the transition of conductivity from the flat plateau region of DC conductivity **(σ_{dc})** to a dispersive region of AC conductivity **(σ_{ac})**. Before this frequency point, all the compositions have nearly a frequency-independent nature. The inclusion of Zr^{4+} and Co^{2+} causes an increase in conductivity in doped compositions as compared to the undoped composition. The reason for low values of DC conductivity is linked to the prevalence of interfacial polarization in dielectric constant parameters as shown in Fig. 4.47.

The values of σ_{ac} are low at high frequencies in compositions x=0.0 and 0.4 which can be validated by the morphology: in x=0.0 a large porosity (Fig. 4.46) can be seen, while in x=0.4 grain size is small (Fig. 4.46), thereby reducing σ_{ac}. However, good grain connectivity in x=1.0 (Fig. 4.46) causes the highest σ_{ac}.

The values of parameter n were determined by curve fitting for all the prepared compositions. The respective values are 0.398, 0.652, 0.674, 0.711, 0.799, and 0.789. Since all the values are less than 1, it indicates that AC conductivity follows the hopping of charge carriers.

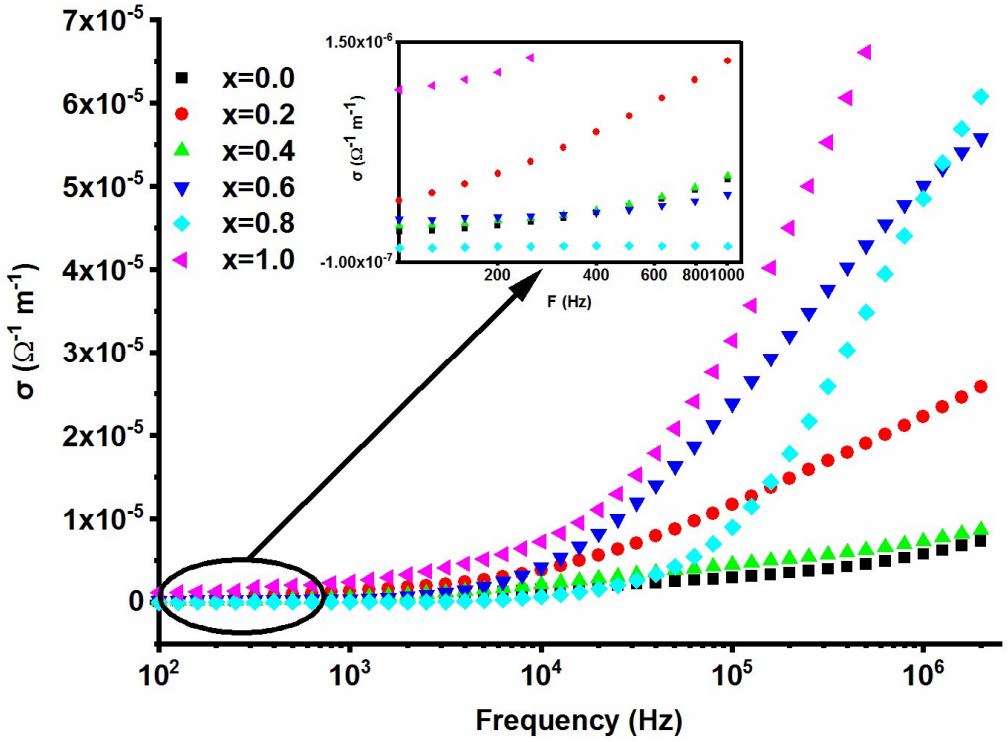

Fig. 4.53 AC conductivity v/s frequency for ferrite $SrCo_xZr_xFe_{12-2x}O_{19}$.

4.3.2.5. Software-based Impedance Simulation

The impedances of the prepared ferrites have been analyzed using circuit modeling by the Electrochemical impedance spectroscopy (EIS) software [86]. The circuit model comprises of series connected by two parallel RC circuits. The first one signifies to resistance and capacitance of grains (R_g, C_g), while the second represents the respective values of grain boundary (R_{gb}, C_{gb}). A constant phase element (CPE) is utilized in place of capacitors due to the non-Debye-type nature of compositions. The capacitance of CPE can be obtained by the expression given in equation 4.1. The parameters are determined from the EIS and put in the equation to obtain the required value of CPE.

The simulated results are shown in Fig. 4.54 which indicates that the measured plots and simulated/fitted plots are in harmony. Table 4.12 enlists the simulated values for the different parameters obtained from EIS.

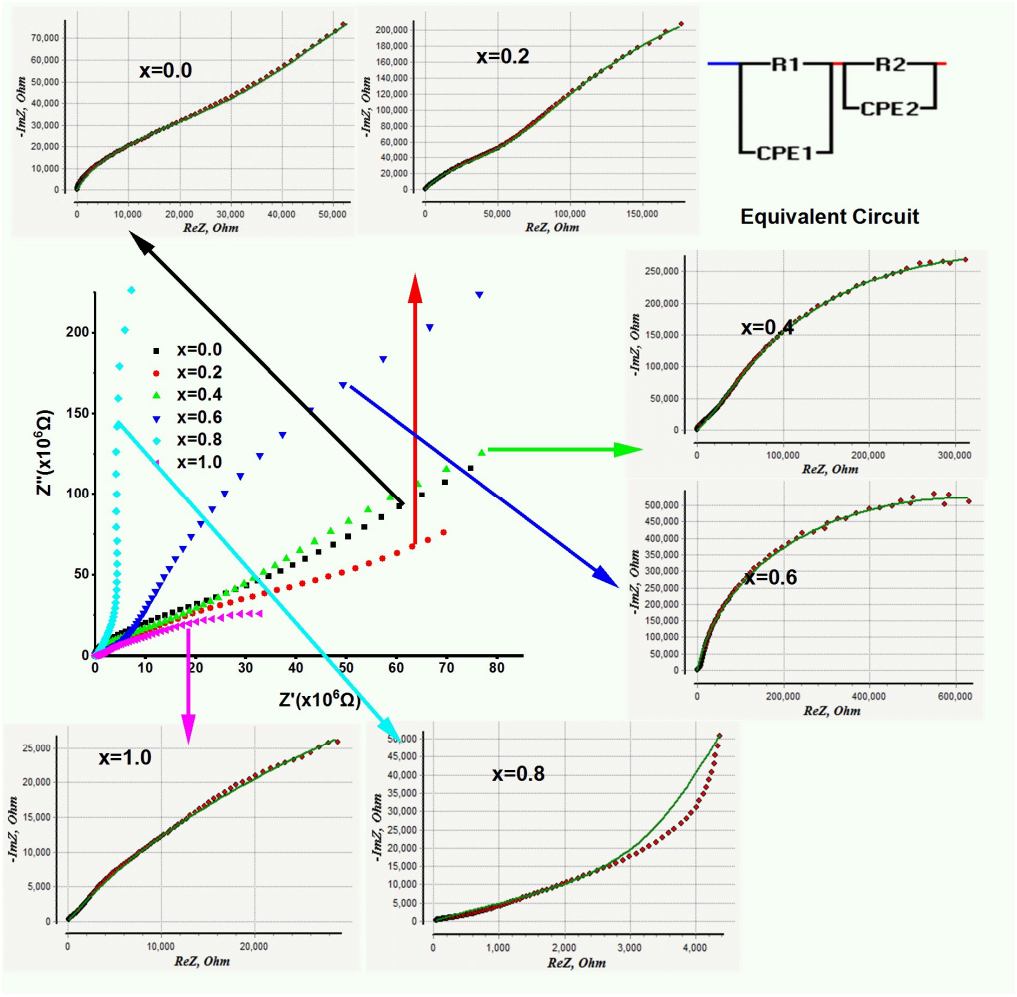

Fig. 4.54 Curve fitting of impedance using EIS software for $SrCo_xZr_xFe_{12-2x}O_{19}$.

Table 4.12. Simulated values of grain/grain boundary resistances and capacitances for $SrCo_xZr_xFe_{12-2x}O_{19}$.

x	R_g (MΩ)	R_{gb} (MΩ)	C_g (μF)	C_{gb} (μF)
0.0	622.05	30.09	31.6	7.02
0.2	694.12	72.56	42.2	423.06
0.4	702.79	20.79	35.52	10.80

0.6	262.09	993.75	3.82	13.51
0.8	4569.70	4.42	0.56	50.04
1.0	229.24	39.01	218.42	14621.17

Correlation between Grain/Grain boundaries simulated parameters and Morphology

The composition x=0.0 possesses large as well as tinny size grains as seen in the micrograph of Fig. 4.46. At the same time, large porosity can be seen which makes the polarization to be weak in turn causes the capacitance of grain boundaries to be low. From Table 4.12 it can be noted that in x=0.0 the simulated grain boundary capacitance C_{gb}=7.02 μF is the lowest among all the compositions. Composition x=0.6 has grains with an irregular/nonuniform surface causing a large number of grain boundaries contributing a maximum simulated grain boundary resistance R_{gb}=993.75 MΩ among all the compositions. Composition x=0.8 has well-connected large grains with flat surfaces contributing to the highest simulated grain resistance R_g=4569.7 MΩ.

The grains of composition x=1.0 are connected in a beehive-like structure (Fig. 4.54) due to which this composition has relatively better inter-grain connectivity. The size of grains is very small due to which closeness of grain boundaries causes a strong polarization at the grain boundary resulting in the highest simulated C_{gb}=14621.17 μF in Table 4.12.

Correlation between Grain/Grain boundaries simulated parameters and Dielectric Parameters

The composition x=0.8 has the lowest while x=1.0 owes the highest value of dielectric constant (Fig. 4.47) at the low-frequency region. As per the Maxwell-Wagner model grain boundaries are prominent in low frequencies, while grains take charge in the high-frequency region. Table 4.12 illustrates that the composition x=0.8 has the minimum grain boundary resistance R_{gb}= 4.42 MΩ referring to the lowest resistance due to the lowest dielectric constant (ε'=11.56 at 100 Hz). Composition 1.0 possesses the highest dielectric constant (ε'=113.20 at 100 Hz) at low frequency attributing to the highest simulated grain boundary capacitance C_{gb}=14621.17 μF referring to a high polarization due to grain boundaries.

Correlation between Grain/Grain boundaries simulated parameters and Electric Modulus

The composition x=0.0 showed the effect of grains as well as grain boundaries since the semi-circle lies in the middle of the frequency region (Fig. 4.50). In the case of x= 0.4 and 0.8, the shifting toward high frequency suggests the dominance of grains, while semi-circles of x=0.2, 0.6, and 1.0 are more towards the low frequencies depicting dominance of grain boundaries. This kind of conduct can be well explained in conjunction with Table 4.12: In compositions x=0.8 and 0.4 grains possess high conductivity relaxation validating the higher simulated grain resistance R_g=4569.7 MΩ and R_g=702.79 MΩ in x=0.8 and 0.4 respectively. The high simulated C_{gb}=423.06 μF in x=0.2 and highest R_{gb}=993.75 MΩ in x=0.6 indicate the prominence of grain boundaries. The large number of small pores causing strong polarization at grain boundaries with C_{gb}=14621.17 μF attributed to an effective role of grain boundaries in x=1.0.

4.3.3 Band gap Characteristics

Tauc plots drawn for the prepared $SrCo_xZr_xFe_{12-2x}O_{19}$ hexaferrites are shown in Fig 4.55. To obtain the required values of the band gap equation 3.4 as given in Chapter 3 is used. The intercept on the x-axis is obtained from the linear region of the Tauc plot to determine the band gap. The band gaps of the prepared compositions x=0.0 to 1.0 are 2.68, 2.34, 2.81, 2.10, 2.91, and 2.42 eV respectively. The obtained values are in the prescribed range of the ferrites which is generally 2 to 3 eV.

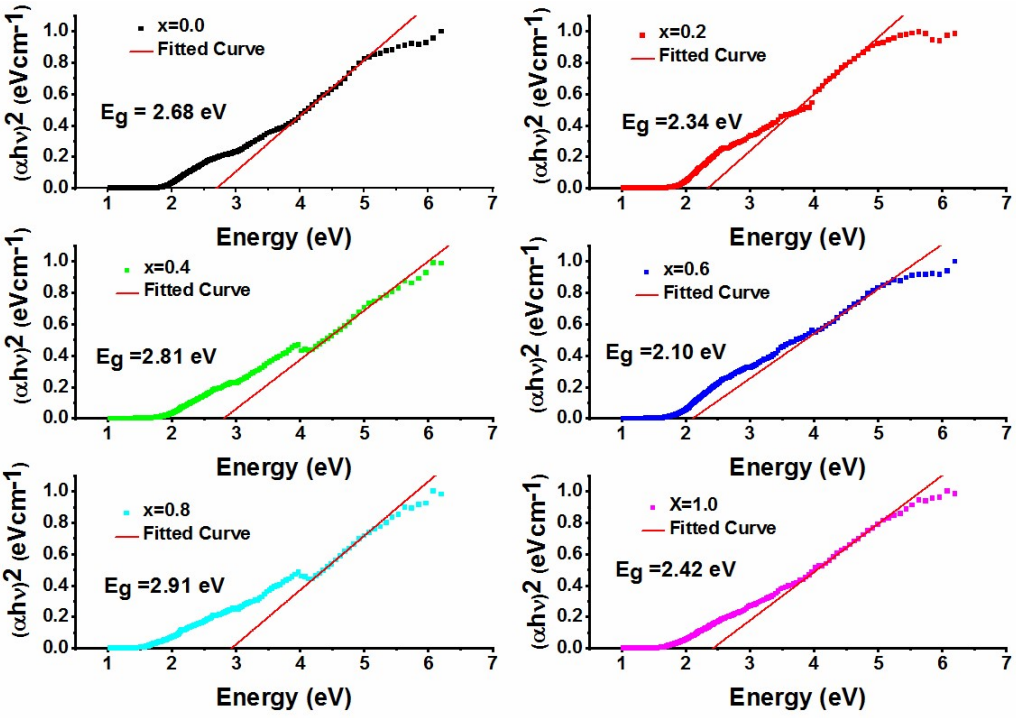

Fig. 4.55 Tauc plots of $SrCo_xZr_xFe_{12-2x}O_{19}$

4.3.4. Magnetic Characteristics

The magnetic characterization of the prepared $SrCo_xZr_xFe_{12-2x}O_{19}$ hexaferrites has been carried out to understand the magnetic characteristics of the prepared compositions. Investigation of magnetic characteristics is done using magnetization (M) versus magnetic field (H) curves. Fig. 4.56 (a) demonstrates the M-H curves drawn for the prepared compositions. The site occupancy of the ions depends on their electronegativity. The higher electronegativity ions generally prefer to occupy octahedral sites than tetrahedral [88]. The electronegativity of Zr^{4+}(1.33) ions are less than that of Co^{2+}(1.88), hence this one will try to acquire tetrahedral site $4f_1(\downarrow)$. As per the ligand field theory, Zr^{4+} prefer tetrahedral site $4f_1(\downarrow)$ due to $3d^{10}$ configuration, while Co^{2+} with $3d^7$preferably choose octahedral sites 12k $(\uparrow), 2a(\uparrow), 4f_2(\downarrow)$ [90]. Godara et al. [109] reported that Zr^{4+}prefer tetrahedral $4f_1$sites while Singh et al. [90] reported that Co^{2+} prefer to occupy octahedral sites.

To calculate saturation magnetization (M_s) and anisotropy field (H_a), the formula given in equation 4.2 is utilized.

In hexagonal ferrites, B is given by $B = H_a^2/15$ with H_a representing the anisotropy field. Fig. 4.56 (a) indicates that M-H loops have a steep rise in magnetization for low-applied fields while it decays for high fields. The undoped composition x=0.0 possesses a large slope at high fields indicating an unsaturated state which reduces with the substitution of Zr^{4+} and Co^{2+}. This is caused by the reduction in anisotropy field. At the high values from 10 KOe to 15 KOe a linear relationship is observed that's why A/H and χ_P maybe removed and B is obtained using relation $M = M_s\ (1 - B/H^2)$. H_a is determined from a relation $H_a^2 = 15\ B$. M_s is determined with the help of graphs plotted between magnetization (M) and the inverse of the square of the anisotropy field ($1/H^2$). The graph plotted as such is fitted using linear fitting which is shown in Fig. 4.56 (b). The determined parameters from M-H loops and M v/s $1/H^2$ plots are listed in Table 4.13.

In hexagonal structure, the magnetic moment with spin-up and down sites is given in equation 4.3. The equation indicates that the substitution of a weak/non-magnetic ion at spin-down sites ($4f_1\downarrow + 4f_2\downarrow$) enhances saturation magnetization while more occupancy at spin-up sites (2a↑ + 12k↑ + 2b↑) reduces it. There is a non-monotonous change in M_s with the inclusion of Co-Zr. The composition x=0.2 has the highest value of M_s=151.84 emu/g while the lowest value is obtained in composition x=0.6 with M_s=87.72 emu/g. Ms increases by 70 % (88.80 to 151.64 emu/g) for x=0.0-0.2 with the addition of Zr^{4+} and Co^{2+}. This is because of the replacement of Fe^{3+} by Zr and Co at spin-down sites.

From the relationship among M_s, M_a, and M_b, it can be said that the occupancy of diamagnetic Zr^{4+} and weak magnetic Co^{2+} at the spin-down sites ($4f_1\downarrow + 4f_2\downarrow$) produces a decrease in the value of M_b which in turn, increases the M_s. Beyond x=0.2 M_s starts decreasing and there is a 38 % decrease in M_s from x=0.2 to x=1.0. This decrease is due to the low magnetic moment of Co^{2+} (3μB) and diamagnetic Zr^{4+} (0 μB). The substitution of Fe^{3+} (5μB) at spin-up sites causes an imbalance in electrical neutrality, hence to maintain it Fe^{3+} is converted into Fe^{2+} which causes a reduction in superexchange interactions in result of which magnetic moment decreases. On the other hand, substitution at spin-up sites (2a↑ + 12k↑ + 2b↑) decreases the net value of M_a which decreases M_s.

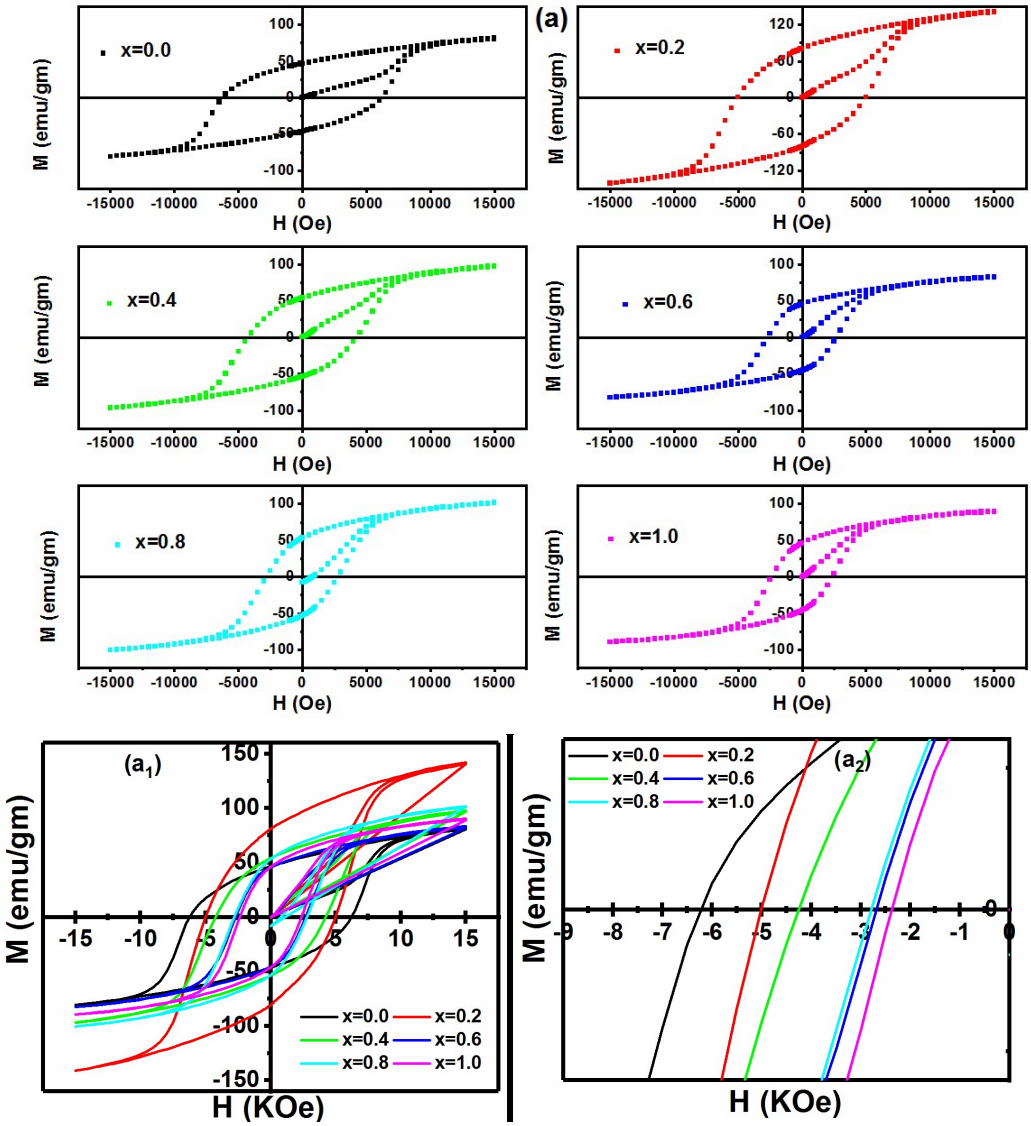
(a)
x=0.0
x=0.2
x=0.4
x=0.6
x=0.8
x=1.0
M (emu/gm)
H (Oe)
(a1)
(a2)
H (KOe)

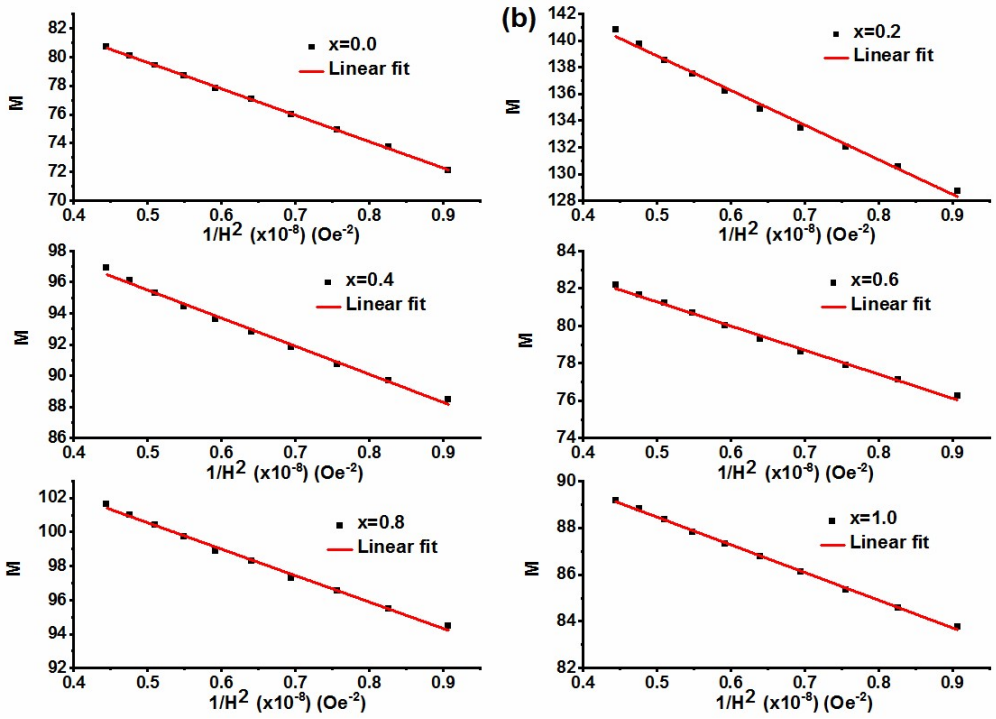

Fig. 4.56 (a) M-H loops (a_1, a_2) combined and enlarged view (b) Ms v/s $1/H^2$ plots of $SrCo_xZr_xFe_{12-2x}O_{19}$

It is worth noting that the soft ferrites having low coercivity are the prime candidates in the design of a microwave absorber. Hence prime requirement in the design of an efficient absorber is the low value of coercivity (H_c). It is evident from Table 4.13 that there is a decrement in the coercivity H_c due to the increase in doping of $Co^{2+} - Zr^{4+}$. The composition x=0.0 has the highest H_c=6236 Oe while the composition x=1.0 possesses the least H_c=2348 Oe. H_c decreases by 62 % due to the fact that the substitution of non-magnetic Zr^{4+} and weak magnetic Co^{2+} made ferrites magnetically soft. There are two factors affecting the values of H_c one is the intrinsic factor involving anisotropy field H_a and the second is morphology an extrinsic factor. Table 4.13 reveals that there is a decrease in the value of H_a which has a direct relation with H_c. The consistent decrement in H_a causes a decrement in the H_c. H_a decreases 22 % from x=0.0 to x=1.0 which is due to the replacement of Fe^{3+} at $4f_2$ and 2b sites, as these sites provide large H_a substitution at these sites causing reduction in H_a. H_a decreases 22 % while H_c decreases more i.e 62 % so another reason for the large reduction in H_c is the large ionic radius of Co^{2+} (0.745 Å) and Zr^{4+}(0.72 Å) in comparison to Fe^{3+} (0.645 Å). The

morphology suggests that there are large pores in the composition x=0.0 which reduces with the increase in doping of Co-Zr and good grain connectivity in composition x=1.0 reduces coercivity H_c.

Table 4.13. Magnetic parameters determined from M-H curves for $SrCo_xZr_xFe_{12-2x}O_{19}$.

x	M_s (emu/g)	M_r (emu/g)	H_a (kOe)	H_c (Oe)	M_r/M_s
0.0	88.80	46.70	17.61	6236	0.53
0.2	151.84	80.96	16.01	5011	0.53
0.4	104.51	54.12	16.08	4260	0.52
0.6	87.72	45.67	14.85	2688	0.52
0.8	108.33	53.35	14.67	2792	0.49
1.0	94.38	46.14	13.72	2348	0.49

The retention of magnetization after the removal of the applied field is given by M_r/M_s ratio. This varies between 0 and 1 and the value less than 0.5 represents randomly oriented multi-domain particles while values greater than 0.5 indicate a single domain. The composition x=0.0 to x=0.6 have M_r/M_s ratio greater than 0.5 shows multi-domain orientation while ratios for x=0.8 and 1.0 indicate single-domain.

4.3.5. Electromagnetic Characteristics

4.3.5.1 Complex permeability and complex permittivity

Fig 4.57 demonstrates the plots of (ε'), (ε''), (μ'), and (μ'') against frequency. The doping of Co-Zr caused a non-monotonical change in dielectric constant and loss. A non-monotonous change in the ε' constant and ε'' is observed in doped compositions as compared to the undoped composition. There is an increment in the value of ε' with the increment in frequency at the lower side while at a middle-frequency region (9.5 to 10.5 GHz) there is a dip in the dielectric constant in all the compositions except x=0.6. At high-frequencies compositions, x=0.8 and 1.0 depict large increments as compared to the others. The compositions x=0.6, 08, and 1.0 show relaxation peaks in ε'. There is a large variation in the values of dielectric loss in all the doped compositions as compared

to undoped composition x=0.0. The x=0.2, 0.8, and 1.0 have relaxation a peak in ε″ around 10 GHz. The x=0.6 has the highest dielectric loss among all compositions.

The Co-Zr doping has a non-monotonous effect on the permeability of the compositions. The doped composition has high values of μ′ as compared to the undoped composition. There is no significant change in composition x=0.2 and 0.6 while μ′ increases highly in composition x=0.4, 0.8, and 1.0. There is an enhancement for μ′ with the increase in frequency in composition x=0.4, 0.8, and 1.0 while x=0.0, 0.2, and 0.6 remain nearly constant. Composition x=1.0 possesses a relaxation peak in μ" at around 11.5 GHz. In a low-frequency area, the composition x=0.0 possesses the maximal of μ" while x=1.0 obtains the maxima in the high frequency range. The complex permittivity and permeability of doped composition x=0.4, 0.8, and 1.0 are showing high values and large variations more than the expected values which is due to measurement uncertainty/the instrumental error.

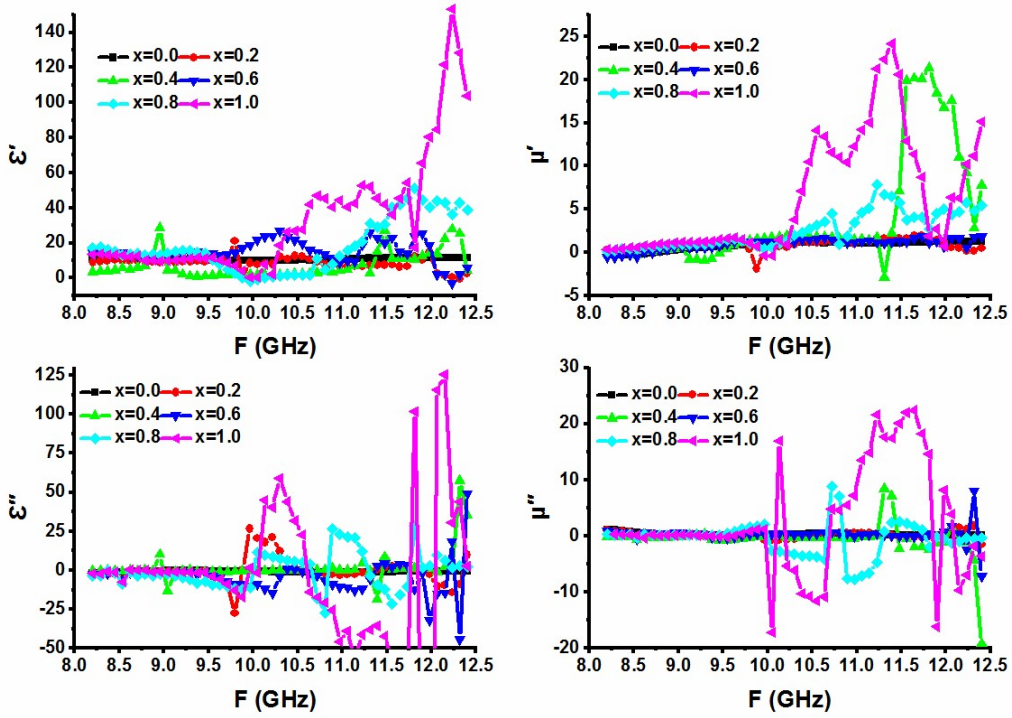

Fig 4.57 Complex permittivity and permeability versus frequency plots for $SrCo_xZr_xFe_{12-2x}O_{19}$.

The porosity, grain size distribution, electron spin, and polarization at the microwave region affect complex permittivity/permeability. The dielectric polarization is caused by the electron hopping in Fe^{2+}/Fe^{3+} [95]. The large porosity depresses polarization and

restrains the field flow. Exchange resonance among Fe^{3+}/Fe^{2+} and ferromagnetic resonance affect the permeability [96-97]. The number of Fe^{3+} decreases due to the doping of Co-Zr which affects the polarization and resonance. There are pores in the micrographs of the prepared compositions that act as non-magnetic voids and affect magnetization related to complex permittivity/permeability. The uneven variation in grain size and grain boundaries (micrographs Fig. 4.46) modifies the permittivity/permeability.

Grain having large size supports electron hopping, however, grain boundaries discourage the field flow. The gathering of charges at grain boundaries promotes polarization, however, permeability increases as the large grains enhance electron spin. The magnetic loss increases by the reduction in exchange resonance due to porosity and small grains. The peaks in complex permittivity/permeability observed in the prepared compositions are attributed to dielectric relaxation and ferromagnetic resonance respectively.

4.3.5.2 Microwave absorption in $SrCo_xZr_xFe_{12-2x}O_{19}$

The absorption characteristics of any material are understood on the basis of reflection losses: the higher the reflection loss better the absorption. It is calculated from the material's input impedance Z_{in} and impedance of air Z_0 using equations 3.13 and 3.14. The $\lambda/4$, impedance matching, and observed losses are used to investigate microwave absorption characteristics as discussed in the following sections.

4.3.5.3 Quarter Wavelength Mechanism

The plots of reflection loss (RL) against frequency at different simulated thicknesses have been used to explain the phenomenon of microwave absorption in the prepared compositions. The RL plots of $SrCo_xZr_xFe_{12-2x}O_{19}$ ferrites are given in Fig. 4.58 (a, c, e), 4.59 (a, c, e), 4.60 (a), 4.61 (a, c), 4.62 (a) and 4.63 (a, c). These are used to determine different parameters. The summarized values of these parameters of the prepared ferrite series are listed in Table 4.14.

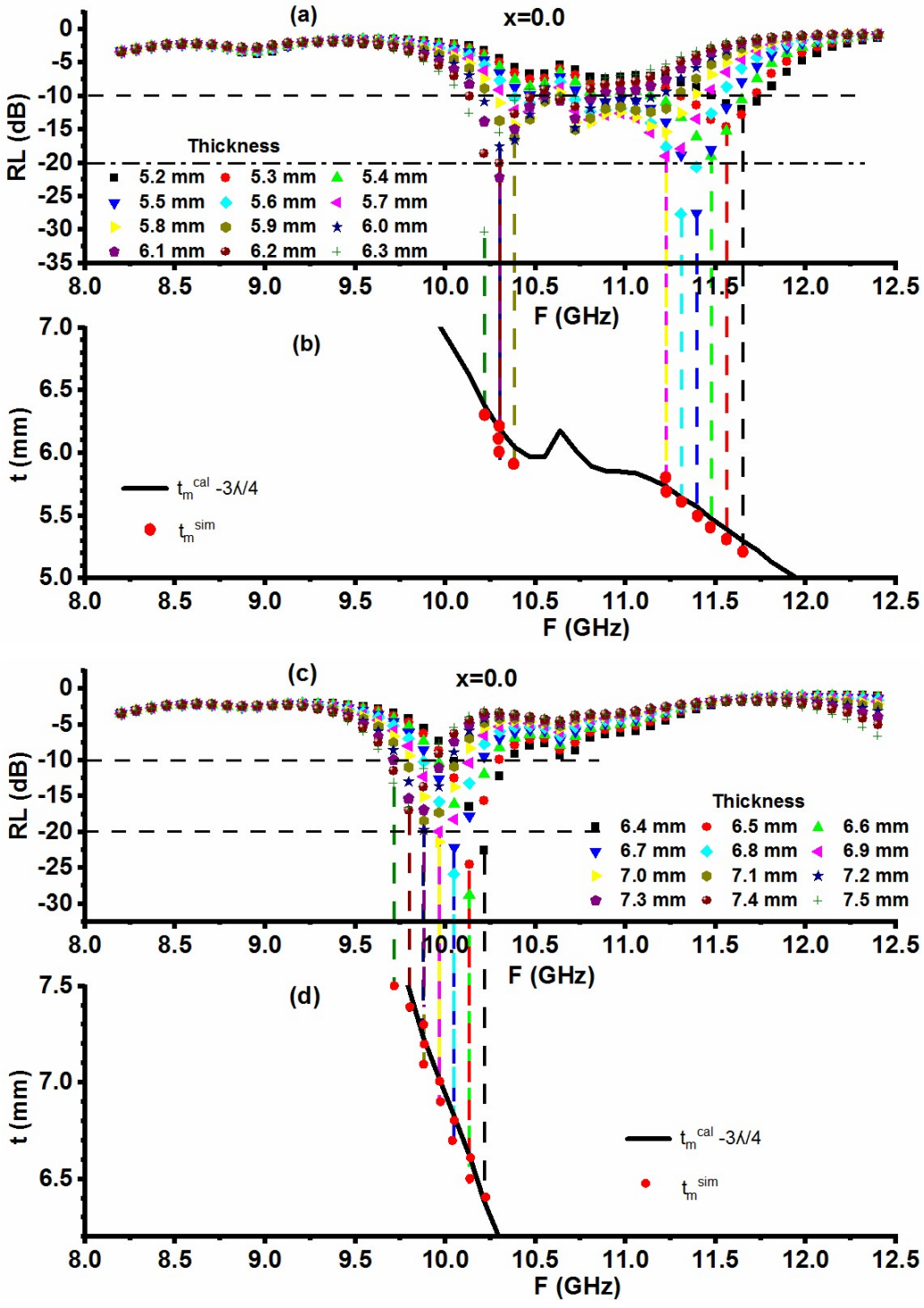
(a)
x=0.0
RL (dB)
Thickness
5.2 mm
5.3 mm
5.4 mm
5.5 mm
5.6 mm
5.7 mm
5.8 mm
5.9 mm
6.0 mm
6.1 mm
6.2 mm
6.3 mm
F (GHz)
(b)
t (mm)
t_m^{cal} -3λ/4
t_m^{sim}
F (GHz)
(c)
x=0.0
RL (dB)
Thickness
6.4 mm
6.5 mm
6.6 mm
6.7 mm
6.8 mm
6.9 mm
7.0 mm
7.1 mm
7.2 mm
7.3 mm
7.4 mm
7.5 mm
F (GHz)
(d)
t (mm)
t_m^{cal} -3λ/4
t_m^{sim}
F (GHz)

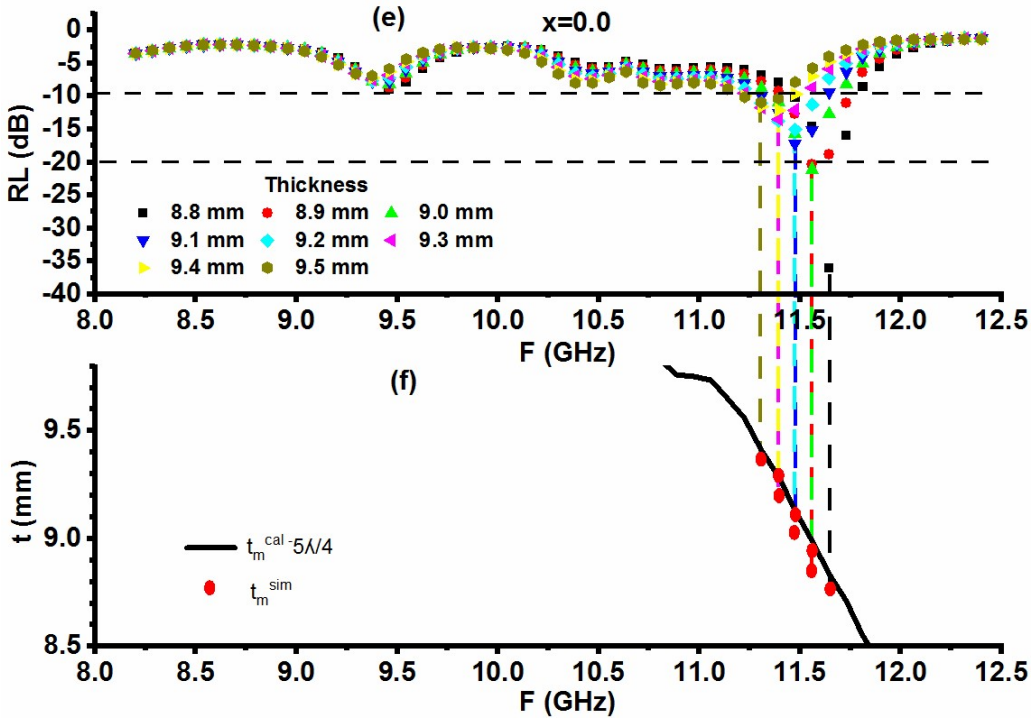

Fig. 4.58 (a, c, e) RL versus frequency (b, d, f) thickness versus frequency in x=0.0 for $SrCo_xZr_xFe_{12-2x}O_{19}$.

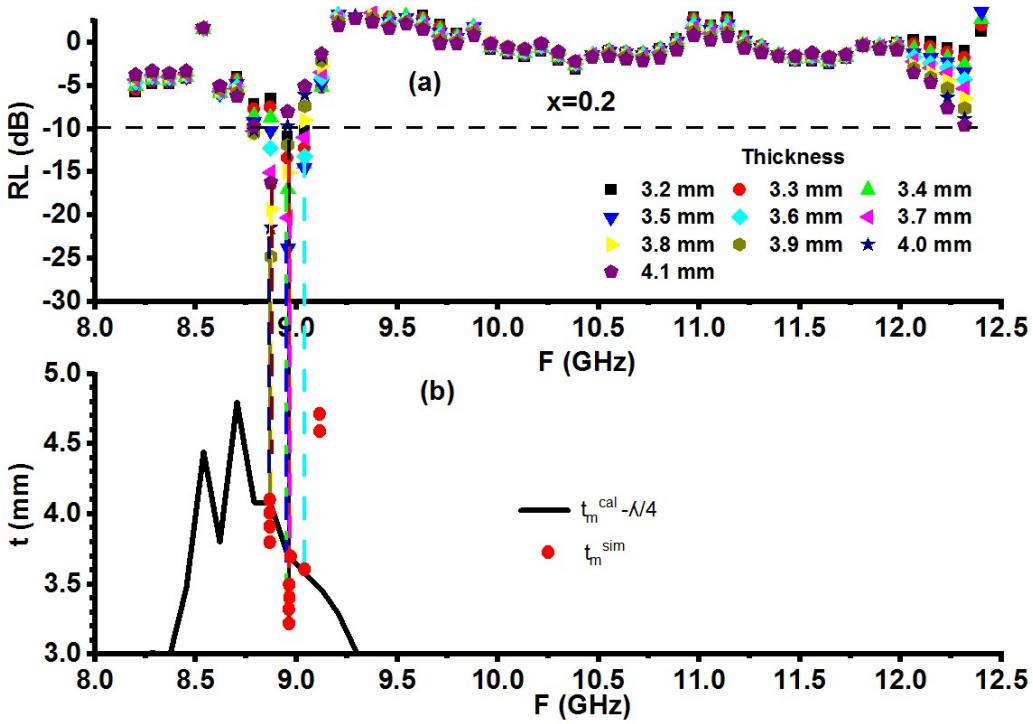

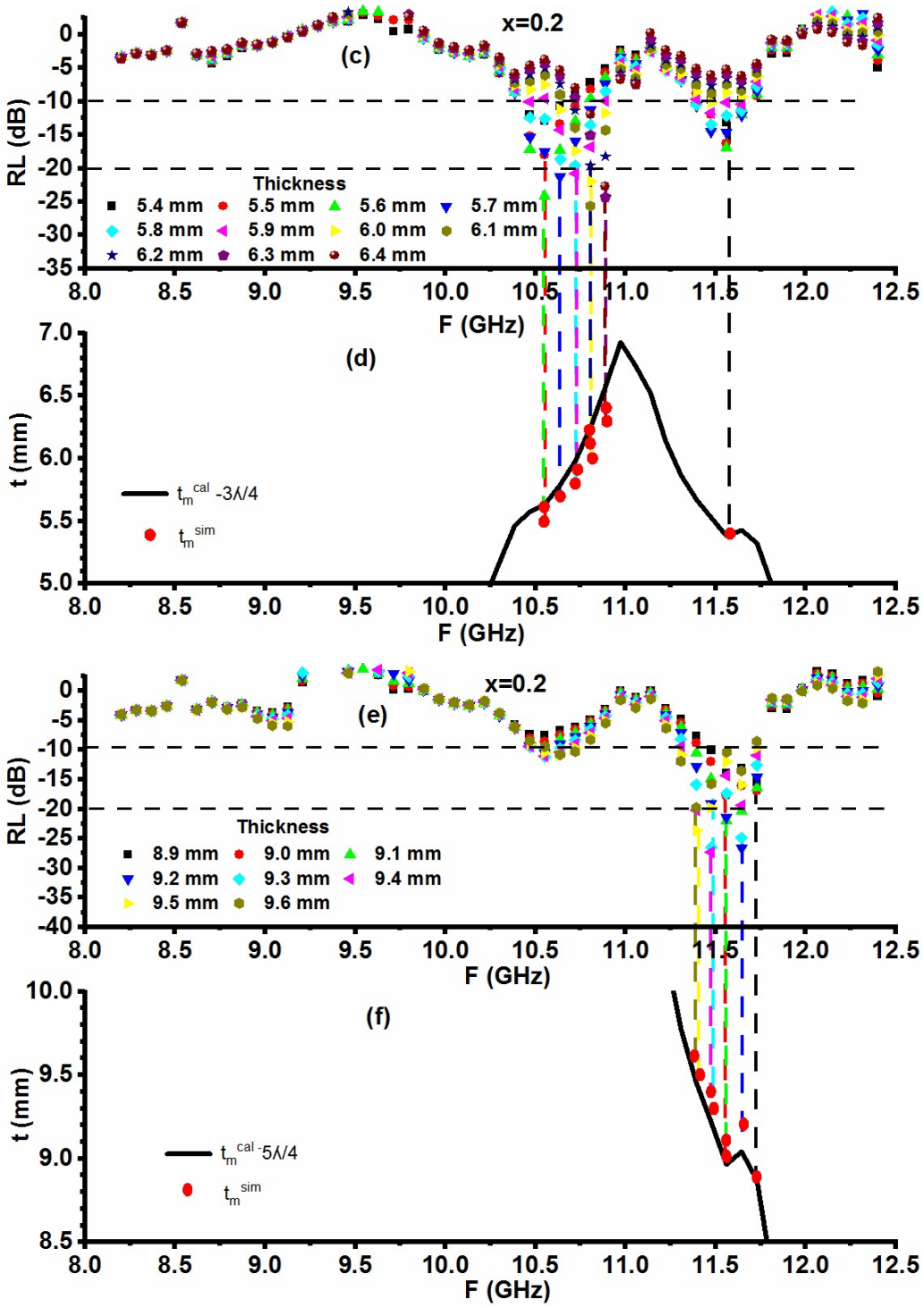

Fig. 4.59 (a, c, e) RL versus frequency (b, d, f) thickness versus frequency in x=0.2 for $SrCo_xZr_xFe_{12-2x}O_{19}$.

The highest RL of -37.69 dB is achieved for composition x=1.0 at 11.31 GHz at a small thickness 2.9 mm. RL of remaining compositions ranges between -11.45 dB and -36.03 dB at 9.04 and 11.64 GHz for thicknesses of 2.4 and 8.8 mm. The increase in thickness has a non-monotonous effect on the RL values. The absorption characteristics of composition x=0.0 are demonstrated in Fig. 4.58 (a, c, e). The reflection loss ≥ -10 dB is achieved from 5.5 to 6.0 mm for the frequency range of 10.80 to 11.14 GHz. The RL peak shifted toward a lower frequency with the increment in thickness. The frequency band of reflection loss ≥ -20 dB from 11.30-11.39 GHz is obtained at the thickness of 5.6 mm.

The composition x=0.2 has an RL=-35.55 dB for 8.98 GHz at the low thickness of 3.6 mm. In this composition thicknesses from 3.2 to 9.6 mm show RL ≥ -10 dB Fig. 4.59 (a, c, e). The RL ≥ -20 dB bands with the RL -26.60 dB at 11.64 and -27.33 dB with 11.48 GHz are obtained for the thicknesses of 9.2 and 9.4 mm respectively The composition x=0.4 owes an -34.87 dB reflection at very low thickness of 1.9 mm at 11.22 GHz Fig. 4.60 (a). The composition x=0.6 owen an RL=-24.53 dB with the matching frequency of 9.29 GHz with the 2.80 mm thickness (Fig. 4.61 (a, c)). In the composition x=0.8 highest RL peak with -24.85 dB at 10.64 GHz is obtained at 2.2 mm (Fig. 4.62 (a)). The x=1.0 shows both *RL* ≥ -10 and -20 dB frequency bands starting from the low thickness i.e. 2.6 mm. This composition has a reflection loss of -37.69 dB at 11.31 GHz at 2.9 mm which is the highest among all compositions. The RL ≥ -20 dB band is observed at thicknesses of 2.6, 2.9, and 3.2 mm (Fig. 4.63 (a, c)).

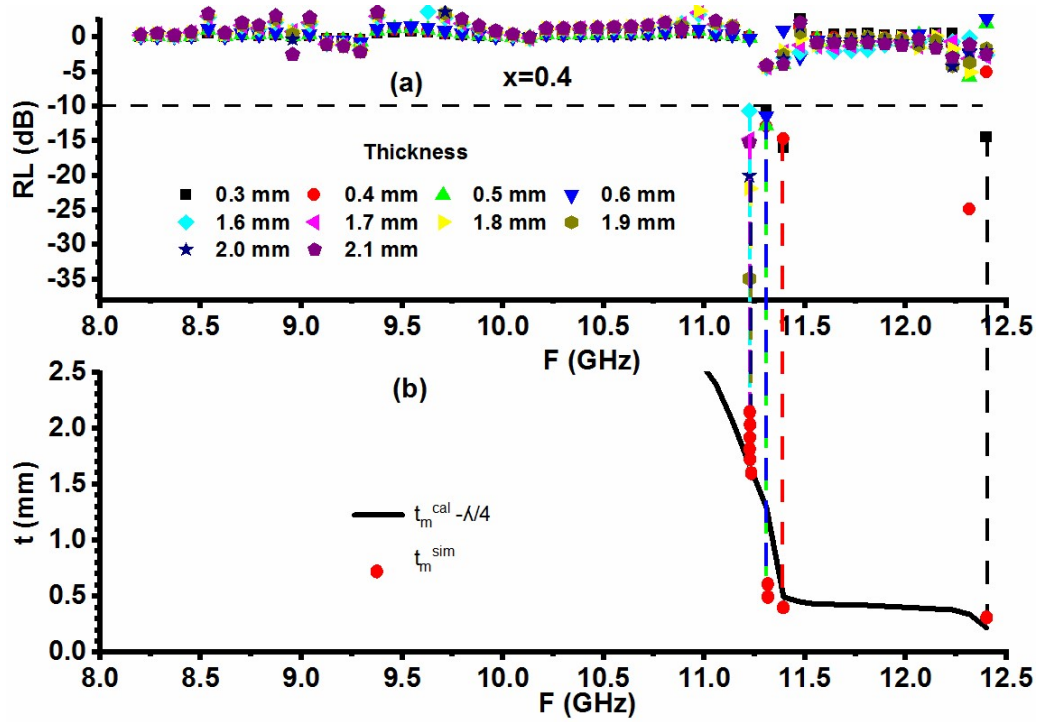

Fig. 4.60 (a) RL versus frequency(b) thickness v/s frequency in x=0.4 for $SrCo_xZr_xFe_{12-2x}O_{19}$.

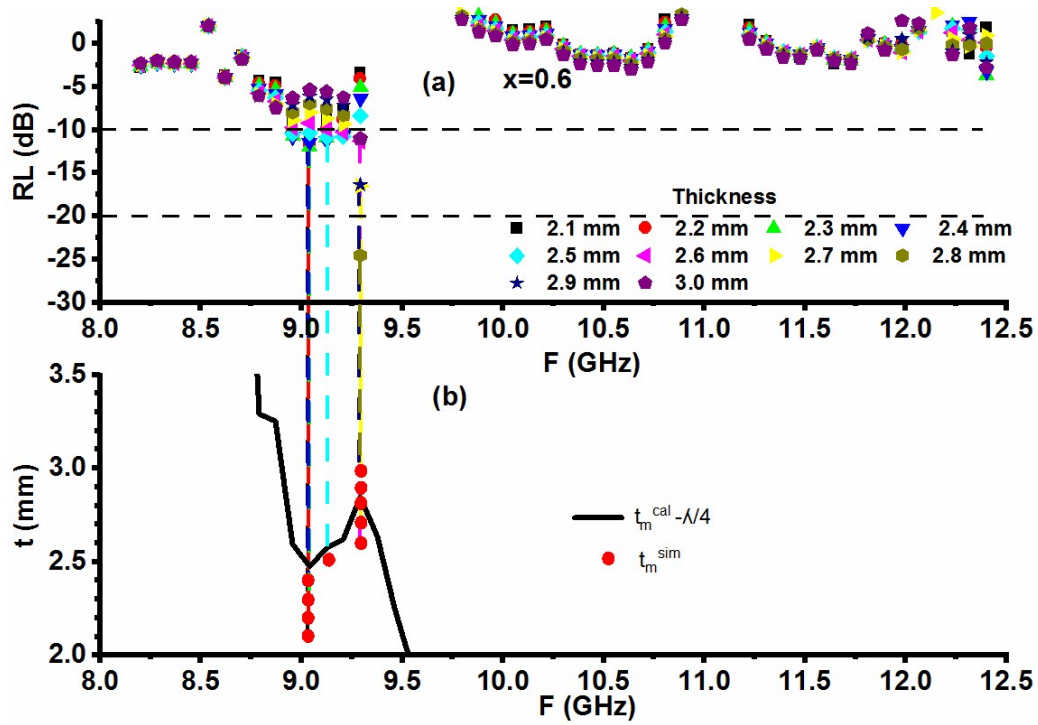

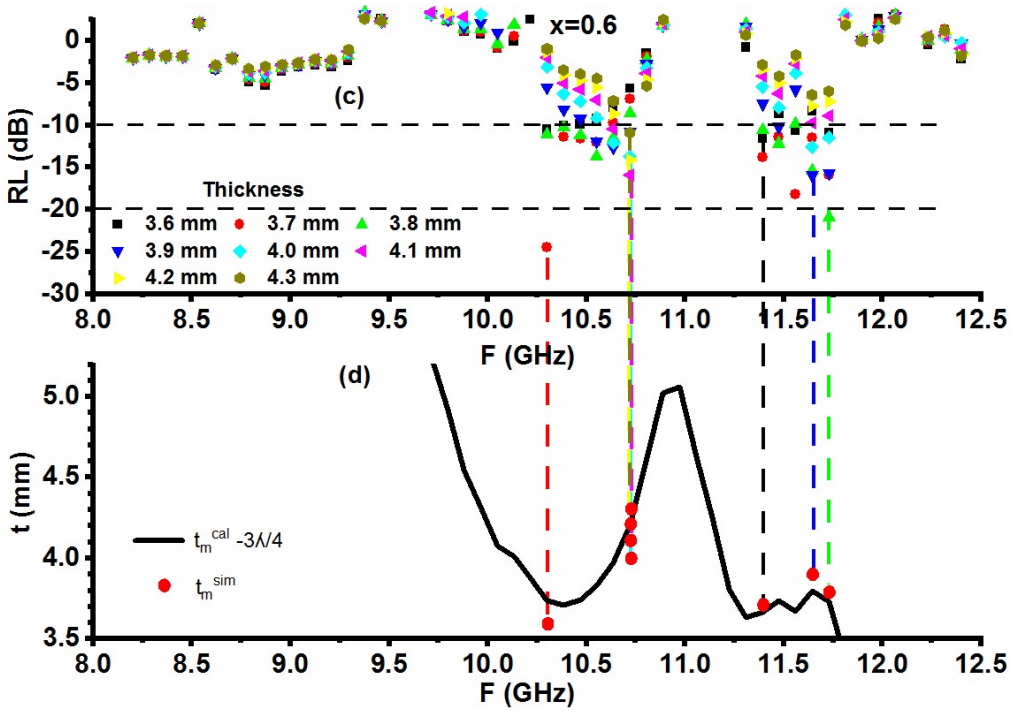

Fig. 4.61 (a, c) RL versus frequency (b, d) thickness v/s frequency in x=0.6 for $SrCo_xZr_xFe_{12-2x}O_{19}$.

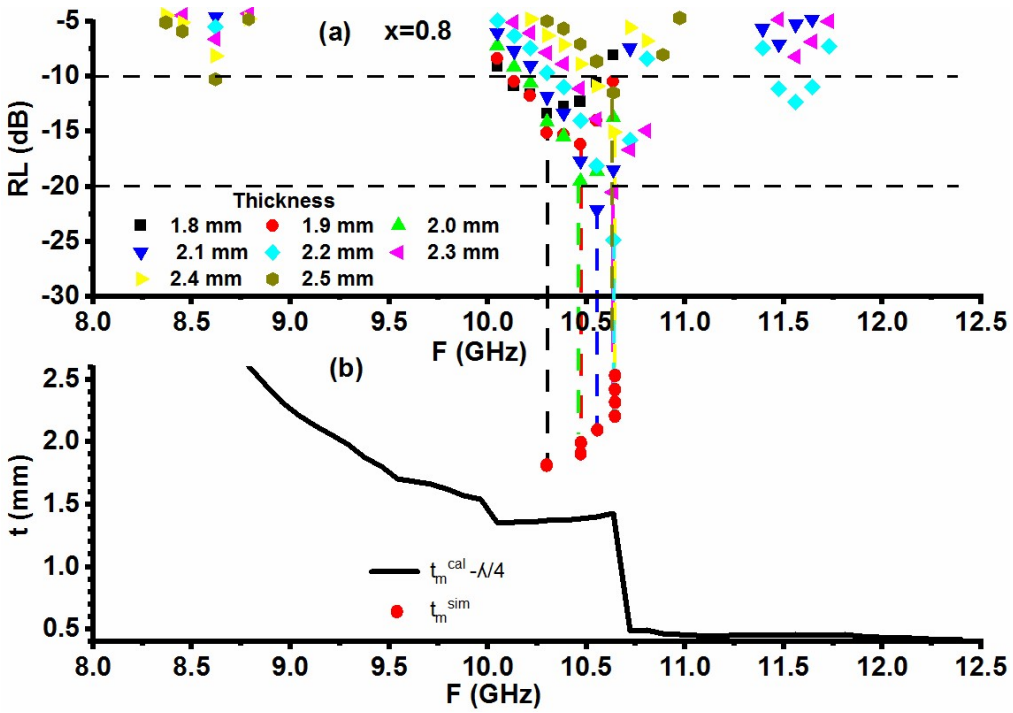

Fig. 4.62 (a) RL v/s frequency (b) thickness versus frequency in x=0.8 for $SrCo_xZr_xFe_{12-2x}O_{19}$.

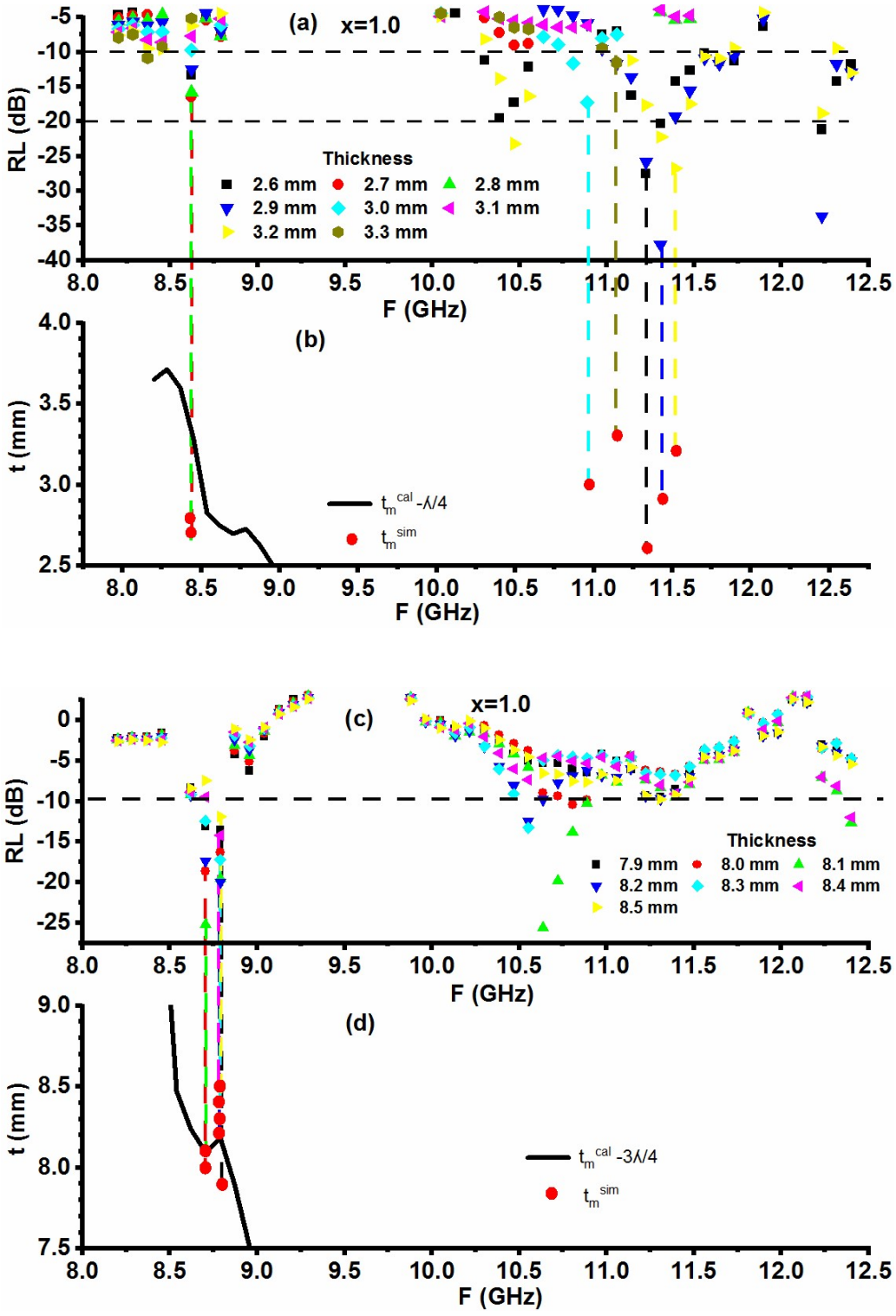

Fig. 4.63 (a, c) RL v/s frequency (b, d) thickness v/s frequency in x=1.0 for $SrCo_xZr_xFe_{12-2x}O_{19}$.

To explore a relation between RL peaks and the λ/4 mechanism a comparison between simulated thickness (t_m^{sim}) and calculated thickness (t_m^{cal}) has been done. Fig. 4.58 (b, d, f), 4.59 (b, d, f), 4.60 (b), 4.61 (b, d), 4.62 (b), and 4.63 (b, d) depicts the graphs for calculated thickness v/s frequency. For comparison between simulated and calculated thickness lines from RL peaks are brought to the thickness-frequency graphs. The mechanism is followed by the compositions x=0.4 and 0.8 for n=1, x=0.6 and1.0 for n=1 and 3, in x=0.0 it exists at n=3 and 5 while the composition x=0.2 is matched for n=1, 3, and 5. The quarter wavelength criteria for composition x=0.0 originates -10 dB bandwidth of 0.25 to 1.09 GHz at thicknesses from 5.6 to 8.8 mm as given in Table 4.14. The composition x=0.2 contains -10 dB peaks for a thickness from 3.2 to 9.6 mm. A -10 dB bandwidth of this composition ranges between 0.17 and 0.34 GHz. The -20 dB bandwidth of 90 MHz and 80 MHz are observed with RL=-27.33 dB and RL=-26.60 dB respectively. The composition x=0.4 has RL values at very low thicknesses from 0.03 to 2.1 mm. This composition has a bandwidth of 80 MHz at thicknesses of 0.03 and 0.04 mm at a matching frequency of 11.39 and 11.39 GHz respectively.

For the composition x=0.6 bandwidth of 0.34 GHz at 3.8 mm for the frequency band of 10.30-10.64 GHz is obtained, while bandwidths of 0.25 GHz at 2.4 and 3.7 mm associated with -10 dB are obtained. The x=0.8 has -10 dB bandwidths of 0.51 GHz for a small thickness i.e. 1.9 mm. A bandwidth of 0.42 GHz at 1.8 and 2.0 mm thickness is observed. The composition x=1.0 has a bandwidth of 0.67 GHz with 2.9 mm thickness with a band of 11.06-11.73 GHz which is highest among all the doped compositions. The bandwidth of 0.59 GHz at 2.6, while the bandwidth of 0.50 GHz at 3.2 mm is also achieved in this composition. The -20 dB bandwidth of 90 MHz is observed at 2.6 and 2.9 mm with a frequency band of 11.22-11.31 GHz.

Table 4.14. RL with matching thickness/frequency, BW, and PBW for $SrCo_xZr_xFe_{12-2x}O_{19}$.

x	RL (dB)	Matching Thickness (mm)	Matching Frequency (GHz)	-10 dB band (GHz)	-10 dB BW (GHz)	-20 dB band (GHz)	-20 dB BW (GHz)	BTR	PBW (%)
0.0	-27.60	5.6	11.31	10.72-11.48	0.76	11.31-11.39	0.08	0.331	6.720
	-16.25	5.9	10.38	10.30-11.22	0.92	-	-	0.405	8.863

	-17.58	6.0	10.30	10.22-11.14	0.92	-	-	0.404	8.932
	-30.29	6.3	10.22	10.13-11.22	1.09	-	-	0.457	10.665
	-36.03	8.8	11.64	11.48-11.73	0.25	-	-	0.063	2.148
0.2	-35.55	3.6	8.96	08.87-09.04	0.17	-	-	0.177	1.897
	-20.29	3.7	8.96	08.79-09.04	0.25	-	-	0.255	2.790
	-21.27	5.7	10.64	10.47-10.80	0.33	-	-	0.154	3.102
	-26.60	9.2	11.64	11.39-11.73	0.34	11.56-11.64	0.08	0.083	2.921
	-27.33	9.4	11.48	11.39-11.73	0.34	11.39-11.48	0.09	0.081	2.962
0.4	-15.95	0.3	11.39	11.31-11.39	0.08	-	-	0.621	0.702
	-14.74	0.4	11.39	11.31-11.39	0.08	-	-	0.466	0.702
	-14.73	1.7	11.22	-	-	-	-	0.000	0.000
	-34.87	1.9	11.22	-	-	-	-	0.000	0.000
	-20.06	2.0	11.22	-	-	-	-	0.000	0.000
0.6	-11.96	2.3	9.04	8.96-9.12	0.16	-	-	0.255	1.769
	-11.45	2.4	9.04	8.96-9.21	0.25	-	-	0.379	2.765
	-24.53	2.8	9.29	-	-	-	-	0.000	0.000
	-24.49	3.7	10.3	10.30-10.55	0.25	-	-	0.187	2.427
	-13.75	3.8	10.55	10.30-10.64	0.34	-	-	0.245	3.223
	-15.93	4.1	10.72	10.64-10.72	0.08	-	-	0.051	0.746
0.8	-13.36	1.8	10.30	10.13-10.55	0.42	-	-	0.655	4.078
	-16.22	1.9	10.47	10.13-10.64	0.51	-	-	0.747	4.871
	-19.52	2.0	10.47	10.22-10.64	0.42	-	-	0.579	4.011
	-24.85	2.2	10.64	10.38-10.72	0.34	-	-	0.417	3.195
1.0	-27.49	2.6	11.22	11.14-11.73	0.59	11.22-11.31	0.09	0.521	5.258
	-37.69	2.9	11.31	11.06-11.73	0.67	11.22-11.31	0.09	0.534	5.924
	-26.77	3.2	11.39	11.14-11.64	0.50	11.31-11.39	0.08	0.362	4.390
	-13.50	7.9	8.79	8.70-8.79	0.09	-	-	0.045	1.023
	-25.58	8.1	10.64	10.64-10.89	0.25	-	-	0.080	2.349

4.3.5.4 Impedance matching mechanism

Since the permittivity/permeability of the material differs from that of free space their impedance also differs. The difference between these two affects the absorption characteristics of the material. Due to the mismatch in these two, the majority of the incident signal gets discarded from the surface and a lesser part of the signal enters the material. However, if they match major portion of it travels into the material and gets absorbed by the material. That's why an investigation of impedance matching is required for the development of an effective absorber.

Fig. 4.64 depicts the plots of reflection loss and $|Z_{in}|$ v/s frequency for the prepared samples. Table 4.15 lists the values of Z_{in} corresponding to the maximum reflection loss of the different compositions. The highest RL peaks in all the compositions (x=0.0

to 1.0) follow the impedance matching mechanism, however, there are some discrepancies at the few frequencies in compositions x=0.4, 0.8, and x=1.0

The RL peak of -36.03 dB at 11.64 GHz for 8.8 mm thickness in composition x=0.0 corresponds to Z_{in}=366.74 Ω which is approximately 377 Ω. An RL peak with -35.55 dB at 8.96 GHz with Z_{in}=382.98 Ω in x=0.2 is in coordination with the value of Z_o=377 Ω. RL peak of -24.53 at 9.29 GHz with Z_{in}=424.33 Ω is observed for composition x=0.6. In composition x=0.4 there is a RL peak of -34.87 at 11.22 GHz with Z_{in}=376.98 Ω while there is no RL peak at 10.22 GHz with a Z_{in}=389.80 Ω which is more close to Z_o=377 Ω than Z_{in}=424.33 Ω in x=0.6. In composition x=0.8 RL peak of -24.85 at 10.64 GHz corresponds to Z_{in}=396.35 Ω while at 10.89 GHz and 8.79 GHz, there are no RL peaks while respective Z_{in}=365.89 Ω and Z_{in}=360.57 Ω. Both the values of Z_{in}=365.89 Ω and 360.57 Ω are closer to Z_o=377 Ω than Z_{in}=396.35 Ω. Similarly a low RL=-10.98 dB at 11.64 GHz with Z_{in}=367.75 Ω is observed in comparison to Z_{in}=396.35 Ω with RL=-24.85 dB. On the same note Z_{in}=368.97 Ω at 8.45 GHz in composition x=1.0 has no RL peak. The RL=-37.69 dB at 11.31 GHz in x=1.0 corresponds to Z_{in}=380.27 Ω which is close to Z_o=377 Ω.

This type of behavior is related to the complex nature of $|Z_{in}|$owing to real and imaginary parts (Z_{real} & Z_{img}). So Z_{real} and Z_{img} are calculated and graphs of Z_{real} and Z_{img} are plotted as shown in Fig. 4.65. The respective values of Z_{real} and Z_{img} are given in Table 4.15. For the successful implementation of the impedance matching the real and imaginary impedances of the material should follow exactly/nearly the criteria of 377 Ω and/or 0. The highest RL of -37.69 dB at 11.31 GHz obtained for x=1.0 satisfies this condition as Z_{real}=380.15 Ω and Z_{img}=9.37 Ω. In the case of x=0.4 no RL at 10.22 GHz with Z_{in}=389.80 Ω is due to Z_{real}=-55.41 Ω and Z_{img}=385.85 Ω which are not satisfying the required criteria. For no RL peak with Z_{in}=365.89 Ω and Z_{in}=360.57 in x=0.8 are due to Z_{real}=-359.50 Ω, Z_{img}=-68.09 Ω and Z_{real}=146.24 Ω, Z_{img}=329.58 Ω.

Hence, it can be said that the discrepancies observed are due to the deviation in Z_{real} and Z_{img} from 377 Ω and/or zero. The input impedance Z_{in} (Z_{real} and Z_{img}) varies in a non-monotonical manner with the doping of Co-Zr. On the final note, it can be said that both λ/4 and impedance matching have their role in the absorption characteristics of prepared compositions.

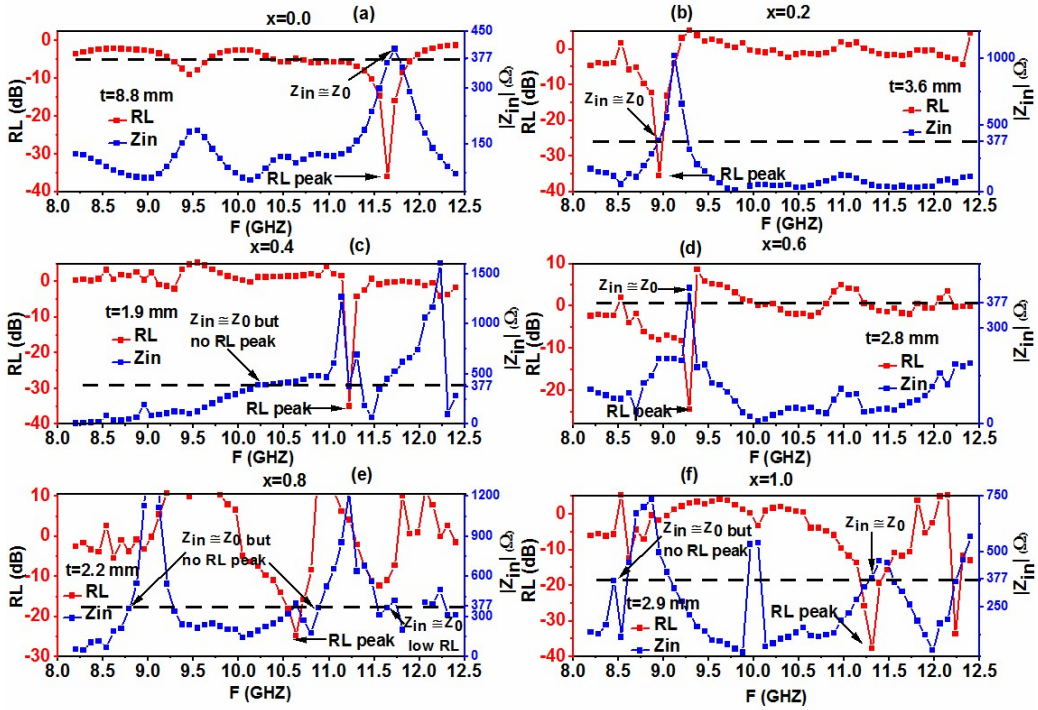

Fig. 4.64 Zin and RL curve against frequency for $SrCo_xZr_xFe_{12-2x}O_{19}$.

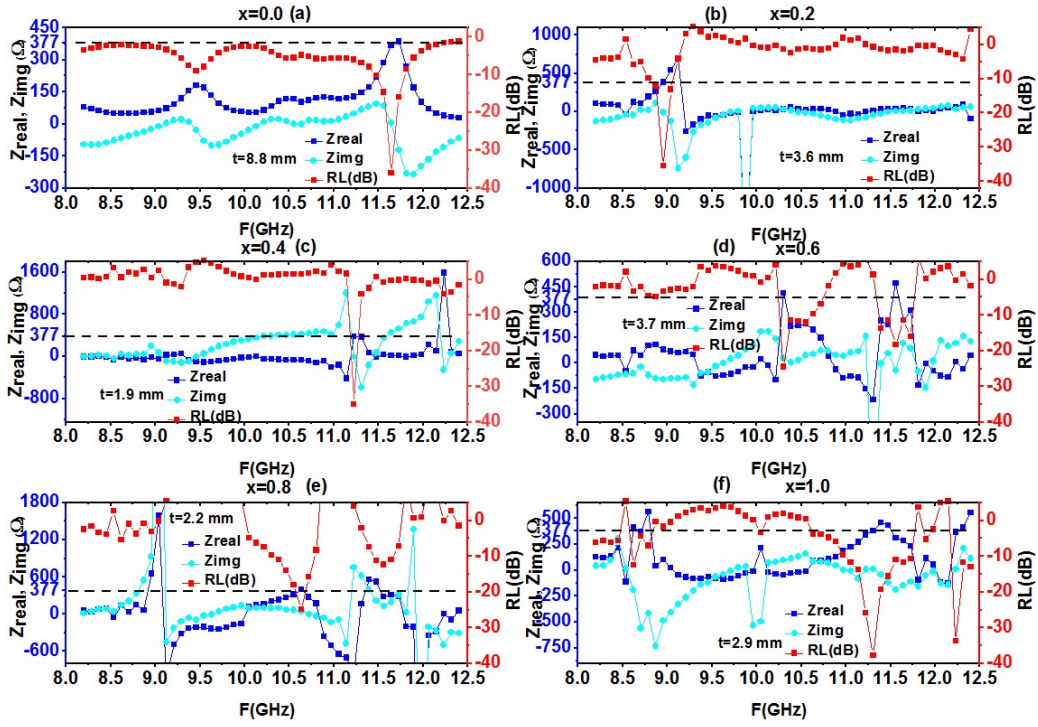

Fig. 4.65 Z_{real}, Z_{imag}, and RL v/s frequency for $SrCo_xZr_xFe_{12-2x}O_{19}$.

Table 4.15. Z_{in}, Z_{real}, and Z_{imag} values corresponding to RL_{max} for $SrCo_xZr_xFe_{12-2x}O_{19}$.

x	RL (dB)	Matching Thickness (mm)	Matching Frequency (GHz)	$\|Z_{in}\|$ (Ω)	Z_{real} (Ω)	Z_{img} (Ω)
0.0	-36.03	8.8	11.64	366.74	366.70	5.66
0.2	-35.55	3.6	8.96	382.98	382.82	-11.27
0.4	-34.87	1.9	11.22	376.98	376.74	-13.58
0.6	-24.53	2.8	9.29	424.33	424.30	4.96
0.8	-24.85	2.2	10.64	396.35	394.25	40.74
1.0	-37.69	11.31	2.9	380.27	380.15	9.37

4.3.5.5 Role of Electromagnetic/Material Parameters

The relaxation peaks complex permittivity/permeability also have their contribution in the absorption which should also be investigated. The peaks observed in complex permittivity/permeability graphs of the prepared compositions are contributing to absorption: in composition x=1.0, *RL*=-27.49 dB at 11.22 GHz for 2.6 mm correspond to the relaxation peak in ε′ peak at 11.22 GHz; for composition x=0.4 the RL=-20.06 dB at 11.22 GHz for 2.0 mm thickness signify to a small ε" peak at 11.22 GHz. The RL=-26.77 at 11.39 GHz for 3.2 mm is attributed to the μ' peak at 11.39 GHz in composition x=1.0. In composition x=0.4 the μ" peak at 11.39 GHz is attributed to the RL peak -14.74 dB at 11.39 GHz with the thickness of 0.4 mm. Thus dielectric and magnetic losses are also contributing to the absorption in the prepared compositions.

4.3.5.6 Eddy Current Loss

There is a significant role of eddy current losses in the absorption characteristics of ferrites. The formula to determine eddy current loss is given as in equation 4.4 which is utilized to explain the effect of eddy current loss.

If C_0 doesn't change with the increase in frequency, there is a contribution of eddy current losses. So a plot of C_0 against the frequency is plotted for all the compositions as given in Fig. 4.66. The plots indicate that after 9 GHz all the compositions are showing flat regions except x=1.0 at 10.0 GHz and x=0.2 at 12.40 GHz. This shows that eddy current loss contributes to the absorption of the prepared compositions.

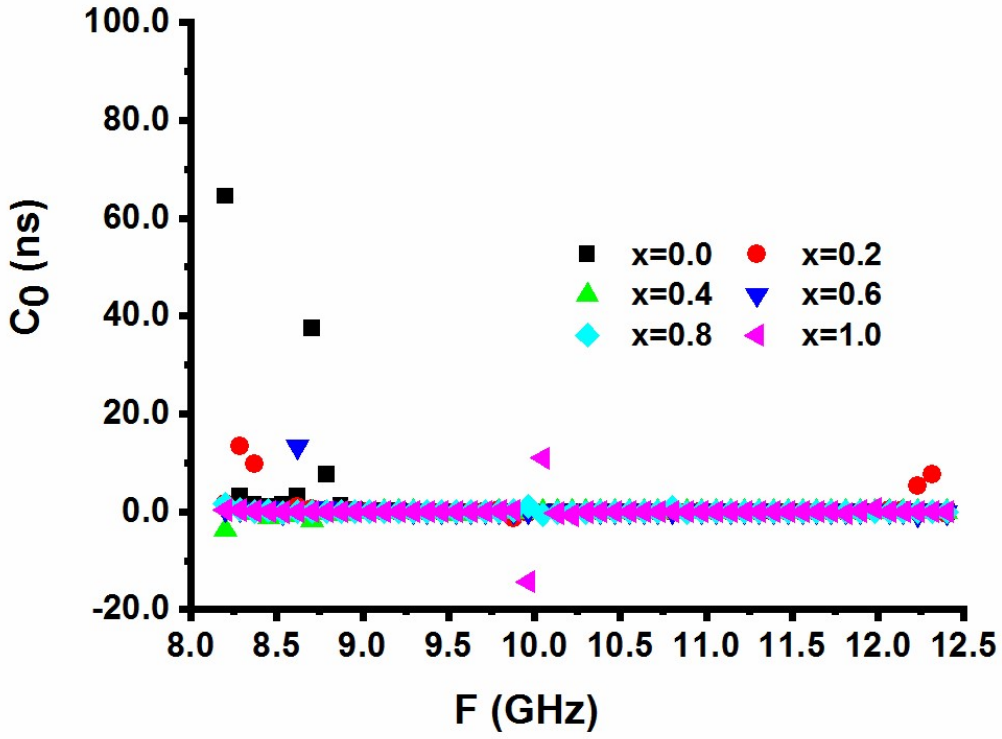

Fig. 4.66 C_0 versus frequency curve for $SrCo_xZr_xFe_{12-2x}O_{19}$.

4.3.5.7 Bandwidth to Thickness Ratio

The broad bandwidths with lesser thickness are very important in the design and characterization of an absorber. After achieving the RL≥-10 dB, one should aim at getting a low thickness, rather than increasing RL values only. Due to this factor bandwidth to thickness ratio (BTR) and percentage bandwidth (PBW) become important to determine which are determined for the prepared composition using equations 4.5 and 4.6.

Table 4.14 lists the BTR and PBW values determined for the prepared compositions. The table indicates that doping has increased BTR. The maximum value of BTR is

obtained in composition x=0.8 BTR=0.747 at 10.47 GHz with RL=-16.22 dB. At the same time, composition x=0.8 also has a high BTR of 0.655 at 10.30 with RL=-13.36 dB and 0.579 at 10.47 GHz with RL=-19.52 dB. The composition x=0.4 also possesses high BTR of 0.621 and 0.466 at 11.39 GHz for thicknesses of 0.3 and 0.4 mm. The highest RL=-37.69 dB of the prepared series corresponds to a BTR of 0.534(composition x=1.0). The doping of Co-Zr has decreased the percentage bandwidth. The composition x=0.0 has the highest PBW of 10.67. The composition x=1.0 owen a maximum PBW=5.92 for 2.9 mm among the doped composition. PBW ranges from 1.02 to 5.92 % in composition x=1.0.

4.4 $SrCo_xZn_xFe_{12-2x}O_{19}$/PANI composites

4.4.1 Microstructural/Morphological Characteristics

For the analysis of the microstructure/morphology of $SrCo_xZn_xFe_{12-2x}O_{19}$/PANI composites scanning electron microscopy is carried out. Micrographs of $SrCo_xZn_xFe_{12-2x}O_{19}$/PANI (x=0.0, 0.6, and 1.0) composites are shown in Fig. 4.67. The doping of Co-Zn has affected the grain distribution and improved inter-grain connectivity. The agglomeration of grains can be seen in the micrographs as well.

This should be noted that the small size of grains has increased the grain boundaries as can be easily viewed in the SEM images of composition x=0.0. This increase in the grain boundaries promotes polarization at the grain boundaries and affects the electrical properties. The micrographs of composition x=0.6 show the formation of grain clusters. The increase in grain size as well as fused grain can be noticed in composition x=1.0 as compared to the composition x=0.0.

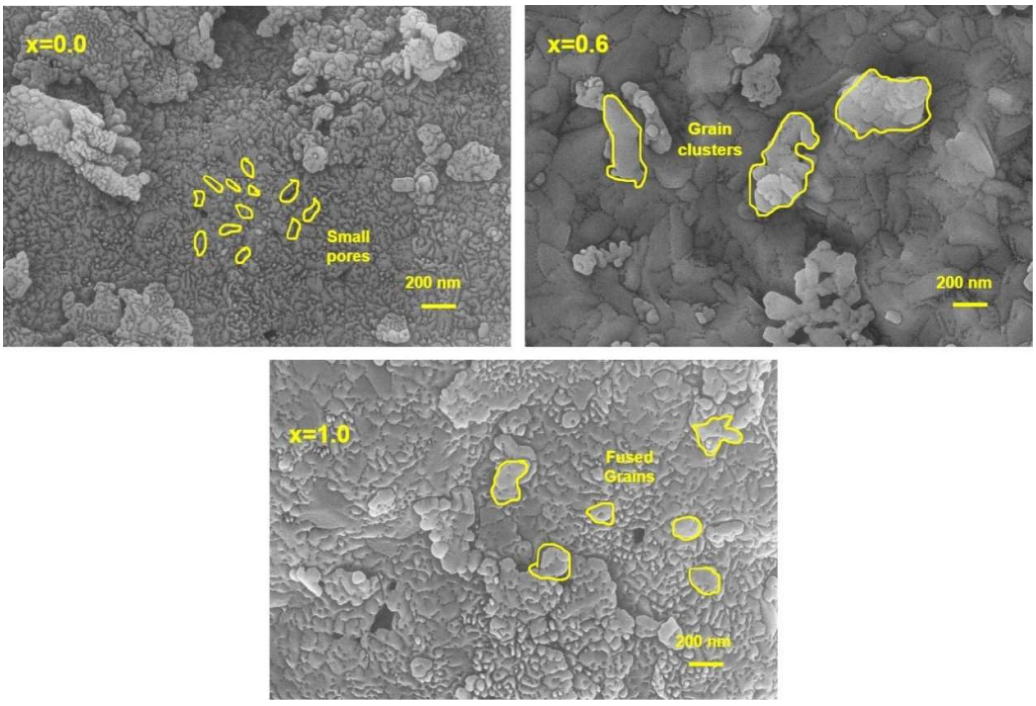

Fig 4.67 SEM images of $SrCo_xZn_xFe_{12-2x}O_{19}$/PANI

4.4.2 Electrical Characteristics

4.4.2.1. Dielectric constant

The graph of ε' and ε'' v/s frequency for the composites are depicted in Fig. 4.68. The dielectric constant of ferrite is found to be a complex value with its real part (ε') indicating the degree of polarization and imaginary part (ε'') representing the dielectric losses. The formula to determine the real part is shown in equation (3.5). Dielectric loss ε'' is calculated using equation (3.6), while the loss tangent ($tan\delta$) can be determined by equation (3.7) as given in chapter 3. The inclusion of PANI in ferrite has enhanced the dielectric properties. As PANI is a dielectric material inclusion of it with the hexaferrites ($SrCo_xZn_xFe_{12-2x}O_{19}$) has increased the value of ε' and ε''. The plots of ε' decrease with the frequency increment. It has high values at the low frequencies while decreasing gradually before attaining a constant value at the high frequency. This behavior is due to the interfacial polarization and complies with the Maxwell-Wagner model [80]. This is noted from the figure that doping has reduced the dielectric constant as it is decreasing with the increment in doping level.

The x=0.0 have the maximum ε' for the low-frequency regime, this is due to the fact that the polarization depends on Fe^{3+}/Fe^{2+} ions and these are maximum in x=0.0. The doping has reduced the number of Fe^{3+}/Fe^{2+} and hence causes a decay in the value of ε'. A similar trend is seen in ε'' as shown in Fig. 4.68 (b).

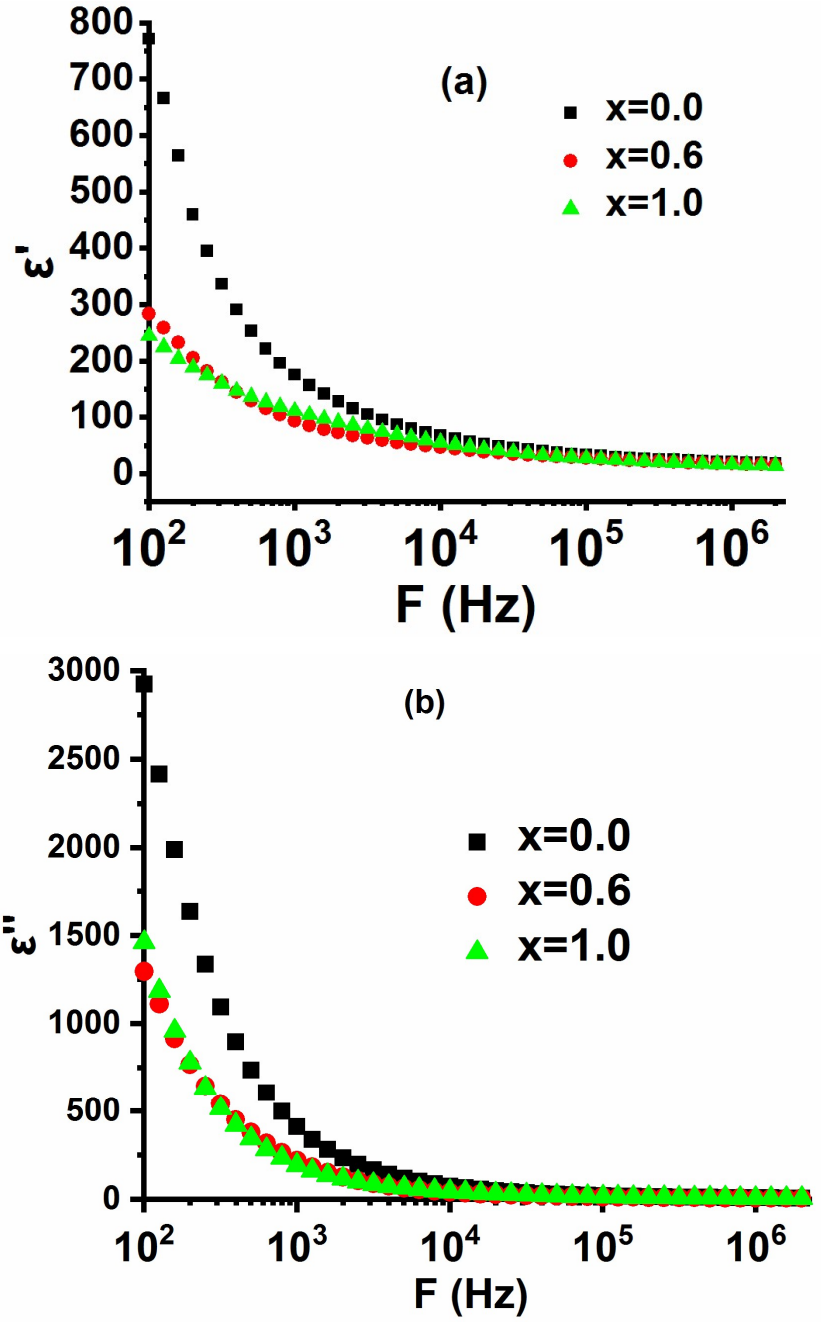

Fig. 4.68. Dielectric constant (a) real (b) imaginary versus frequency of $SrCo_xZn_xFe_{12-2x}O_{19}$/PANI.

The graphs of loss tangent (tanδ) against frequency for the composites have been given in Fig. 4.69 which indicates the gradual decrease with the increment in frequency. This behavior is due to the interfacial polarization and complies with the Maxwell-Wagner model for Koop phenomenon of dielectrics At low frequencies, grain boundaries are more effective while grains are at high frequencies. The loss tangent increases with the addition of Co-Zn in the composites. The x=1.0 has the highest tanδ at the initial stage however it reduces as the frequency increases.

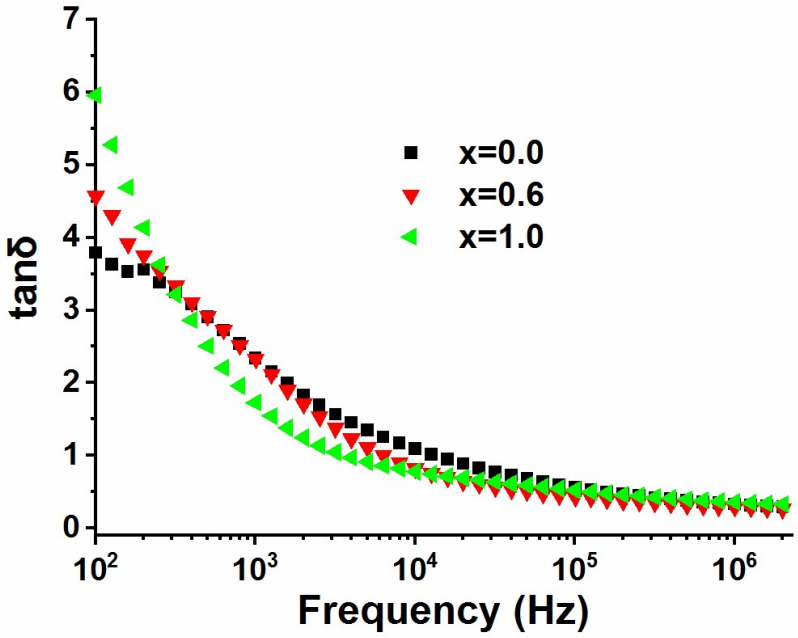

Fig. 4.69 Plots of loss tangent of $SrCo_xZn_xFe_{12-2x}O_{19}$/PANI composites.

4.4.2.2. Electric modulus

The plots of M′ and M″ for $SrCo_xZn_xFe_{12-2x}O_{19}$/PANI composites are given in Fig. 4.70 (a) and (b) respectively. M′ possesses a low value at a low-frequency regime while increasing with the frequency increment. This sigmoidal increase in the curve of M′ with an increase in frequency corresponds to the charge carrier's short-range mobility. The absence of a saturated region (M′) at high frequency signifies the lack of long-range mobility of charge carriers. There is an increment M′ with the addition of PANI and Co-Zn content as can be noted from the plots of composition x=0.6 and x=1.0. The composition x=1.0 has the highest value of M′ among all.

The M″ curve provides information about the conductivity relaxation mechanism. The graphs showed asymmetric peaks where the low-frequency area of a peak shows a long-distance movement while the high-frequency region shows localized motion only. The height of M″ gets increased by the higher doping of Co-Zn. The highest value is for composition x=1.0. There is a shifting of peaks toward the low-frequency region due to the inclusion of Co-Zn. This shifting with doping of Co-Zn toward a low-frequency region indicates an increase in the relaxation time. The broadening of relaxation peaks can be noticed with the increase in doping level.

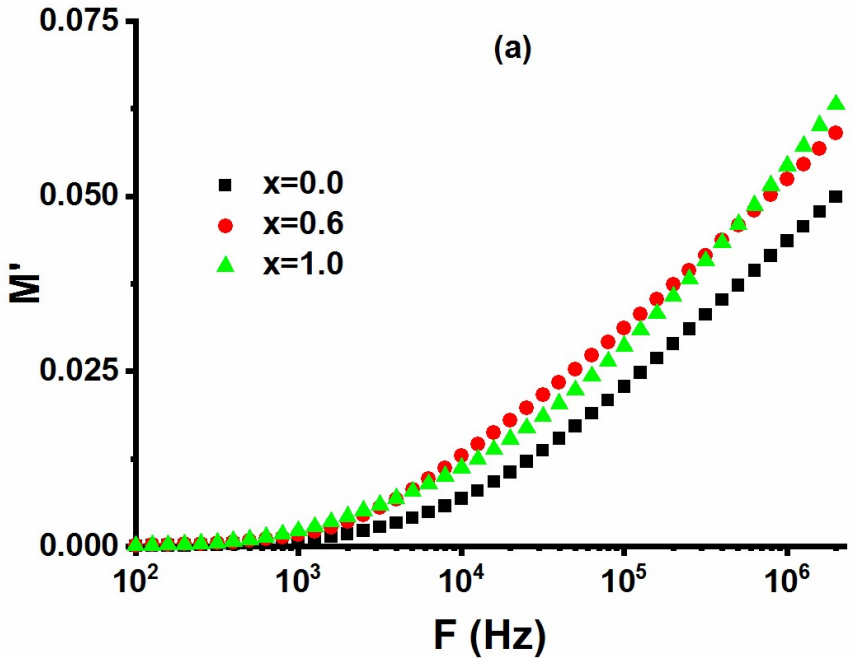

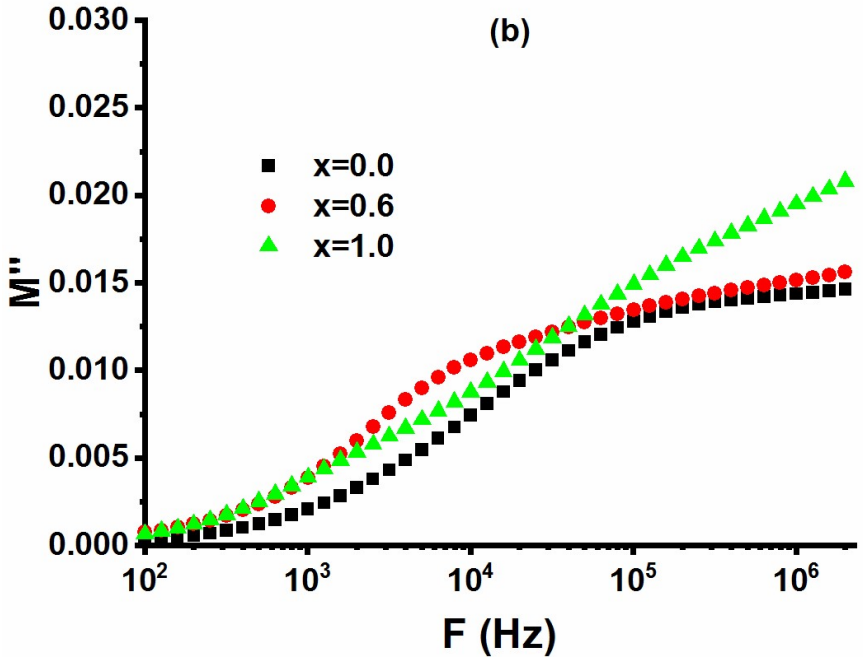

Fig. 4.70 M′ and M″ curves against frequency of $SrCo_xZn_xFe_{12-2x}O_{19}$/PANI.

Cole-Cole plot ($M'v/s\ M''$) of $SrCo_xZn_xFe_{12-2x}O_{19}$/PANI composites are shown in Fig 4.71. The plots of all the composites contain asymmetric deformed semicircles. An asymmetric deformed semicircle can be seen for all the prepared compositions with the center deviating from the x-axis which implies a non-Debye behavior. The semicircle of composition x=0.0 lies more toward a low-frequency regime indicating a role of grain boundary in charge transport. Compositions x=0.6 and x=1.0 have their semicircles in both low as well as high-frequency regions. Hence both grain and grain boundaries are responsible for charge transport. The height of the semicircles increases with the increase in doping of Co-Zn. Besides this, the semicircles also shifted toward the low-frequency region which indicates an increase in the relaxation time.

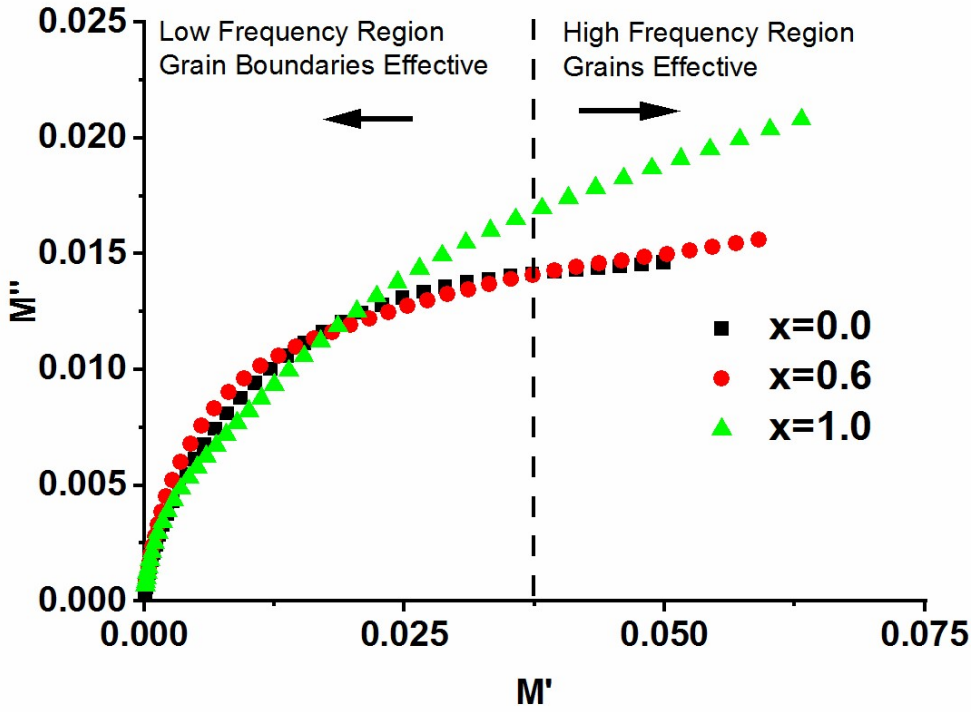

Fig. 4.71 Cole-Cole plot of M′ v/s M″ of $SrCo_xZn_xFe_{12-2x}O_{19}$/PANI.

4.4.2.3. Complex impedance spectra

Fig. 4.72 (a) indicates the graphs of Z′ and frequency The curve of Z′ continuously decays with frequency and reaches a constant value thereafter. This decrease is following the Maxwell-Wagner model. Here is a rise in the values of Z′with the doping of Co-Zn in the composites. Micrographs depict an increment in the grain size that enhances the resistances of grains. Z′is highest in composition x=1.0.

Z″ v/s frequency graphs of the composites are given in Fig. 4.72 (b). The value of *Z″* of composites increases by the doping of Co-Zn in the low-frequency regime. This is due to the decrement in space charge polarization with an increase of Co-Zn content. The asymmetric broad peaks are viewed in the plots of all the compositions. The height of the peak is increased as Co-Zn doping increases. These peaks are associated with dielectric relaxation.

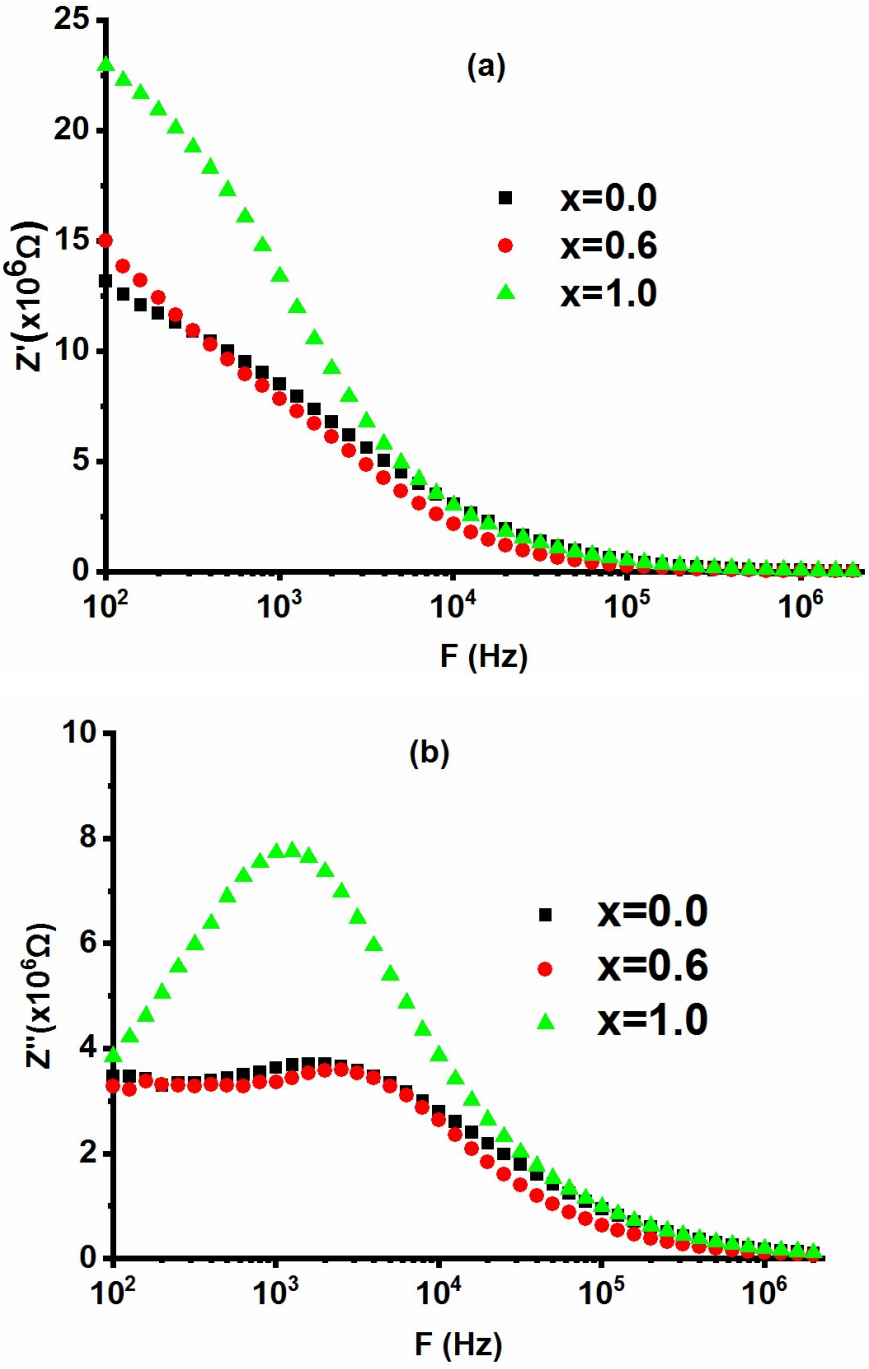

Fig. 4.72 Z′ and *Z″*versus frequency plots of $SrCo_xZn_xFe_{12-2x}O_{19}$/PANI.

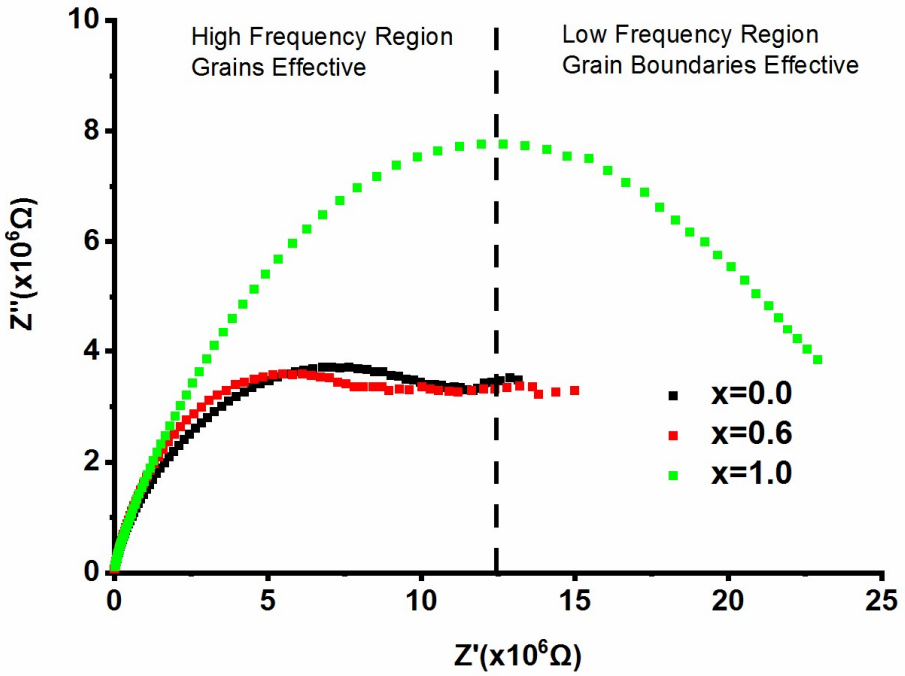

Fig. 4.73. Cole-Cole plots (Z' versus Z'') of $SrCo_xZn_xFe_{12-2x}O_{19}$/PANI.

Cole-Cole plots ($Z''vs\ Z'$) of prepared composites are demonstrated in Fig. 4.73. The plots show deformed semi-circles for all compositions. The plots for x=0.0 and 0.6 lie in the high frequency area showing a dominance of grains. The composition x=0.0 and 0.6 shows two semicircles a large size semicircle in high frequency and a small one in low frequency. It signifies that the role of grain boundaries is less prominent for these compositions. Composition x=1.0 has its curve almost equally in both low and high-frequency regions signifying a role of both grain and grain boundary. The height of the semicircle has increased with the increase in doping of Co-Zn which shows an increase in relaxation time.

4.4.2.4. AC Conductivity

Fig. 4.74 displays a graph between ac conductivity **(σ_{ac})** and frequency for the composites. The value of conductivity is low at the initial level and starts increasing after a particular frequency called hopping frequency. With the inclusion of PANI a conductive polymer, the conductivities of the ferrite composites have enhanced as compared to the ferrite alone. This hopping frequency indicates the transition from the

flat plateau region of dc conductivity **(σ_{dc})** to the dispersive region of ac conductivity **(σ_{ac})**. The non-monotonous decrement in the value of **(σ_{ac})** of the composites is observed with the inclusion of Co-Zn content. It can be noted that the hopping frequency also shifted to the high frequency with the doping level. This is due to the morphology: the highest value of σ_{ac} in x=0.0 is due to the good inter-grain connectivity (Fig. 4.67) while composition x=0.6 has the lowest value due to the formation of large grain clusters (Fig. 4.67).

The ac conductivity curves are fitted according to the Jonscher power law as explained in Chapter 3 is used to explain the frequency-dependence nature of ac conductivity. By fitting the curves, values of n were calculated for the prepared composites. The determined values are 0.562, 0.648, and 0.623. According to Funke n<1 shows the motion with sudden hoping. The values are less than 1 which signifies that ac conductivity follows the hopping mechanism.

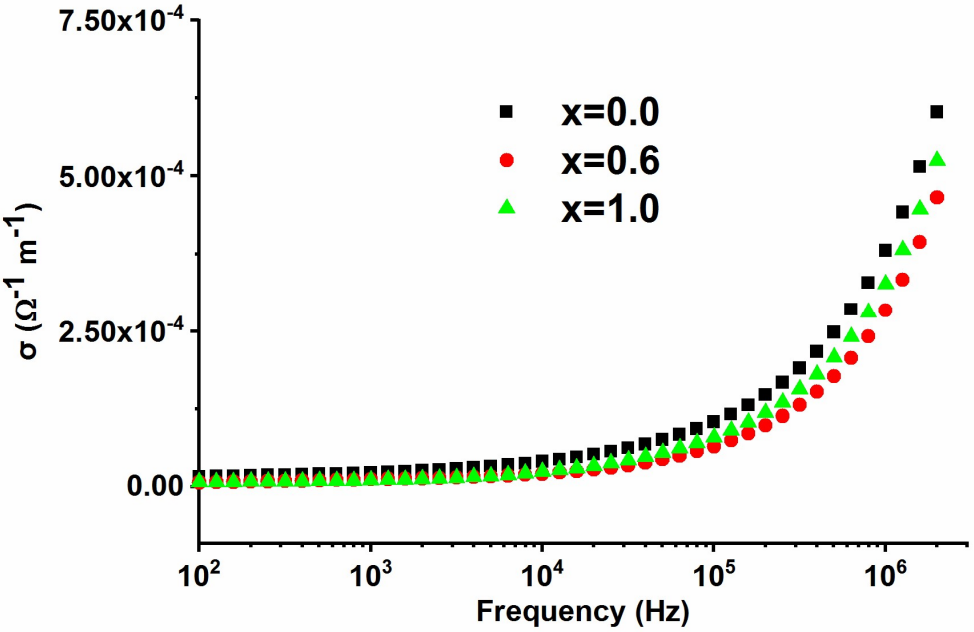

Fig. 4.74. AC conductivity of $SrCo_xZn_xFe_{12-2x}O_{19}$/PANI.

4.4.2.5 Software-based Impedance Simulation

Impedance spectroscopy has been done using EIS software as depicted in Fig. 4.75. The simulated parameters for grain and grain boundaries are given in Table 4.16.

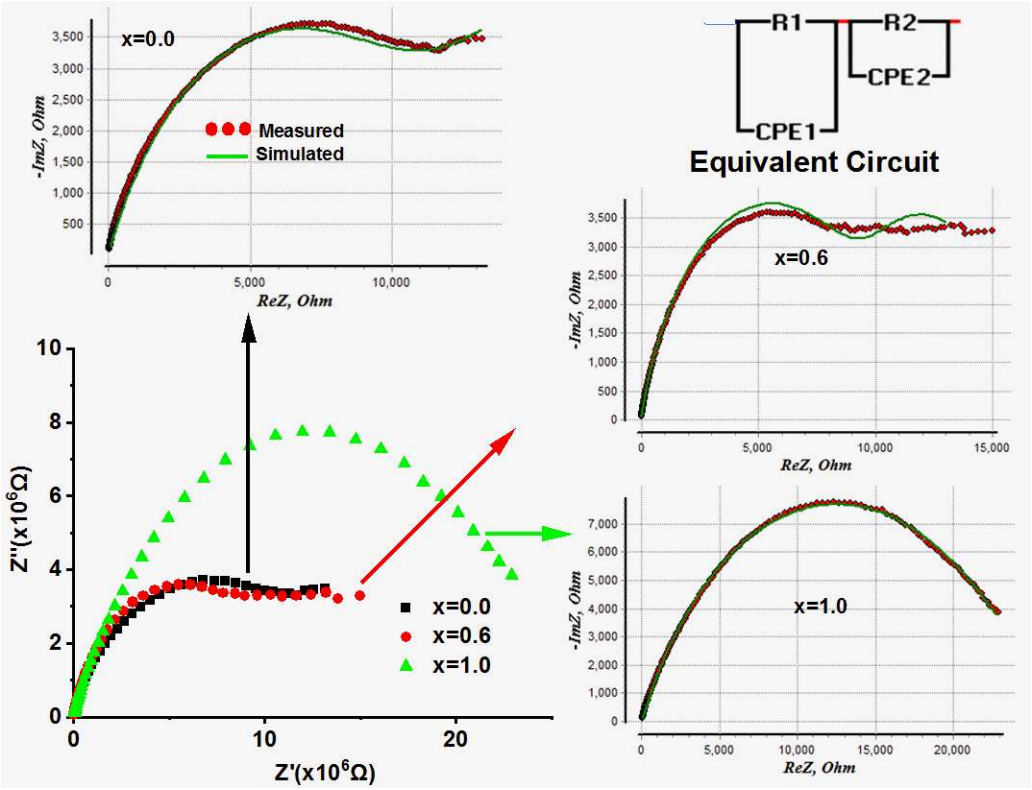

Fig. 4.75 Fitting of Impedance curves using EIS for $SrCo_xZn_xFe_{12-2x}O_{19}$/PANI.

Table 4.16. Simulated parameters derived from EIS software for $SrCo_xZn_xFe_{12-2x}O_{19}$/PANI.

x	R_g (MΩ)	R_{gb} (MΩ)	C_g (μF)	C_{gb} (μF)
0.0	10.68	16.78	4957.4	$9.41x10^6$
0.6	5.55	10.18	252.8	326.77
1.0	22.66	4.93	1302.0	$11511.7x10^6$

Correlation between Grain/Grain boundaries simulated parameters and Morphology

The composition x=1.0 has well-connected large as well as small grains enhancing grain boundaries as seen in the micrograph of Fig. 4.67. This promotes polarization at the grain boundaries that in turn enhances the capacitance of grain boundaries to be high. This can be validated by Table 4.16 with the highest simulated grain boundary capacitance C_{gb}=11511.7 x 10^6 μF. Composition x=0.0 has small pores which causes

polarization at grain boundaries causing high grain boundaries capacitance C_{gb}=9.41 x 10^6 μF.

Correlation between Grain/Grain boundaries simulated parameters and Dielectric Parameters

The composition x=1.0 has the lowest while x=0.0 has the highest dielectric constant (Fig. 4.68). Maxwell-Wagner model suggests that grain boundaries are dominant at low, however, grains are at high frequency. Table 4.16 shows that the composition x=1.0 has the minimum grain boundary resistance R_{gb}= 4.93 MΩ due to the lowest dielectric constant. (ε'=245.01). The highest dielectric constant (ε'=770.90) in x=0.0 attributing to the highest simulated grain capacitance C_g=4957.4 μF.

Correlation between Grain/Grain boundaries simulated parameters and Electric Modulus

The major portion of the curves of x=0.0, 0.6, and 1.0 are inclined towards the low-frequency side showing the dominance of grain boundaries. Table 4.16 validates this behavior attributing the high values of grain boundary capacitances C_{gb}=9.41 x 10^6 μF and C_{gb}=11511.7 x 10^6 μF in compositions x=0.0, and 1.0. Composition x=0.6 has high grain boundary capacitance C_{gb}=326.77 μF as compared to grain capacitance C_g=252.8 μF referring prominence of grain boundaries.

4.4.3. Band gap Characteristics

Tauc plots drawn for the prepared $SrCo_xZn_xFe_{12-2x}O_{19}$/PANI composites have been given in Fig 4.76. Equation 3.4 as given in the experimental section in Chapter 3 is used to calculate the required values of band gap. To obtain the required band gap the interception on the x-axis was found from the linear curve of the Tauc plot. The band gaps of the prepared compositions x=0.0, 0.6, and 1.0 are 2.15, 1.56, and 1.47 eV respectively.

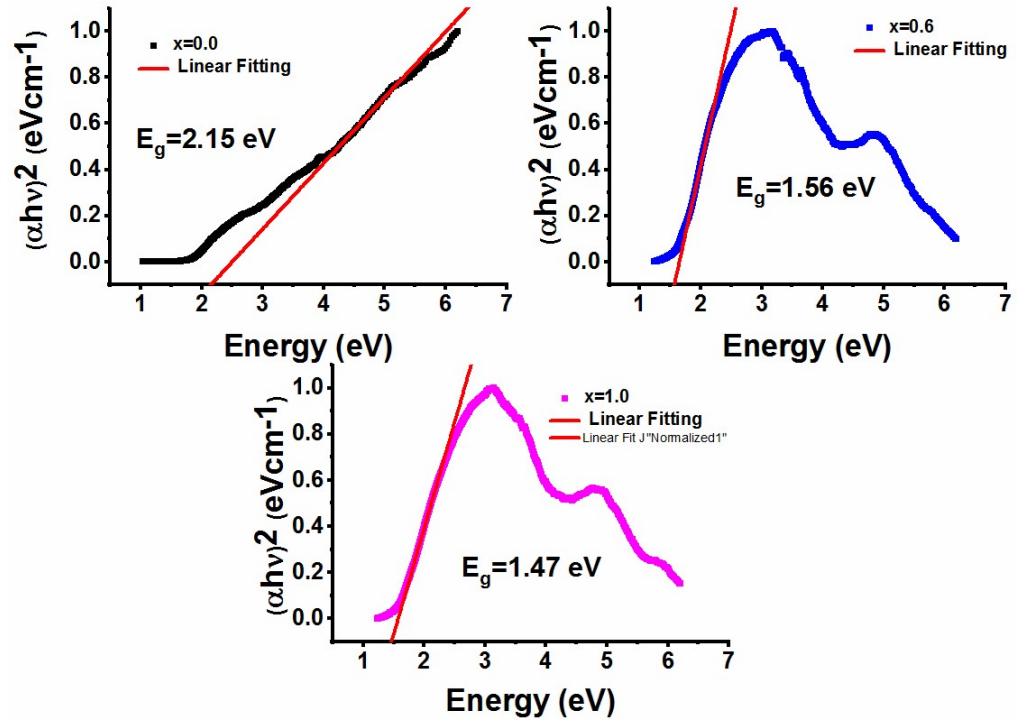

Fig. 4.76 Tauc plots of $SrCo_xZn_xFe_{12-2x}O_{19}$/PANI

4.4.4 Magnetic Characteristics

For the analysis of magnetic characteristics of $SrCo_xZn_xFe_{12-2x}O_{19}$/PANI composites magnetization (M) versus magnetic field (H) plots are drawn as shown in Fig. 4.77 (a). The electronegativity of the ions affects their site occupancy. The ions having high electronegativity mostly try to first hold octahedral sites as compared to tetrahedral. The electronegativity of Zn^{2+}(1.65) is lesser than that of Co^{2+}(1.88) hence they will tend to occupy the tetrahedral sites $4f_1(\downarrow)$. Zn^{2+}due to the $3d^{10}$ configuration will not have any site preference as all the cells are filled while Co^{2+} with $3d^7$preferably choose octahedral sites 12k $(\uparrow), 2a(\uparrow), 4f_2(\downarrow)$ as per the ligand field theory. Kim et al. [110] and Karim et al. [105] reported that Zn^{2+}prefer tetrahedral, while Thakur et al. [111] reported that Co^{2+} prefer to acquire an octahedral.

Formula to derive saturation magnetization (M_s) and anisotropy field (H_a) is as given in equation 4.2.

Fig. 4.77 (a) shows a steep rise in magnetization at lower fields that reduces in high fields. There is a large slope at high fields indicating the unsaturated state in undoped

composition x=0.0 which reduces with the substitution of Zn^{2+} and Co^{2+}. The reduction in the anisotropy field is the reason behind it. It can be seen that above 10 KOe a linear curve is present hence A/H and χ_P is removed. Thus the simplified form for M can be written as $M = M_s\,(1 - B/H^2)$. Thus plots of M v/s $1/H^2$ have been plotted and linear fitting is performed to calculate the value of M_s and B as given in Fig. 4.77 (b). For the hexaferrites, B is related to H_a as $B = H_a^2/15$ with H_a representing the anisotropy field. The calculated parameters are listed in Table 4.17. The magnetic moment is given by the relation between spin-up and down sites as shown in equation 4.2.

The relation indicates that the substitution of weak/non-magnetic ion on spin-down sites Mb ($4f_1\downarrow + 4f_2\downarrow$) enhances saturation magnetization while substitution at spin-up sites Ma (2a↑ + 12k↑ + 2b↑) reduces it. The prepared ferrite composites showed a decrease in M_s. The value of M_s decreases by 31% with the substitution of Zn^{2+} and Co^{2+} from x=0.0 (47.8 emu/g) to x=1.0.6 (32.8 emu/g). This is due to the substitution of Zn^{2+} and Co^{2+} at octahedral spin-up sites. The replacement of Fe^{3+}(5μB) by weak magnetic Co^{2+} (3μB) and diamagnetic Zn^{2+} (0μB) causes decrease at M_a ($2a\uparrow + 12k\uparrow + 2b\uparrow$) which reduces the value of M_s. Besides it, the replacement of Fe^{3+} at octahedral spin-up sites 2a↑ and 12k↑ causes an imbalance in electrical neutrality and to maintain it Fe^{3+} is converted into Fe^{2+} which causes a reduction of the superexchange interactions due to which magnetic moment decreases. There is a decrease in Ha which indicates that more substitution of Zn^{2+} and Co^{2+} is at octahedral sites 2a↑ and 12k↑ which reduces the value of M_s.

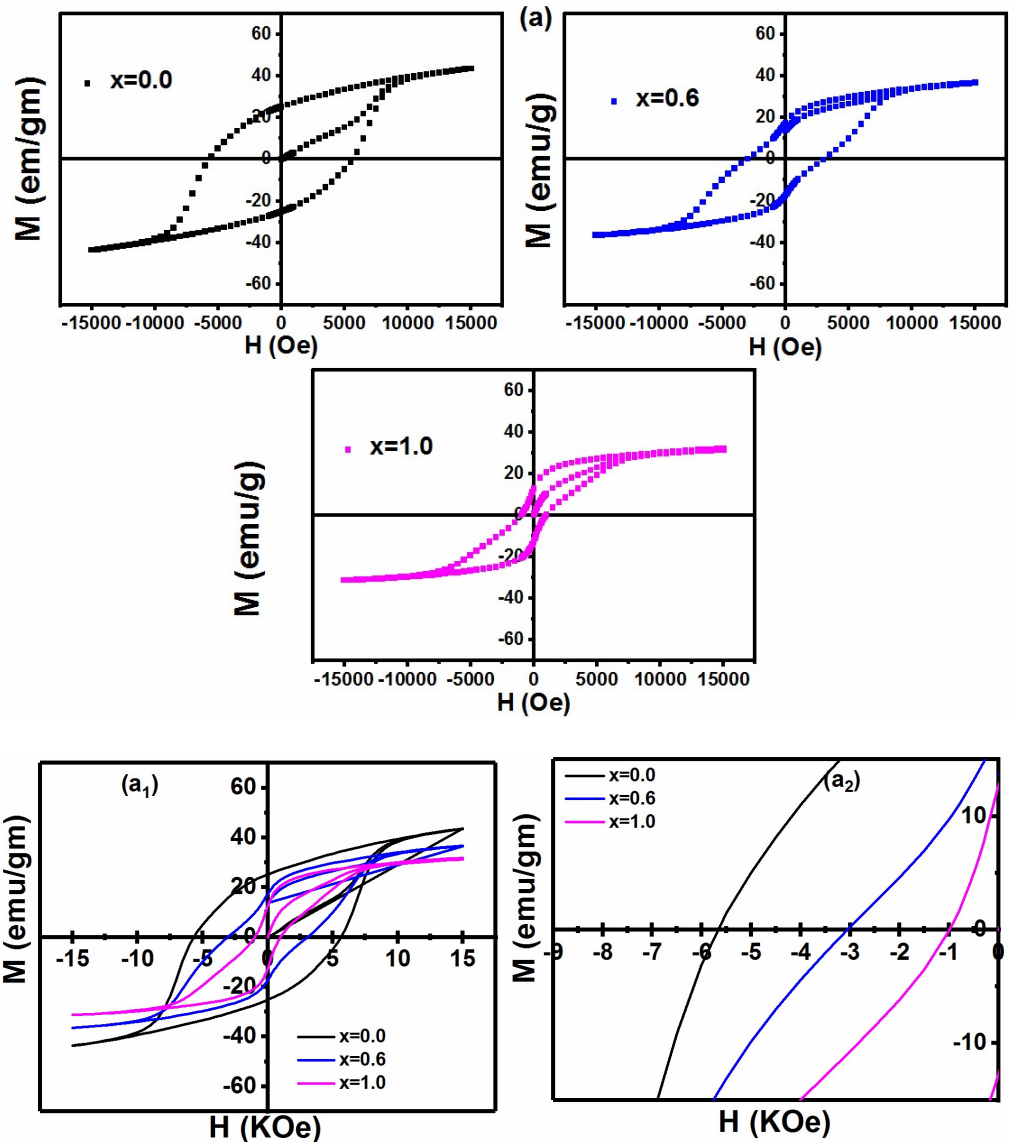
(a)
x=0.0
x=0.6
x=1.0
M (em/gm)
M (emu/g)
H (Oe)
60
40
20
0
-20
-40
-60
-15000 -10000 -5000 0 5000 10000 15000

(a1)
(a2)
x=0.0
x=0.6
x=1.0
M (emu/gm)
H (KOe)
60
40
20
0
-20
-40
-60
-15 -10 -5 0 5 10 15
10
-10
-9 -8 -7 -6 -5 -4 -3 -2 -1 0

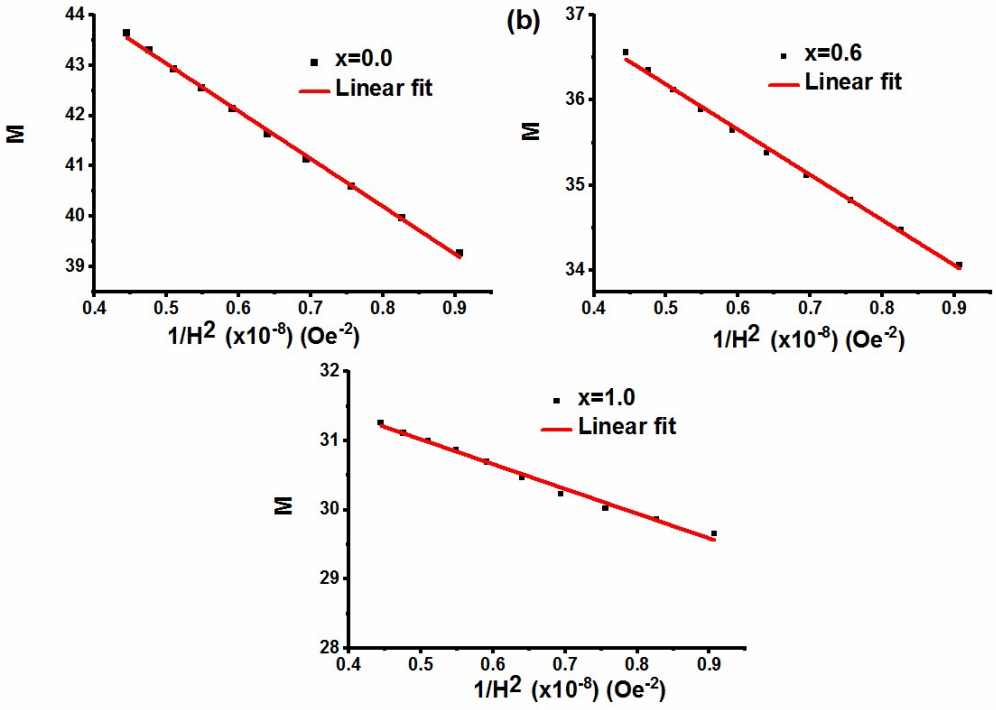

Fig. 4.77 (a) M-H loops (a_1, a_2) combined and enlarged view (b) Ms v/s $1/H^2$ plots of $SrCo_xZn_xFe_{12-2x}O_{19}$/PANI.

Table 4.17. Magnetic parameters determined from M-H loops of $SrCo_xZn_xFe_{12-2x}O_{19}$/PANI.

x	M_s(emu/g)	M_r(emu/g)	H_a (kOe)	H_c (Oe)	M_r/M_s
0.0	47.8	25.17	17.2	5679	0.53
0.6	38.8	17.38	14.3	3057	0.45
1.0	32.8	12.73	12.8	987	0.39

The design of an efficient absorber requires a low value of coercivity (H_c). Table 4.17 indicates that the addition of Co-Zn has reduced the value of H_c. The highest H_c=5679 Oe is obtained in x=0.0, while the smallest H_c=987 Oe is achieved in composition

x=1.0. There is a 46 % decrease in the value of H_c from 5679 to 3057 Oe for x=0.0-0.6, while there is a very large 83 % reduction for x=0.0-1.0 (5679-987 Oe). There are two factors affecting the values of H_c one is the intrinsic factor involving anisotropy field H_a and the second is extrinsic related to morphology. A reduction in the value of H_a can be noted in Table 4.17. H_c directly depends on the value of H_a, hence decrease in the value of H_a reduces H_c. H_a decreases around 26 % for x=0.0 to x=1.0 due to the replacement of Fe^{3+} at octahedral sites. H_c decreases 83 %, while a 26 % decrease in H_a, so another reason for a large reduction in H_c is the large ionic radius of $Co^{2+}(0.745\ Å)$ and $Zn^{2+}(0.74\ Å)$ in comparison to Fe^{3+} (0.645 Å). The morphology of the prepared composites illustrates an increase in grain size as the doping of Co-Zn increases. This also supports the decrease in the H_c as both are inversely related. The composition x=0.0 has a higher grain size in comparison to composition x=0.0 thus having low H_c.

M_r/M_s ratio describes the retention of magnetization after the removal of the field. The range for it is from 0 to 1 and a value less than 0.5 represents randomly oriented multi-domain particles while values higher than 0.5 indicate single-domain. The ratio in composition x=0.0 is 0.53 showing single domain while compositions x=0.6 and 1.0 have less than 0.5 showing multi-domain orientation.

4.4.5 Electromagnetic Characteristics

4.4.5.1 Complex permeability and complex permittivity

Fig 4.78 displayed graphs of $SrCo_xZn_xFe_{12-2x}O_{19}$/PANI composites for ($\varepsilon'$), ($\varepsilon''$), ($\mu'$), ($\mu''$) versus frequency. ε' decreases with the doping of Co-Zn. The loss increases at low frequency but decreases at high frequency. The ε' increases with the increase in frequency. The composition x=1.0 has the lowest value of ε' among all the compositions. There are dual relaxation peaks in ε' one around 9.25 GHz and another at 10.25 GHz in x=0.0. The composition x=1.0 shows a ε' peak at 11.5 GHz. All the compositions show dual relaxation peaks in ε'' plots.

The permeability of the prepared composites varies non-monotonous way with the doping of Co-Zn. The composition x=0.6 has low values of μ' while x=1.0 shows high values as compared to the undoped composition. The x=1.0 has a large relaxation peak

around 10 GHz while x=0.0 has a small peak at 9.5 GHz. μ′ increases with the increase in frequency in all compositions. Composition x=1.0 has the highest μ′ among all the compositions. The compositions x=0.0 and 1.0 show relaxation peaks in μ". The maximum μ" is obtained for composition x=1.0. At the low frequencies, x=0.0 has the highest μ" but with the increase in frequency, it becomes highest in x=1.0.

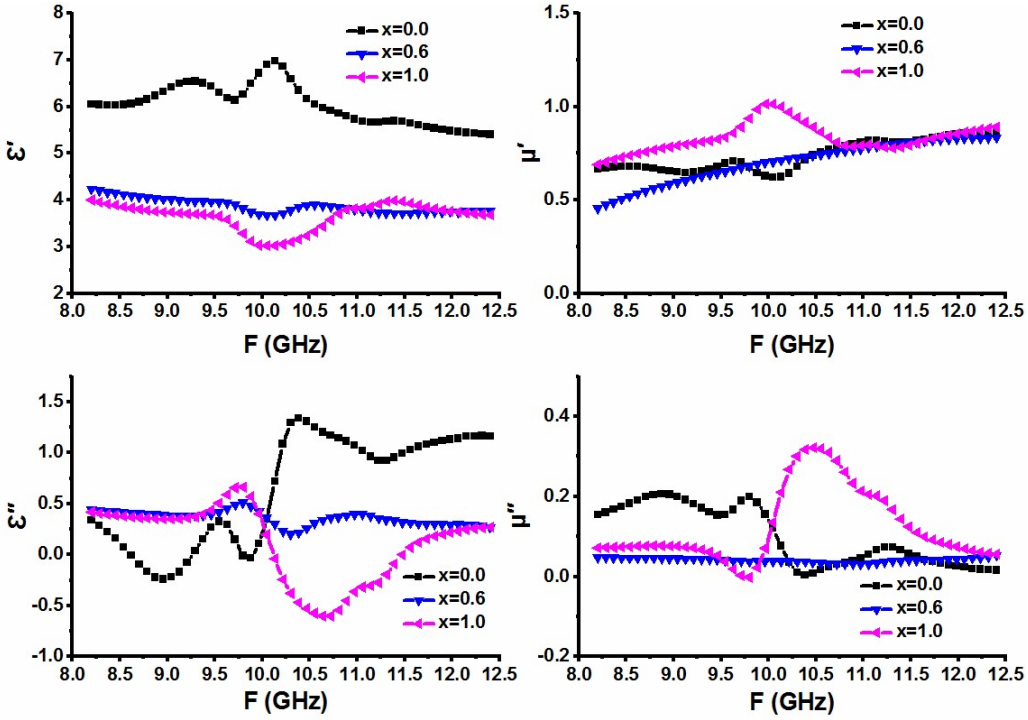

Fig. 4.78 Complex permittivity and permeability versus frequency plots of $SrCo_xZn_xFe_{12-2x}O_{19}$/PANI.

The porosity, grain size distribution, space charge polarization, electron spin, and dipole polarization affect complex permittivity/permeability. The electron hopping in Fe^{2+}/Fe^{3+} promotes dielectric polarization [95]. The polarization is reduced by the large porosity as it obstructs the field flow. The exchange resonance among Fe^{3+}/Fe^{2+} and ferromagnetic resonance affects permeability [96-97]. The doping of Co-Zn decreases the number of Fe^{3+} ions which affects the polarization and resonance. The pores seen in the micrographs of the prepared compositions are non-magnetic voids which affects magnetization/polarization. The inconsistent variation in grain/grain boundary (micrographs Fig. 4.67) also affects permittivity/permeability.

The grain boundaries discourage the field flow while large-size grains support electron hopping. The gathering of charges at grain boundaries promotes polarization while large grains increase electron spin that increases permeability. Magnetic loss between Fe^{3+} and Fe^{2+} is caused by the reduction in exchange resonance due to porosity and small grains. The relaxation peaks in complex permittivity/permeability in the prepared compositions correspond to the dielectric relaxation and ferromagnetic resonance respectively.

4.4.5.2 Microwave absorption in $SrCo_xZn_xFe_{12-2x}O_{19}$/PANI

The absorption characteristics of the prepared composites are investigated by determining the reflection losses. It is calculated from the material's input impedance Z_{in} and impedance of air Z_0 using equations 3.13 and 3.14. The absorption characteristics of $SrCo_xZn_xFe_{12-2x}O_{19}$/PANI composites are analyzed based on the impedance matching, $\lambda/4$, and reflection losses as explained in the following sections.

4.4.5.3 Quarter Wavelength Mechanism

The reflection loss (RL) versus frequency graphs at different simulated thicknesses are used to explain microwave absorption in the prepared ferrite composites. The RL plots of prepared $SrCo_xZn_xFe_{12-2x}O_{19}$/PANI ferrites are shown in Fig. 4.79 (a, c, e, g), 4.80 (a), and 4.81 (a). The different parameters are determined from these. The summarized values of these parameters are listed in Table 4.18.

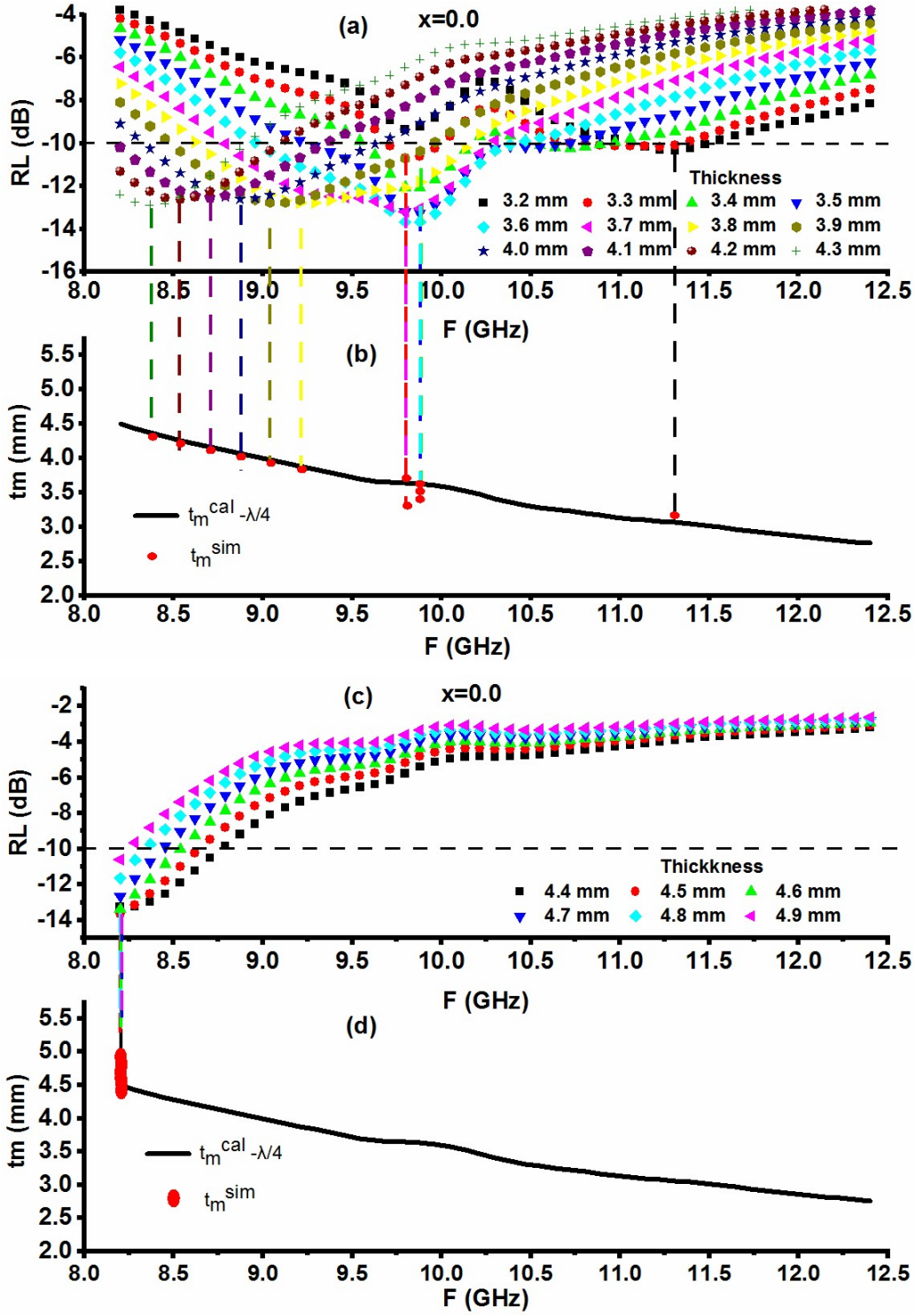
(a)
x=0.0
RL (dB)
F (GHz)
Thickness
3.2 mm
3.3 mm
3.4 mm
3.5 mm
3.6 mm
3.7 mm
3.8 mm
3.9 mm
4.0 mm
4.1 mm
4.2 mm
4.3 mm
(b)
tm (mm)
tm cal -λ/4
tm sim
(c)
x=0.0
Thickkness
4.4 mm
4.5 mm
4.6 mm
4.7 mm
4.8 mm
4.9 mm
(d)

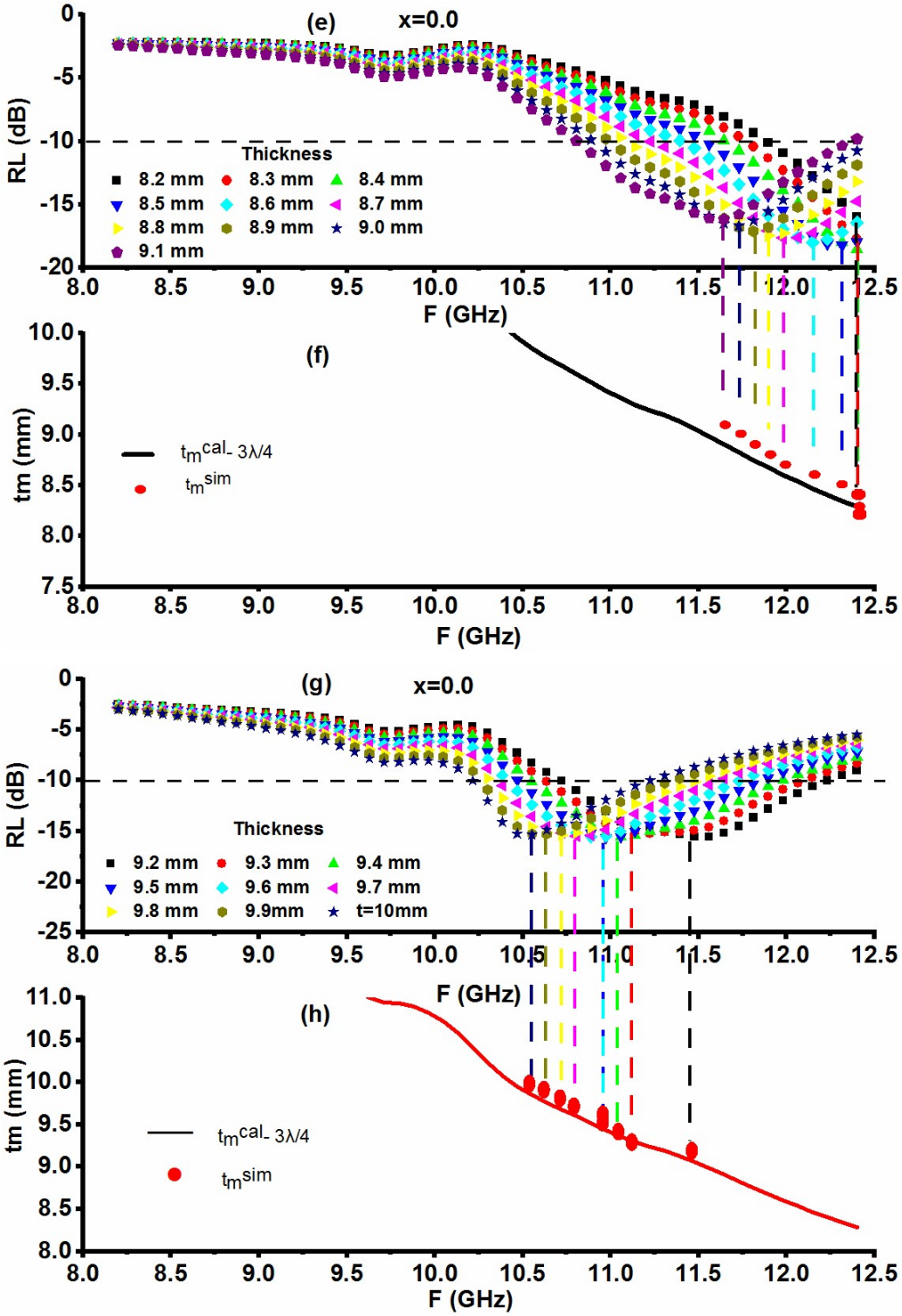

Fig. 4.79 (a, c, e, g) RL versus frequency (b, d, f, h) thickness versus frequency in x=0.0 of $SrCo_xZn_xFe_{12-2x}O_{19}$/PANI.

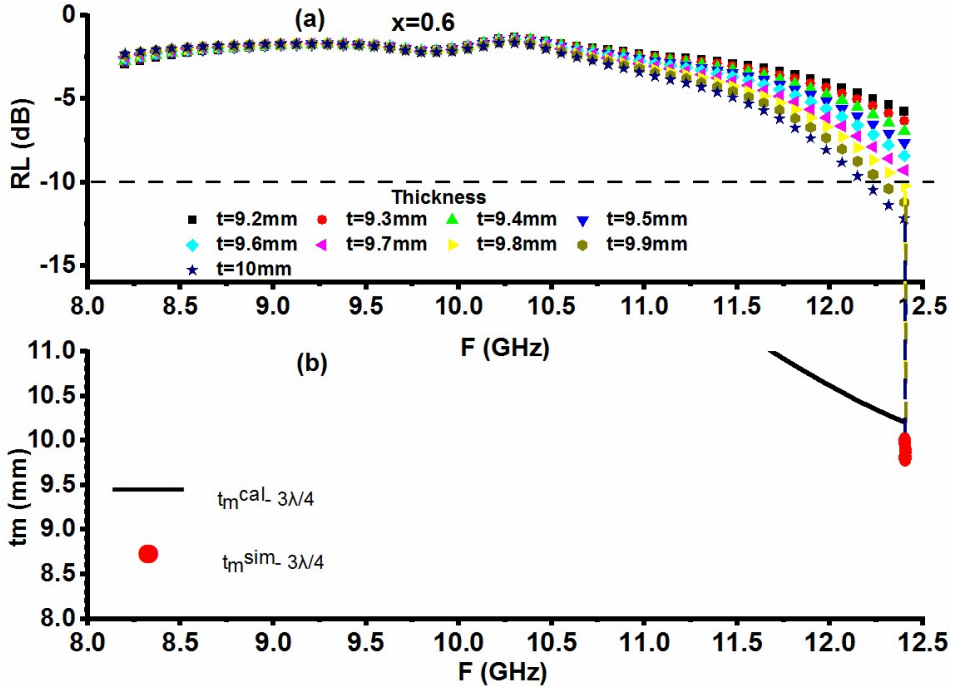

Fig. 4.80 (a) RL versus frequency (b) thickness versus frequency in x=0.6 of $SrCo_xZn_xFe_{12-2x}O_{19}$/PANI.

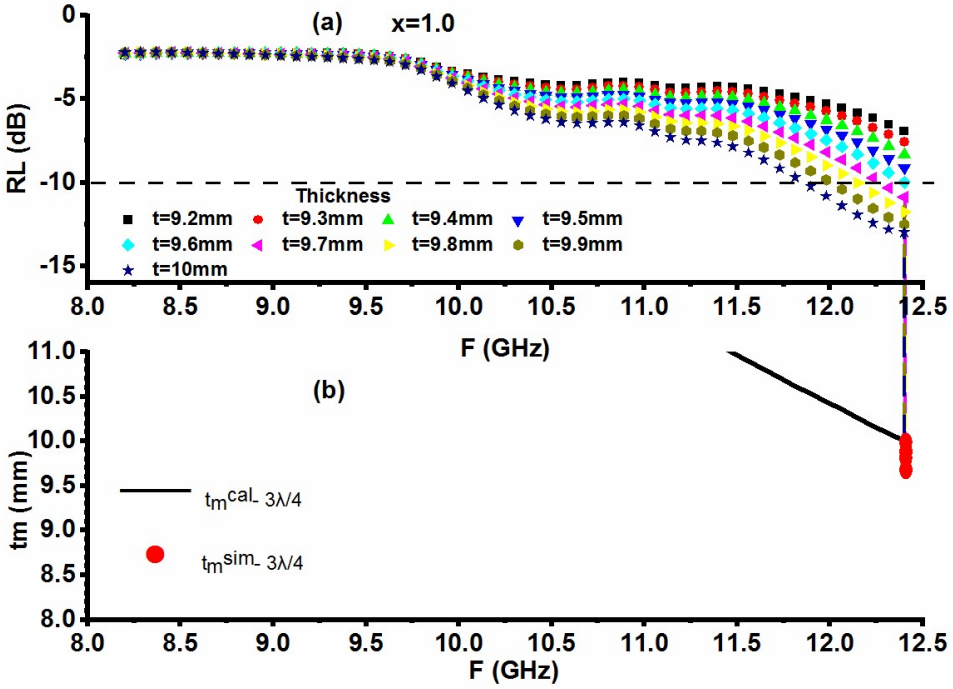

Fig. 4.81 (a) RL versus frequency (b) thickness versus frequency in of $SrCo_xZn_xFe_{12-2x}O_{19}$/PANI.

An RL of -18.53 dB is obtained in composition x=0.0 at a frequency of 12.40 GHz at 8.4 mm thickness. RL ranges between -10.21 dB and -18.53 dB at 12.40 GHz with the thickness of 9.8 and 8.4 mm respectively. RL peak in the composition x=0.0 varies non-monotonically, while in x=0.6 and 1.0 RL increases with an increase of thickness. Reflection loss versus frequency graphs at different thicknesses of x=0.0 are depicted in Fig. 4.79 (a, c, e, g). It is evident that the thickness from 3.2 mm (RL=10.35 dB at 11.31 GHz) to 10.0 mm (-15.35 dB at 11.14 GHz) has a reflection loss ≥ -10 dB. Corresponding to matching frequency the RL peak shifted non-monotonically with the increase in thickness. An RL≥ -20 dB frequency band is obtained at thicknesses of 8.4, 8.5, and 8.8 mm.

Composition x=0.6 has an RL of -12.18 dB at 12.40 GHz for a thickness of 10.0 mm. This composition possesses an RL ≥ -10 dB frequency band ranging from 12.32-12.40 GHz for a thickness from 9.8 to 10.0 mm Fig. 4.80 (a). Corresponding to the matching frequency RL peaks in all the thicknesses are obtained at a matching frequency of 12.40 GHz. The RL peak at 9.9 mm corresponds to a band of 12.32-12.40 GHz, while at 10.0 mm it is obtained comparatively for a high-frequency band ranging from 12.23-12.40 GHz. In the composition x=1.0, maximum RL= -12.97 is obtained at 10.0 mm for a matching frequency of 12.40 GHz Fig. 4.81 (a). The thicknesses from 9.7 mm to 10.0 mm possess *RL* ≥ -10 dB with RL=-10.98 dB at 12.40 GHz and RL=-12.97 dB at 12.40 GHz respectively. The *RL* ≥ -10 dB frequency band ranges from 11.90 GHz to 12.40 GHz. In association with matching frequency, RL peaks at all the thicknesses are obtained at 12.40 GHz. The largest -10 dB frequency band among all the thicknesses in this composition ranging from 11.90-12.40 GHz is obtained at the thickness of 10.0 mm.

To explore the relation between RL and the λ/4 mechanism, simulated thickness (t_m^{sim}) and calculated thickness (t_m^{cal}) are compared. Fig. 4.79 (b, d, f, h), 4.80 (b), and 4.81 (b) show the graphs of the calculated thickness (nλ/4) v/s frequency. For comparison between simulated and calculated thickness lines from RL peaks are brought to the thickness v/s frequency graphs. Composition x=0.0 matches the nλ/4 mechanism for n=1 and 3, while in compositions x=0.6 and 1.0, it is satisfied for n=3. The quarter-wavelength mechanism originates -10 dB bandwidths in all the compositions as given

in Table 4.18. The composition x=0.0 has RL values for both -10/-20 dB at low thicknesses from 3.5 to 9.2 mm. The highest bandwidth of 1.51 GHz associated with a -10 dB band is observed at 9.2 mm. This is obtained for a band of 10.72-12.23 GHz. Besides this, broad bandwidths of 1.43, 1.43, 1.35, 1.34, and 1.26 GHz are also obtained in this composition at the respective thickness of 3.7, 9.0, 3.5, 3.9, and 8.8 mm respectively. A bandwidth of 0.25 GHz at 8.5 mm thickness and 12.32 GHz matching frequency is obtained with RL>-20 dB. Another bandwidth of 170 MHz is also obtained for 8.4 and 8.8 mm.

In composition x=0.6 a -10 dB bandwidth of 170 MHz from 12.23-12.40 GHz is obtained at the thickness of 10.0 mm. The thickness of 9.9 mm possesses a narrow bandwidth of 80 MHz from 12.32-12.40 GHz. x=1.0 possesses its maximum bandwidth of 0.50 GHz for the thickness of 10.0 mm with -10 dB band of 11.90 to 12.40 GHz. On the same note, a bandwidth of 0.34 GHz and 0.25 GHz at thickness of 9.9 mm and 9.7 mm with a frequency band of 12.06-12.40 GHz and 12.32-12.40 GHz are also observed in composition x=1.0.

Table 4.18. RL with matching thickness/frequency, BW, and PBW for $SrCo_xZn_xFe_{12-2x}O_{19}$/PANI.

x	Max. RL (dB)	Matching Thickness (mm)	Matching Frequency (GHz)	-10 dB band (GHz)	-10 dB BW (GHz)	-20 dB band (GHz)	-20 dB BW (GHz)	BTR	PBW (%)
0.0	-13.25	3.5	9.88	9.29-10.64	1.35	-	-	1.171	13.664
	-13.19	3.7	9.80	8.79-10.22	1.43	-	-	1.291	14.592
	-12.77	3.9	9.04	8.54-9.88	1.34	-	-	1.222	14.823
	-18.53	8.4	12.4	11.73-12.40	0.67	12.23-12.40	0.17	0.165	5.403
	-18.19	8.5	12.32	11.56-12.40	0.84	12.15-12.40	0.25	0.207	6.818
	-17.45	8.8	11.90	11.14-12.40	1.26	11.81-11.98	0.17	0.311	10.588
	-16.67	9.0	11.73	10.97-12.40	1.43	-	-	0.350	12.191
	-15.59	9.2	11.48	10.72-12.23	1.51	-	-	0.376	13.153
0.6	-10.21	9.8	12.40	-	-	-	-	0.000	0.000
	-11.21	9.9	12.40	12.32-12.40	0.08	-	-	0.016	0.645
	-12.18	10.0	12.40	12.23-12.40	0.17	-	-	0.034	1.371
1.0	-10.88	9.7	12.40	12.32-12.40	0.08	-	-	0.016	0.645
	-11.75	9.7	12.40	12.15-12.40	0.25	-	-	0.051	2.016

-12.49	9.9	12.40	12.06-12.40	0.34	-	-	0.069	2.742
-12.97	10	12.40	11.90-12.40	0.50	-	-	0.102	4.032

4.4.5.4 Impedance matching mechanism

Since the permittivity/permeability of the material differs from that of the free space there is a difference in the impedance of the material from air. The difference between these two affects the absorption characteristics of the material. The mismatch causes reflection of the major part of the incident signal from the surface of the material and less portion of the signal enters the material. However, if they match major portion of the signal travels into the material and gets absorbed by the material. Hence it becomes necessary to analyze the impedance matching mechanism for the development of an effective absorber.

The reflection loss and impedance i.e. $|Z_{in}|$ versus frequency plots for the prepared composites are displayed in Fig. 4.82. Table 4.19 enlists the values of Z_{in} for the different compositions. Composition x=0.0 follows the impedance matching for the highest RL peak while there are deviations in x=0.6 and 1.0. x=0.0 has an RL peak of -18.53 dB with 12.40 GHz for 8.4 mm with a corresponding value of Z_{in}=298.88 Ω which is in proximity to Z_o=377 Ω. In composition x=0.6 there is a problem with $|Z_{in}|$ as there is a RL peak of -12.18 dB at 12.40 GHz with Z_{in}=552.95 Ω while there is no RL peak RL=-6.75 dB at 11.81 GHz with a Z_{in}=367.25 Ω which is more close to Z_o=377 Ω than Z_{in}=552.95 Ω. Similarly at 11.90 GHz a low RL=-7.35 dB with Z_{in}=397.26 Ω is observed which is also closer to Z_o=377 Ω than Z_{in}=552.95 Ω. A similar situation occurs in x=1.0 at 11.73 GHz where low RL of -9.16 dB with Z_{in}=379.77 Ω is observed while a RL peak of RL= -12.97 dB with Z_{in}=593.72 Ω at 12.40 GHz is obtained.

This type of behavior is due to the complex nature of $|Z_{in}|$ involving real and imaginary terms Z_{real} and Z_{img}. Hence, Z_{real} and Z_{img} are determined and graphs of Z_{real} and Z_{img} are plotted as given in Fig. 4.83. The respective values of Z_{real} and Z_{img} are listed in Table 4.19. For the successful implementation of impedance matching the material's impedances shall follow exactly/nearly the criteria of 377 Ω and/or 0. Table 4.19 indicates that the highest *RL* value of -18.53 dB at 12.40 GHz obtained in x=0.0 follows this condition Z_{real}=298.47 Ω and Z_{img}=15.55 Ω which are close to 377 Ω and

0. Low RL=-6.75 dB at 11.81 GHz with a Z_{in}=367.25 Ω in composition x=0.6 is due to Z_{real}=239.23 Ω and Z_{img}=278.64 Ω which are far away from the required criteria. In the same way at 11.90 GHz a low RL=-7.35 dB with Z_{in}=397.26 Ω correspond to Z_{real}=274.66 Ω and Z_{img}=287.0 Ω. For composition x=1.0 low RL of -9.16 dB at 11.73 GHz with Z_{in}=379.77 Ω is due to Z_{real}=297.57 Ω and Z_{img}=235.96 Ω, while RL=-12.97 dB with Z_{in}=593.72 Ω at 12.40 GHz correspond to Z_{real}=593.04 Ω and Z_{img}=28.34 Ω

Thus it can be summarized that the discrepancies observed in x=0.6 and x=1.0 are due to the mismatch in obtained Z_{real}/Z_{img} values from the required Z_{real}/Z_{img} values of 377 Ω and/or zero. There is an increase in input impedance Z_{in} (Z_{real} and Z_{img}) with the doping of Co-Zn.

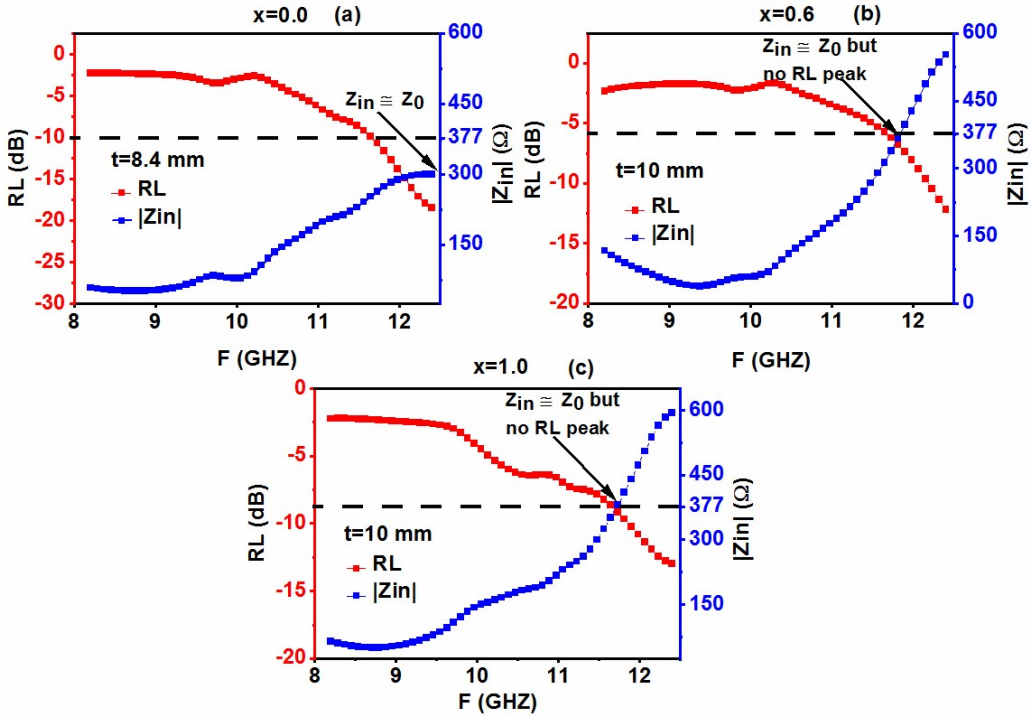

Fig. 4.82 Z_{in} and RL curve against frequency for $SrCo_xZn_xFe_{12-2x}O_{19}$/PANI.

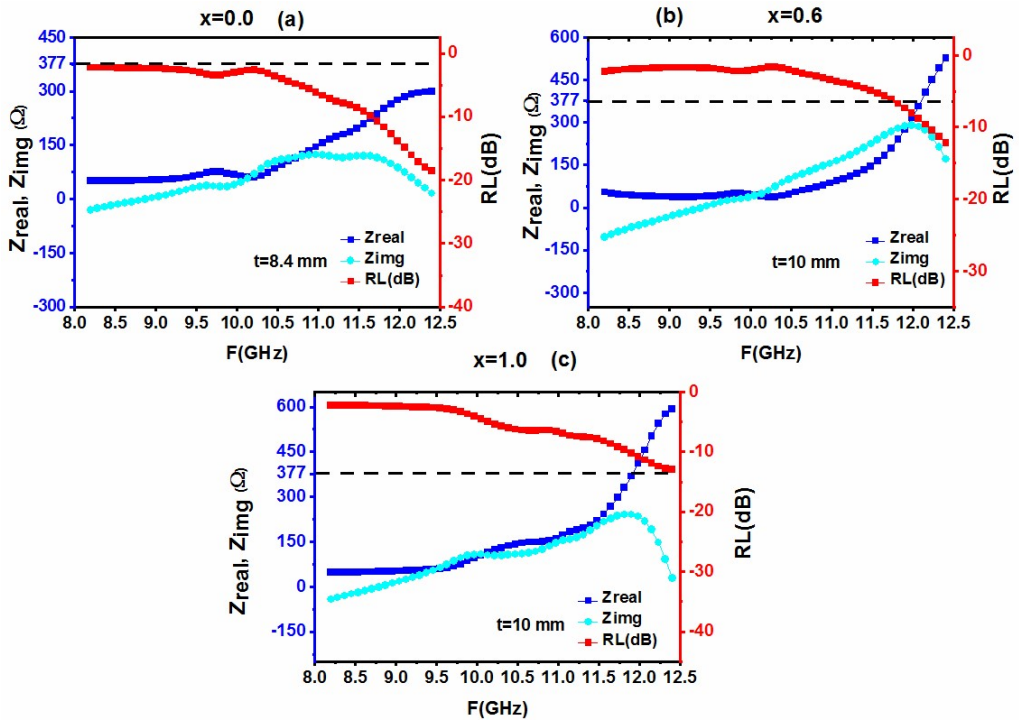

Fig. 4.83 Z_{real}, Z_{imag}, and RL v/s frequency for $SrCo_xZn_xFe_{12-2x}O_{19}$/PANI.

Table 4.19. Z_{in}, Z_{real}, and Z_{imag} values corresponding to RL_{max} for $SrCo_xZn_xFe_{12-2x}O_{19}$/PANI.

x	RL (dB)	Matching Thickness (mm)	Matching Frequency (GHz)	$\|Z_{in}\|$ (Ω)	Z_{real} (Ω)	Z_{img} (Ω)
0.0	-18.53	8.4	12.40	298.88	298.47	15.55
0.6	-12.18	10	12.40	552.95	526.15	170.03
1.0	-12.97	10	12.40	593.72	593.04	28.35

4.4.4.5 Role of Electromagnetic/Material Parameters

The λ/4 and impedance matching have been discussed but due to the complex nature of permittivity/permeability (ε'') and (μ'') also contribute to the absorption which should also be analyzed.

The peaking nature of ε″ and μ" in the prepared composites is also contributing to the absorption: in x=0.0 an RL =-12.57 dB at 9.54 GHz for 3.7 mm corresponds to ε″ peak at 9.54 GHz, for composition x=1.0, the maximum *RL*=-12.97 dB at 12.40 GHz with the thickness of 10.0 mm correspond to ε″ peak at 12.40 GHz; *RL*=-13.25 at 3.5 mm to μ" peak at 9.88 GHz in x=0.0; the maxima in μ' at 12.40 GHz attribute to the maximum RL=-12.18 dB in composition x=0.6. Thus dielectric and magnetic losses are also contributing to absorption.

4.4.5.6 Eddy Current Loss

In ferrites, the eddy current loss has an impact on absorption characteristics in the form of magnetic loss. The formula used to determine the eddy current loss is given as in equation 4.4.

If C_0 has a constant value with the frequency increment, there is a contribution of the eddy current loss. Hence plot of C_0 versus frequency is drawn and demonstrated in Fig. 4.84. The plots indicate a flat line in all the compositions showing constant values of C_0 against the increase in frequency which indicates the eddy current loss has contributed to the absorption of ferrite composites.

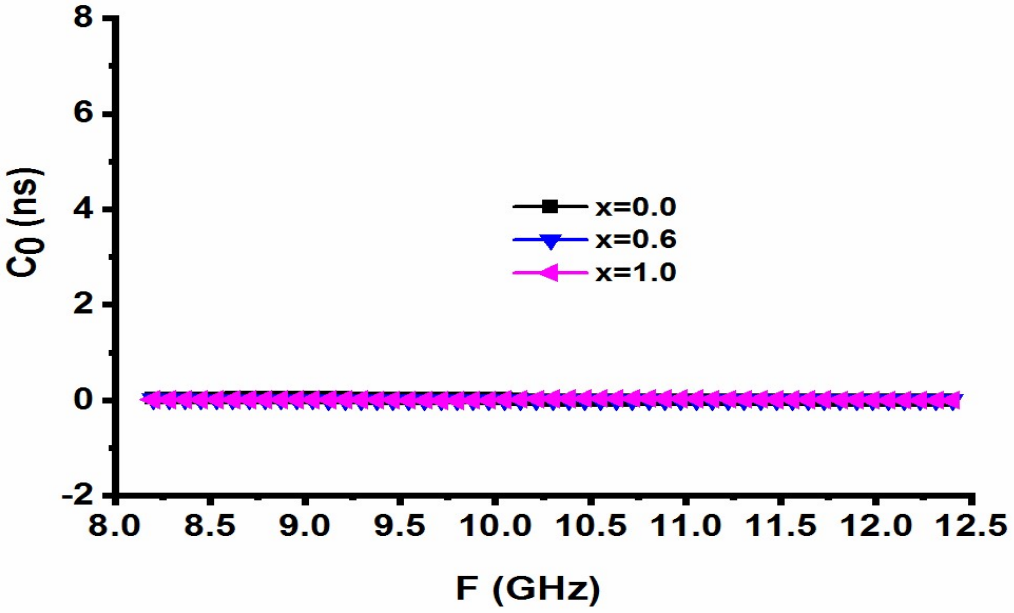

Fig. 4.84 C_0 versus frequency curve for $SrCo_xZn_xFe_{12-2x}O_{19}$/PANI.

4.4.5.7 Bandwidth to Thickness Ratio

The broad bandwidths with less thickness are an important factor in the design and characterization of an absorber besides the RL≥-10 dB. With the achievement of the desired RL≥-10 dB benchmark, one should target achieving low thicknesses, rather than only an increase in RL. Due to this factor bandwidth to thickness ratio (BTR) and percentage bandwidth (PBW) are determined as given in Eq 4.5 and 4.6.

Table 4.19 indicates that the doping of Co-Zn in PANI composites reduced BTR. The x=0.0 owen the highest BTR of 1.291 at 9.80 GHz with RL=-13.19 dB. Besides this, this composition also has a high BTR of 1.222 at 9.04 GHz with RL=-12.77 dB and 1.171 at 9.88 GHz with RL=-13.25 dB. The composition x=0.6 has BTR=0.034 at a frequency of 12.40 GHz for RL= -12.18 dB. In the composition x=1.0, a BTR of 0.102 and 0.069 are obtained at 10.0 mm and 9.9 mm. The percentage bandwidth also decreases with the doping increment for Co-Zn. The composition x=0.0 has the highest PBW=14.823 at 3.9 mm. Also high PBW=14.592. 13.664, and 13.153 are observed at 3.7, 3.5, and 9.2 mm. The composition x=0.6 possesses a PBW of 1.371 at 10.0 mm, however, the composition x=1.0 has a comparatively high PBW of 4.032 at 10.0 mm.

4.5 $SrCo_xNi_xFe_{12-2x}O_{19}$/PANI composites

4.5.1 Microstructural/Morphological Characteristics

To study the microstructure/morphology of $SrCo_xNi_xFe_{12-2x}O_{19}$/PANI composites SEM is carried out. The micrographs of $SrCo_xNi_xFe_{12-2x}O_{19}$/PANI (x=0.0, 0.6, and 1.0) composites are shown in Fig. 4.85. The doping of Co^{2+} and Ni^{2+} has affected the grain distribution and agglomeration of grains can be seen in the micrographs.

The grain size has been increased with the doping of Co-Ni as composition x=1.0 possesses large grains. The composition x=0.0 has a significantly small size of grains hence increasing the number of grain boundaries as compared to other compositions. The small pores at grain boundaries promote polarization and affect the electrical properties. The composition x=0.6 shows the formation of large grain clusters as well as small grain.

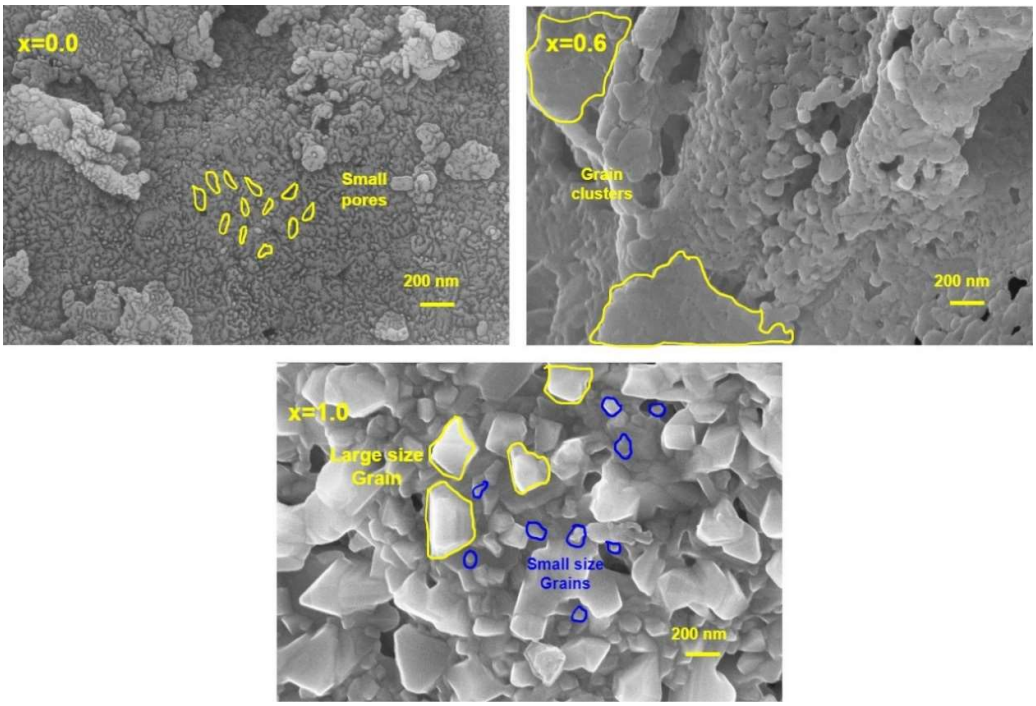

Fig. 4.85 SEM images of $SrCo_xNi_xFe_{12-2x}O_{19}$/PANI composites.

4.5.2 Electrical Characteristics

4.5.2.1. Dielectric constant

Ferrites have permittivity in a complex number where its real part (ε') indicates its charge storage capacity, while the imaginary part (ε'') shows the loss capabilities. The formula to determine the real part is shown in equation (3.5). Dielectric loss ε'' is calculated using equation (3.6), while the loss tangent ($tan\delta$) can be determined by equation (3.7) as given in Chapter 3

Fig 4.86 depicts the plot of ε' and ε'' versus frequency of the $SrCo_xNi_xFe_{12-2x}O_{19}$/PANI composites. From the figures, it is noticed that the dielectric constant/loss has increased significantly as compared to the pure ferrites ($SrCo_xNi_xFe_{12-2x}O_{19}$). This increase is because the PANI is a dielectric material and has a large dielectric constant which has enhanced the dielectric constant/loss of the composites. There is a gradual decay in ε' with the increment in frequency. In low-frequency region ε' has high values and acquires constant values after a decrease for the high-frequency regime following the Maxwell-Wagner model. A non-monotonic variation in ε' with the doping of Co-Ni is noticed.

The composition x=1.0 have the maximum ε' while composition x=0.6 possesses the least value. A similar trend can be seen in the plots of ε'' as given in Fig. 4.86 (b).

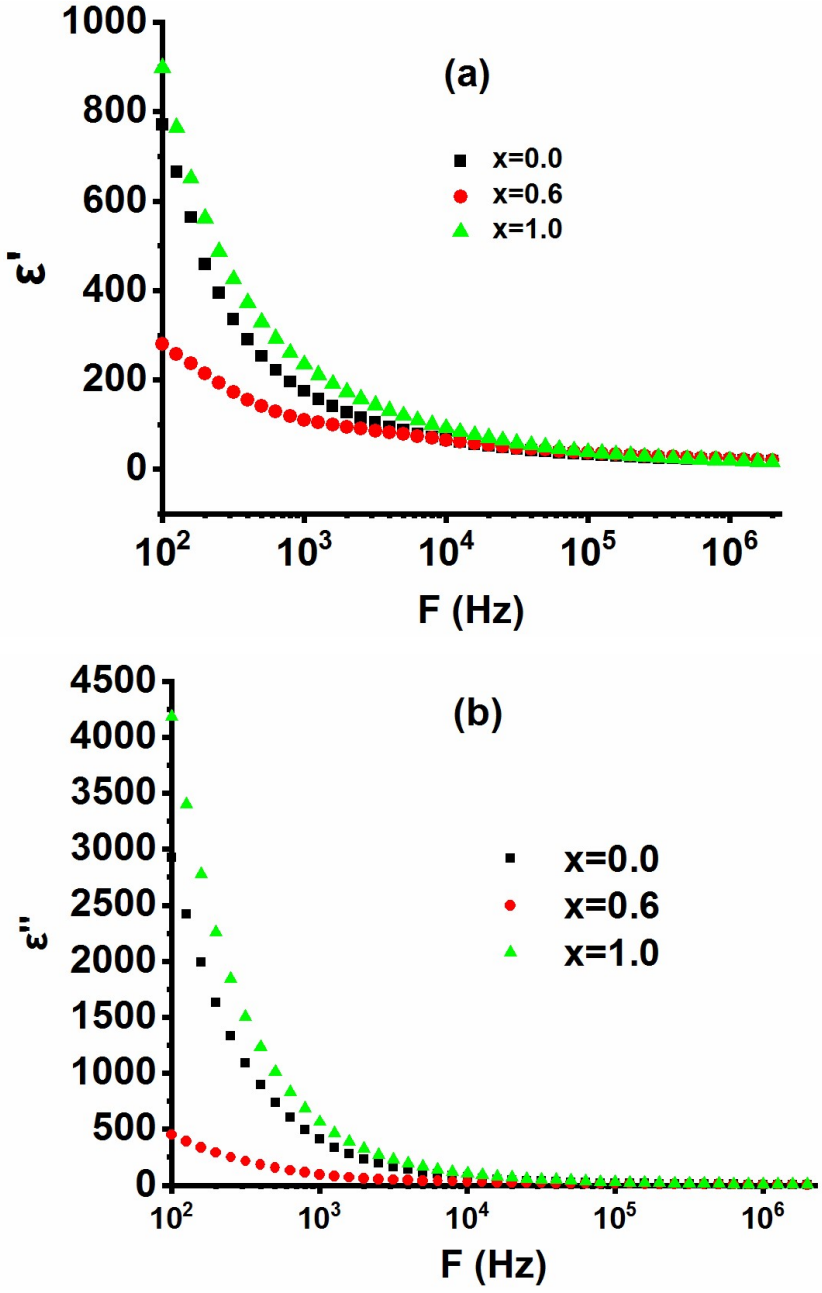

Fig. 4.86. Dielectric constant (a) real (b) imaginary versus frequency for $SrCo_xNi_xFe_{12-2x}O_{19}$/PANI.

The plots of loss tangent (tanδ) v/s frequency of the composites are demonstrated in Fig. 4.87. The loss tangent showed a gradual decrease with the increase in frequency.

This behavior is associated with the Maxwell-Wagner model [80]. Here is a non-monotonical variation in the values of tanδ with the doping of Co-Ni. The maximum tanδ is obtained for the composition x=1.0 while x=0.6 possesses the least values of tanδ.

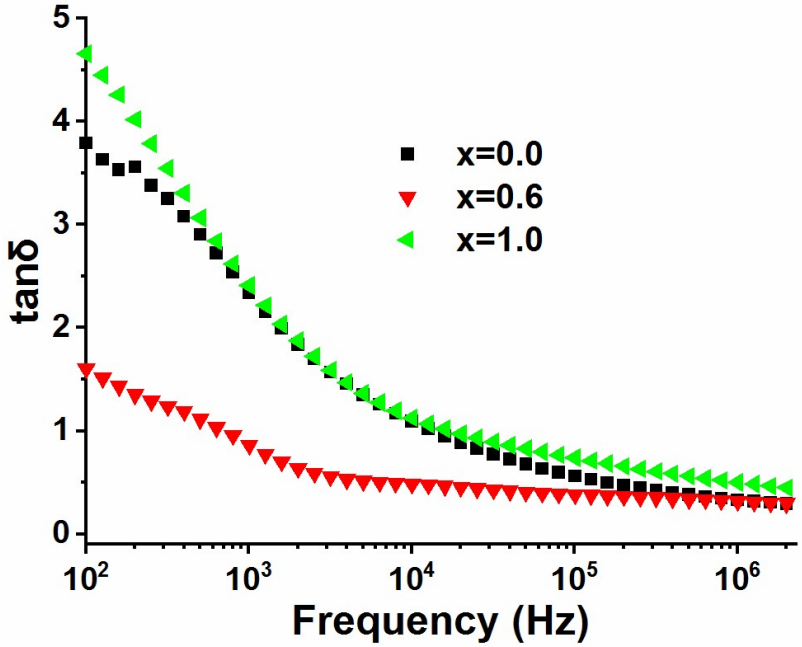

Fig. 4.87 Plots of loss tangent of $SrCo_xNi_xFe_{12-2x}O_{19}$/PANI composites.

4.5.2.2 Electric modulus

Fig. 4.88 (a) and (b) display the variation of M′ and M″ versus frequency for the prepared composites respectively. M′ owes low values at low frequency and increases with the frequency increment. The increase in M′ for the low-frequency region is associated with the charge carrier's short-range mobility while a saturation in M′ signifies the long-range mobility. The inclusion of PANI and Co-Ni content causes a non-monotonical variation in the value of M′. All three compositions have approximately equal values at higher frequencies while at low frequencies there is a change in the values of M′.

The conductivity relaxation is described with the help of M″ versus frequency plot. The asymmetric peaks in M″ represent the conductivity relaxation mechanism. The low-frequency side of the peak denotes the long-distance movement while the high-frequency depicts localized motion only. The values of M″ vary non-monotonically

with the doping of Co-Ni. The height of M″ increases in the composition x=1.0 which represents the increase in relaxation time. The broadening of relaxation peaks can be noticed with the increase in doping level.

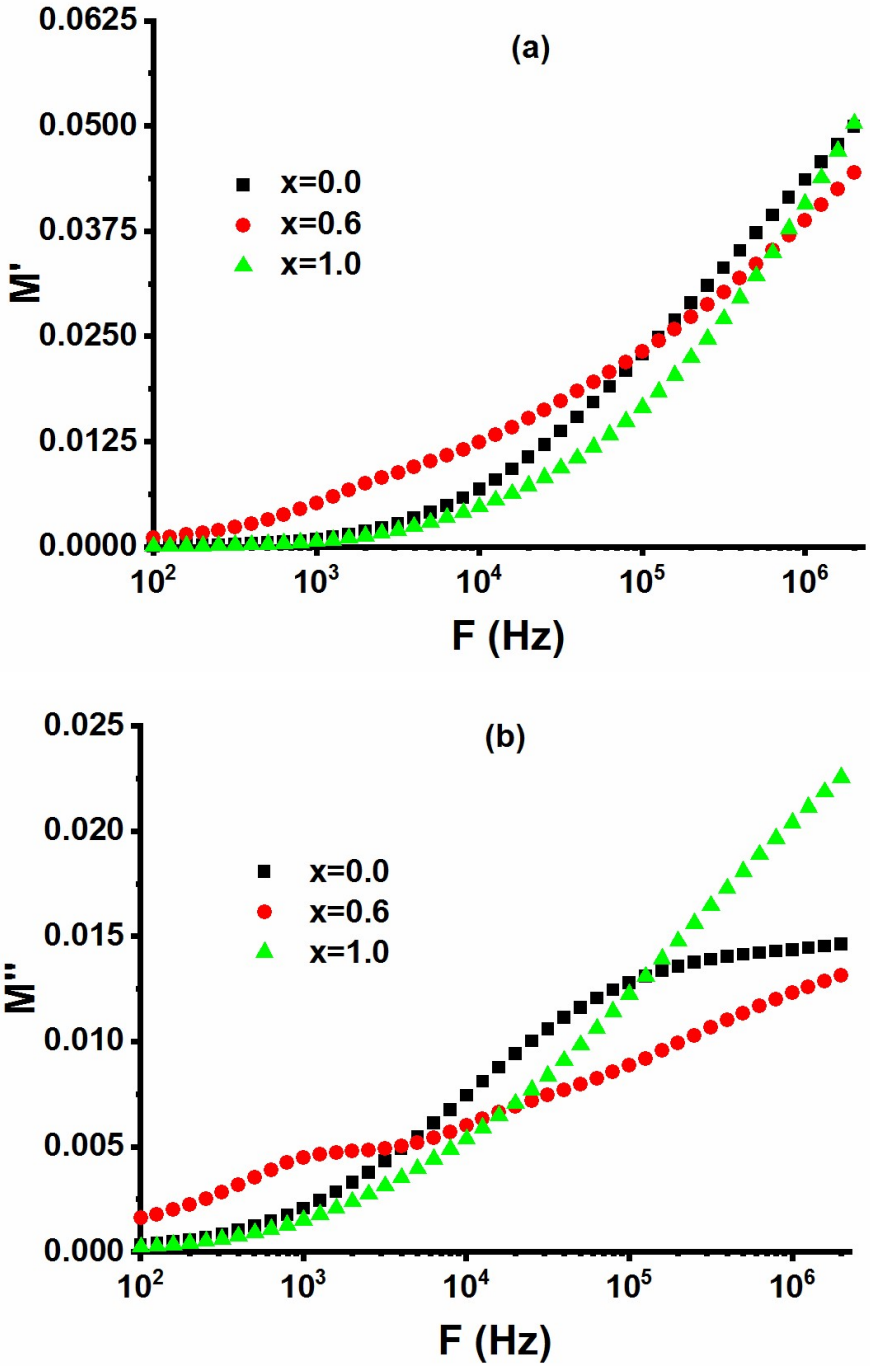

Fig 4.88 M′ and M″ curves against frequency for $SrCo_xNi_xFe_{12-2x}O_{19}$/PANI.

Cole-Cole graph ($M''v/s\ M'$) of $SrCo_xNi_xFe_{12-2x}O_{19}$/PANI is displayed in Fig 4.89. The plots of all the composites show asymmetric deformed semicircles with their center deviating from the x-axis attributing a non-Debye relaxation. Co-Ni doping has a non-monotonous change in the height of the semicircles. The semicircle of x=0.0 lies approximately equal in the low and high-frequency regions. This indicates the role of both grain and grain boundaries in charge transport. A semicircle of composition x=1.0 is more towards the high-frequency region attributing that grains are more dominant in the charge transport mechanism. The composition x=0.6 shows dual semicircles which is due to the morphology: The composition x=0.6 has large grain clusters as well as well-connected small grains. The composition x=0.6 has a major portion in the low frequency area signifying that grain boundaries are prominent in that case.

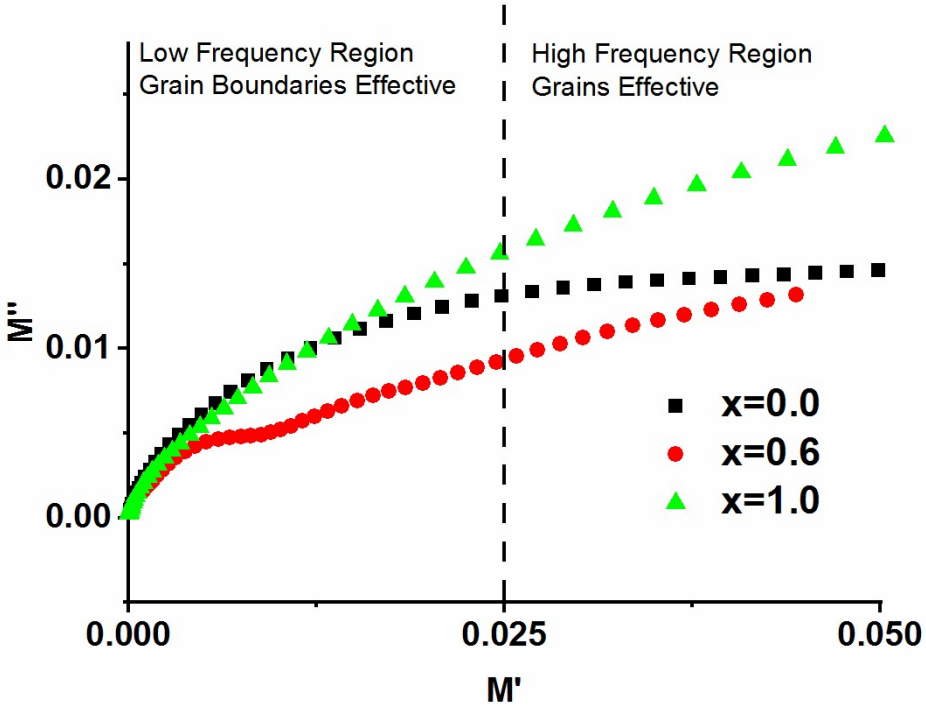

Fig. 4.89 Cole-Cole plot of M′ v/s M″ for $SrCo_xNi_xFe_{12-2x}O_{19}$/PANI.

4.5.2.3 Complex Impedance Spectra

Fig. 4.90 (a) depicts the plot of Z′ versus frequency. The curve of Z′ decreases with frequency and becomes constant thereafter. This dispersion in Z′ follows the Maxwell-Wagner model. A non-monotonical change is present in Z′as the doping level of Co-Ni increases. The composition x=0.6 possesses the highest value of Z′while there is a

decrement in the case of x=1.0. The micrograph of composition x=1.0 has well-connected large fused grains causing improvement in the inter-grain connectivity which reduces the resistance. The composition x=0.6 has porosity causing an impediment to the charge flow and enhancing the resistivity.

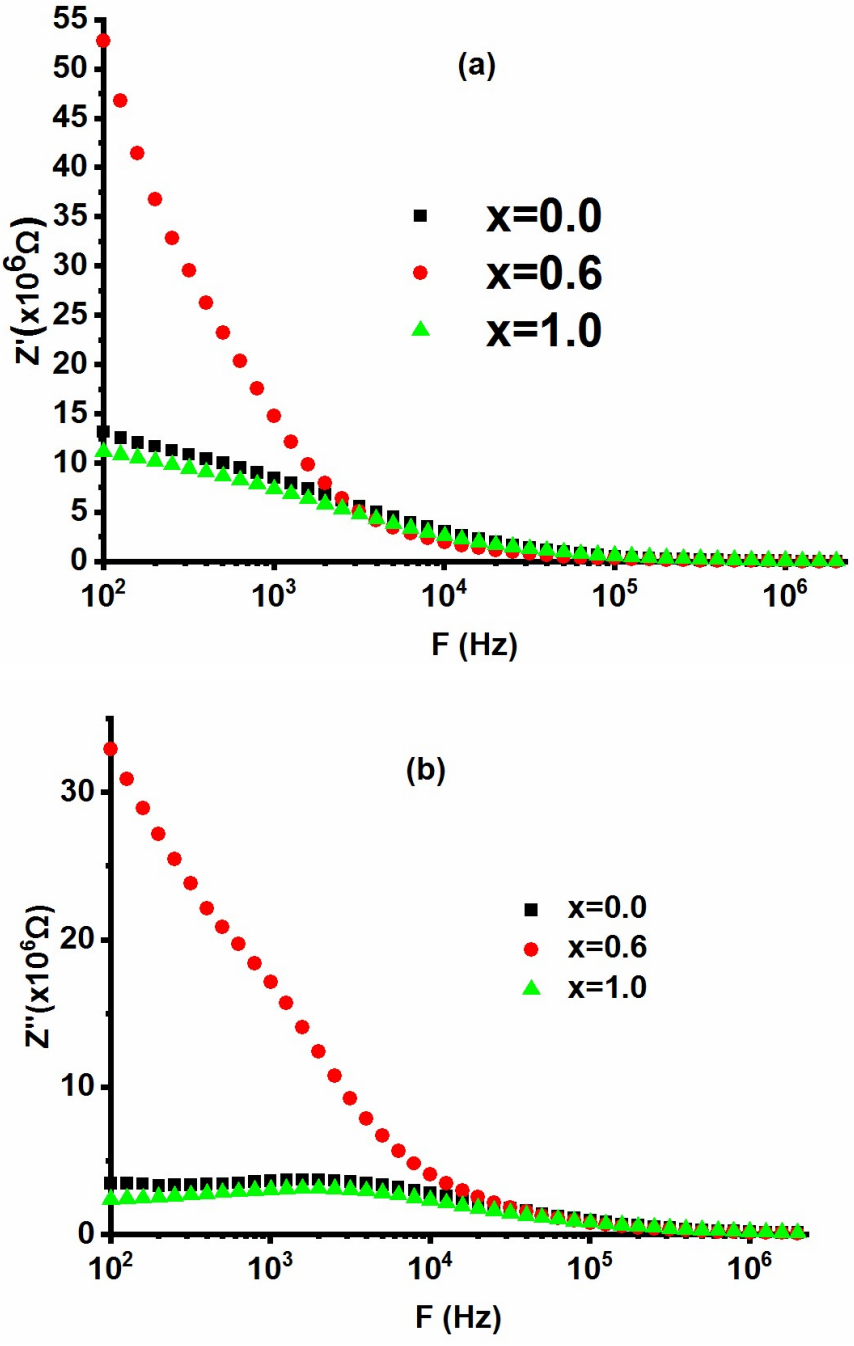

Fig. 4.90 Z′ and Z″ versus frequency plots for $SrCo_xNi_xFe_{12-2x}O_{19}$/PANI.

Fig. 4.90 (b) shows the graphs of Z''against frequency. Z''possesses high values at low frequency while having a decrement with the frequency increment. At low frequencies Z''changes non-monotonically with doping of Co-Ni. This is because of a variation in space charge polarization with the inclusion of Co-Ni. Asymmetric peaks can be viewed in the plots of compositions x=0.0 and 1.0. These peaks are associated with dielectric relaxation.

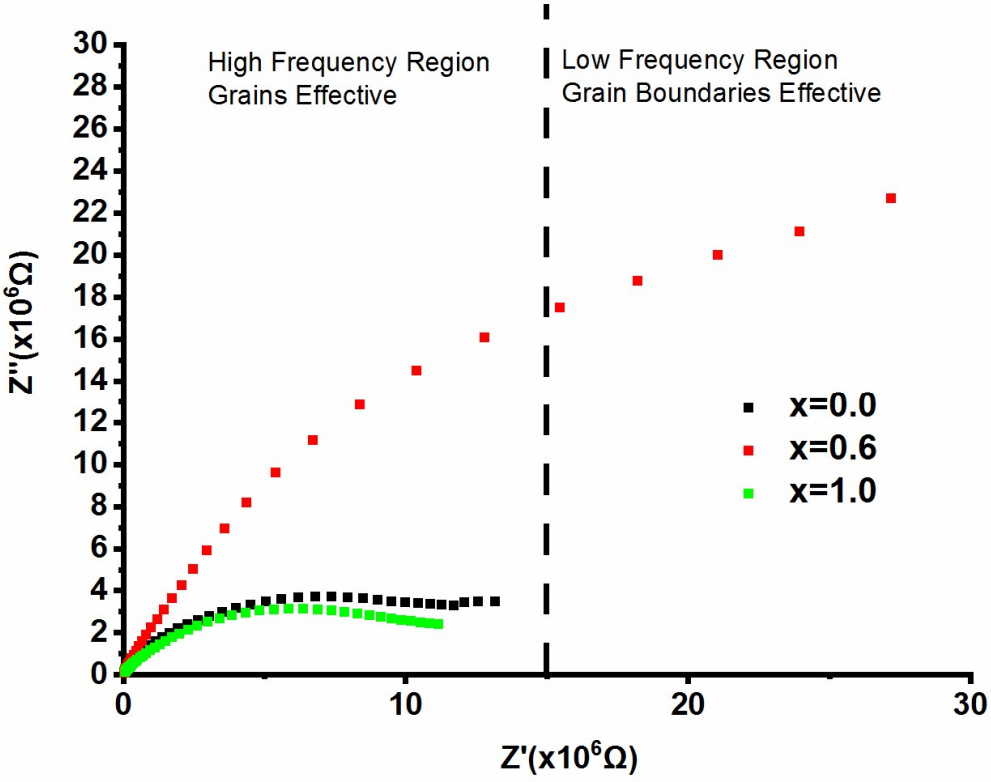

Fig. 4.91. Cole-Cole plots (Z''v/s Z') for $SrCo_xNi_xFe_{12-2x}O_{19}$/PANI.

Fig. 4.91 demonstrate the Cole-Cole plots (Z''versus Z') for prepared composites. All the compositions consist of deformed semicircles that comply with the non-Debye relaxation. The inclusion of Co-Ni has a non-monotonical variation in the height of the semicircle. The height of the semicircle increases in the case of x=0.6 while it decreases in x=1.0. The reason behind it is the morphological difference between these two compositions. The composition x=1.0 has large and connected grains while x=0.6 has porosity in between the grain structure. The composition x=0.6 shows a semicircle in the middle of the frequency band thus owing to the role of both grain as well as grain

boundary. The plots for x=0.0 and 1.0 lie completely in a high frequency area attributing the dominance of grains.

4.5.2.4 AC Conductivity

A plot of ac conductivity **(σ_{ac})** against frequency of the $SrCo_xNi_xFe_{12-2x}O_{19}$/PANI composites is displayed in Fig. 4.92. It can be noted that the conductivity of PANI composites has been increased due to the inclusion of PANI in the ferrites as the conductivity of the composites is much higher than that of the pure ferrites. Initially, the conductivity is low but starts increasing after the hopping frequency. This frequency shows the transition from the flat plateau region of dc conductivity **(σ_{dc})** to the dispersive region of ac conductivity **(σ_{ac})**. There is an increase in the value of σ_{ac} of the composites with the increase in doping of Co-Ni. The composition x=1.0 has the maximum value of conductivity. The morphology of the composition x=1.0 is the reason behind this. The composition x=1.0 has well-connected large as well as small grains enhancing the conductivity.

The ac conductivity curves are fitted according to the Jonscher power law as explained in Chapter 3 is used to explain the frequency dependence behavior of ac conductivity. By fitting the curves, values of n were calculated for the prepared composites. The determined values are 0.562, 0.711, and 0.526. According to Funke $n<1$ shows the motion with sudden hoping. The values are less than 1 which signifies that ac conductivity follows the hopping mechanism.

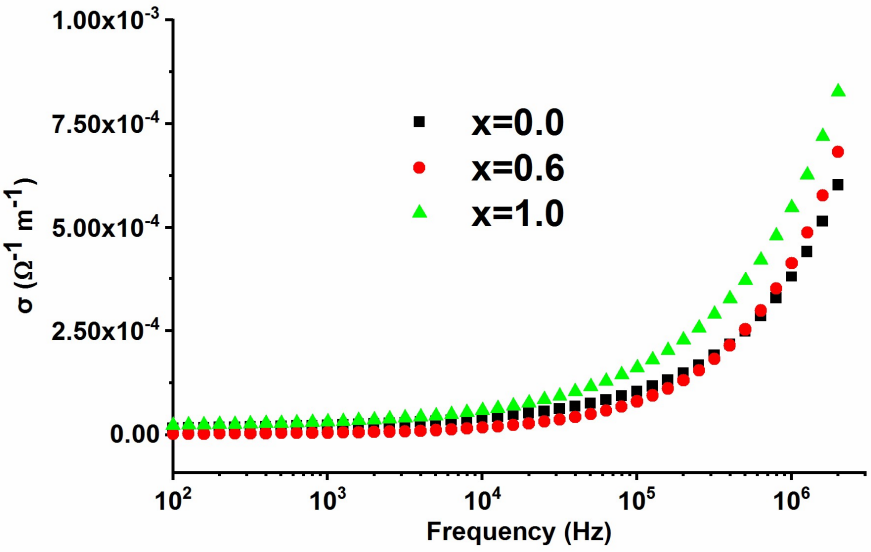

Fig. 4.92. AC conductivity for $SrCo_xNi_xFe_{12-2x}O_{19}$/PANI.

4.5.2.5 Software-based Impedance Simulation

Impedance spectroscopy has been done using Electrochemical Impedance Spectroscopy (EIS) software. The fitting using EIS software is shown in Fig. 4.93. The simulated parameters for grain and grain boundaries are given in Table 4.20.

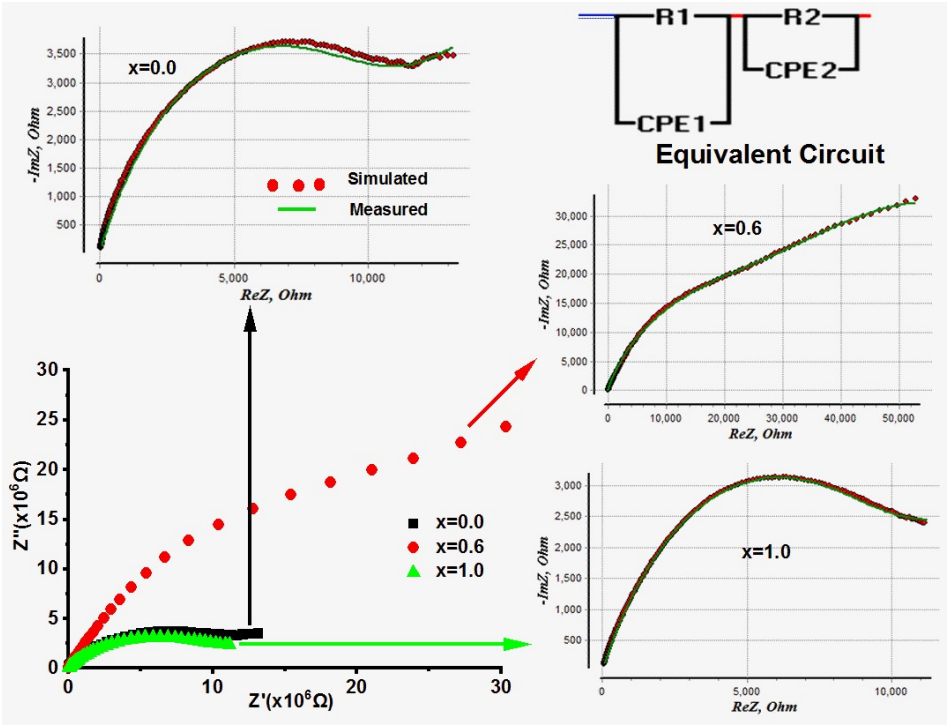

Fig. 4.93 Fitting of Impedance curves using EIS for $SrCo_xNi_xFe_{12-2x}O_{19}$/PANI.

Table 4.20. Simulated parameters derived from EIS software for $SrCo_xNi_xFe_{12-2x}O_{19}$/PANI.

x	R_g (MΩ)	R_{gb} (MΩ)	C_g (μF)	C_{gb} (μF)
0.0	10.68	16.78	4957.4	$9.41x10^6$
0.6	53.73	38.28	41.83	240.81
1.0	10.32	9.05	22357.6	$45.48x10^6$

Correlation between Grain/Grain boundaries simulated parameters and Morphology

The composition x=1.0 has large and well-connected fused grains enhancing grain boundaries as seen in the micrograph of Fig. 4.85 This causes polarization at the grain and grain boundaries that in turn causes the capacitance of grain and grain boundaries to be high. From Table 4.20 it is evident that the simulated grain/grain boundary capacitances C_g=22357.6 μF and C_{gb}=45.8 x 10^6 μF are high. Composition x=0.0 has small pores which causes polarization at grain boundaries causing high grain boundaries capacitance C_{gb}=9.41 x 10^6 μF.

Correlation between Grain/Grain boundaries simulated parameters and Dielectric Parameters

The composition x=0.6 has the lowest while x=1.0 owes the highest ε' (Fig. 4.86). Maxwell-Wagner model suggests that a grain boundary is dominant at low frequency, while the grain is at high frequency. Table 4.20 shows that the composition x=0.6 has the minimum grain boundary capacitance C_{gb}= 240.81 μF due to the lowest dielectric constant. (ε'=280.71). The highest dielectric constant (ε'=898.76) in x=1.0 attributing to the highest simulated grain boundary capacitance C_{gb}=45.8 x 10^6 μF referring to a high polarization due to grain boundaries.

Correlation between Grain/Grain boundaries simulated parameters and Electric Modulus

The composition x=0.0 has the role of grains, as well as grain boundaries as the semi-circle of this composition, lies in the mid-frequency region (Fig. 4.89). The curve of compositions x=1.0 is more towards the high-frequency region as compared to x=0.0. Table 4.20 validates this behavior attributing the high values of grain/grain boundary capacitances in composition x=0.0 and 1.0. The composition x=0.6 shows more portion in low-frequency region attributing to dominance of grain boundaries which can be validated by the high value of C_{gb}=240.81 µF as compared to C_g=41.83 µF.

4.5.3 Band gap Characteristics

Fig. 4.94 demonstrates the Tauc plots drawn for the prepared $SrCo_xNi_xFe_{12-2x}O_{19}$/PANI. Equation 3.4 as given in Chapter 3 is utilized to achieve the required values of band gaps. An intercept on the x-axis from the linear region of the Tauc plot provides the value of the band gap. The band gaps of the compositions x=0.0, 0.6, and 1.0 are 2.15, 1.54, and 1.39 eV respectively.

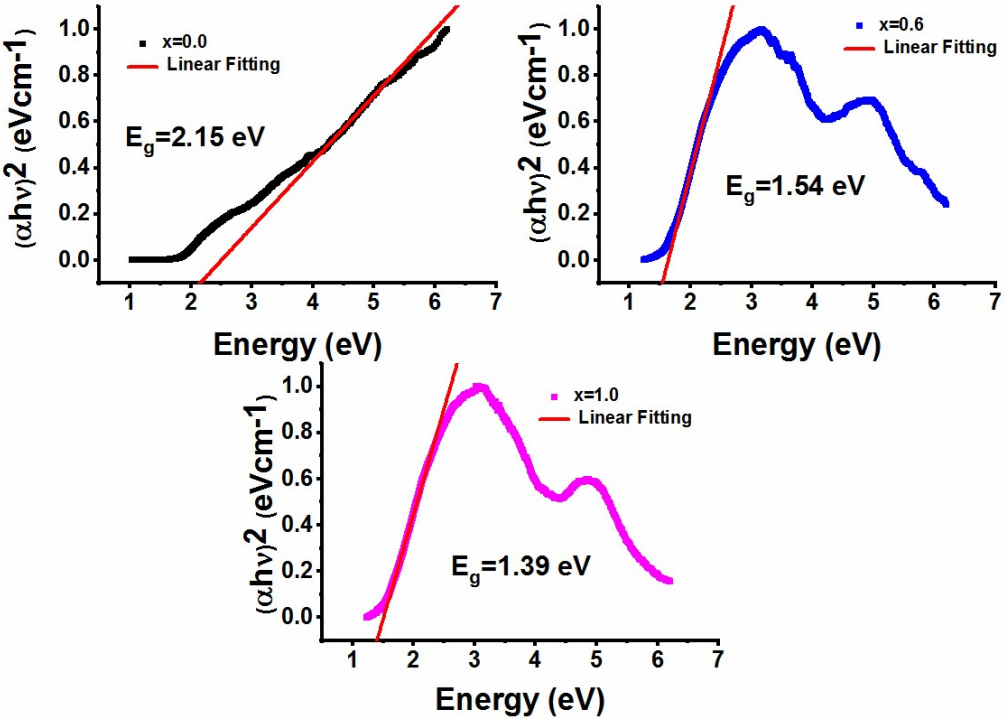

Fig. 4.94 Tauc plots of $SrCo_xNi_xFe_{12-2x}O_{19}$/PANI

4.5.4 Magnetic Characteristics

The magnetic characteristics of $SrCo_xNi_xFe_{12-2x}O_{19}$/PANI composites are investigated with the help of magnetization (M) versus magnetic field (H) curves. Fig. 4.95 (a). demonstrate the plots drawn for all compositions. It can be noted that the site occupancy of the ions is dependent on the electronegativity of the ions. The ions with electronegativity prefer octahedral sites than the tetrahedral ones. The electronegativity of Ni^{2+}(1.91) is higher than that of Co^{2+}(1.88) hence they will tend to occupy the octahedral sites $4f_2(\downarrow)$. Based on the ligand field theory Ni^{2+}due to $3d^8$ configuration and Co^{2+} with $3d^7$preferably choose octahedral sites $12k(\uparrow), 2a(\uparrow), 4f_2(\downarrow)$. It is reported by Karim et al. [105] that Ni^{2+}prefer octahedral $4f_2$ sites while Thakur et al. [111] reported that Co^{2+} also prefer to occupy octahedral sites.

In the M-H loops shown in Fig. 4.95 (a) a steep rise in magnetization at the low is observed that decays for the high fields. In undoped composition x=0.0, there is a large slope at high fields indicating the unsaturated state which gets reduced with the substitution of Ni^{2+} and Co^{2+}. The reduction in the anisotropy field is the reason behind it. Above 10 KOe a linear curve is present in the plots, hence A/H and χ_P is removed from the relation given in Eq. 4.2. So the simplified form for M can be written as $M = M_s\ (1 - B/H^2)$. The plots of magnetization (M) versus the inverse of the square of the applied field (H^2) have been plotted and linear fitting is carried out to calculate the value of M_s and B as given in Fig. 4.95 (b). In hexaferrites, B is related to the anisotropy field H_a as $B = H_a^2/15$. For this relation values of H_a are determined. All the calculated parameters are listed in Table 4.21. The relation for magnetic moment can be expressed as in Eq. 4.3.

In view of this relation, the substitution of a weak/non-magnetic ion at spin-up site Ma $(2a \uparrow + 12k \uparrow + 2b \uparrow)$ reduces M_s, however, substitution at spin-down sites Mb $(4f_1 \downarrow + 4f_2 \downarrow)$ enhances it. The prepared ferrite composites showed a decrease in M_s from x=0.0 to 0.6 while it increases from x=0.6-1.0. There is a 33% decrease from (47.8 emu/g) to (32.1 emu/g) in the value of M_s for composition x=0.0 to 0.6 with the substitution of Ni^{2+} and Co^{2+}. The substitution of Ni^{2+} and Co^{2+} at octahedral spin-up sites is the reason for this decrease. The replacement of Fe^{3+}(5μB) by weak magnetic

Co^{2+} (3μB) and Ni^{2+} (2μB) causes decrease at M_a (2a ↑ + 12k ↑ + 2b ↑) which reduces the value of M_s. Also, the replacement of Fe^{3+} at octahedral spin-up sites 2a↑ and 12k↑ causes an imbalance in electrical neutrality and to maintain it, Fe^{3+} is converted into Fe^{2+} which has reduced the superexchange interactions due to which magnetic moment decreases. The value of Ha is also decreasing which indicates that the more substitution of Ni^{2+} and Co^{2+} is at octahedral sites 2a↑ and 12k↑ which reduces the value of M_s. There is an increment in M_s from x=0.6 to 1.0 due to the substitution of Ni^{2+} and Co^{2+} at octahedral spin-down sites $4f_2$↓ which causes reduction in M_b that causes an increase in M_s.

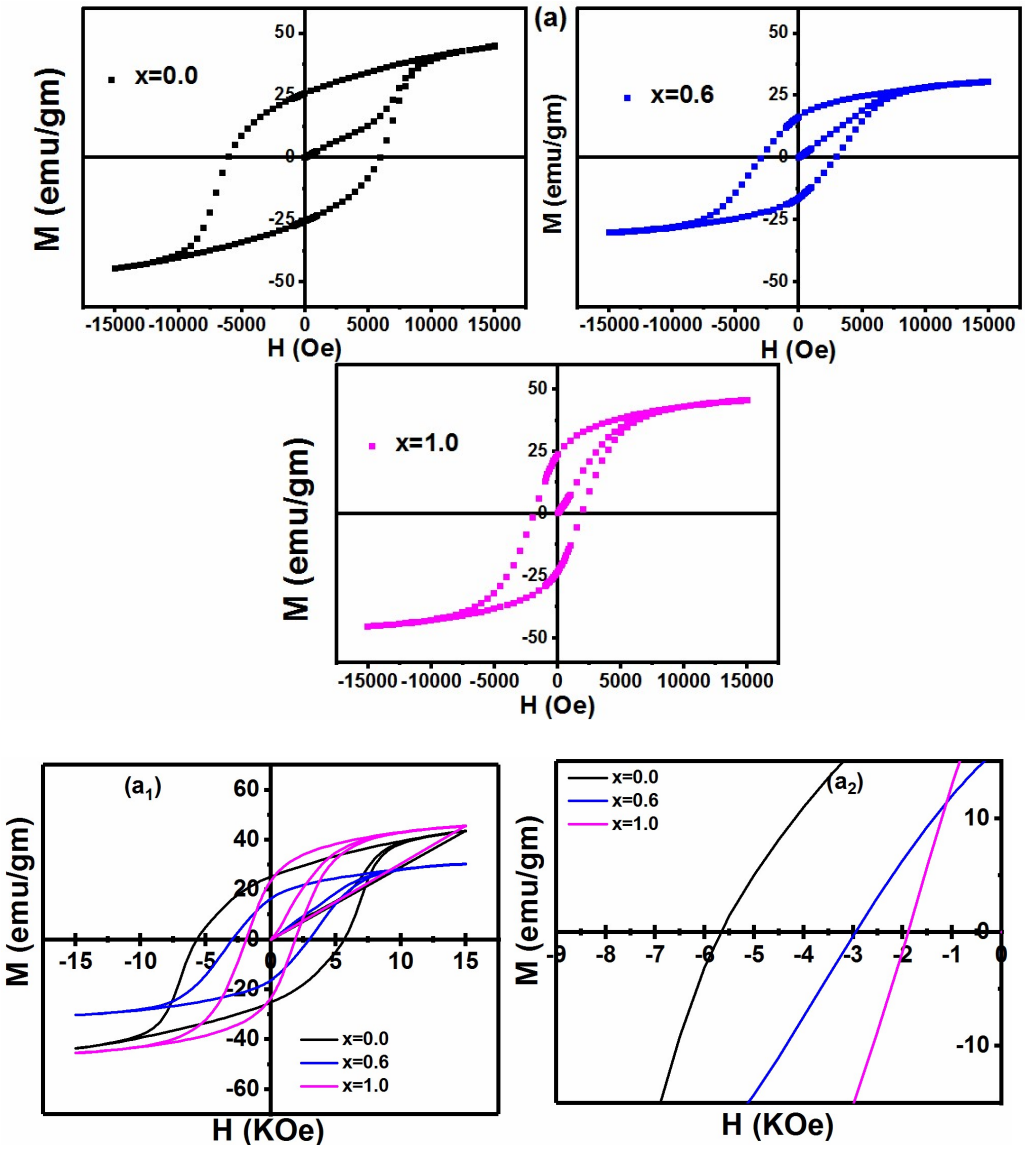

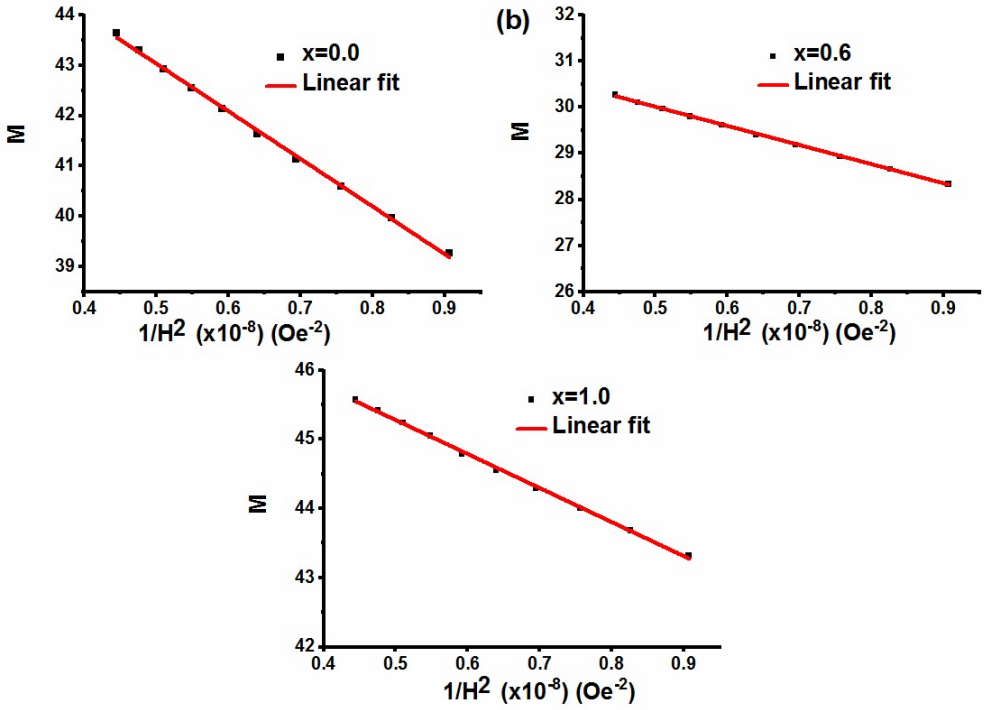

Fig. 4.95 (a) M-H loops (a_1, a_2) combined and enlarged view (b) Ms v/s $1/H^2$ plots of $SrCo_xNi_xFe_{12-2x}O_{19}$/PANI.

Table 4.21. Magnetic parameters determined from M-H loops for $SrCo_xNi_xFe_{12-2x}O_{19}$/PANI.

x	M_s (emu/g)	M_r (emu /g)	H_a (kOe)	H_c (Oe)	M_r/M_s
0.0	47.8	25.17	17.2	5679	0.53
0.6	32.1	16.39	13.9	2955	0.51
1.0	47.7	23.53	12.4	1882	0.49

The low coercivity (H_c) is beneficial in the design of an efficient absorber. Table 4.21 indicates that the addition of Co^{2+} and Ni^{2+} has reduced the value of H_c. Hc decreases 67 % from x=0.0 (5679 Oe) to x=1.0 (1882 Oe). H_c depends on two factors one is

intrinsic involving anisotropy field H_a and the second is extrinsic related to morphology. H_c directly depends on the value of H_a, and H_a is decreasing as can be noted from Table 4.21. Thus the decrease in the value of H_a causes a reduction in H_c. H_a decreases around 28 % (x=0.0-1.0) due to the replacement of Fe^{3+} at octahedral sites 12k and 2a. There is a 67 % decrease in H_c while a 26 % decrease in H_a, so another reason for the large reduction in H_c is the large ionic radius of Co^{2+}(0.745 Å) and Ni^{2+}(0.69 Å) in comparision to Fe^{3+} (0.645 Å). From the morphology of the prepared composites, it is seen that grain size increased with the inclusion of Co-Ni. Since H_c inverse relation with the grain size the formation of large grains in composition x=1.0 causes a decrease in H_c. M_r/M_s ratio is determined to explain the orientation of the ions. M_r/M_s ratio has a range of 0 to 1 and a value less than 0.5 represents randomly oriented multi-domain particles while values greater than 0.5 indicate a single domain. The ratio in composition x=0.0 and x=0.6 are above 0.5 showing single domain while composition x=1.0 has values less than 0.5 showing multi-domain orientation.

4.5.5. Electromagnetic Characteristics

4.5.5.1 Complex permeability and complex permittivity

Fig. 4.96 demonstrates the graphs of (ε'), (ε''), (μ'), and (μ'') versus frequency of the prepared $SrCo_xNi_xFe_{12-2x}O_{19}$/PANI composites. The doping of Co-Ni decreases (ε') while ε'' varies non-monotonically with doping. There is a decrement in the ε' with the increase in frequency. There are dual relaxation peaks in composition x=0.0 in ε' one around 9.25 GHz and another at 10.25 GHz. The compositions x=0.2 and 0.6 have small relaxation peaks. The plots of ε'' of all the compositions show relaxation peaks. Composition x=1.0 has a large relaxation peak around 8.7 GHz.

The permeability of the prepared composites varies in a non-monotonical way with the doping of Co-Ni. μ' increases with the increase in frequency for all the compositions. The composition x=0.6 has the lowest values of μ' at low frequencies however, it becomes highest at high frequencies. The composition x=1.0 has dual relaxation peaks one around 9.5 GHz and another near 10.5 GHz. The composition x=0.0 has a small peak around 9.5 GHz. The relaxation peaks in μ'' are also present in compositions x=0.0

and 1.0. There is a large relaxation peak in composition x=1.0 around 10.75 GHz. Composition x=0.6 has the high value of μ" at high frequencies.

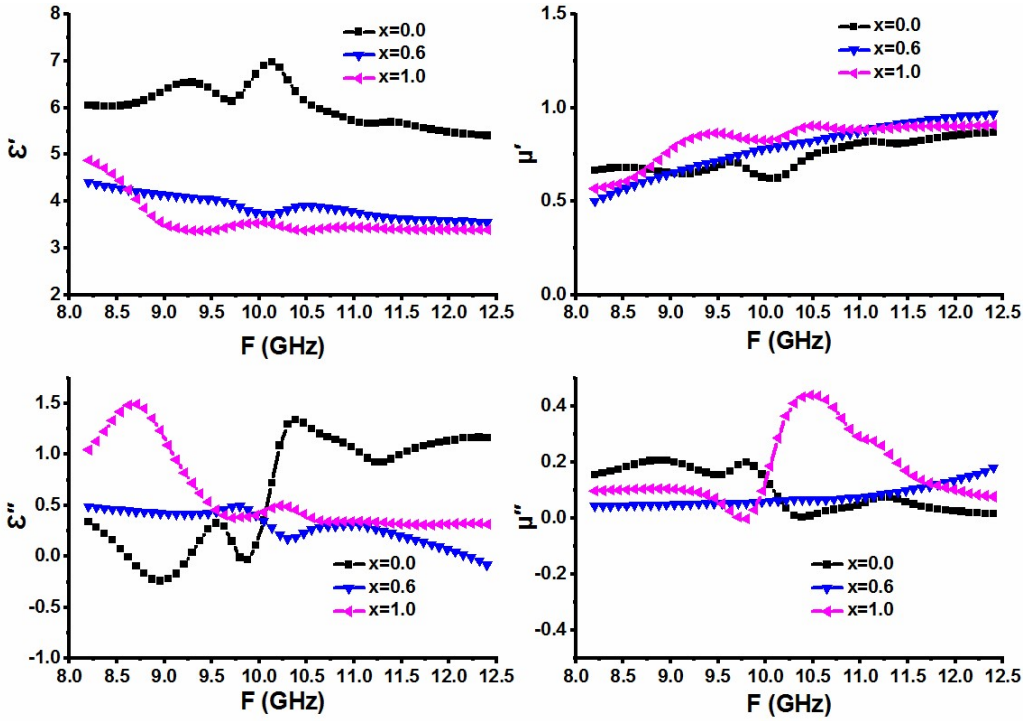

Fig. 4.96 Complex permittivity and permeability versus frequency plots of $SrCo_xNi_xFe_{12-2x}O_{19}$/PANI.

The porosity, grain size distribution, space charge polarization, electron spin, and dipole polarization affect the complex permittivity/permeability. The electron hopping in Fe^{2+}/Fe^{3+} promotes the dielectric polarization [95]. The complex permeability is affected by the exchange resonance among Fe^{3+}/Fe^{2+} and ferromagnetic resonance [96-97]. The doping of Co-Ni decreases the number of Fe^{3+} which varies the polarization and resonance. The variation in magnetization/polarization corresponding to the permittivity/permeability is due to the non-magnetic voids having demagnetizing fields as can be seen in the morphology of the prepared composites. The change in the size of the grain/grain boundary (micrographs Fig. 4.85) also causes variation in the permittivity and permeability.

The grain boundaries obstruct the field flow while the large-size grains support electron hopping. The polarization is enhanced by the gathering of charges at grain boundaries which promotes dielectric losses, however, large grains increase electron spin which

increases permeability. The magnetic loss is enhanced by the reduction in exchange resonance due to porosity and small grains which get magnetized easily. For the prepared composites, the relaxation peaks observed in ε′/ε″ and μ′/μ″ correspond to the dielectric relaxation and ferromagnetic resonance respectively.

4.5.5.2 Microwave absorption in $SrCo_xNi_xFe_{12-2x}O_{19}$/PANI

The absorption characteristics in the prepared composites are investigated by the help of reflection loss (RL). To determine the values of RL the material's input impedance Z_{in} and free space characteristic impedance Z_0 are utilized as per equations 3.13 and 3.14 as discussed in Chapter 3. To explain the absorption characteristics of the prepared composites λ/4 mechanism, impedance matching mechanism, and dielectric/magnetic loss are used as investigated in the following sections.

4.5.5.3 Quarter Wavelength Mechanism

The RL plots of prepared $SrCo_xNi_xFe_{12-2x}O_{19}$/PANI are shown in Fig. 4.97 (a, c, e, g), 4.98 (a), and 4.99 (a, c, e, g). These graphs of RL versus frequency at different simulated thicknesses are used to investigate the microwave absorption in the prepared composites. The parameters such as matching frequency/thickness, bandwidth, and -10/-20 dB RL frequency band are determined from the plots. The summary of these parameters is given in Table 4.22.

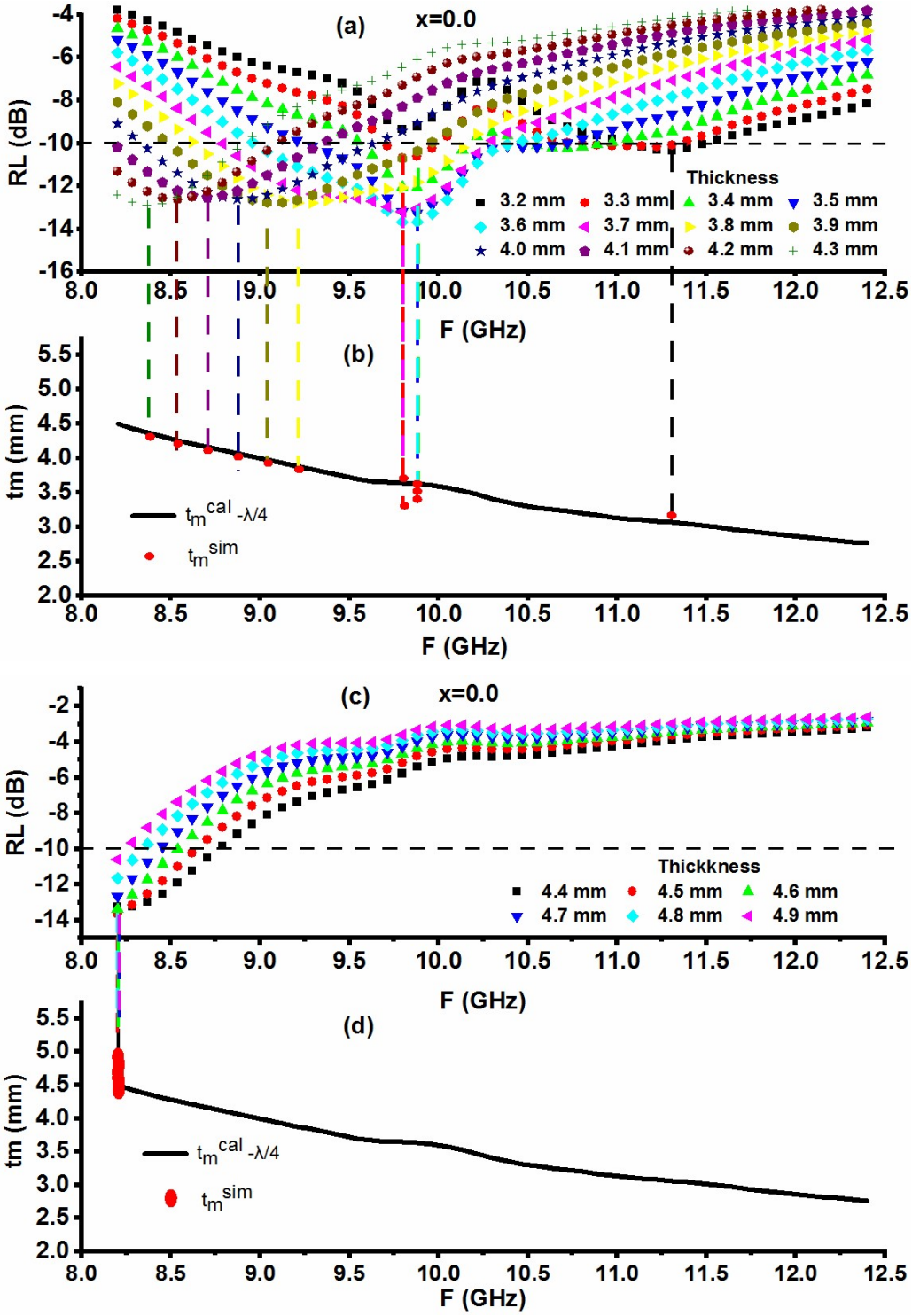
(a)
x=0.0
RL (dB)
F (GHz)
Thickness
3.2 mm
3.3 mm
3.4 mm
3.5 mm
3.6 mm
3.7 mm
3.8 mm
3.9 mm
4.0 mm
4.1 mm
4.2 mm
4.3 mm
(b)
tm (mm)
tm cal -λ/4
tm sim
(c)
x=0.0
Thickkness
4.4 mm
4.5 mm
4.6 mm
4.7 mm
4.8 mm
4.9 mm
(d)

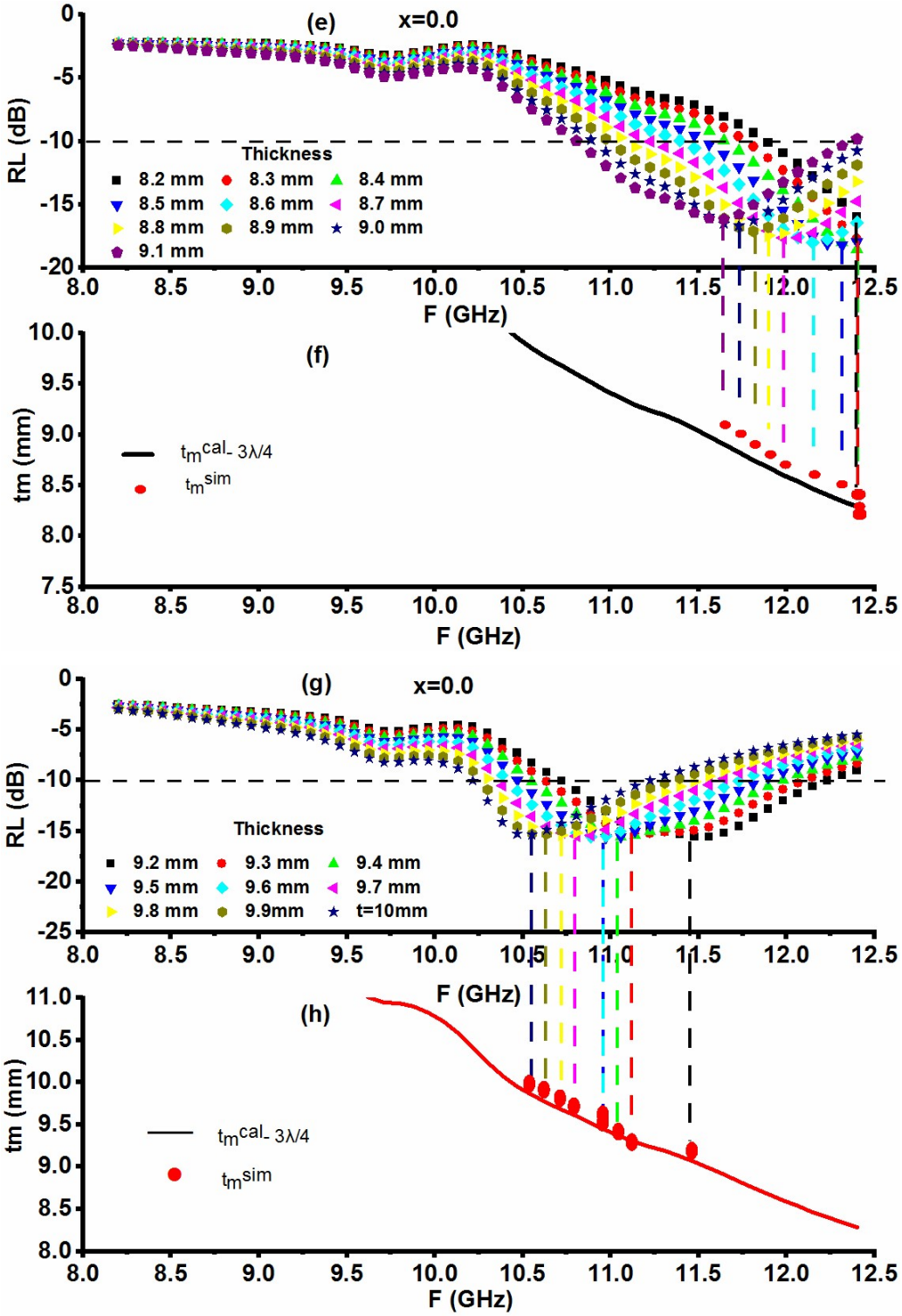

Fig. 4.97 (a, c, e, g) RL versus frequency (b, d, f, h) thickness versus frequency in x=0.0 for $SrCo_xNi_xFe_{12-2x}O_{19}$/PANI.

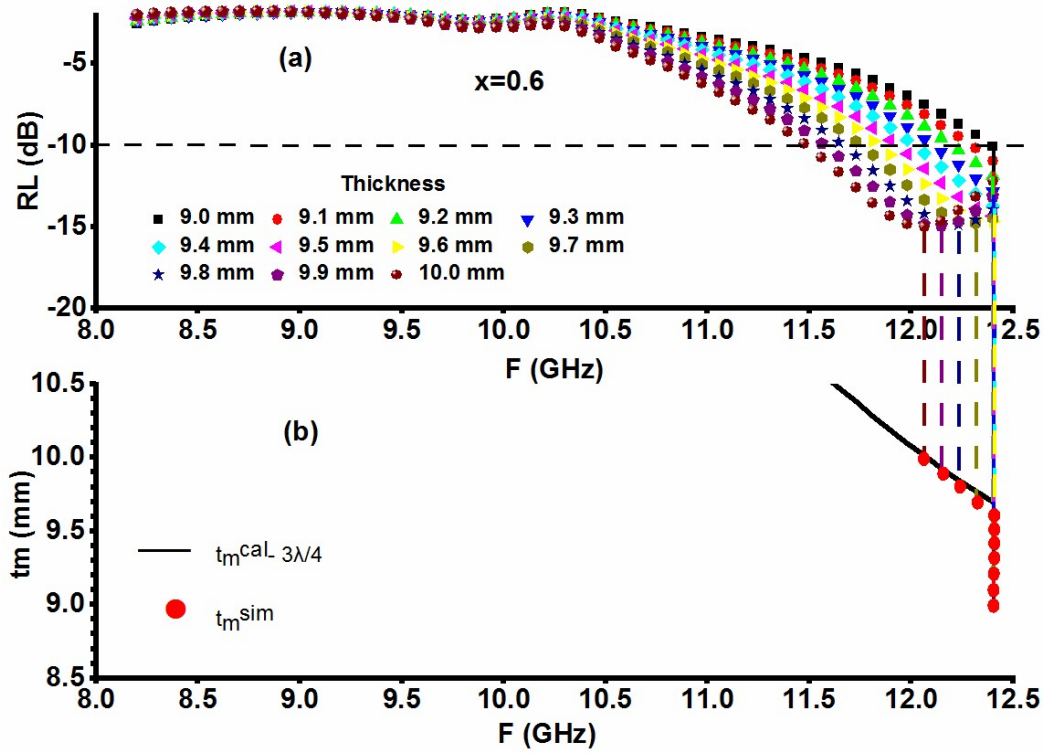

Fig. 4.98 (a) RL versus frequency (b) thickness versus frequency in x=0.6 for $SrCo_xNi_xFe_{12-2x}O_{19}$/PANI.

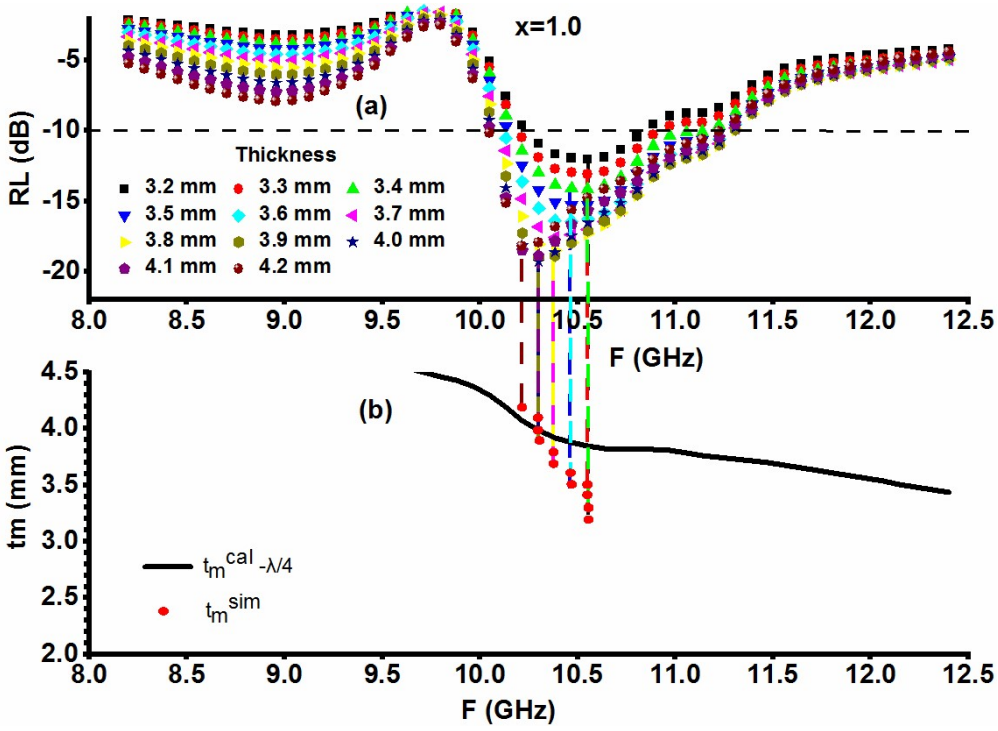

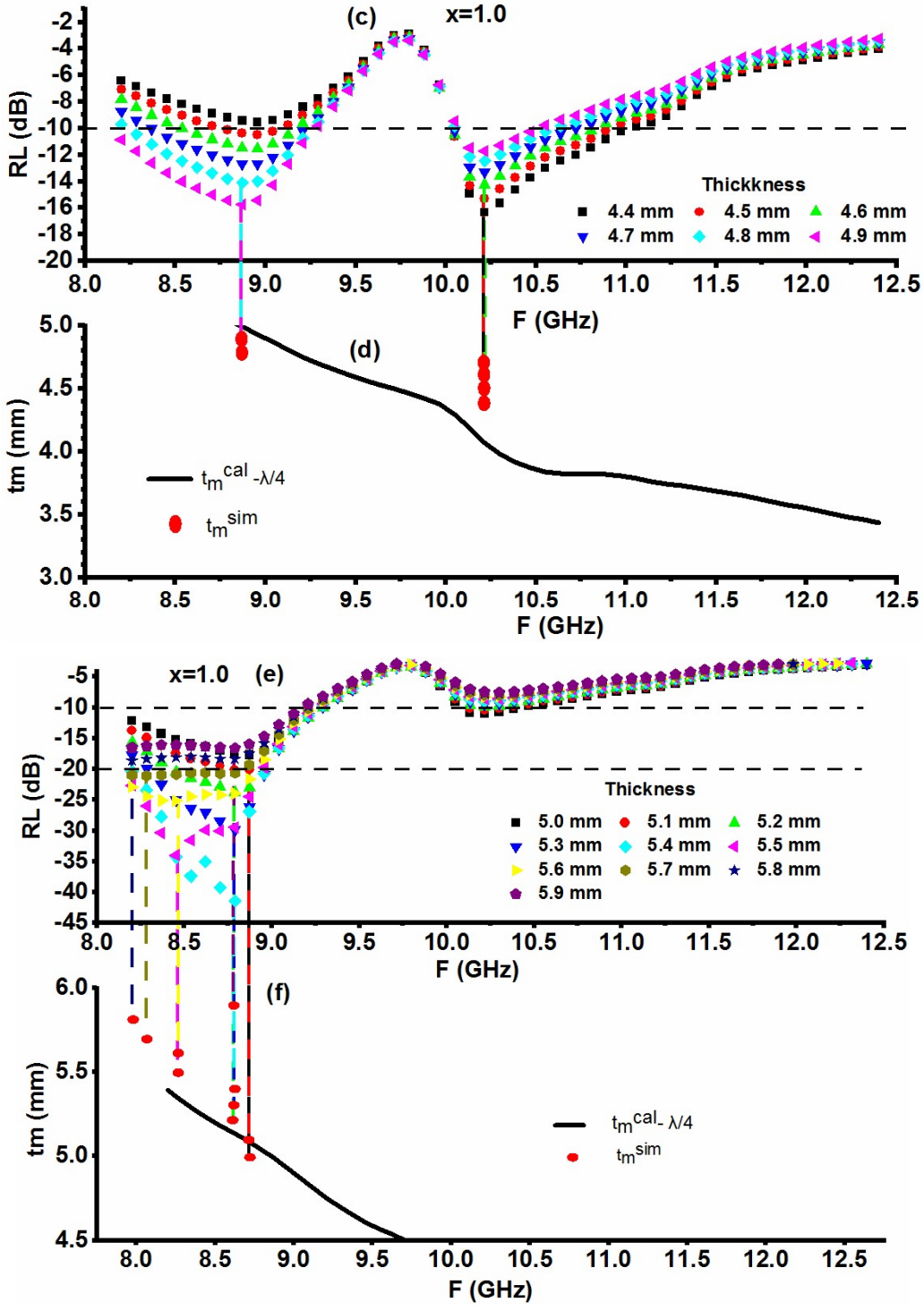
(c)
x=1.0
RL (dB)
F (GHz)
Thickness
4.4 mm
4.5 mm
4.6 mm
4.7 mm
4.8 mm
4.9 mm
(d)
tm (mm)
t_m^{cal} -λ/4
t_m^{sim}
x=1.0 (e)
Thickness
5.0 mm
5.1 mm
5.2 mm
5.3 mm
5.4 mm
5.5 mm
5.6 mm
5.7 mm
5.8 mm
5.9 mm
(f)
t_m^{cal}- λ/4
t_m^{sim}

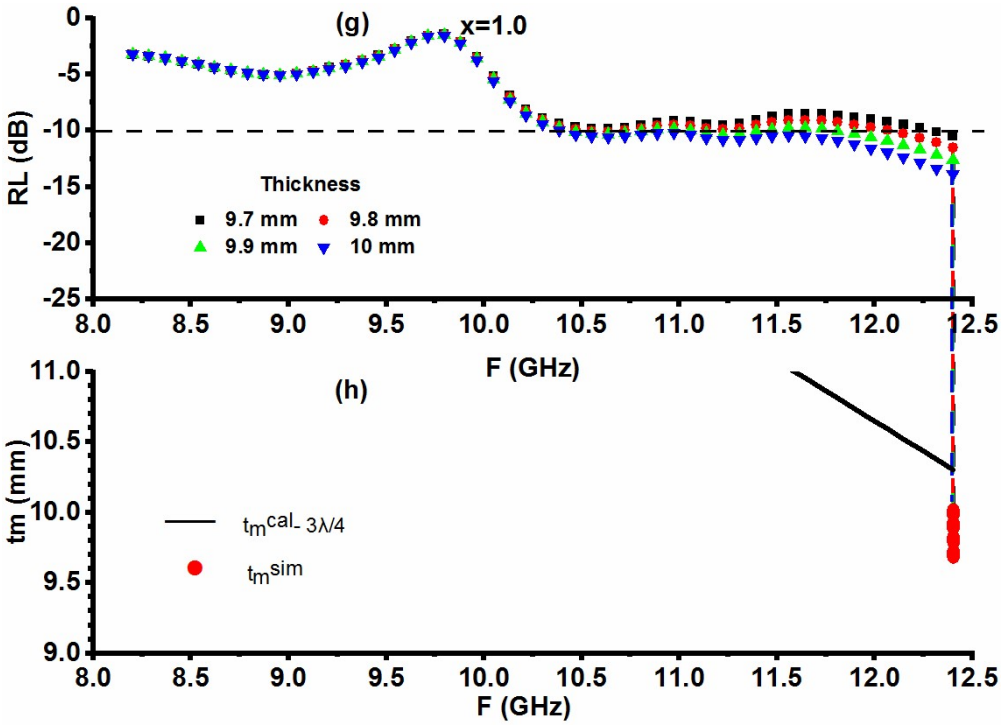

Fig. 4.99 (a, c, e, g) RL versus frequency (b, d, f, h) thickness versus frequency in x=1.0 for $SrCo_xNi_xFe_{12-2x}O_{19}$/PANI.

The RL of -41.39 dB is obtained for composition x=1.0 at the frequency of 8.79 GHz for a low thickness of 5.4 mm. The RL peaks have non-monotonous variation in regard to the frequency with the increment in thickness. RL versus frequency graphs at different thicknesses in composition x=0.0 are demonstrated in Fig. 4.97 (a, c, e, g). A reflection loss ≥ -10 dB is observed for the thickness from 3.2 mm (RL=10.35 dB at 11.31 GHz) to 10.0 mm (-15.35 dB at 11.14 GHz) in this composition. In this composition, regarding the matching frequency, RL peaks shifted non-monotonically with the increase in thickness. RL≥ -20 dB frequency band is obtained at various thicknesses of 8.4, 8.5, and 8.8 mm.

The composition x=0.6 owes its maximum RL=-15.01 at 10.0 mm with a matching frequency of 12.06 GHz Fig. 4.98 (a). The thicknesses from 9.3 mm to 9.9 mm possess *RL* ≥ -10 dB with respective values of RL=-12.83 dB at 12.40 GHz and RL=-14.92 dB at 12.15 GHz respectively. RL peaks shifted towards low frequency with the increment in the thicknesses concerning the matching frequency. In this composition, the largest -10 dB frequency band ranging from 11.56-12.40 GHz is obtained at a thickness of 10.0

mm. Composition x=1.0 has an RL of -41.39 dB at 8.79 GHz with the thickness of 5.4 mm Fig. 4.99 (a, c, e, g). The largest *RL* ≥ -10 dB frequency band ranging from 10.47-12.40 GHz with an RL=-13.84 dB is obtained for a thickness of 10.0 mm. RL peaks switch to low frequency with the increase in thickness for thicknesses 3.2 to 5.9 mm, however, at high thicknesses 9.7 to 10.0 mm it remains at 12.40 GHz. This composition also has an *RL* ≥ -20 dB frequency band for the thickness from 5.1 to 5.7 mm. The largest *RL* ≥ -20 dB frequency band ranging from 8.20-8.96 GHz is obtained at the thickness of 5.4 mm.

The analysis of the λ/4 mechanism the simulated thickness (t_m^{sim}) and the calculated thickness (t_m^{cal}) are compared. The graphs of the calculated thickness versus frequency are displayed in Fig. 4.97 (b, d, f, h), 4.98 (b), and 4.99 (b, d, f, h). For the comparison vertical lines from RL peaks are drawn towards thickness-frequency graphs. The compositions x=0.0 and 1.0 match the nλ/4 mechanism for n=1 and 3, while in composition x=0.6 it is satisfied for n=3. The -10/-20 dB bandwidths were obtained at different thicknesses as listed in Table 4.22. The x=0.0 shows both -10/-20 dB RL bands at thicknesses from 3.5 to 9.2 mm. In this composition maximum -10 dB bandwidth of 1.51 GHz is achieved at 9.2 mm thickness with a respective frequency band of 10.72-12.23 GHz. This composition also possesses broad bandwidths of 1.43, 1.43, 1.35, 1.34, and 1.26 GHz at the respective thickness of 3.7, 9.0, 3.5, 3.9, and 8.8 mm respectively. An *RL* ≥-20 dB bandwidth of 0.25 GHz at 8.5 mm thickness and 12.32 GHz matching frequency is also obtained. Also, a bandwidth of 170 MHz at 8.4 and 8.8 mm corresponding to *RL* ≥ -20 dB is obtained.

The composition x=0.6 has its maximum -10 dB bandwidth of 0.84 GHz from 11.56-12.40 GHz at 10.0 mm thickness. The high bandwidths 0.76, 0.59, and 0.42 GHz are also achieved at the thicknesses of 9.9, 9.7, and 9.5 mm respectively. The highest bandwidth of 1.93 GHz is obtained in composition x=1.0 at the thickness of 10.0 mm with a -10 dB RL band of 10.47-12.40 GHz. On the same note, the broad bandwidth of 1.17, 1.09, 1.01, and 1.0 GHz are obtained for the respective thicknesses of 4.2, 3.9 and 5.2, 5.2 to 5.7, and 3.5 mm. The highest *RL* ≥-20 dB bandwidth 0.76 GHz at 5.4 mm with an RL=-41.39 GHz is obtained. Besides this, *RL* ≥ -20 dB bandwidths of 0.67 GHz at 5.6 and 5.7 mm, 0.59 GHz at 5.3 and 5.7 mm, and 0.51 GHz at 5.2 mm are also achieved.

Table 4.22. RL with matching thickness/frequency, BW, and PBW for $SrCo_xNi_xFe_{12-2x}O_{19}$/PANI.

x	Max. RL (dB)	Matching Thickness (mm)	Matching Frequency (GHz)	-10 dB band (GHz)	-10 dB BW (GHz)	-20 dB band (GHz)	-20 dB BW (GHz)	BTR	PBW (%)
0.0	-13.25	3.5	9.88	9.29-10.64	1.35	-	-	1.171	13.664
	-13.19	3.7	9.80	8.79-10.22	1.43	-	-	1.291	14.592
	-12.77	3.9	9.04	8.54-9.88	1.34	-	-	1.222	14.823
	-18.53	8.4	12.4	11.73-12.40	0.67	12.23-12.40	0.17	0.165	5.403
	-18.19	8.5	12.32	11.56-12.40	0.84	12.15-12.40	0.25	0.207	6.818
	-17.45	8.8	11.90	11.14-12.40	1.26	11.81-11.98	0.17	0.311	10.588
	-16.67	9.0	11.73	10.97-12.40	1.43	-	-	0.350	12.191
	-15.59	9.2	11.48	10.72-12.23	1.51	-	-	0.376	13.153
0.6	-12.83	9.3	12.40	12.15-12.40	0.25	-	-	0.054	2.016
	-14.35	9.5	12.40	11.98-12.40	0.42	-	-	0.089	3.387
	-14.78	9.7	12.32	11.81-12.40	0.59	-	-	0.125	4.789
	-14.92	9.9	12.15	11.64-12.40	0.76	-	-	0.160	6.255
	-15.01	10.0	12.06	11.56-12.40	0.84	-	-	0.176	6.965
1.0	-13.07	3.3	10.55	10.22-10.89	0.67	-	-	0.547	6.351
	-15.28	3.5	10.47	10.22-11.22	1.00	-	-	0.748	9.551
	-19.0	3.9	10.30	10.13-11.22	1.09	-	-	0.738	10.583
	-18.17	4.2	10.22	10.05-11.22	1.17	-	-	0.741	11.448
	-15.74	4.9	08.87	08.20-09.21	1.01	-	-	0.819	11.387
	-20.10	5.1	08.87	08.20-09.29	1.09	08.79-08.87	0.08	0.842	12.289
	-23.71	5.2	08.79	08.20-09.21	1.01	08.45-08.96	0.51	0.772	11.490
	-29.77	5.3	08.79	08.20-09.21	1.01	08.37-08.96	0.59	0.757	11.490
	-41.39	5.4	08.79	08.20-09.21	1.01	08.20-08.96	0.76	0.743	11.490
	-39.22	5.4	08.70	08.20-09.21	1.01	08.20-08.96	0.76	0.743	11.609
	-33.95	5.5	08.45	08.20-09.21	1.01	08.20-08.87	0.67	0.730	11.953
	-25.10	5.6	08.45	08.20-09.21	1.01	08.20-08.87	0.67	0.716	11.953
	-21.11	5.7	08.28	08.20-09.21	1.01	08.20-08.79	0.59	0.704	12.198
	-12.62	9.9	12.40	11.81-12.40	0.59	-	-	0.122	4.758

-13.84	10	12.40	10.47-12.40	1.93	-	-	0.446	15.565

4.5.5.4 Impedance matching mechanism

There is a difference between the impedance of a material (Z_{in}) and that of air (Z_o=377 Ω) because they differ in their permittivity/permeability. As per the impedance matching mechanism if these two impedances match with each other the major part of the incident signal will be absorbed. Hence investigation of the impedance matching mechanism for the prepared composites has been carried out. Fig. 4.100 depicts the plots of reflection loss and impedance i.e. $|Z_{in}|$ with frequency for the composites. Table 4.23 enlists the values of Z_{in} related to the reflection loss of the different composites. The composite x=0.0 and 1.0 satisfied the impedance matching for their highest RL while there are some deviations in composites x=0.6 and x=1.0 at few frequencies.

In composite x=0.0, the RL peak of -18.53 dB observed at 12.40 GHz has a corresponding value of Z_{in}=298.88 Ω which is close to Z_o=377 Ω. The highest RL peak of RL=-41.39 at 9.80 GHz in composition x=1.0 has Z_{in}=382.57 Ω which is in proximity to Z_o=377 Ω. In composition x=0.6 there is a discrepancy as there is a RL peak of -15.01 dB at 12.06 GHz with Z_{in}=539.78 Ω while there is no RL peak at 11.39 GHz with a Z_{in}=376.23 Ω which is more close to Z_o=377 Ω than Z_{in}=539.78 Ω. In the same way for composition x=1.0 no RL peak is present at 10.05 GHz with Z_{in}=364.13 Ω.

The complex nature of $|Z_{in}|$ involving real and imaginary terms Z_{real} and Z_{img} is responsible for this deviation. That's why, Z_{real} and Z_{img} are determined and graphs of Z_{real} and Z_{img} are plotted as given in Fig. 4.101. The determined values of Z_{real} and Z_{img} are listed in Table 4.23. It should be remembered that successful implementation of the impedance matching mechanism depends upend the fact that the impedance should follow exactly/nearly the criteria of Z_{real}=377 Ω and/or Z_{img}=0. From Table 4.23 it can be noted that the highest *RL* of -41.398 dB at 8.79 GHz obtained in x=1.0 follows this condition with Z_{real}=382.55 Ω and Z_{img}=-3.34 Ω which are near 377 Ω and 0. No RL peak at 11.39 GHz with a Z_{in}=376.23 Ω in composition x=0.6 is due to Z_{real}=294.72 Ω and Z_{img}=233.86 Ω which are far away from 377 Ω and/or 0. Similarly for composition

x=1.0, no RL peak at 10.05 GHz with Z_{in}=364.13 Ω is due to Z_{real}=252.75 Ω and Z_{img}=-262.12 Ω.

Thus it can be summarized that the discrepancies observed in x=0.6 and x=1.0 are due to the mismatch in obtained Z_{real}/Z_{img} values from the required Z_{real}/Z_{img} values of 377 Ω and/or zero. It can be noted that the doping of Co-Ni has increased the input impedance Z_{in} (Z_{real} and Z_{img}).

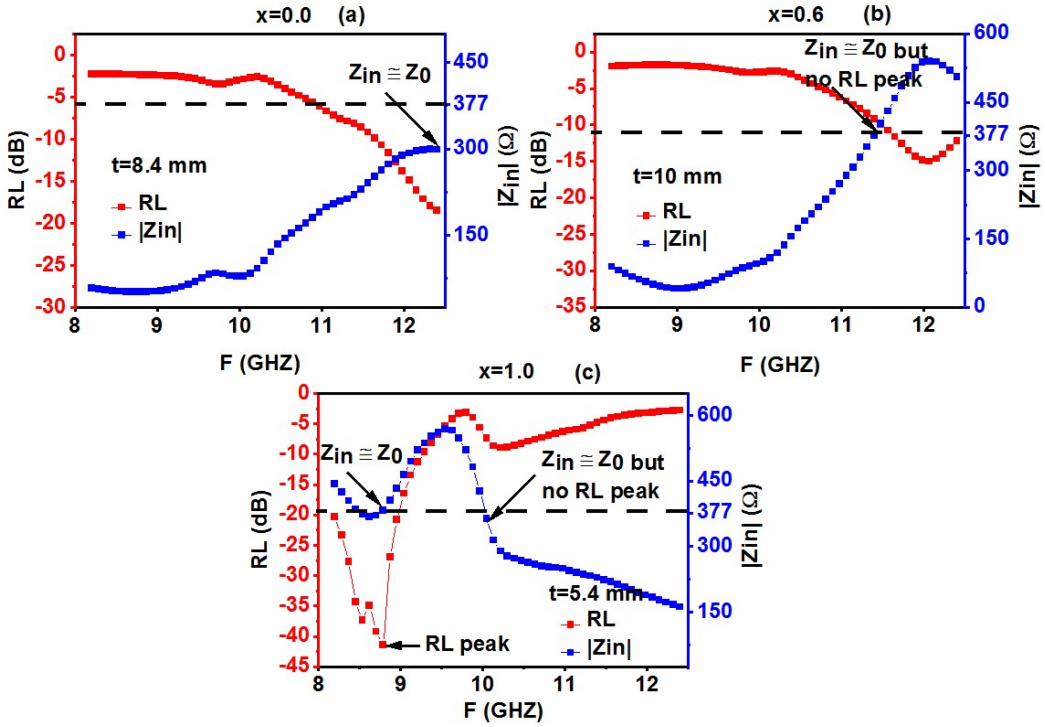

Fig. 4.100 Z_{in} and RL curve against frequency for $SrCo_xNi_xFe_{12-2x}O_{19}$/PANI.

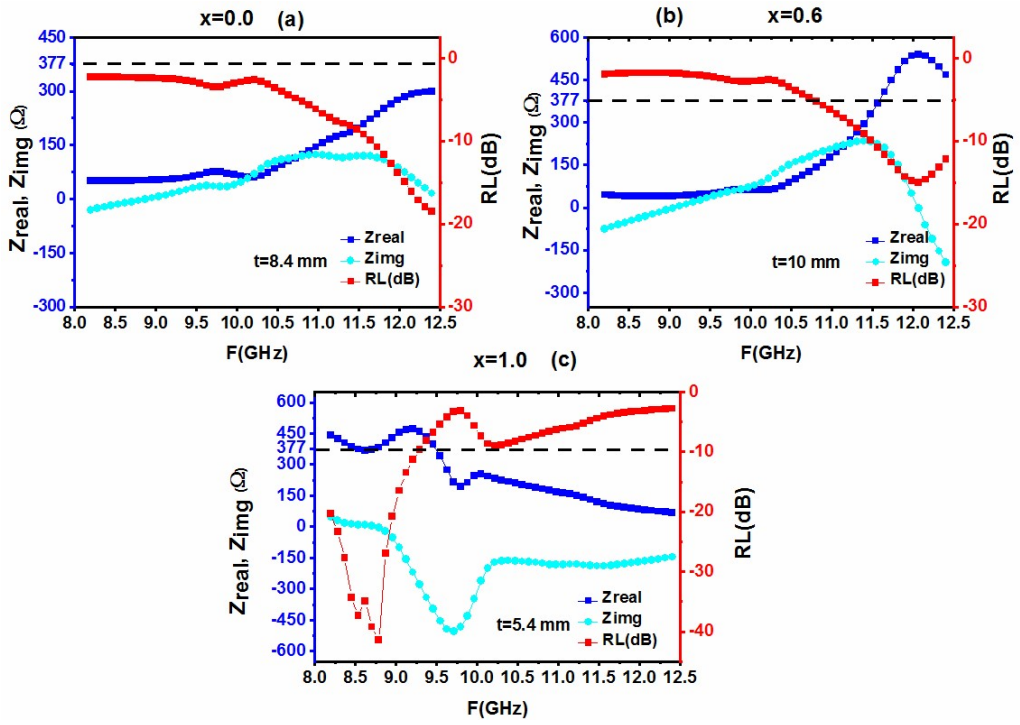

Fig. 4.101 Z_{real}, Z_{imag}, and RL v/s frequency for $SrCo_xNi_xFe_{12-2x}O_{19}$/PANI.

Table 4.23. Z_{in}, Z_{real}, and Z_{imag} values corresponding to RL_{max} for $SrCo_xNi_xFe_{12-2x}O_{19}$/PANI.

x	RL (dB)	Matching Thickness (mm)	Matching Frequency (GHz)	$\|Z_{in}\|$ (Ω)	Z_{real} (Ω)	Z_{img} (Ω)
0.0	-18.53	8.4	12.40	298.88	298.47	15.55
0.6	-15.01	10.0	12.06	539.78	539.77	-3.47
1.0	-41.39	5.4	8.79	382.57	382.55	-3.34

4.5.5.5 Role of Electromagnetic/Material Parameters

No doubt, the λ/4 and input impedance matching have their roles in absorption, however, the dielectric loss (ε'') and magnetic loss (μ'') due to the complex nature of permittivity/permeability also contribute to the absorption which also requires an investigation.

The contribution of relaxation peaks observed in ε″ and μ" to absorption can be understood as: ε″ peak at 9.54 GHz attribute to an RL =-12.57 dB at 9.54 GHz for 3.7 mm in x=0.0; ε″ peak with 8.70 GHz in composition x=1.0 correspond to *RL*=-39.22 dB with 8.70 GHz at the thickness of 5.4 mm; composition x=0.0 has an *RL*=-13.25 at 3.5 mm attributing μ" peak at 9.88 GHz; a μ" peak at 10.55 GHz in composition x=1.0 attribute *RL*=-13.07 dB at 3.3 mm; in composition x=0.6 the maximum μ" at 12.40 GHz correspond to the RL=-14.35 dB at 9.5 mm. In summary, dielectric and magnetic loss in prepared composites are also contributing to microwave absorption.

4.5.5.5 Eddy Current Loss

In ferrites, eddy current loss has an impact on absorption characteristics in terms of magnetic loss. The eddy current loss contributes when C_0 does not vary with the frequency increment. Hence to evaluate the role of it the plot of C_0 versus frequency has been plotted as given in Fig. 4.102. There is a flat line in all the compositions showing constant values of C_0 with the increment in frequency which indicates the contribution of eddy current loss in the absorption of ferrite composites.

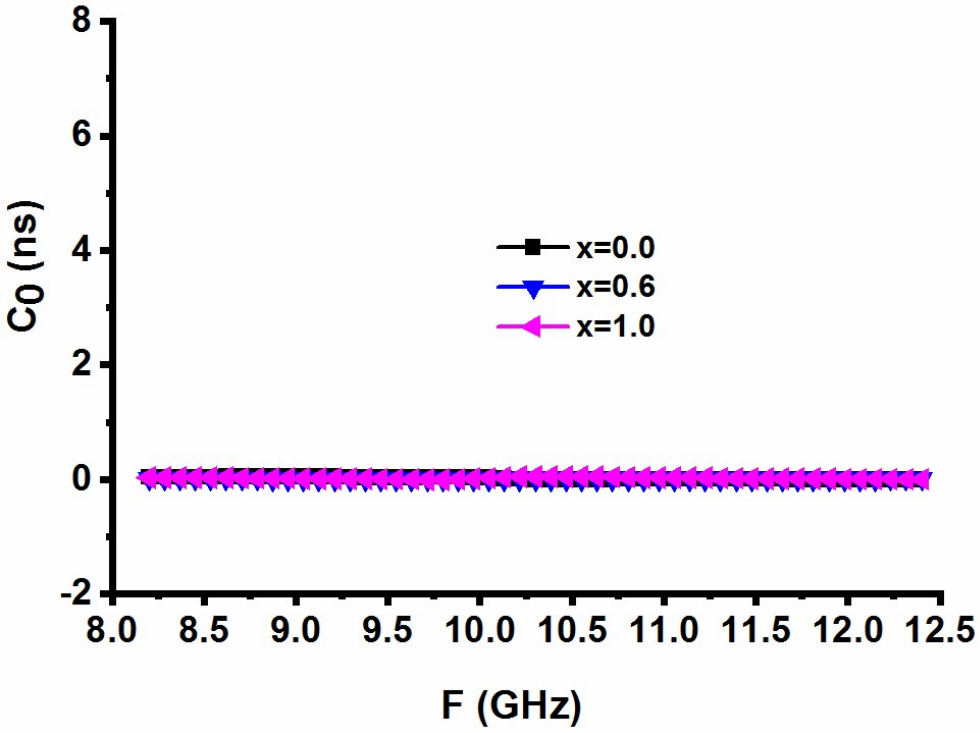

Fig. 4.102 C_0 versus frequency curve for $SrCo_xNi_xFe_{12-2x}O_{19}$/PANI.

4.5.5.7 Bandwidth to Thickness Ratio

Bandwidth to-thickness ratio (BTR) is an important parameter that should be taken care of in the design of an effective absorber. The formulas associated with BTR and percentage bandwidth (PBW) are given in Eq. 4.5 and 4.6.

The highest BTR of 1.291 at 9.80 GHz with RL=-13.19 dB is obtained in composition x=0.0. A high BTR of 1.222 at 9.04 GHz with RL=-12.77 dB and 1.171 at 9.88 GHz with RL=-13.25 dB are also observed in this composition. The maximum RL=-15.01 dB at 12.06 GHz of x=0.6 has a comparatively small BTR=0.176. The composite x=1.0 has its maximum BTR of 0.842 at 5.1 mm with RL=-20.10 GHz. The high BTR of 0.819, 0.772, 0.757, and 0.743 are observed at thicknesses of 4.9, 5.2, 5.3, and 5.4 mm.

There is an increase in percentage bandwidth with the increment in the doping of Co-Ni. The composition x=0.0 has its maximum PBW=14.823 at 3.9 mm. Also high PBW=14.592. 13.664, and 13.153 are observed at 3.7, 3.5, and 9.2 mm thickness. PBW ranges from 5.40 to 14.82 %. The highest PBW of 15.57 at 10.0 mm thickness is obtained in composite x=1.0. The PBW ranges from 4.76 to 15.76 % in this composition.

4.6 $SrCo_xZr_xFe_{12-2x}O_{19}$/PANI composites

4.6.1 Microstructural/Morphological Characteristics

SEM is carried out to analyze the morphology of the $SrCo_xZr_xFe_{12-2x}O_{19}$/PANI composites. The micrographs of $SrCo_xZr_xFe_{12-2x}O_{19}$/PANI composites are given in Fig. 4.103. The grain distribution has been affected by the doping of Co-Zr. The composition x=0.0 has small grains while composition x=0.2 and 0.6 possess large grains. Thus the increase in doping level of Co-Zr has increased the grain size. The composition x=0.2 has both small as well as large fused grains while composition x=0.6 shows large fused grains with agglomeration. The composition x=0.6 shows a platelet-type structure.

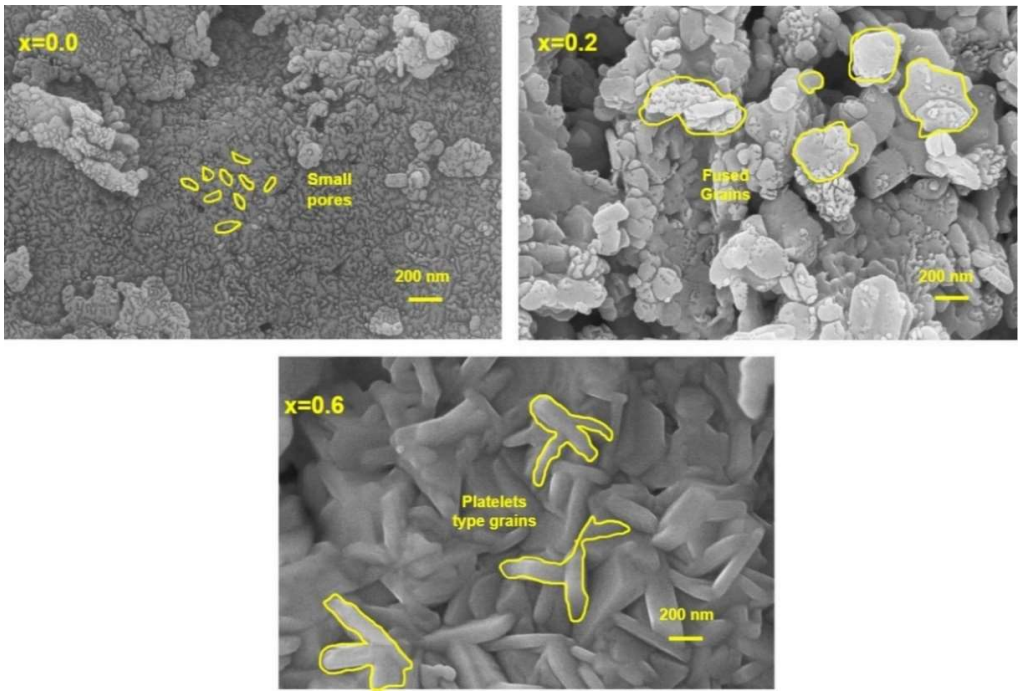

Fig. 4.103 SEM images of $SrCo_xZr_xFe_{12-2x}O_{19}$/PANI.

4.6.2 Electrical Characteristics

4.6.2.1 Dielectric constant

The variation of ε' and ε'' against the frequency of $SrCo_xZr_xFe_{12-2x}O_{19}$/PANI are depicted in Fig. 4.104. Since the dielectric constant of PANI is high, the dielectric constant of ferrite composites is much higher as compared to the pure ferrite ($SrCo_xZr_xFe_{12-2x}O_{19}$)**.** Further **t**he curve of ε' decreases with the frequency increment. At low frequencies, it has a high value which continuously decreases as the frequency increases and becomes constant at high frequencies. This behavior signifies the interfacial polarization and follows with the Maxwell-Wagner model [80]. The doping of Co-Zr in PANI composites has a non-monotonical variation in the dielectric constant. The value of ε' decreased in the case of x=0.2 while it increased to a very high value in composition x=0.6. This abrupt change in the case of x=0.6 is due to the morphology (Fig. 4.103): The agglomeration of platelet type structure of grains increases grain boundaries supporting the polarization and hence increase in ε'. A similar kind of behavior is shown in ε'' as can be viewed in Fig. 4.104 (b).

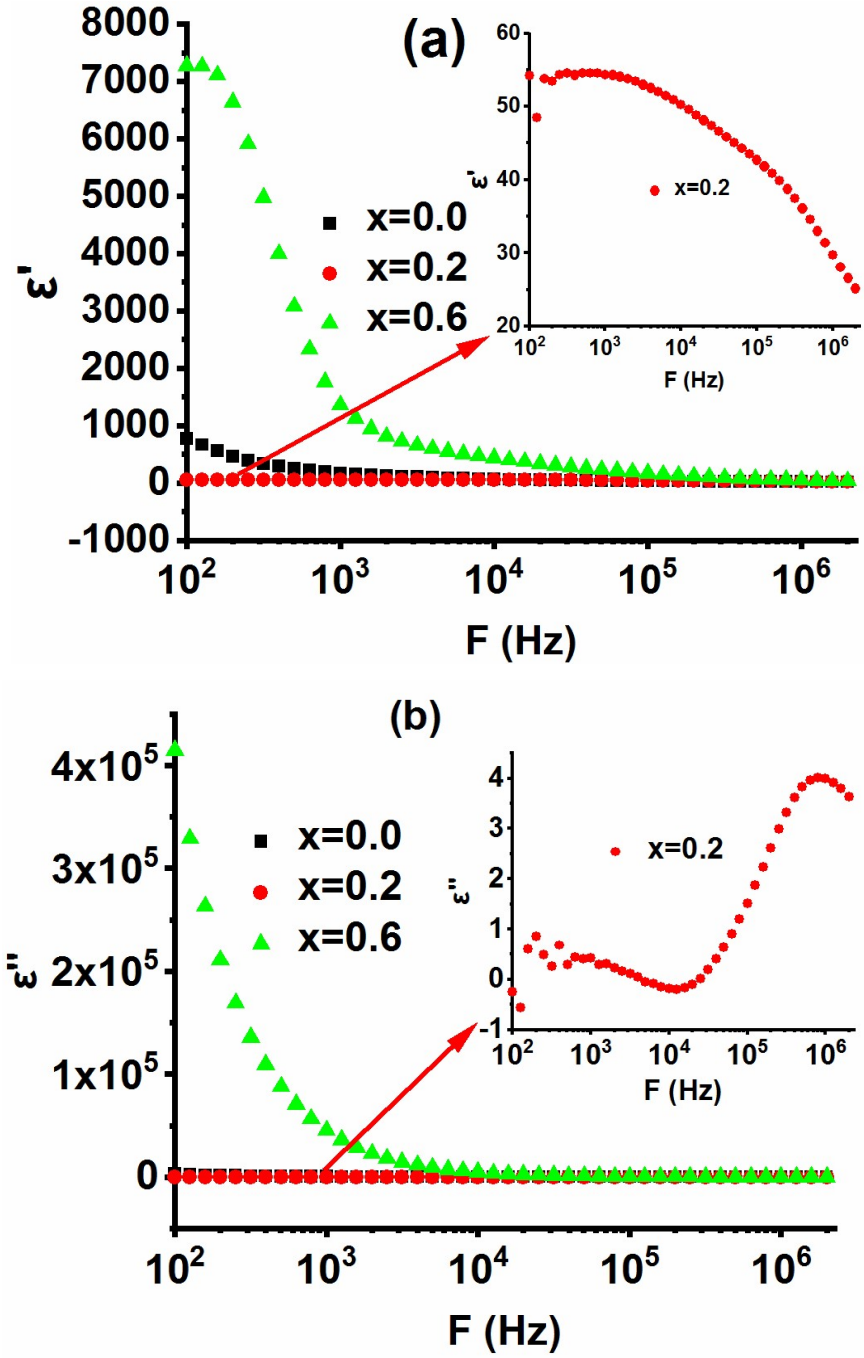

Fig. 4.104. Dielectric constant (a) real (b) imaginary versus frequency for $SrCo_xZr_xFe_{12-2x}O_{19}$/PANI.

Fig. 4.105 shows the tanδ versus the frequency plot of the composites. There is a decrease in the tanδ with the increase in frequency. This behavior is according to Koop's theory of dielectrics [80]. The inclusion of Co-Zr in PANI composites has a

non-monotonical effect on the loss tangent as in the case of ε' and ε''. Composition x=0.6 has the highest tanδ among all the compositions. The relaxation peak can also be seen in the composition x=0.6. This relaxation peak is obtained when the charge hopping frequency for Fe^{2+} and Fe^{3+} matches the frequency of the applied fields.

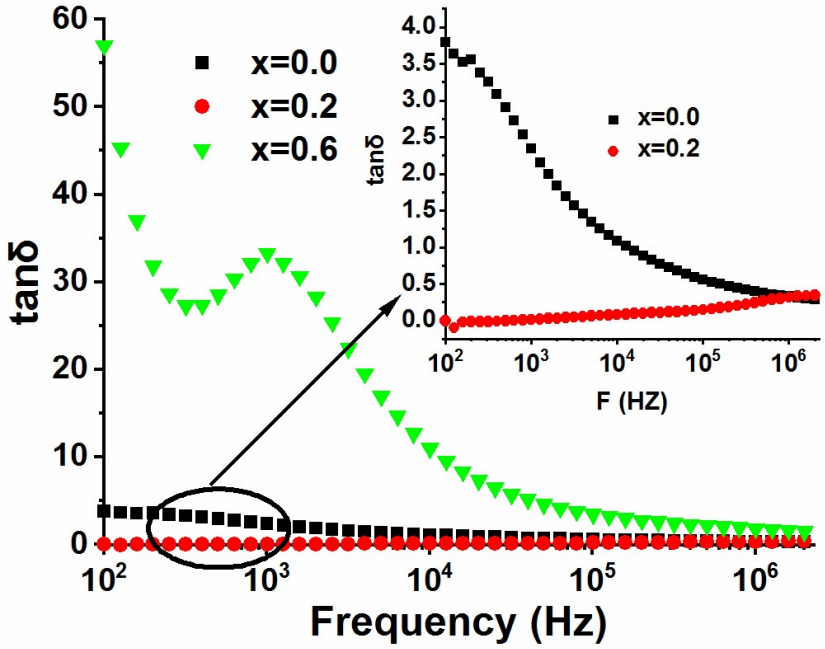

Fig. 4.105 Plots of loss tangent of $SrCo_xZr_xFe_{12-2x}O_{19}$/PANI composites.

4.6.2.2 Electric modulus

The graphs of M′ and M″ for $SrCo_xZr_xFe_{12-2x}O_{19}$/PANI composites are depicted in Fig. 4.106 (a) and (b). At low frequencies M′ has low values, however, it increases with the frequency increment. This increase in the curve of M′ with an increase in frequency is related to the charge carrier's short-range mobility. The absence of a saturated region in M′ at high frequency signifies the lack of long-range mobility of charges. There is a non-monotonous variation in the values of M′ with the inclusion of Co-Zr in PANI composites. M′ increases in the case of x=0.2 at low frequencies, however, it reduces in the composition x=0.6. Besides, composition x=0.2 cannot maintain high values at high frequencies and becomes low as compared to undoped composition x=0.0.

The M″ curves provide information about the conductivity relaxation. The broad asymmetric peak in M″ is the basic feature of modulus M. The low-frequency area of

the peaks is associated with long-distance movement while the high-frequency area indicates the localized motion within the potential well. The height of M″ reduces with the doping of Co-Zr. The reason behind it is the decrease in Fe^{3+} ions with the inclusion of Co-Zr content.

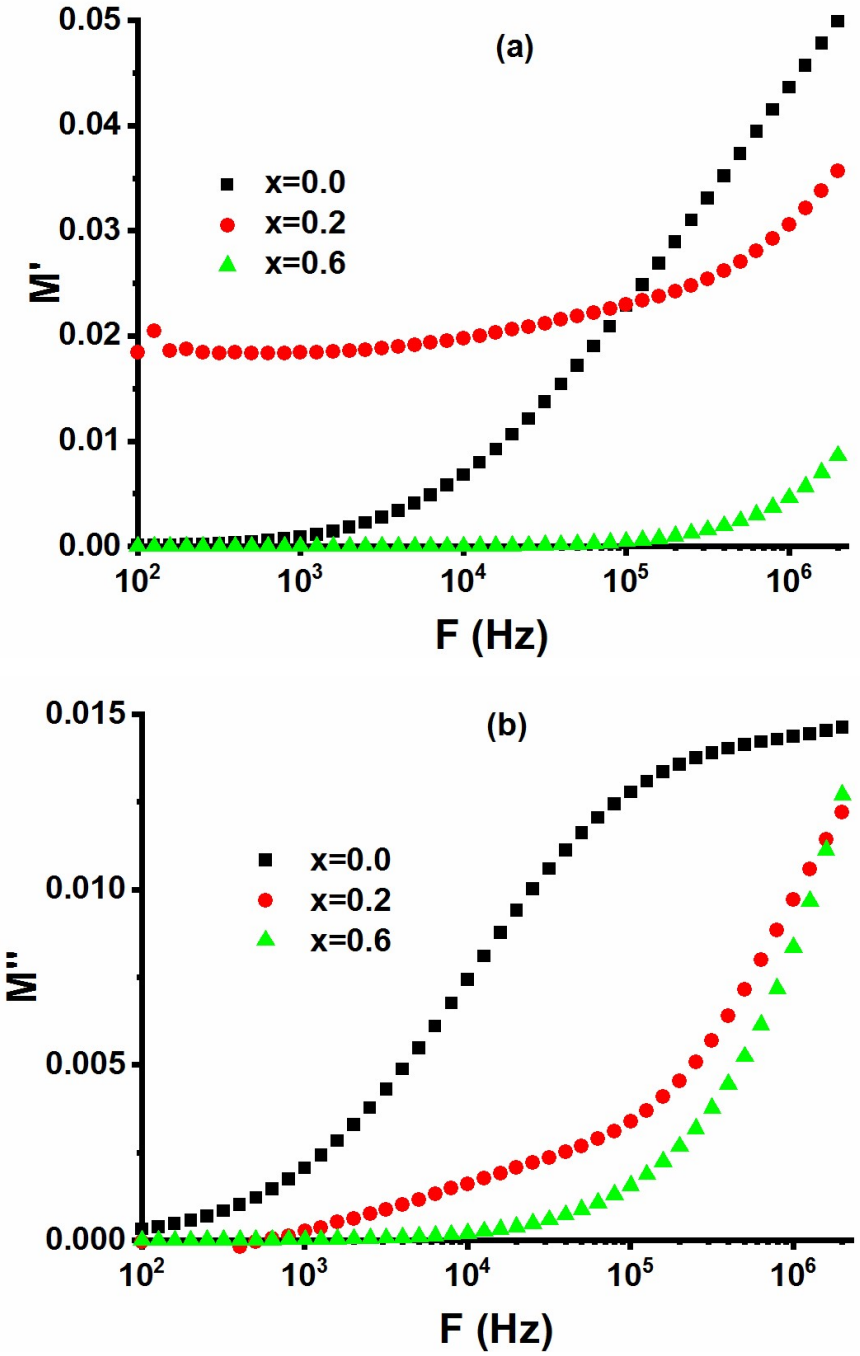

Fig. 4.106 M′ and M″ curves against frequency for $SrCo_xZr_xFe_{12-2x}O_{19}$/PANI.

Fig. 4.107 depicts the Cole-Cole plots ($M'v/s\ M'$) of $SrCo_xZr_xFe_{12-2x}O_{19}$/PANI. The plots of all the composites show asymmetric deformed semicircular arcs. The deviation of the center of these from the x-axis is attributed to the non-Debye relaxation. The inclusion of Co-Zr in the PANI composite has a non-monotonical variation in the height and shape of the semicircles. The curve of composition x=0.0 lies equally in both low frequency and high frequency signifying the contribution of both grain and grain boundaries. The composition x=0.2 also has its curve in both low as well as high frequency showing the contribution of both grain and grain boundaries. The composition x=0.6 has its curve in low frequency region indicating that grain boundaries have a prominent role in charge transport. This is due to the morphology (Fig. 4.103): The platelet-type grains cause an increase in the number of grain boundaries.

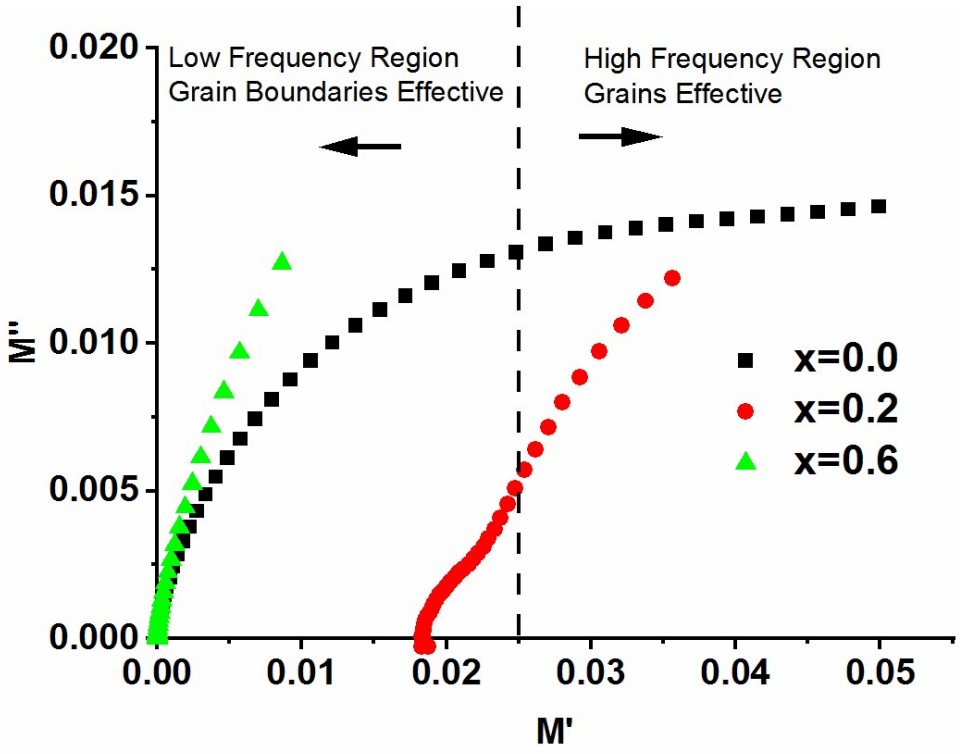

Fig. 4.107 Cole-Cole plot of M′ v/s M″ for $SrCo_xZr_xFe_{12-2x}O_{19}$/PANI.

4.6.2.3. Complex impedance spectra

The graph of Z′ against frequency is displayed in Fig. 4.108 (a). Z′ first decreases with the frequency increment and then acquires a constant value at higher frequencies. This

behavior follows the Maxwell-Wagner model accompanied by the effectiveness of grain boundary at low frequency and grains at high frequency. The doping of Co-Zr in the composites has an adverse effect on the value of Z′ as it decreases with the increase in doping level. Micrographs show improvement in inter-grain connectivity which reduces the resistance of individual grain boundaries

Fig. 4.108 (b) demonstrates the variation in Z'' to frequency. The value of Z'' PANI-composites varies non-monotonically with the inclusion of Co-Zr. The composition x=0.2 obtains the highest value among all the compositions, however, it is decreased in the case of x=0.6. The decay in Z'' is because of the enhancement in the space charge polarization due to the platelet structure which increases polarization at grain boundaries that in turn, reduces the reactance. The dielectric relaxation peaks can be seen in the plots of x=0.0 and x=0.6 as shown in the inset diagram.

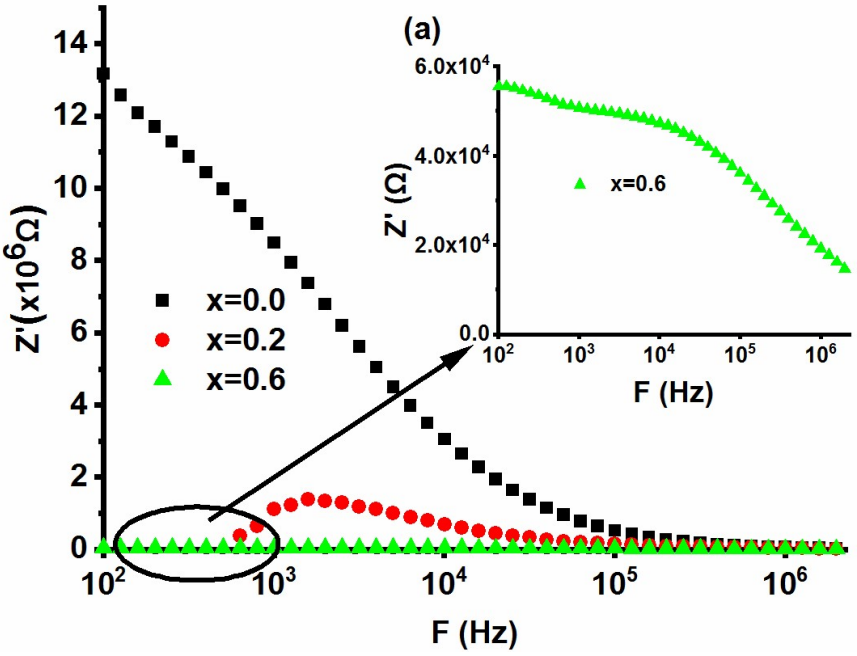

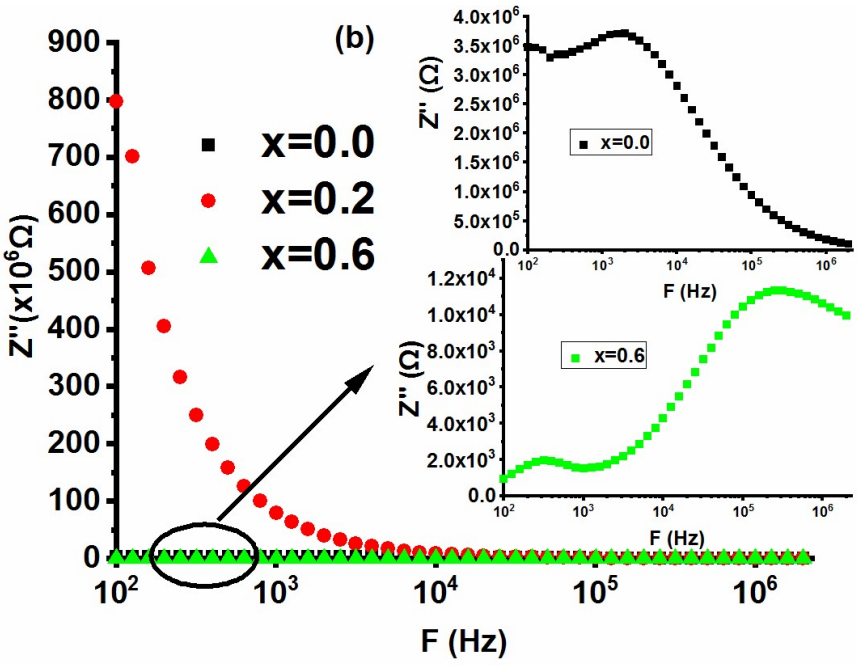

Fig. 4.108 Z' and Z''versus frequency plots for $SrCo_xZr_xFe_{12-2x}O_{19}$/PANI.

Cole-Cole plot ($Z''v/s\ Z'$) for the composites are demonstrated in Fig. 4.109 which show deformed semi-circles. There is a large difference between the values of the three compositions. The composition x=0.2 possesses very large values of Z''as compared to other compositions. Hence, due to the low values, the curves of composition x=0.6 are shown in the inset diagram. The inclusion of Co-Zr in the composites has a non-monotonous variation in the height and shape of semicircles. The plots for x=0.2 occur completely in the high frequency area indicating the dominance of grains. The composites x=0.0 and x=0.6 have their curves almost equally in both low and high frequency regions referring to the contribution of both grain and grain boundaries.

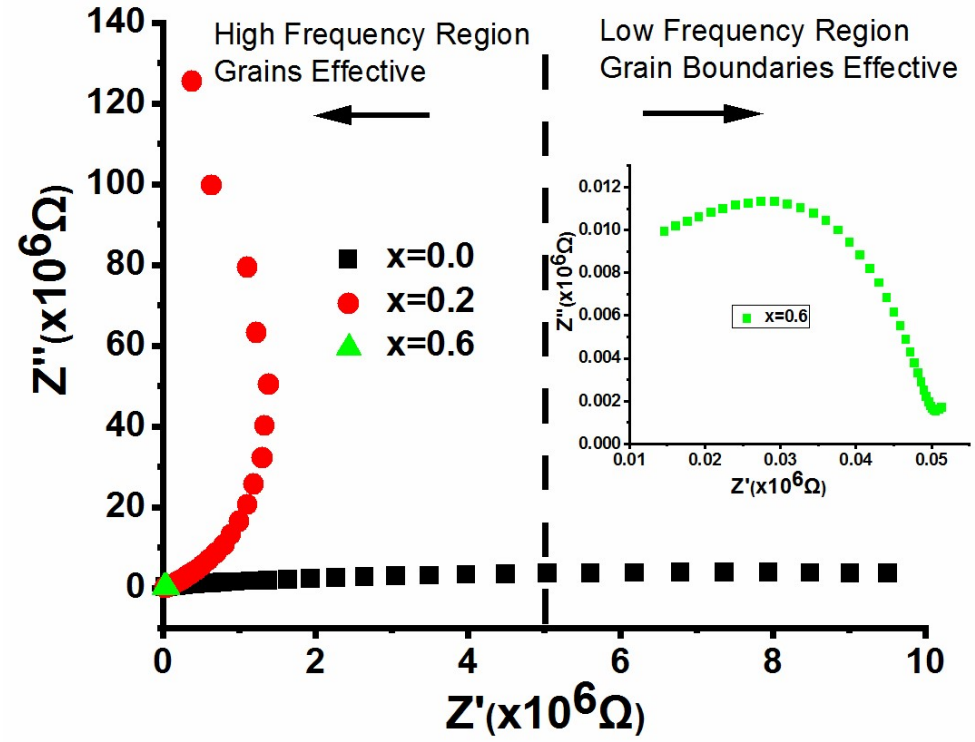

Fig. 4.109. Cole-Cole plots (*Z′* versus *Z″*) for $SrCo_xZr_xFe_{12-2x}O_{19}$/PANI.

4.6.2.4. AC Conductivity

The frequency dependence curves of ac conductivity **(σ_{ac})** are shown in Fig. 4.110. The conductivity of ferrite composites is high as compared to the parent ferrite ($SrCo_xZr_xFe_{12-2x}O_{19}$). The reason behind this is the inclusion of conductive polymer PANI in the ferrites. At the low frequencies, conductivity shows a frequency-independent behavior but it starts increasing when the frequency increases. The frequency after which it starts is called hopping frequency. This hopping frequency represents the transition of conductivity from the flat plateau region to a dispersive region. There is an enhancement in the value of conductivity with an increase in the doping of Co-Zr. The composition x=0.6 possesses the highest value among all the compositions. This can be correlated with the morphology: the platelet grain structure enhances the grain connectivity. It is noted that the hopping frequency also shifts to a low frequency with the doping level.

AC conductivity curves are fitted according to the Jonscher power law as explained in Chapter 3 is used to explain the frequency-dependence nature of ac conductivity. By

fitting the curves, values of n were calculated for the prepared composites. The determined values are 0.562, 0.998, and 0.200. According to Funke n<1 shows the motion with sudden hoping. The values are less than 1 which signifies that ac conductivity follows the hopping mechanism.

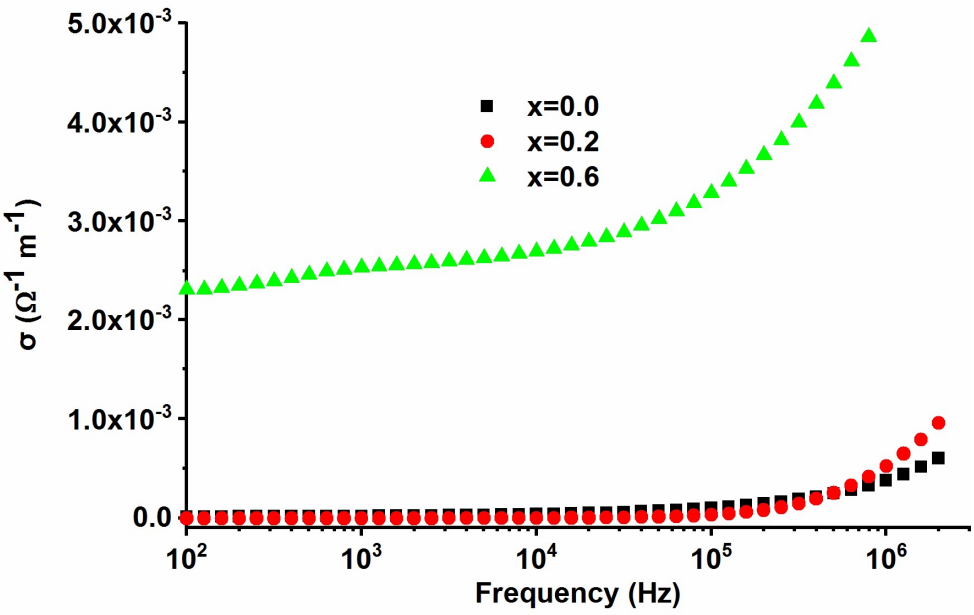

Fig. 4.110. AC conductivity for $SrCo_xZr_xFe_{12-2x}O_{19}$/PANI.

4.6.2.5 Software-based Impedance Simulation

Electrochemical Impedance Spectroscopy (EIS) software is employed to perform the impedance spectroscopy of the prepared composites. The fitting using EIS software is shown in Fig. 4.111. The simulated parameters for grain/grain boundaries are given in Table 4.24.

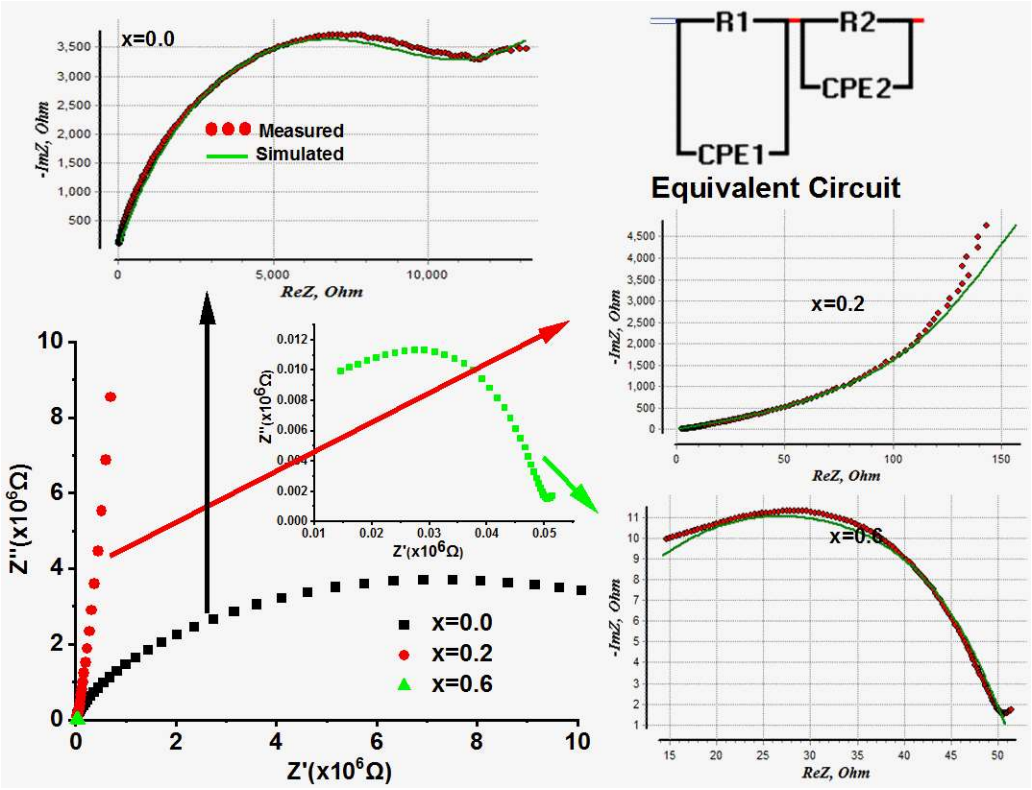

Fig. 4.111. Fitting of Impedance curves using EIS for $SrCo_xZr_xFe_{12-2x}O_{19}$/PANI.

Table 4.24. Simulated parameters derived from EIS software for $SrCo_xZr_xFe_{12-2x}O_{19}$/PANI.

x	R_g (MΩ)	R_{gb} (MΩ)	C_g (μF)	C_{gb} (F)
0.0	10.68	16.78	4957.4	9.41
0.2	10000	1.64	199.4	1.32
0.6	0.005	0.046	7503.9	1.42

Correlation between Grain/Grain boundaries simulated parameters and Morphology

The size of the grain is small in composition x=0.0, as well as small pores can be seen in the micrograph. The small size of grains and pores between grains promotes polarization at grain boundaries. Table 4.24 validates this behavior with the highest

grain boundaries capacitance C_{gb}=9.41 F. The composition x=0.2 has large fused grains enhancing grain resistance R_g=10000 MΩ being the highest among all the compositions. The composition x=0.6 has large and well-connected platelet-type grains enhancing grain boundaries as seen in the micrograph. This causes polarization at the grains and grain boundaries that in turn causes capacitance of grain and grain boundaries to be high. This is validated by the high values of C_g=7503.9 μF and C_{gb}=1.42 F in Table 4.24.

Correlation between Grain/Grain boundaries simulated parameters and Dielectric Parameters

The composition x=0.2 has the lowest while x=0.6 owes the maximum dielectric constant (Fig. 4.104) at the lower frequencies. Maxwell-Wagner model suggests that grain boundary is dominant at low, however, grain at high frequency. Table 4.24 shows that the composition x=0.2 has the minimum grain capacitance C_g= 199.4 μF due to the lowest dielectric constant (ε'=54.16). The highest dielectric constant (ε'=7273.12) in x=0.6 attributing to the highest simulated grain capacitance C_g=7503.9 μF referring to a high polarization due to platelet type grains.

Correlation between Grain/Grain boundaries simulated parameters and Electric Modulus

The composition x=0.0 has the impact of both grain and grain boundaries as the semi-circle of this composition, lies in the mid-frequency region (Fig. 4.107). Thus having high values of C_g=4957.4 μF and C_{gb}=9.41 F. The composition x=0.2 also has its curve in both regions but possesses a major portion in low frequency attributing dominance of grain boundaries over grain which can be validated by high C_{gb}=1.32 F as compared to C_g=199.4 μF. The curve of compositions x=0.6 lies in the low-frequency region causing high C_{gb}=1.42 F.

4.6.3 Band gap Characteristics

Fig 4.112 displayed the Tauc plots drawn for the prepared $SrCo_xZr_xFe_{12-2x}O_{19}$/PANI composites. The required values of the band gap are acquired using equation 3.4 as given in chapter 3. The intercept on the x-axis is obtained from the linear region of the Tauc plot to determine the band gap. The band gaps of the prepared compositions x=0.0, 0.2, and 0.6 are 2.15, 1.63, and 1.37 eV respectively.

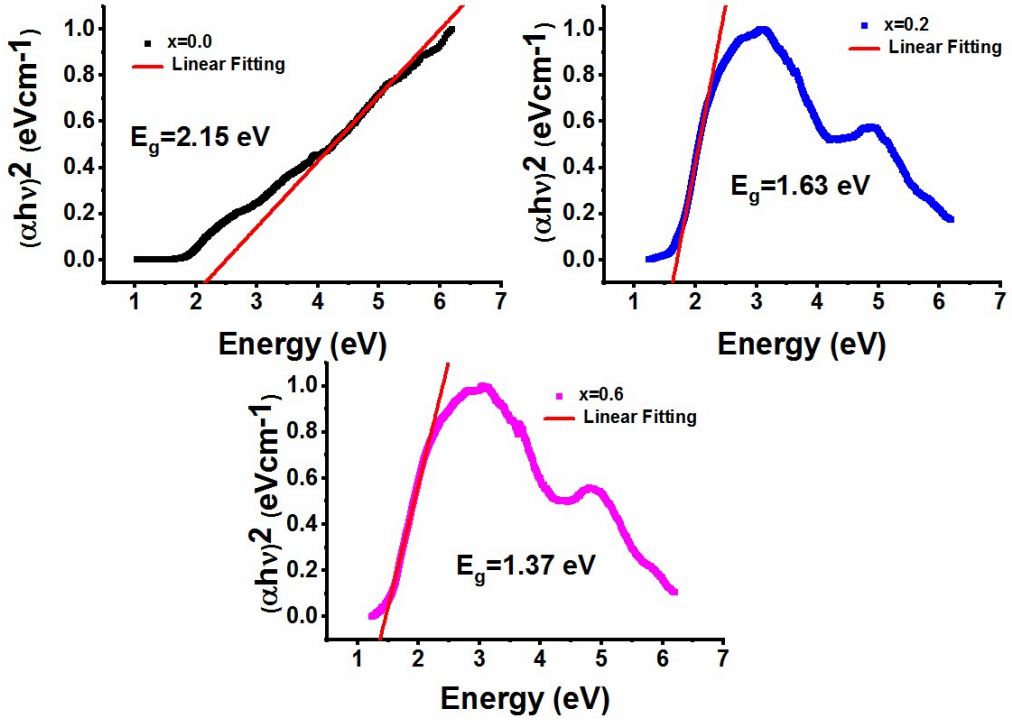

Fig. 4.112 Tauc plots for $SrCo_xZr_xFe_{12-2x}O_{19}$/PANI.

4.6.4 Magnetic Characteristics

The magnetic characterization of the prepared $SrCo_xZr_xFe_{12-2x}O_{19}$/PANI composites has been performed to understand the magnetic properties. The analysis is carried out using the plots between magnetization (M) and magnetic field (H). The M-H curves drawn for the prepared composites are shown in Fig. 4.113 (a). The site occupancy of the ions depends on their electronegativity. The higher electronegativity ions mostly prefer octahedral sites than the tetrahedral ones. The electronegativity of Zr^{4+}(1.33) are less than that of Co^{2+}(1.88) so they will prefer to occupy the tetrahedral site $4f_1(\downarrow)$. As per the ligand field theory, Co^{2+} with $3d^7$preferably choose octahedral sites 12k (↑), $2a(\uparrow), 4f_2(\downarrow)$ while Zr^{4+}prefer tetrahedral $4f_1(\downarrow)$ sites due to $3d^{10}$ configuration. Singh et al. [90] reported that Co^{2+} prefer to occupy octahedral sites and Godara et al. [109] reported that Zr^{4+}prefer tetrahedral $4f_1$ sites.

For hexaferrites, B is given as $B = H_a^2/15$ with H_a representing the anisotropy field. M-H loops show a steep rise in magnetization at low applied fields while it decays at the high fields as indicated in Fig. 4.113 (a). There is a large slope at a high field in

composition x=0.0 indicating an unsaturated state which reduces with the substitution of Zr^{4+} and Co^{2+}. This is due to the reduction in anisotropy field. The linear relationship above 10 KOe suggests that A/H and χ_P maybe removed and B is obtained from the relation $M = M_s\,(1 - B/H^2)$. After the determination of B, the values of H_a can be obtained from the relation $H_a^2 = 15\,B$. The M versus $1/H^2$ graphs are used to determine M_s.The linear fitting is used to obtain the required value as shown in Fig. 4.113 (b). Table 4.25 enlist the obtained parameters.

The relation of M_s with respective site values is given in Eq. 4.3. The relation shows that the occupation of weak/non-magnetic ions at spin-down sites ($4f_1\downarrow + 4f_2\downarrow$) enhances saturation magnetization while more occupancy at spin-up sites (2a↑ + 12k↑ + 2b↑) reduces it. In the prepared composites, there is an increment in M_s with the doping of Co-Zr. Ms increases by 9 % (47.80 to 52.3 emu/g) for x=0.0 to 0.2 due to the substitution of Zr^{4+} and Co^{2+}. As explained above Zr^{4+} prefer $4f_1(\downarrow)$ while Co^{2+} prefer $4f_2(\downarrow)$, hence the exchange of Fe^{3+} with diamagnetic Zr^{4+} and weak magnetic Co^{2+} decreases the value of M_b which intern increases the M_s. From composition x=0.2 to x=0.6, M_s decreased around 7 % which is because of the low magnetic moment of Co^{2+} (3μB) and diamagnetic Zr^{4+} (0 μB). The replacement of Fe^{3+} (5μB) causes an imbalance in electrical neutrality, hence to maintain it Fe^{3+} is converted into Fe^{2+} which causes a reduction in superexchange interactions which reduces M_s.

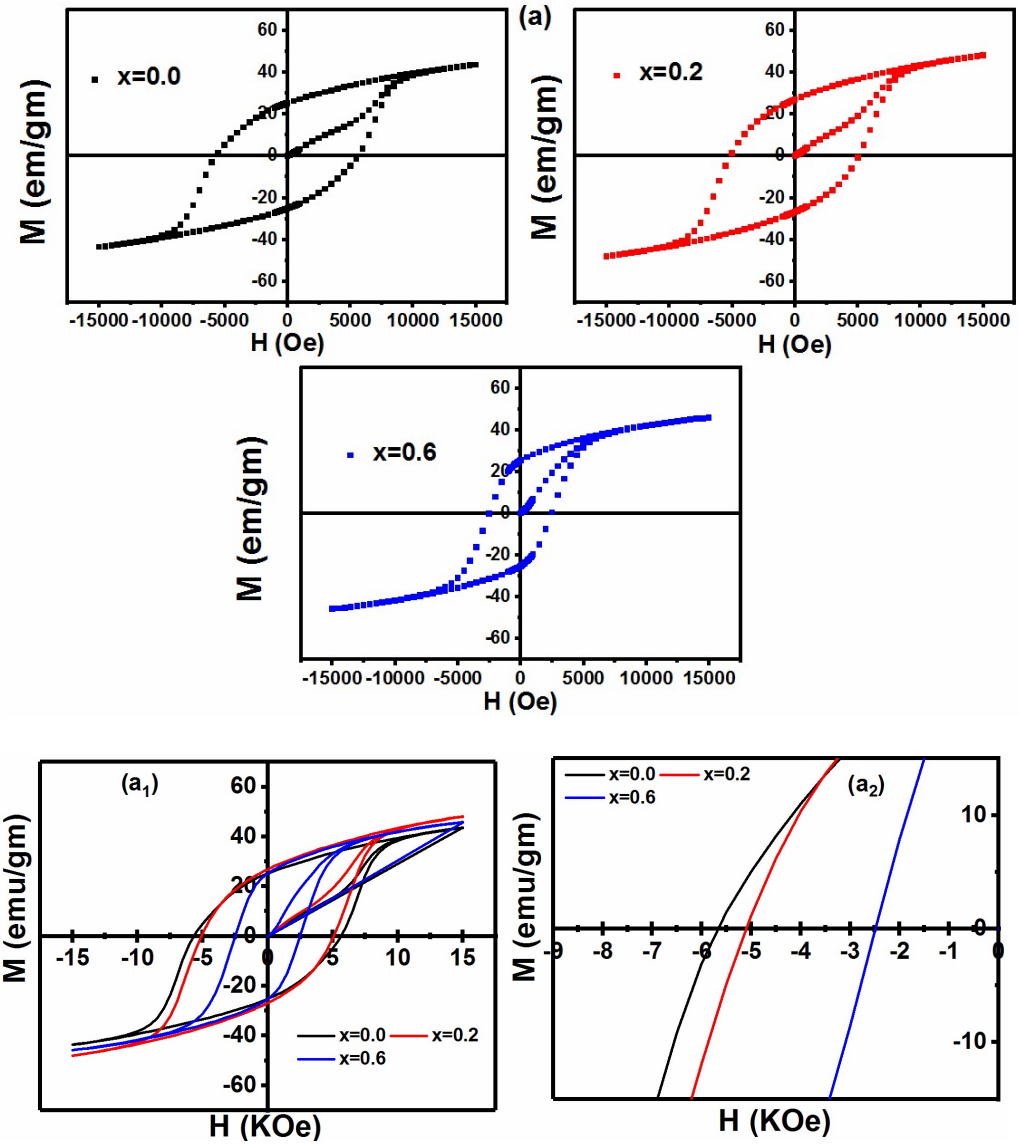
(a)
x=0.0
x=0.2
x=0.6
M (em/gm)
H (Oe)
60
40
20
0
-20
-40
-60
-15000 -10000 -5000 0 5000 10000 15000

(a1)
(a2)
x=0.0
x=0.2
x=0.6
M (emu/gm)
H (KOe)
60
40
20
0
-20
-40
-60
-15 -10 -5 0 5 10 15
10
0
-10
-9 -8 -7 -6 -5 -4 -3 -2 -1 0

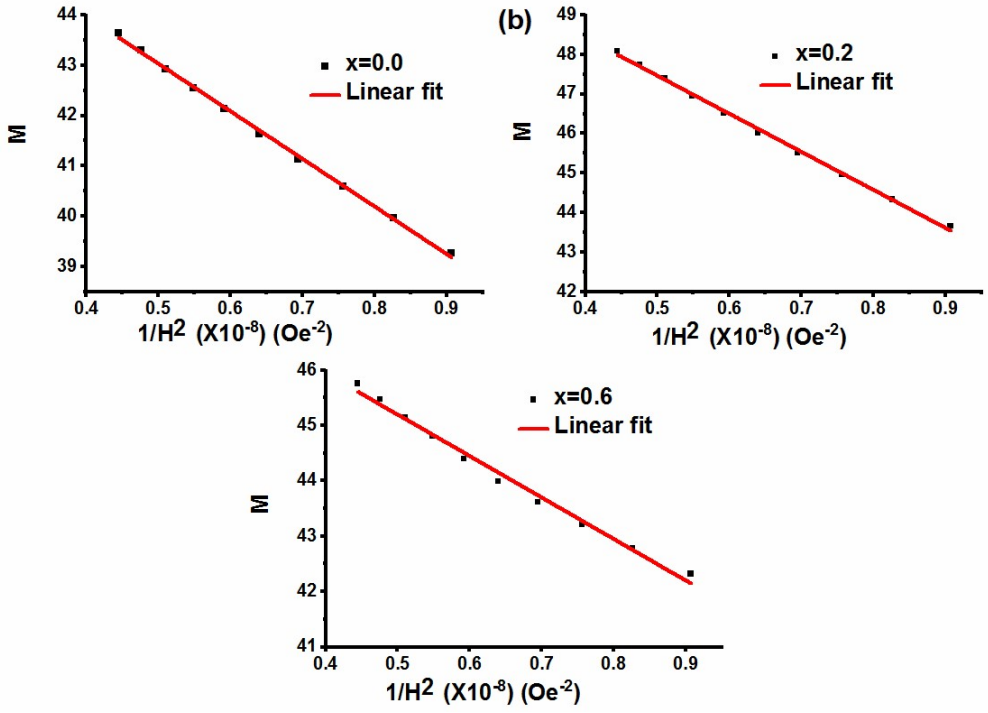

Fig. 4.113 (a) M-H loops (a_1, a_2) combined and enlarged view (b) Ms v/s $1/H^2$ plots of $SrCo_xZr_xFe_{12-2x}O_{19}$/PANI.

Table 4.25 indicates the coercivity (H_c) decreased by enhancing the doping of Co-Zr. It is well known that soft ferrites having low coercivity are the prime candidates in the design of a microwave absorber. The composite x=0.0 has the highest H_c=5679 Oe while the x=1.0 has the lowest value of H_c=2483 Oe. The substitution of diamagnetic Zr^{4+} and weak magnetic Co^{2+} caused a 56 % decrease in H_c and made the composites magnetically soft. There are two factors influencing the values of H_c one is intrinsic involving anisotropy field H_a and the second is morphology as an extrinsic factor. From the table, it can be noted that there is a decrease in the value of H_a. The consistent fall in H_a causes a decrease in H_c as both are proportional to each other. H_a decreases 22 % from x=0.0 to x=1.0 which is due to the replacement of Fe^{3+} at $4f_2$ and 2b sites, as they contribute to large H_a, substitution at these sites causing a reduction in H_a. H_a decreases around 12 % while H_c decreases more i.e 56 % so the reason for more reduction in H_c is the large ionic radius of Co^{2+} (0.745 Å) and Zr^{4+} (0.72 Å) and as compared to Fe^{3+} (0.645 Å). Considering the morphology, a large increase in the grain size by the increase of Co-Zr is viewed. The large platelet-type grains can be seen in the composition x=1.0.

Since H_c is related in reverse to the grain size the increase in grain size causes a reduction in H_c.

Table 4.25. Magnetic parameters determined from M-H loops for $SrCo_xZr_xFe_{12-2x}O_{19}$/PANI.

x	M_s (emu/g)	M_r (emu/g)	$H_a(kOe)$	H_c (Oe)	M_r/M_s
0.0	47.8	25.17	17.2	5679	0.53
0.2	52.3	26.86	16.6	5106	0.51
0.6	48.9	25.19	15.2	2483	0.52

M_r/M_s represents the retention of magnetization with the removal of the applied field. This ranges between 0 and 1 and a value less than 0.5 represents randomly oriented multi-domain particles while values greater than 0.5 indicate the single domain. All the compositions have M_r/M_s ratio more than 0.5 showing a single domain.

4.6.5 Electromagnetic Characteristics

4.6.5.1 Complex permeability and complex permittivity

The plots of (ε'), (ε''), (μ'), (μ'') against the frequency for the prepared $SrCo_xZr_xFe_{12-2x}O_{19}$/PANI composites are given in Fig 4.113. ε' varies non-monotonically with the inclusion of Co-Zr. The ε'' decreased with the increase in frequency. There is a decrease in the dielectric constant with the increase in frequency. In composition x=0.2 the ε' first decreased with the frequency, however, for high frequency it increases. The composition x=0.0 has dual relaxation peaks in ε' one around 9.25 GHz and another at 10.25 GHz. The compositions x=0.2 and x=0.6 have a relaxation peak around 10.5 GHz. The relaxation peaks can also be seen in the plots of ε'' for all the compositions.

The doping of Co-Zr has a non-monotonous variation in the permeability of the prepared composites. μ' increases with the increase in frequency for all the compositions. The composition x=0.6 has the lowest values of μ' at low frequencies but

attains the highest value at high frequencies among all the composites. The composition x=0.2 has the large relaxation peak near 11.5 GHz, however, x=0.0 has a small peak at 9.5 GHz. The compositions x=0.0 and 0.2 show relaxation peaks in μ". The composition x=0.2 has a large relaxation peak at the high frequency. The maximum μ" is also obtained in composition x=0.2.

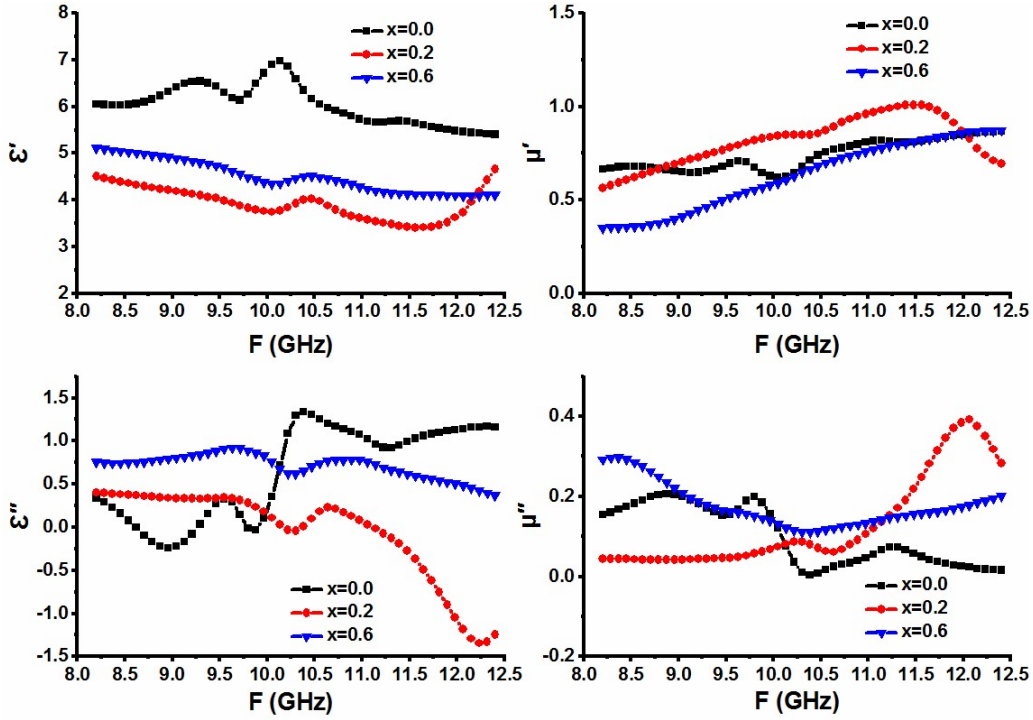

Fig. 4.114 Complex permittivity and permeability versus frequency plots of $SrCo_xZr_xFe_{12-2x}O_{19}$/PANI.

The permittivity/permeability depends on porosity, grain size, electron spin, and dipole polarization. The dielectric polarization is caused by the electron hopping in Fe^{2+}/Fe^{3+} [95]. The polarization is reduced by the large porosity as it causes hindrance to the field flow. The exchange resonance among Fe^{3+}/Fe^{2+} and ferromagnetic resonance affects the complex permeability [96-97]. The decrement in the number of Fe^{3+} is due to the increase in doping of Co-Zr which affects the polarization and resonance. The non-magnetic pores having demagnetizing fields present in the morphology of the prepared composites affect magnetization/polarization associated with the permittivity/permeability. The inconsistent change in the size of the grain/grain boundary (micrographs Fig. 4.103) also affects the permittivity and permeability.

The larger grains support electron hopping, however, the grain boundaries obstruct the field flow. The accumulation of charges at grain boundaries promotes polarization while large grains increase electron spin that increases permeability. The reduction in exchange resonance due to porosity and small grains is responsible for magnetic loss for Fe^{3+} and Fe^{2+}. The relaxation peak observed in ε', ε'' and μ', μ'' for the prepared composites are attributed to the dielectric relaxation and ferromagnetic resonance respectively.

4.6.5.2 Microwave absorption in $SrCo_xZr_xFe_{12-2x}O_{19}$/PANI

The reflection loss is used to investigate the absorption characteristics of the prepared composites. RL is determined using the material's input impedance Z_{in} and free space characteristic impedance Z_0 using the equations 3.13 and 3.14 as discussed in Chapter 3. The impedance matching mechanism, $\lambda/4$ mechanism, and dielectric/magnetic loss are used to explain the absorption characteristics of the prepared composites as discussed in the following sections.

4.6.5.3 Quarter Wavelength Mechanism

The graphs of RL versus frequency at different simulated thicknesses are used to explain microwave absorption in the prepared ferrite composites. The RL plots of prepared $SrCo_xZr_xFe_{12-2x}O_{19}$/PANI ferrites are shown in Fig. 4.115 (a, c, e, g), 4.116 (a, c), and 4.117 (a, c, e, g). The parameters are determined from these figures. Table 4.26 summarizes the values of these parameters.

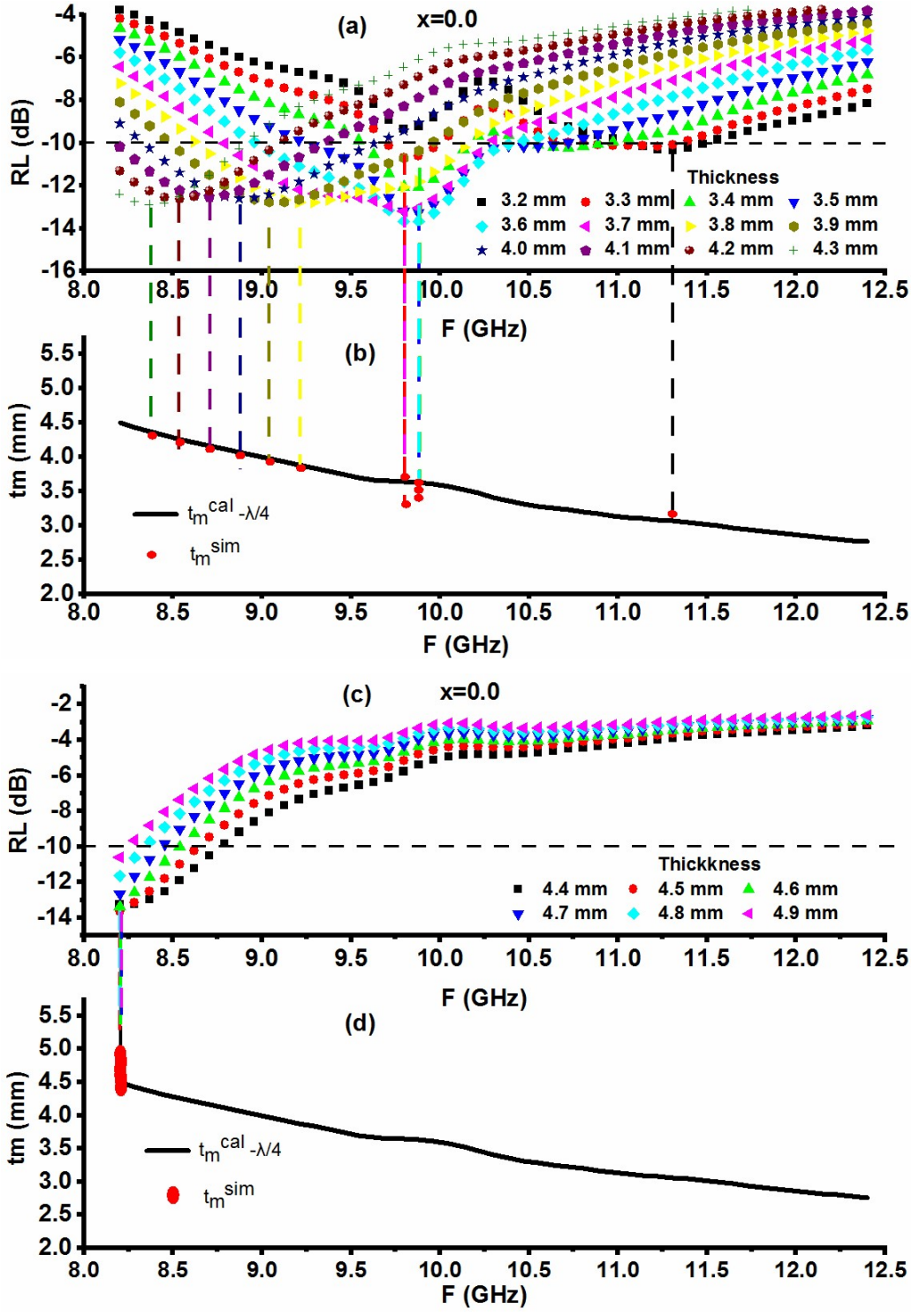
(a)
x=0.0
RL (dB)
F (GHz)
Thickness
3.2 mm
3.3 mm
3.4 mm
3.5 mm
3.6 mm
3.7 mm
3.8 mm
3.9 mm
4.0 mm
4.1 mm
4.2 mm
4.3 mm
(b)
tm (mm)
tm cal -λ/4
tm sim
(c)
x=0.0
Thickkness
4.4 mm
4.5 mm
4.6 mm
4.7 mm
4.8 mm
4.9 mm
(d)

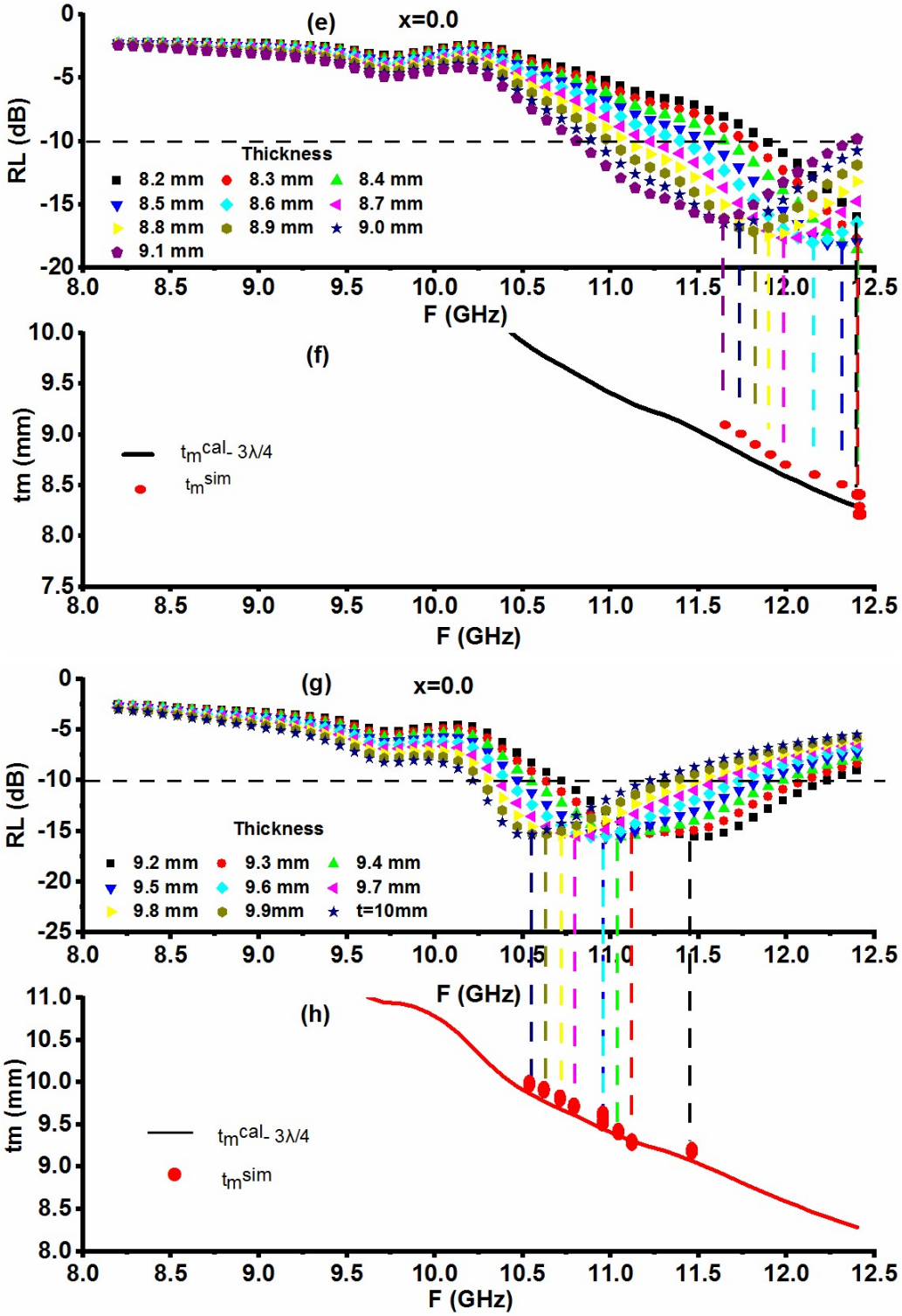

Fig. 4.115 (a, c, e, g) RL versus frequency (b, d, f, h) thickness versus frequency in x=0.0 for $SrCo_xZr_xFe_{12-2x}O_{19}$/PANI.

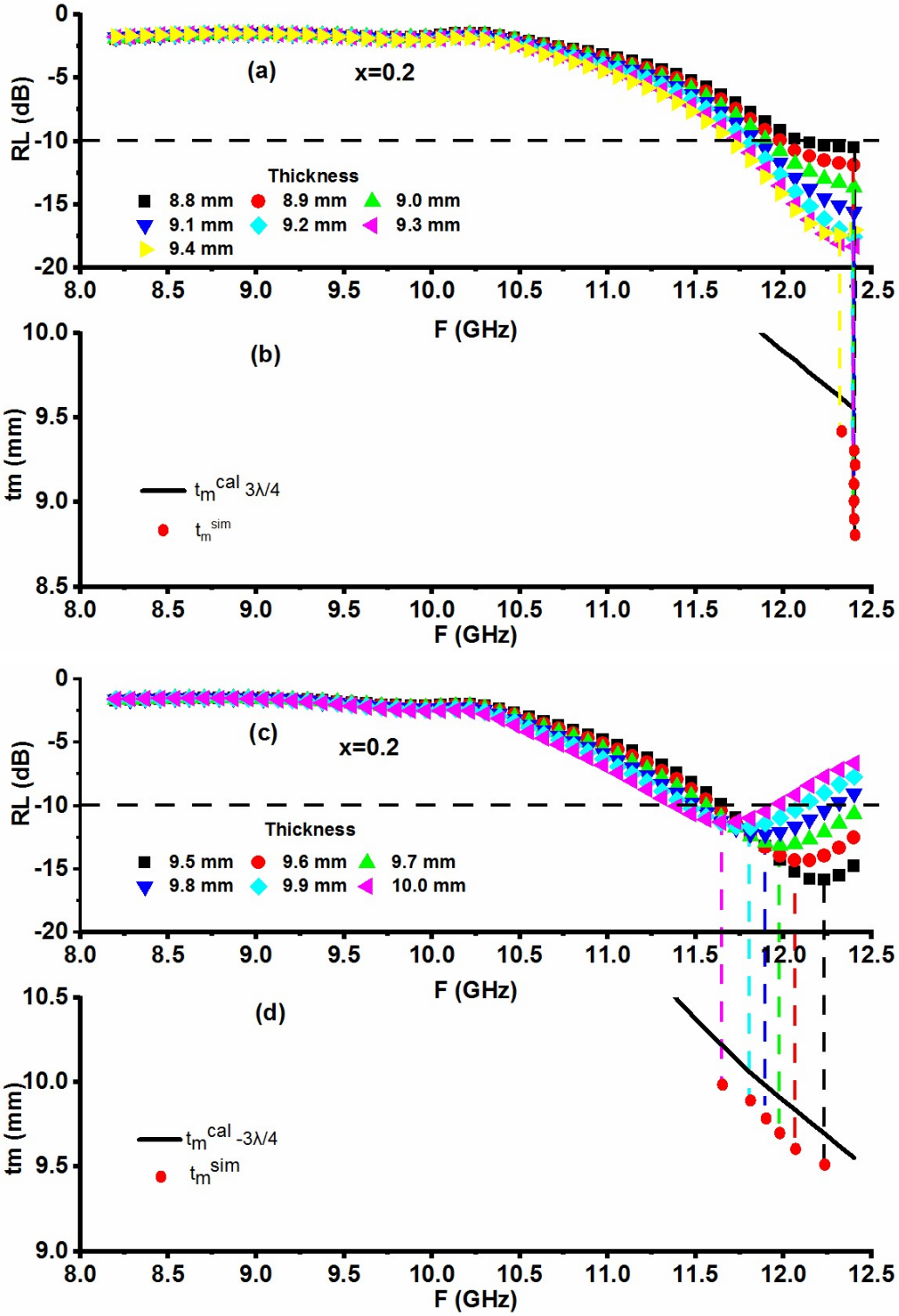

Fig. 4.116 (a, c) RL versus frequency (b, d) thickness versus frequency in x=0.2 for $SrCo_xZr_xFe_{12-2x}O_{19}$/PANI.

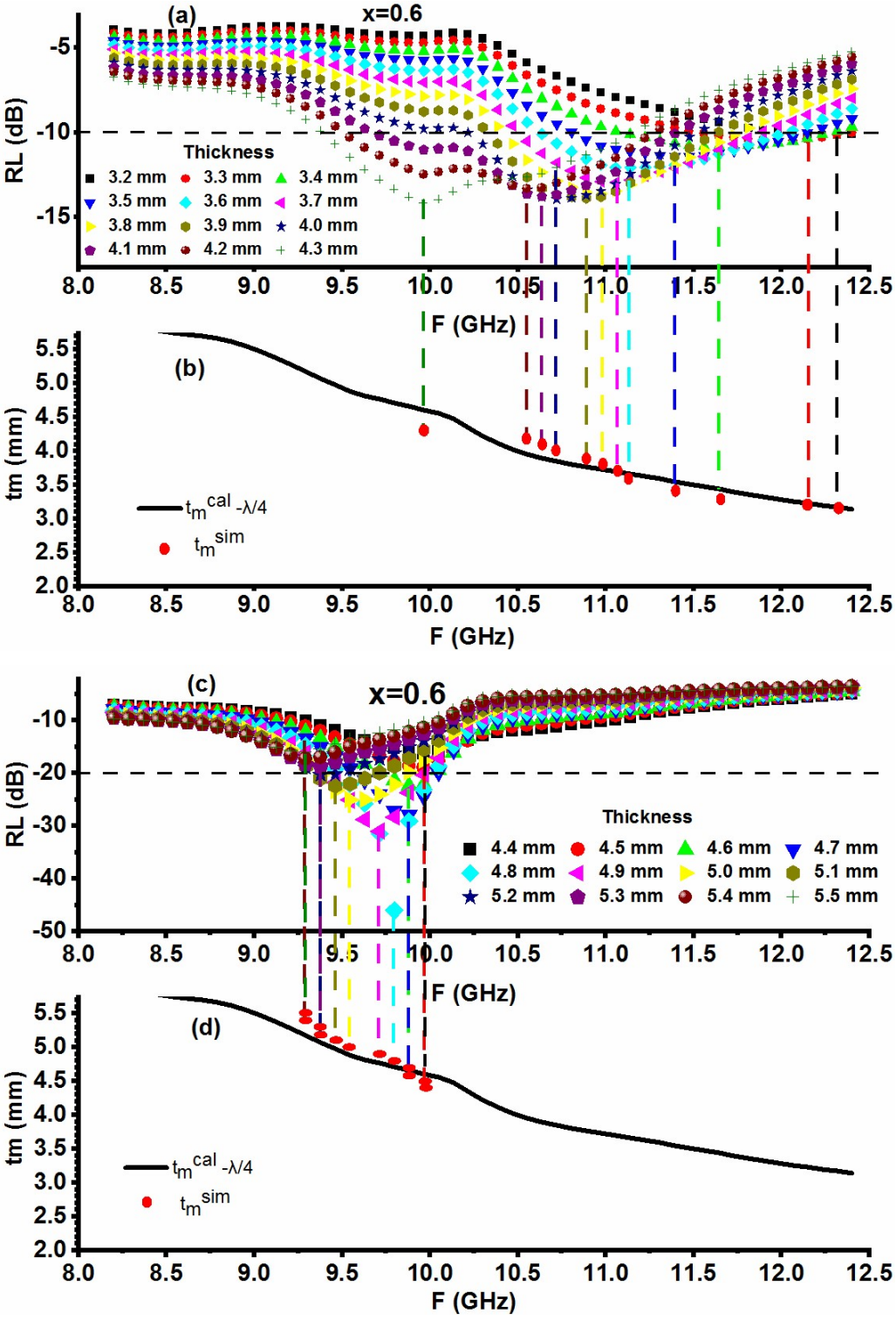
(a)
x=0.6
RL (dB)
Thickness
3.2 mm
3.3 mm
3.4 mm
3.5 mm
3.6 mm
3.7 mm
3.8 mm
3.9 mm
4.0 mm
4.1 mm
4.2 mm
4.3 mm
F (GHz)
(b)
tm (mm)
t_m^{cal} -λ/4
t_m^{sim}
F (GHz)
(c)
x=0.6
RL (dB)
Thickness
4.4 mm
4.5 mm
4.6 mm
4.7 mm
4.8 mm
4.9 mm
5.0 mm
5.1 mm
5.2 mm
5.3 mm
5.4 mm
5.5 mm
F (GHz)
(d)
tm (mm)
t_m^{cal} -λ/4
t_m^{sim}
F (GHz)

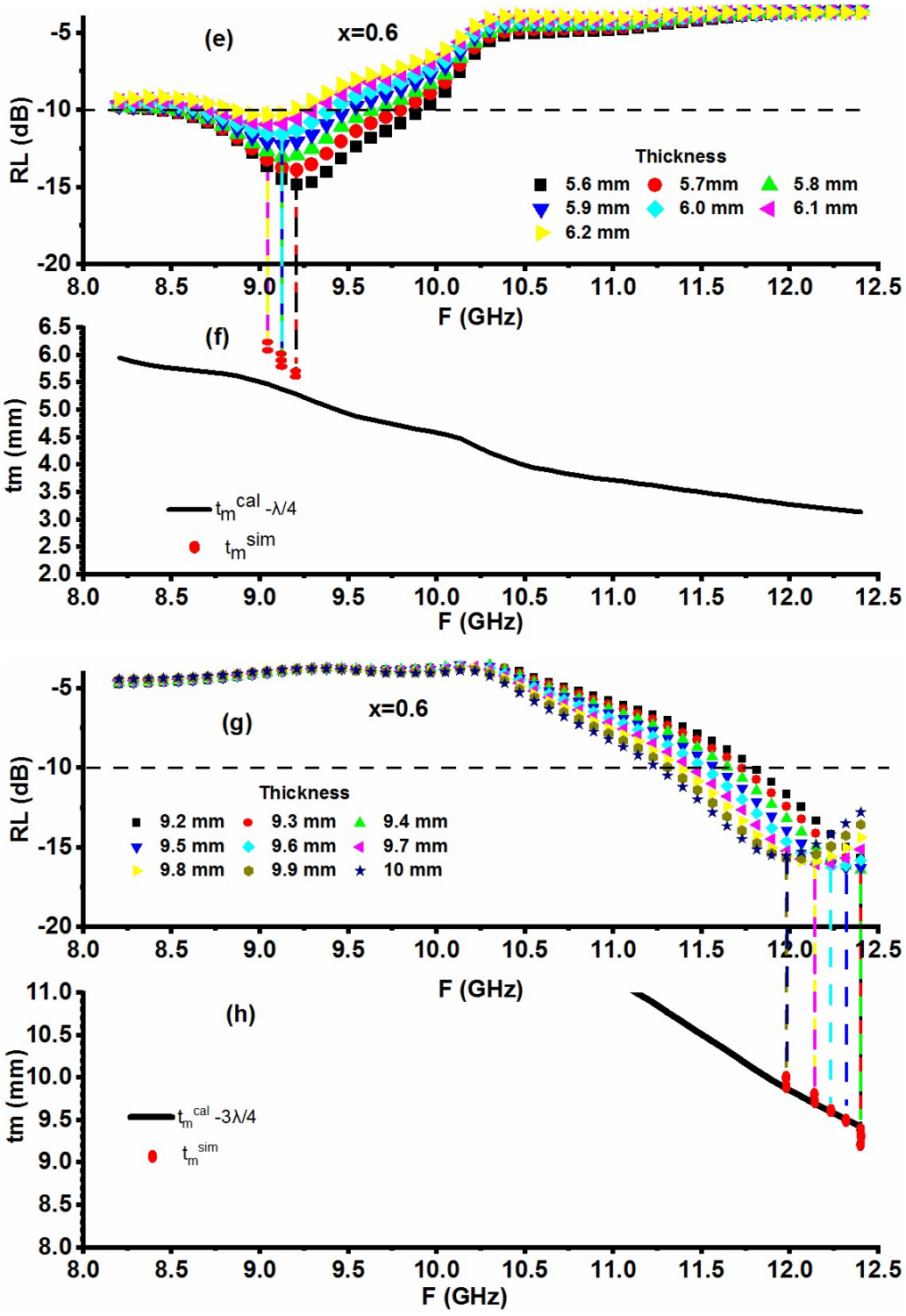

Fig. 4.117 (a, c, e, g) RL versus frequency (b, d, f, h) thickness versus frequency in x=0.6 for $SrCo_xZr_xFe_{12-2x}O_{19}$/PANI.

RL of -45.98 dB is achieved in composition x=0.6 at 9.80 GHz frequency for a low thickness of 4.8 mm. RL ranges between -12.08 dB and -45.98 dB at 11.14 GHz and 9.80 GHz for a thickness of 3.6 and 4.8 mm. RL peak varies non-monotonically with the increment in thickness. Fig. 4.115 (a, c, e, g) displayed the RL versus frequency graphs at various thicknesses for composition x=0.0. In this composition, the thickness from 3.2 mm (RL=10.35 dB at 11.31 GHz) to 10.0 mm (-15.35 dB at 11.14 GHz) has a reflection loss of -10 dB. With respect to the matching frequency, RL peaks shifted non-monotonically with the increase in thickness. The various thicknesses of 8.4, 8.5, and 8.8 mm show RL≥ -20 dB frequency band.

An RL=-18.29 is obtained at 9.3 mm with a matching frequency of 12.40 GHz in x=0.2 Fig. 4.116 (a, c). The thicknesses from 8.8 mm to 10.0 mm possess $RL \geq$ -10 dB with respective values of RL=-10.50 dB at 12.40 GHz and RL=-11.29 dB at 11.64 GHz respectively. In association with matching frequency, RL peak shifts to low frequency with the enhancement in the thicknesses. The largest -10 dB frequency band among all the thicknesses ranging from 11.56-12.40 GHz is obtained at 9.7 mm in this composite. In composition x=0.6, the highest RL of -45.98 dB at 9.80 GHz for a thickness of 4.8 mm is observed. This composition possesses an RL ≥ -10 dB frequency band ranging from 8.45-12.40 GHz for a thickness from 3.6 to 10.0 mm Fig. 4.117 (a, c, e, g). Corresponding to the matching frequency RL peaks shifted towards low frequency for low thicknesses, however, at high thicknesses, it moves to high frequency. $RL \geq$ -20 dB frequency band is also observed in this composition at thicknesses of 4.7, 4.8, 4.9, 5.0, and 5.1 mm.

The simulated thickness (t_m^{sim}) and calculated thickness (t_m^{cal}) were compared to explain the relation between RL peaks and the λ/4 mechanism. The graphs of the calculated thickness in the observed range are demonstrated in Fig. 4.115 (b, d, f, h), 4.116 (b, d), and 4.117 (b, d, f, h). For the comparison lines from RL peaks are brought to thickness versus frequency graphs. The composition x=0.0 and x=0.6 matches the nλ/4 mechanism for n=1 and 3, while in composition x=0.2 it is satisfied for n=3. The quarter-wavelength mechanism originates -10 dB bandwidths in all the compositions as given in Table 4.26. -10/-20 dB RL bands are obtained in composition x=0.0 from 3.5 to 9.2 mm. For this composition maximum bandwidth of 1.51 GHz associated with a

-10 dB band is observed at 9.2 mm thickness with the respective band of 10.72-12.23 GHz. Besides this, broad bandwidths of 1.43, 1.43, 1.35, 1.34, and 1.26 GHz are also obtained in this composition at the respective thickness of 3.7, 9.0, 3.5, 3.9, and 8.8 mm respectively. An *RL* ≥ -20 dB bandwidth of 0.25 GHz at 8.5 mm thickness and 12.32 GHz matching frequency is also obtained. Also, a bandwidth of 170 MHz at 8.4 and 8.8 mm corresponding to *RL* ≥ -20 dB is achieved.

The composition x=0.2 has its maximum -10 dB bandwidth of 0.84 GHz from 11.56-12.40 GHz at the thickness of 9.7 mm. Bandwidths of 0.76, 0.67, 0.59, and 0.59 GHz are also obtained at the thicknesses of 9.6, 9.4, 9.3, and 9.2 mm respectively. The composition x=0.6 has the highest bandwidth of 1.68 GHz for a low thickness of 4.1 and 4.4 mm with a -10 dB frequency band of 9.71-11.39 and 9.29-10.97 GHz respectively. Besides this, the broad bandwidth of 1.60, 1.43, 1.43, 1.35, 1.34, 1.34, and 1.26 GHz are achieved at a thickness of 5.4, 5.1, 5.0, 4.9, 4.8, 3.6, and 4.7 mm. The highest *RL* ≥ -20 dB bandwidth of 0.50 GHz at 4.9 mm thickness and 9.71 GHz matching frequency is also obtained. *RL* ≥ -20 dB bandwidths of 0.42, 0.42, 0.33, and 0.25 GHz at respective thicknesses of 4.8, 5.0, 4.7, and 5.1 mm are also observed in this composition.

Table 4.26. RL with matching thickness/frequency, BW, and PBW for $SrCo_xZr_xFe_{12-2x}O_{19}$/PANI.

x	Max. RL (dB)	Matching Thickness (mm)	Matching Frequency (GHz)	10 dB band (GHz)	-10 dB BW (GHz)	-20 dB band (GHz)	-20 dB BW (GHz)	BTR	PBW (%)
0.0	-13.25	3.5	9.88	9.29-10.64	1.35	-	-	1.171	13.664
	-13.19	3.7	9.80	8.79-10.22	1.43	-	-	1.291	14.592
	-12.77	3.9	9.04	8.54-9.88	1.34	-	-	1.221	14.823
	-18.53	8.4	12.4	11.73-12.40	0.67	12.23-12.40	0.17	0.165	5.403
	-18.19	8.5	12.32	11.56-12.40	0.84	12.15-12.40	0.25	0.207	6.818
	-17.45	8.8	11.90	11.14-12.40	1.26	11.81-11.98	0.17	0.311	10.588
	-16.67	9.0	11.73	10.97-12.40	1.43	-	-	0.350	12.191
	-15.59	9.2	11.48	10.72-12.23	1.51	-	-	0.376	13.153
0.2	-13.61	9.0	12.40	11.98-12.40	0.42	-	-	0.094	3.387
	-17.53	9.2	12.40	11.81-12.40	0.59	-	-	0.131	4.758
	-18.29	9.3	12.40	11.81-12.40	0.59	-	-	0.130	4.758

	-17.42	9.4	12.32	11.73-12.40	0.67	-	-	0.147 5.438
	-14.31	9.6	12.06	11.64-12.40	0.76	-	-	0.165 6.344
	-13.14	9.7	11.98	11.56-12.40	0.84	-	-	0.181 7.012
0.6	-12.08	3.6	11.14	10.64-11.98	1.34	-	-	0.876 12.029
	-13.79	4.1	10.64	9.71-11.39	1.68	-	-	1.112 15.789
	-16.30	4.4	9.96	9.29-10.97	1.68	-	-	1.124 16.867
	-27.81	4.7	9.88	9.04-10.30	1.26	9.63-9.96	0.33	0.864 12.753
	-45.98	4.8	9.80	8.96-10.30	1.34	9.54-9.96	0.42	0.908 13.673
	-30.97	4.9	9.71	8.87-10.22	1.35	9.46-9.96	0.50	0.912 13.903
	-24.98	5.0	9.63	8.79-10.22	1.43	9.38-9.80	0.42	0.955 14.849
	-22.44	5.1	9.46	8.70-10.13	1.43	9.38-9.63	0.25	0.955 15.116
	-17.25	5.4	9.29	8.45-10.05	1.60	-	-	1.047 17.223
	-15.85	9.8	12.15	11.39-12.40	1.01	-	-	0.219 8.313
	-15.53	10.0	11.98	11.31-12.40	1.09	-	-	0.233 9.098

4.6.5.4 Impedance matching mechanism

The input impedance of the material (Z_{in}) is different from that of the free space (Z_o=377 Ω) due to the different permittivity/permeability. The difference between these two affects the absorption characteristics of the material. Due to this mismatch, the major part of the incident signal gets reflected from the surface of the material and less portion enters the material. However, with impedance matching major portion of the signal travels into the material and gets absorbed by the material. Hence analysis of the impedance matching mechanism becomes essential for the development of an effective absorber.

The graphs of reflection loss and impedance i.e. $|Z_{in}|$ with frequency for the composites are displayed in Fig. 4.118. Table 4.27 enlists the values of Z_{in} corresponding to the maximum reflection loss of the different compositions. Impedance matching is satisfied in composition x=0.0 and x=0.6 for their highest RL peaks while there is a deviation in compositions x=0.2 and x=0.6 at few frequencies. An RL peak of -18.53 dB at 12.40 GHz for 8.4 mm observed in the composition x=0.0 has a corresponding value of Z_{in}=298.88 Ω which is close to Z_o=377 Ω. The highest RL peak of RL=-45.98 at 9.80 GHz in composition x=0.6 has Z_{in}=380.60 Ω which is in

proximity to Z_o=377 Ω. Composition x=0.2 there is a discrepancy with $|Z_{in}|$ as there is an RL peak of -18.29 dB at 12.40 GHz with Z_{in}=473.75 Ω while there is no RL peak at 11.64 GHz with a Z_{in}=382.79 Ω which is more close to Z_o=377 Ω than Z_{in}=473.75 Ω. Similarly in composition x=0.6 at 10.47 GHz no RL peak is present with Z_{in}=362.39 Ω.

This deviation is due to the complex nature of $|Z_{in}|$ involving real and imaginary terms Z_{real} and Z_{img}. That's why, Z_{real} and Z_{img} are determined and plots of Z_{real} and Z_{img} are plotted as given in Fig. 4.119. The determined values of Z_{real} and Z_{img} are listed in Table 4.27. For the successful implementation of the impedance matching the impedances of the material must follow exactly/nearly the criteria of 377 Ω and/or 0. From Table 4.27 it can be noted that the highest *RL*=-45.98 dB at 9.80 GHz obtained in x=0.6 follows this condition with Z_{real}=380.60 Ω & Z_{img}=1.22 Ω which are close to 377 Ω and 0. For composite x=0.2 no RL peak at 11.64 GHz with a Z_{in}=382.79 Ω is due to Z_{real}=293.17 Ω, Z_{img}=246.12 Ω which are far away from Z_{real}=377 Ω, Z_{img}=0 criteria. In the same way for composition x=0.6, no RL peak at 10.47 GHz with Z_{in}=362.39 Ω dB is due to Z_{real}=276.54 Ω and Z_{img}=-234.21 Ω.

Thus it can be summarized that the discrepancies observed in x=0.2 and x=0.6 are due to the mismatch in obtained Z_{real}/Z_{img} values from the required Z_{real}/Z_{img} values of 377 Ω and/or zero. The doping of Co-Zr has enhanced the input impedance Z_{in} (Z_{real} and Z_{img}).

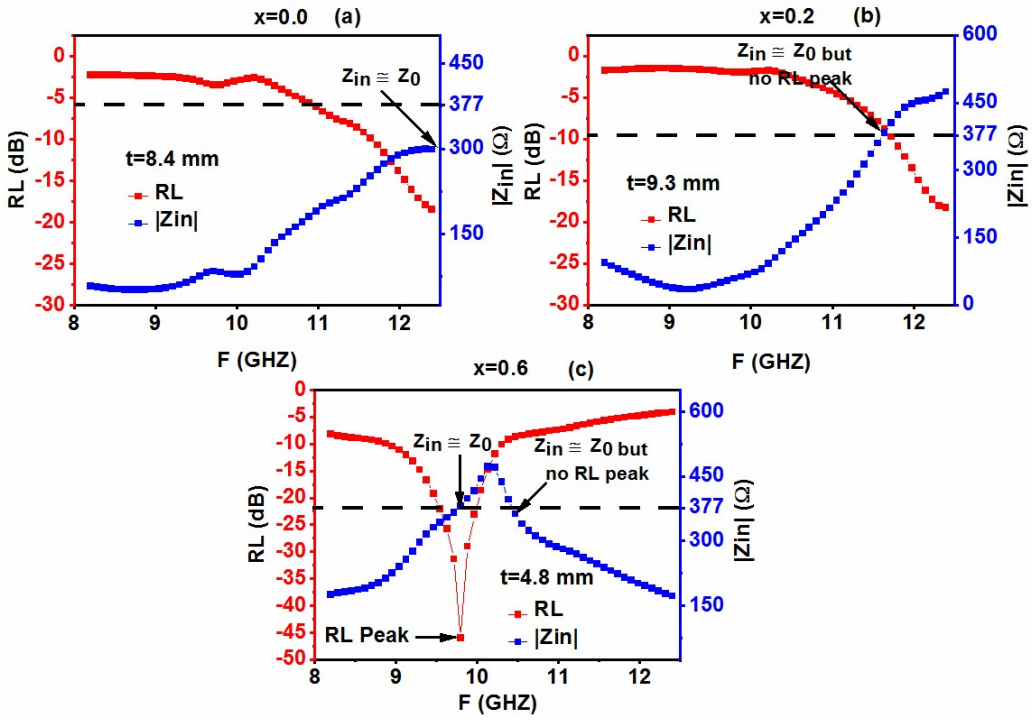

Fig. 4.118 Z_{in} and RL curve against frequency for $SrCo_xZr_xFe_{12-2x}O_{19}$/PANI.

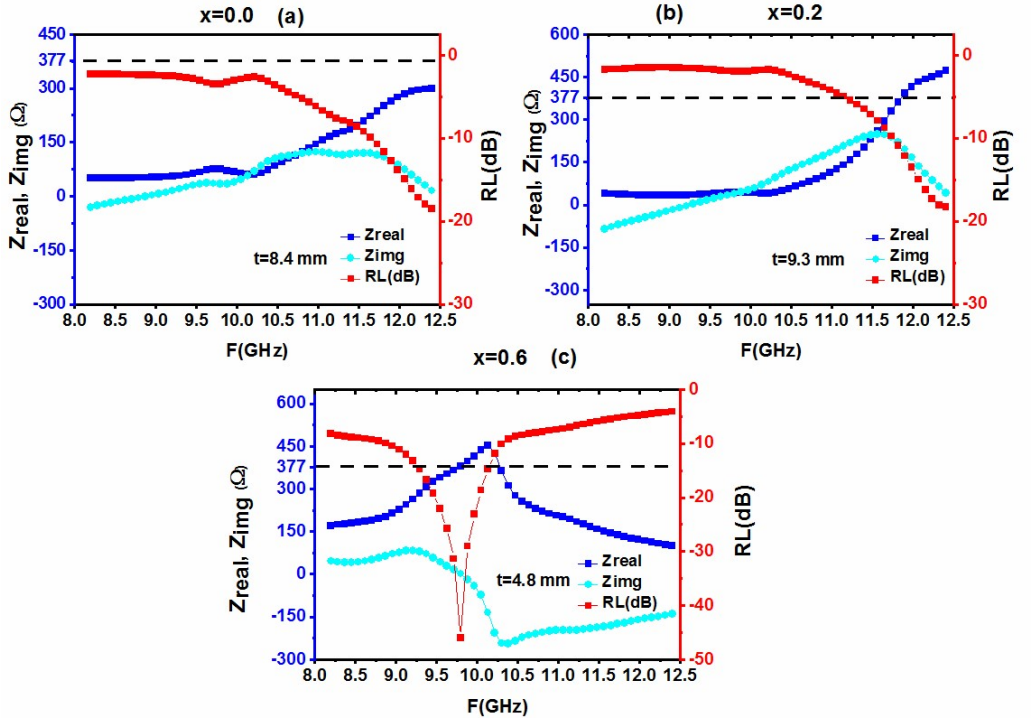

Fig. 4.119 Z_{real}, Z_{imag}, and RL v/s frequency for $SrCo_xZr_xFe_{12-2x}O_{19}$/PANI.

Table 4.27. Z_{in}, Z_{real}, and Z_{imag} values corresponding to RL_{max} for $SrCo_xZr_xFe_{12-2x}O_{19}$/PANI.

x	RL (dB)	Matching Thickness (mm)	Matching Frequency (GHz)	$\|Z_{in}\|$ (Ω)	Z_{real} (Ω)	Z_{img} (Ω)
0.0	-18.53	8.4	12.40	298.88	298.47	15.55
0.6	-18.29	9.3	12.40	473.75	471.98	40.96
1.0	-45.98	4.8	9.80	380.60	380.60	1.22

4.6.5.5 Role of Electromagnetic/Material Parameters

No doubt, the λ/4 mechanism, and input impedance matching have their roles in absorption, however, the dielectric/magnetic losses (ε''), (μ'') due to the complex nature of permittivity/permeability also contribute to the absorption which also requires an investigation.

The contribution of relaxation peaks observed in ε″ and μ" to absorption can be understood as: ε″ peak at 9.54 GHz in composition x=0.0 attribute to an *RL* =-12.57 dB at 9.54 GHz for 3.7 mm; in x=0.6 the *RL*=-30.97 dB at 9.71 GHz with the thickness of 4.9 mm correspond to ε″ peak at 9.71 GHz; composition x=0.0 has an *RL*=-13.25 at 3.5 mm attributing μ" peak at 9.88 GHz; a μ" peak at 12.06 GHz correspond to *RL*=-14.31 dB at 9.6 mm and the maxima in μ" at 12.40 GHz attribute to the maximum *RL*=-18.29 dB in composition x=0.2. Hence dielectric and magnetic loss are contributing for absorption in the prepared composites.

4.6.5.6 Eddy Current Loss

Eddy current loss in ferrites also has an impact on absorption. The formula used to determine the eddy current loss is given in Eq. 4.4.

When C_0 does not vary with the frequency increment it shows it is contributing to absorption. Hence to evaluate the role of it the plot of C_0 versus frequency has been

plotted as given in Fig. 4.120. There is a flat line in all the compositions showing constant values of C_0 for change in frequency which indicates the role of eddy current loss in the absorption of ferrite composites.

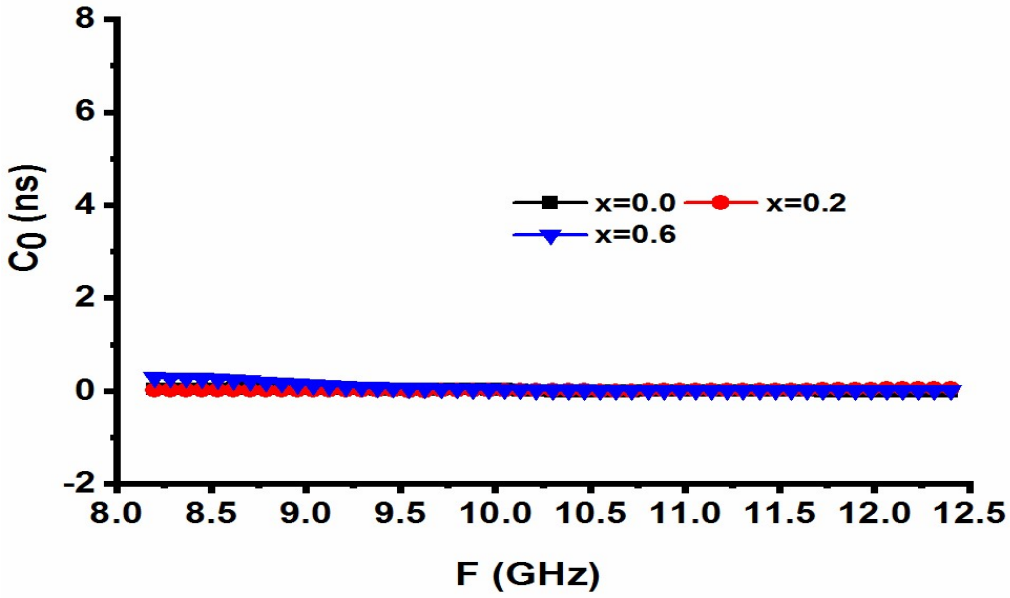

Fig. 4.120 C_0 versus frequency curve for $SrCo_xZr_xFe_{12-2x}O_{19}$/PANI.

4.6.5.7 Bandwidth to Thickness Ratio

Besides RL≥-10 dB, the broad bandwidth with less thickness is an important factor in the design and characterization of an absorber. After achieving the desired RL≥-10 dB benchmark, one should aim at achieving low thicknesses, rather than only increasing reflection loss. Hence, BTR and PBW are determined from Eq. 4.5 and 4.6.

The doping of Co-Zr in PANI composites increased BTR as can be seen in Table 4.26. In composition x=0.0 the largest BTR of 1.291 at 9.80 GHz with RL=-13.19 dB is obtained. A high BTR of 1.222 at 9.04 GHz with RL=-12.77 dB and 1.171 at 9.88 GHz with RL=-13.25 dB are also observed in this composition. Comparatively small BTR=0.181 at the frequency of 11.98 GHz with RL= -13.14 dB is obtained in x=0.2. In composite x=0.6, the highest BTR of 1.124 is achieved at 4.4 mm thickness. The high BTR of 1.112, 1.047, 0.955, 0.955, and 0.912 are obtained at thicknesses of 4.1, 5.4, 5.0, 5.1, and 4.9 mm. There is an increase in percentage bandwidth with the increase in Co-Zr dopant. The composition x=0.0 has its maximum PBW=14.823 at 3.9

mm. Also high PBW=14.592. 13.664, and 13.153 are observed at 3.7, 3.5, and 9.2 mm thickness. The highest PBW of 17.22 for the thickness of 5.4 mm is obtained in composition x=0.6. The high PBW of 16.87, 15.79, 15.12, 14.85, and 13.90 are also achieved in this composition.

4.7 Application areas for developed absorbers

Thus, based on the investigation done in the research work, it can be concluded that the objective of the research work which was to develop an efficient RF absorber has been achieved successfully. The developed ferrites and their composites showed good absorption. The $SrCo_xZr_xFe_{12-2x}O_{19}$/PANI composites gave the highest absorption with -45.98 dB with a low thickness of 4.8 mm. $SrCo_xNi_xFe_{12-2x}O_{19}$/PANI composites provide a -41.39 dB reflection loss at 5.4 mm. The application of microwave absorbers is well-known in anechoic chambers. An anechoic chamber is a room that is free from the reflection/echo of the signals. The walls and floor are designed using absorbers which absorb the unwanted signal. Antenna testing is performed in anechoic chambers as the reflected signals during testing affect the testing process as these will work as source signals which will affect the performance of the antenna. As we have developed absorbers having thin thicknesses, these can be used in the form of tiles on the floor/walls of an anechoic chamber.

X-band radars are the radars that use X-band spectrum i.e. 8.2 to 12.4 GHz. Due to the short wavelength (3.75-2.42 cm), these radars are utilized in weather monitoring and air traffic control. Besides that, they are also used in sea navigation and ship traffic control. The electromagnetic signal from these radars causes interference in the electronic devices in the surroundings. Since we have developed the absorbers for the X-band frequency range these can be utilized at these places to protect those devices. Besides the radar application, the X-band is also used in satellite communication for example Sknet, XTAR-EUR, and Spainsat are the satellites that use X-band. The meteorological satellite uses this frequency band for weather monitoring. The frequency range of 10.0-10.5 GHz is used for amateur radio operations, as well as the range from 10.45-10.5 GHz is utilized for amateur satellite operations. Both the ranges come under our investigated frequency range and the designed absorbers can be utilized to reduce electromagnetic interference in this sector.

Terrestrial communication uses a frequency range of 10.15-10.7 GHz for terrestrial broadband. This frequency range comes under the X-band frequency range for which the absorbers are designed in this research work. So another application of the developed absorbers can be in this field. Stealth technology is another major field of application for microwave absorbers. In this technology, the aircraft is covered with material that absorbs the incident signal and no reflection of the signal happens and the aircraft becomes untraceable by the Radar. When the radio signal fall on the aircraft they get absorbed and not reflected back to the Radar and hence radar can not detect the aircraft. The prepared ferrite $SrCo_xZr_xFe_{12-2x}O_{19}$ showed a reflection loss of -15.9 dB at 0.3 mm and -14.74 dB at 0.4 mm while a -34.87 dB at 1.9 mm thickness. These absorbers can be used in the form of paint which can be used for coating any device to make it free from reflections. The developed absorber can also be used in the textile industries to develop EMI-shielded cloth.

4.8 Limitations of research work

In this research the 3D materials could be used as a filler material for better performance, however, due to the high cost limitation these materials are not used. Another limitation in the research is the unavailability of instrument for higher frequency band due to which parameter are measured only on X-band, however, measurement can be done on higher bands like K, Ka and Ku bands. Free space communication analysis has not been done due to the unavailability of set up.

CHAPTER 5

SUMMARY AND CONCLUSION

M-type hexaferrites with chemical composition $SrCo_xZn_xFe_{12-2x}O_{19}$ have been synthesized successfully. The gist of the investigated work: The M-phase formation without any secondary phase has been validated using X-ray diffraction. Morphological analysis reveals that the sizes of synthesized ferrites are in the range of nanoparticles. The increase in the content of Zn and Co causes the formation of honeycomb-like grain structures. The crystallite size of prepared hexaferrite compositions ranges between 40.66 to 26.42 nm, among these the composition x=1.0 has the smallest crystallite size of 26.42 nm. The dielectric constant and dielectric loss of prepared ferrites follow the Verwey-De Boer hopping mechanism and Maxwell-Wagner model. Compositions x=0.2 has the highest and x=0.4 owe the lowest value of dielectric constant ε'=35.97 and ε'=17.35 respectively at 100 Hz.

Cole-Cole plots of electric modulus displayed semi-circles in accordance with loss tangent peaks. The semicircle in undoped composition x=0.0 lies almost equally along high as well as low-frequency regions, hence both grains and grain boundaries are responsible for charge transport. The doping of Co-Zn (x=0.2, 0.6, 0.8, and 1.0) shifts the arc towards a low-frequency regime while for x=0.4 it is toward high-frequency. This trend indicates that grains contribute more in composition x=0.4, while grain boundaries are dominant in the rest of the compositions. The asymmetric and broad peaks of M″ indicate the non-Debye type behavior. Shifting of peaks toward the high-frequency area indicates a reduction in relaxation time. The decrease in ac conductivity with Co-Zn doping is noticed at low frequency which is because of the reduction in electron hopping for Fe^{3+} and Fe^{2+}. Simulated curves are aligned with the measured curves; on the other hand, derived parameters from EIS validate the micrographs. The band gaps of the developed compositions x=0.0 to 1.0 are 2.68, 2.82, 2.56, 2.86, 2.71, and 2.58 eV respectively. The highest coercivity Hc=6263 Oe is obtained in x=0.0 which decreased to 948 Oe in x=1.0, however, the saturation magnetization varies non-monotonically.

The prepared hexaferrite $SrCo_xZn_xFe_{12-2x}O_{19}$ shows very good microwave absorption characteristics. The microwave absorption has been enhanced due to the doping of Co-Zn. The high reflection loss is observed for x=0.2, 0.4, 0.8, and 1.0 associated with permittivity/permeability losses, eddy current losses, λ/4, and impedance matching criteria. RL of -41.72 dB with a low 1.9 mm thickness is achieved in x=1.0. Also, a wide bandwidth of 2.02 GHz is obtained for the same thickness. The composition x=1.0 has a large BTR of 2.478 at 11.81 GHz for 1.9 mm, while a PBW of 17.87% at 2.0 mm. Thus the tuning of absorption can be opted by varying *RL* peak at the required frequency and wide absorption bandwidth can be achieved with the variation in thickness, doping level, and impedances.

M-type ferrites with the chemical formula $SrCo_xNi_xFe_{12-2x}O_{19}$ were synthesized successfully. X-ray diffractograms illustrate the development of a magnetoplumbite-type structure with no secondary phase. The inclusion of Co–Ni formed a needle-shaped grain structure. The smallest crystallite size of 23.24 nm is obtained in composition x=0.8. The conductivity relaxation is observed in Cole-Cole plots of electric modulus in agreement with loss tangent peaks. The non-Debye type relaxation is shown by the asymmetric and broad peaks of M″. A reduction in relaxation time is caused as the peaks are shifting toward the high-frequency region. The simulated results from EIS are in agreement with the measured parameters. The band gaps of the prepared compositions x=0.0 to 1.0 are 2.68, 2.54, 2.92, 2.90, 2.89, and 3.01 eV respectively. The coercivity drops from 5710 to 1974 Oe with the doping, however, Ms varies non-monotonically with the doping.

The prepared hexaferrite $SrCo_xNi_xFe_{12-2x}O_{19}$ shows very good microwave absorption characteristics. The microwave absorption has been enhanced due to the doping of Co-Ni. The high reflection loss is observed in all the compositions associated with dielectric/magnetic losses, eddy current loss, λ/4, and impedance matching criteria. The highest RL of -37.46 dB at a thickness of 8.0 mm is obtained in composition x=0.8. It is observed that doping of Co-Ni has enhanced the bandwidth. The large bandwidth of 1.35 GHz is achieved in composition x=1.0. The composition x=1.0 also possesses the highest BTR of 1.211 at 9.88 GHz and PBW of 12.44% at 8.3

mm. Thus the absorption can be tuned and a wide bandwidth can be obtained by changing the doping level, and thickness.

Synthesis and investigation of parameters of prepared M-type hexaferrites with the chemical composition $SrCo_xZr_xFe_{12-2x}O_{19}$ has been performed successfully. The essence of the investigation is as follows: M-type hexagonal ferrite structure was validated by X-ray diffraction analysis. Morphology illustrates that the prepared hexaferrites are in the nanoparticle range. The Co-Zr doping causes the development of needle-shaped grain structures. The smallest crystallite size of 29.77 nm is obtained in composition x=1.0. All compositions showed semi-circles in the Cole-Cole plots of electric modulus in compliance with loss tangent peaks. A non-Debye type relaxation is confirmed by the asymmetric and broad peaks of M''. A reduction in relaxation time may occur due to the shifting of the peak toward the high-frequency regime. The conductivity **(σ)** follows the Jonscher power law with a transition from the flat plateau σ_{dc} to a dispersive σ_{ac}**.** There is an enhancement in ac conductivity with the inclusion of Co-Zr content. The simulated and measured curves are in good agreement. The simulated parameters obtained using EIS software are validated through micrographs, dielectric constant, and electric modulus. The band gaps of the prepared compositions x=0.0 to 1.0 are 2.68, 2.34, 2.81, 2.10, 2.91, and 2.42 eV respectively. Hc drops from 6236 to 2348 Oe (x=0.0-1.0). However, saturation magnetization varies non-uniformly.

The investigation of microwave absorption characteristics of $SrCo_xZr_xFe_{12-2x}O_{19}$ has been carried out based on λ/4, impedance matching, magnetic/dielectric losses, and eddy current loss. The prepared hexaferrites have shown very good microwave absorption characteristics. The doping of Co-Zr has enhanced the absorption characteristics of the prepared ferrites. A high RL is obtained in all the compositions. The highest RL=-37.69 dB for a small 2.9 mm thickness at 11.31 GHz is obtained in composition x=1.0. Co-Zr dopants have reduced the bandwidth but the bandwidth-to-thickness ratio is increased by doping. The highest bandwidth of 1.09 GHz is obtained in composition x=0.0. The highest BTR of 0.747 at 10.47 GHz is observed in x=0.8.

The micrographs of the $SrCo_xZn_xFe_{12-2x}O_{19}$/PANI composites show the development of fused grains with the inclusion of Co-Zn. The $\varepsilon'$and ε'' follow the Maxwell-Wagner

model. The composition x=0.0 has the highest and x=1.0 has the lowest dielectric constant ε'=770.9 and ε'=245.0 respectively. The Cole-Cole plots of electric modulus show conductivity relaxation. The asymmetric and broad peaks of M″ indicate the non-Debye type relaxation. An increase in relaxation time is caused as the peaks are shifting toward the low-frequency regime. A dielectric relaxation is also shown by asymmetric peaks of Z″. The decrease in ac conductivity with Co-Zn doping is observed at low frequency which is because of the decay in electron hopping of Fe^{3+} and Fe^{2+}. The band gaps of the prepared compositions x=0.0, 0.6, and 1.0 are 2.15, 1.56, and 1.47 eV respectively. Coercivity decreased from 5679 to 987 Oe while Ms decreased from 47.8 to 32.8 emu/g.

The prepared $SrCo_xZn_xFe_{12-2x}O_{19}$/PANI composites possess good microwave absorption characteristics. The doping of Co-Zn has reduced the absorption by reducing reflection loss in PANI composites. The high RL is obtained in x=0.0, 0.6, and 1.0 associated with dielectric/magnetic losses, eddy current loss, λ/4, and impedance matching. The highest RL of -18.53 dB at 8.4 mm thickness is obtained in x=0.0. Also, a large 1.51 GHz bandwidth is obtained at 9.2 mm thickness. BTR of 1.291 at 9.80 GHz and 1.222 at 9.04 GHz for 3.7 mm and 3.9 mm is acquired. The highest PBW of 14.82% is at 3.9 mm. Hence, it can be concluded that the absorption can be tuned by varying thickness, dopants, and impedance.

The micrographs of the $SrCo_xNi_xFe_{12-2x}O_{19}$/PANI composites show the development of large fused grains with the inclusion of Co-Ni. The $\varepsilon'$and ε'' follow the Maxwell-Wagner model. The composition x=1.0 has the highest and x=0.6 has the lowest dielectric constant ε'=898.7 and ε'=280.7 respectively. The Cole-Cole plots of electric modulus show semicircles as per the non-Debye relaxation. The dielectric relaxation is shown by the asymmetric peaks of Z″. The increase in ac conductivity with Co-Ni doping is observed which is due to the improvement in the grain connectivity. The band gaps of the compositions x=0.0, 0.6, and 1.0 are 2.15, 1.54, and 1.39 eV respectively. Hc reduces from 5679 Oe to 1882 Oe with doping while a non-monotonous change in Ms.

$SrCo_xNi_xFe_{12-2x}O_{19}$/PANI composites show good microwave absorption characteristics. The doping of Co-Ni has enhanced the absorption characteristics by improving reflection loss in the prepared composites. In association with

dielectric/magnetic losses and eddy current loss high RL is obtained in compositions x=0.0, 0.6, and 1.0. The highest RL of -41.39 dB at a 5.4 mm thickness is obtained for composition x=1.0. The broad bandwidth of 1.93 GHz with the RL band ranging from 10.47-12.40 GHz is achieved in x=1.0. A -20 dB bandwidth of 0.76 GHz is obtained at 5.4 mm in composition x=1.0. The highest BTR of 1.291 at 3.7 mm thickness is acquired in composition x=0.0. The highest PBW of 15.57 % is obtained in composition x=1.0. On the final note, it can be stated that the absorption can be varied according to doping levels, thicknesses, and impedance.

The micrographs of the $SrCo_xZr_xFe_{12-2x}O_{19}$/PANI composites portray the platelet-type grain structure with the inclusion of Co-Zr. The composition x=0.6 has the highest and x=0.2 has the lowest dielectric constant ε'=7273.1 and ε'=54.1 respectively. The conductivity relaxation is shown by the Cole-Cole plots of the electric modulus. The asymmetric and broad peaks of M″ indicate the non-Debye type nature. Shifting of peak toward the high-frequency is observed which signifies a reduction in relaxation time. Z″ possesses asymmetric peaks following the dielectric relaxation. The ac conductivity increases with the doping of Co-Zr. The band gaps of the prepared compositions x=0.0, 0.2, and 0.6 are 2.15, 1.63, and 1.37 eV respectively. The coercivity decreases with doping from 5679 to 2483 Oe, however, Ms increased with doping.

$SrCo_xZr_xFe_{12-2x}O_{19}$/PANI composites show good microwave absorption characteristics. The doping of Co-Zr has increased microwave absorption in terms of reflection loss in the prepared PANI composites. The high RL is acquired by compositions x=0.0, 0.2, and 0.6 associated with λ /4, impedance matching criteria, dielectric/magnetic losses, and eddy current loss. The highest RL of -45.98 dB at 4.8 mm thickness is obtained in composition x=0.6. The 1.68 GHz broad bandwidth is obtained at a thickness of 4.1 and 4.4 mm in composition x=0.6. A BTR of 1.124 at 9.96 GHz at the thickness of 4.4 mm is obtained. The high PBW of 17.22 % at the 5.4 mm thickness is obtained. On the final note, it can be stated that the absorption can be tuned by changing doping levels, thicknesses, and impedance.

The research focuses on the development of the ferrite composite-based RF absorber. In the present article, PANI is used to prepare the composite material, further different polymers such as polypyrrole, epoxy resin, 3D materials, biomass, etc. can be used to

tune the performance metrics and a comparative investigation can be performed. Furthermore, research with different frequency bands can also be performed.

References

[1] R Acharya, D Kumar, G Mathur, Study of Electromagnetic Radiation Effects on Human Body and Reduction Techniques, Lect. Notes Electr. Eng. 472 (2018) 497-505.

[2] V. Shurenkov, V. Pershenkov, Electromagnetic pulse effects and damage mechanism on the semiconductor electronics, FU Elec Energ. 29 (2016) 621- 629.

[3] J.Y. Shin, J.H. Oh, The Microwave Absorbing Phenomenon of Ferrite Microwave Absorbers, IEEE Trans. Magn. 29 (1993) 3437-3439.

[4] H. Ahmad, A. Tariq, A. Shehzad, M.S. Fahim, M. Shafiq, I.A. Rashid, A. Afzal, A. Munir, M.T. Riaz, H.T. Haider, A. Afzal, M.B. Qadir, Z. Khali, Stealth technology: Methods and composite materials-A review, Polym. Compo. 40 (2019) 1–16.

[5] M. Amano, Y. Kotsuka, A method of effective use of ferrite for microwave absorber, IEEE Trans. Microw. Theory Techn. 51 (2003) 238–245.

[6] A. Raveendran, M.T. Sebastian, S. Raman, Applications of Microwave Materials: A Review, J. Electron. Mater. 48 (2019) 2601-2634. https://doi.org/10.1007/s11664-019-07049-1.

[7] Raul Valenzuela, Noval applications of ferrites, Phys. Res. Int. 2012 (2012) 1-9. https://doi.org/10.1155/2012/591839.

[8] R.K. Kotnala, J. Shah, Ferrite Materials: Nano to Spintronics Regime, Handb. Magn. Mater. 23 (2015) 291-379. https://doi.org/10.1016/B978-0-444-63528-0.00004-8.

[9] R.C. Pullar, Hexagonal ferrites: A review of the synthesis, properties, and applications of hexaferrite ceramics, Prog. Mater. Sci. 57 (2012) 1191-1334. https:// doi.org/10.1016/j.pmatsci.2012.04.001.

[10] W. Emerson, Electromagnetic wave absorbers and anechoic chambers through the years, IEEE Trans. Antennas Propag. 21 (1973) 484-490. https://doi.org/10.1109/TAP.1973.1140517.

[11] X. Zeng, X. Cheng, R. Yu, G.D. Stucky, Electromagnetic microwave absorption theory and recent achievements in microwave absorbers, Carbon 168 (2020) 606–623. https://doi.org/10.1016/j.carbon.2020.07.028.

[12] S.T.A. Naqvi, C. Singh, S.K. Godara, Functionalization and synthesis of biomass and its composites as renewable, lightweight and eco-efficient microwave-absorbing

materials: A review. J. Alloys Compd. 968 (2023) 171991. https://doi.org/10.1016/j.jallcom.2023.171991.

[13] B. Wang, J. Wei, Y. Yang, T. Wang, F. Li, Investigation on peak frequency of the microwave absorption for carbonyl iron/epoxy resin composite, J. Magn. Magn. Mater. 323 (2011) 1101–1103. https://doi.org/10.1016/j.jmmm.2010.12.028

[14] J. Singh, C. Singh, D. Kaur, S.B. Narang, R. Joshi, S.R. Mishra, R. Jotania, M. Ghimire, C.C. Chauhan, Tunable microwave absorption in Co Al substituted M-type Ba Sr hexagonal ferrite, Mater. Des. 110 (2016) 749–761. https://doi.org/10.1016/j.matdes.2016.08.049.

[15] X. Jing, Z. Chen, Q. Zhao, Z. Li, X. Xiong, X. Yang, Q. Wang, H. Huang, H. Jiang, T. Zhao, H. Gong, Praseodymium dysprosium co-doped M-type strontium ferrite: Intentionally manufacturing heterophase growth to improve microwave absorption performance, Mater. Today Chem. 39 (2024) 102151. https://doi.org/10.1016/j.mtchem.2024.102151.

[16] Y. Jin, W. Xiao, L. Ma, X. Liang, S. Ma, W. Sun, P. Zhang, J. Cui, D. Wang, Effect of Ce doping on electromagnetic characteristics and absorbing properties of M-type barium ferrite, Mater. Today Chem. 39 (2024) 108596. https://doi.org/10.1016/j.mtcomm.2024.108596.

[17] H. Wei, Z. Huang, J. Cui, P. Zhang, S. Ma, W.Sun, X.Liang, Y. Zhang, Y. Wu, Tailoring electromagnetic wave absorption properties of M-type barium ferrite through Nd3+–(Nb5+/Ta5+) cosubstitution, Mater. Today Chem. 39 (2024) 109378. https://doi.org/10.1016/j.mtcomm.2024.109378.

[18] M.N. Panwar, H.M. Khan, N. Bano, M. Zahid, M.E. Mazhar, M. Bilal, M.I. Saleem, G.F.B. Solre, P. Gomez, Z. Li, Influence of bismuth and cobalt doping on structural, dielectric, and magnetic properties of M-type calcium hexagonal ferrites, J. Alloys Compd. 994 (2024) 174623. https://doi.org/10.1016/j.jallcom.2024.174623.

[19] X. Yang, Z. Chen, D. Zhou, X. Xiong, X. Jing, T. Zhao, H. Gong, B. Shen, Effect of the interaction of Fe- and Ce-contents on the structure and magnetic properties of M-type strontium ferrites, Ceram. Int. 50 (2024) 32465-32476. https://doi.org/10.1016/j.ceramint.2024.06.055.

[20] Z. Chen, Bo xu, Z. Li, N. Zhou, H. Gong, X. Jing, The influence of Ho doping on the morphology and magnetic properties of M-type strontium ferrite with different

Fe/Sr, Mater. Chem. Phys. 312 (2024) 128635. https://doi.org/10.1016/j.matchemphys.2023.128635.

[21] K. Kayalvizhi, L.J. Kennedy, D. Ratna, Negative permittivity and permeability behaviour of SrFe12O19/rGO metacomposite for microwave absorption in 2–18 GHz range, Ceram. Int. 50 (2024) 16241-16252. https://doi.org/10.1016/j.ceramint.2024.02.104.

[22] H.Yang, Z. Jian, K.Li, H. Chang, W. Yang, S. Liu, Band gap, ferromagnetic resonance and strong microwave absorption of BaFe12-2xZnxSnxO19 compounds and enhanced dielectric loss in BaFe12-2xZnxSnxO19/carbon nano tube composites, J. Magn. Magn. Mater. 596 (2024) 171997. https://doi.org/10.1016/j.jmmm.2024.171997.

[23] S. Wei, X. Wang, B. Wang, Y. Wang, Y. Liang, Z. Liu, H. Zhang, Q. Xu, H. Mou, Constructing and optimizing epoxy resin-based carbon Nanotube/Barium ferrite microwave absorbing coating system, Mater. Res. Bull. 179 (2024) 112928. https://doi.org/10.1016/j.materresbull.2024.112928.

[24] R. Shu, L. Nie, Z. Zhao, X. Yang, Synthesis of nitrogen-doped reduced graphene oxide/magnesium ferrite/polyaniline composite aerogel as a lightweight, broadband and efficient microwave absorber, J. Mater. Sci. Technol. 175 (2024) 115-124. https://doi.org/10.1016/j.jmst.2023.08.015.

[25] M. Mudasar, X.U. ZH, L. SY, X. Li, X. Cheng, Tailoring permittivity and permeability of M-type hexagonal ferrite and 2D Ti3C2Tx MXene composites for broadband microwave stealth performance, Mater. Chem. Phys. 315 (2024) 129031. https://doi.org/10.1016/j.matchemphys.2024.129031.

[26] M. Bala, V.D. Shivling, S. Tyagi, Enhancing X-band microwave absorption properties with nickel ferrite and carbon-based composites, Ceram. Int. 50 (2024) 34123-34132. https://doi.org/10.1016/j.ceramint.2024.06.231.

[27] Yunasfi, S.H. Dewi, Mashadi, D.S. Winatapura, J. Setiawan, A. Mulyawan, Y.E. Gunanto, W.A. Adi, Exploring the structural and magnetic properties of La-doped nickel ferrite for microwave absorbing application, J. Magn. Magn. Mater. 603 (2024) 172267. https://doi.org/10.1016/j.jmmm.2024.172267.

[28] M. Kaur, S. Bahel, Characterization of sol-gel synthesized Zn0.25Co0.75(NiZr)xFe2-2xO4 ($0.05 \leq x \leq 0.25$) spinel ferrites based microwave

absorbers in Ka frequency band, J. Phys. Chem. Solids 184, 2024, https://doi.org/10.1016/j.jpcs.2023.111671.

[29] M.A. Siddique, M. Irfan, R.T. Rasool, M. Arshad, G.A. Ashraf, M.N. Akhtar, S. Manzoor, M.R. Raza, M.A. Khan, Role of Zn cations substitution on structural, vibrational, elastic, dielectric, bandwidth, and microwave absorbance of Co–Cd ferrites at high frequencies, Mater Chem. Phys. 315 (2024) 128972. https://doi.org/10.1016/j.matchemphys.2024.128972.

[30] M.N. Akhtar, N. Alomayrah, M.A. Baqir, M. Irfan, M.A. Khan, A. Almohammedi, M. Alelyani, M. Yousaf, Z.A. Alrowaili, M.S. Al-Buriahi, Design and tuneable magnetodielectric ferrite-based meta-absorbers for high-frequency microwave absorption applications, Mater. Res. Bull. 174 (2024) 112716. https://doi.org/10.1016/j.materresbull.2024.112716.

[31] F. Tian, Yu Gao, A. Wang, L. Xiang, Q. Man, H. Xu, B. Shen, Effect of Mn substitution on structural, magnetic and microwave absorption properties of Co2Y hexagonal ferrite, J. Magn. Magn. Mater. 587 (2023) 171229. https://doi.org/10.1016/j.jmmm.2023.171229.

[32] S. Verma, A. Singh, S. Sharma, P. Kaur, S.K. Godara, P.S. Malhi, J. Ahmad, P.D. Babu, M. Singh, Magnetic and structural analysis of $BaZn_xZr_xFe_{12-2x}O_{19}$ (x=0.1-0.7) hexaferrite samples for magnetic applications, J. Alloys Compd. 930 (2023) 167410, https://doi.org/10.1016/j.jallcom.2022.167410.

[33] S. Sahu, P.P. Mohapatra, H.K. Singh, P. Dobbidi, Enhanced microwave absorbing performance of Sr2+ substituted Nickel-Cobalt nano ferrite for radar and stealth applications, Mater. Sci. Eng. B 294 (2023) 116514. https://doi.org/10.1016/j.mseb.2023.116514.

[34] S. Gulbadan, M.A. Khan, G.A. Ashraf, K. Mahmood, M. Shahid, M. Irfan, A. Ahmad, Insight of structural, dielectric and spectroscopic characteristics of Ba0.6Sr0.4-xYbxFe12-yCoyO19 M-type hexaferrite, Ceram. Int. 49 (2023) 6487-6499, https://doi.org/10.1016/j.ceramint.2022.10.162.

[35] D. Gui, X. Ren, Investigation on electromagnetic properties of La–Al co-doped Co2W hexagonal ferrites for microwave absorption, Ceram. Int. 49 (2023) 14079-14089, https://doi.org/10.1016/j.ceramint.2022.12.289.

[36] W. Zhang, J. Li, J. Li, J. Guo, Y. Wang, P. Zu, P. Li, Structural, optical, dielectric, and magnetic properties of Sr0.7La0.3Zn0.3Fe11.7–XAlxO19 hexaferrite synthesized by the solid-state reaction method. J. Solid State Chem. 306 (2022) 122766. https://doi.org/10.1016/j.jssc.2021.122766.

[37] M.N. Akhtar, M. Yousaf, Y. Lu, M. Z. Mahmoud, J. Iqbal, M.A. Khan, M.U. Khallidoon, S. Ullah, M. Hussien, Magnetic, structural, optical band alignment and conductive analysis of graphene-based REs (Yb, Gd, and Sm) doped NiFe2O4 nanocomposites for emerging technological applications, Synthetic Metals 284 (2022) 116994, https://doi.org/10.1016/j.synthmet.2021.116994.

[38] N. Aggarwal, S.B. Narang, Synthesis of Ni-Zn-Mg-Zr spinel ferrites as high-performance electromagnetic wave absorber in Ku band, Mater. Today Proc. 52 (2022) 1294-1301, https://doi.org/10.1016/j.matpr.2021.11.056.

[39] Z. Hassan, I. Sadiq, R. Hussain, F. Sadiq, M. Idrees, S. Hussain, S. Riaz, S. Naseem, Determination of dual magnetic phases and the study of structural, dielectric, electrical, surface morphological, optical properties of Ce^{3+} substituted hexagonal ferrites. J. Alloys Compd. 906, (2022) 164324. https://doi.org/10.1016/j.jallcom.2022.164324.

[40] J. Singh, C. Singh, Y. Bai, D. Kaur, S.B. Narang, K.C.J. Raju, P.N. Dhurv, R. Jotania, A. Joseph, R. Joshi, Role of phase, grain morphology and impedance properties in tailoring of Barium Strontium hexaferrites for microwave absorber/attenuator applications, Mater. Sci. Eng. B, 281 (2022) 115679. https://doi.org/10.1016/j.mseb.2022.115679.

[41] M. Dilshad, H.M. Khan, M. Zahid, S. Honey, M.A. Assiri, M. Imran, Structural, optical and dielectric properties of aluminum-substituted SrAl2xFe12-2xO19 x = (0.0,0.2,0.4,0.6,0.8,1.0) M-type hexagonal ferrites, J Mater Sci: Mater Electron. 33 (2022) 21519-21530. https://doi.org/10.1007/s10854-022-08943-x.

[42] D.B. Basha, N.S. Kumar, K.C.B. Naidu, G.R. Kumar, Structural, electrical, and magnetic properties of nano $Sr_{1-X}La_XFe_{12}O_{19}$ (X = 0.2–0.8), Sci. Rep. 12 (2022) 12723. https://doi.org/10.1038/s41598-022-15250-2.

[43] M. Yousaf, Y. Lu, E. Hu, B. Wang, M.N. Akhtar, A. Noor, M. Akbar, M.A.K.Y. Shah, F. Wang, B. Zhu, Tunable magneto-optical and interfacial defects of Nd and Cr-

doped bismuth ferrite nanoparticles for microwave absorber applications, J. Colloid Interface Sci. 608 (2022) 1868-1881. https://doi.org/10.1016/j.jcis.2021.09.182.

[44] M. Zahid, H.M. Khan, I. Sadiq, A.U. Rehman, A. Waheed, E. Mazhar, M.A. Assiri, M. Imran, N. Usmani, I. Khan, Structural Elucidation with Improved Dielectric and Magnetic Properties of Sol-Gel Synthesized Cr3+ Substituted M-Type Sr2+ Hexaferrites, J. Mater. Eng. Perform. 31 (2022) 1350-1359. https://doi.org/10.1007/s11665-021-06263-5.

[45] B. Purnama, R. Arilasita, N. Rikamukti, Utari, S. Budiawanti, Suharno, A.T. Wijayanta, Suharyana, D. Djuhana, E. Suharyadi, T. Tanaka, M. Matsuyama, Annealing temperature dependence of crystalline structure and magnetic properties in nano-powder strontium-substituted cobalt Ferrite, Nano-Struct. Nano-Objects 30 (2022) 100862. https://doi.org/10.1016/j.nanoso.2022.100862.

[46] H. Habib, Y. Atassi, A. Salloum, N.N. Ali, M. Jafarian, An Ecofriendly, Cost-Effective, Lightweight Microwave Absorber Based on Waste Toner, J. Elec. Mater. 50 (2021) 2049–2056.

[47] E. Lim, H.K.D. Kim, Y. Kang, Control of electromagnetic wave absorption properties in La-Co-Ti substituted M-type hexaferrite–epoxy composites, J. Magn. Magn. Mater. 517 (2021) 167393.

[48] J. Singh, C. Singh, D. Kaur, S.B. Narang, R.B. Jotania, A. Kagdi, R. Joshi, A.S.B. Sombra, D. Zhou, S. Trukhanov, L. Panina, A. Turkhanov, Optimization of Performance Parameters of Doped Ferrite-Based Microwave Absorbers: Their Structural, Tunable Reflection Loss, Bandwidth, and Input Impedance Characteristics, IEEE Trans. Magn. 57 (2021) 1–19. https://doi.org/10.1109/tmag.2021.3063175.

[49] S. Kumar, V. Verma, R. Walia, Magnetization and thickness dependent microwave attenuation behaviour of Ferrite-PANI composites and embedded composite-fabrics prepared by in situ polymerization, AIP Advances 11 (2021) 015106.

[50] J. Singh, C. Singh, D. Kaur, S.B. Narang, R.B. Jotania, E. Ateia, A. Kagdi, R. Joshi, A.S.B. Sombra, D. Zhou, S. Trukhanov, L. Panina, Development of doped Ba-Sr hexagonal ferrites for microwave absorber applications: Structural characterization, tunable thickness, absorption peaks and electromagnetic parameters, J. Alloys Compd. 855 (2021) 1-19.

[51] V.K. Chakradhary, M.J. Akhtar, Absorption properties of CNF mixed cobalt nickel ferrite nanocomposite for radar and stealth applications, J. Magn. Magn. Mater. 525 (2021)167592.

[52] M. Zhang, L. Chen, Y. Yu, X. Meng, J. Xiang, Cabon nanofiber supported cobalt ferrite composites with tunable microwave absorption properties, Ceram. Int. 47 (2021) 9392-9399.

[53] N. Aggarwal, S. B. Narang, Effect of co-substitution of Co–Zr on electromagnetic properties of Ni–Zn spinel ferrites at microwave frequencies, J. Alloys Compd. 866, (2021) 157461.

[54] L. Chang, X. Ren, H. Yin, Y. Tang, X. Pu, H. Yuan, The tunable microwave absorption properties of the Co^{2+}–Zr^{4+} co-substituted Co_2W-type hexagonal ferrites, J Mater Sci: Mater Electron. 31 (2020) 20908–20918, 2020. https://doi.org/10.1007/s10854-020-04605-y.

[55] T. Ma, Yu Cui, Y. Sha, Li Liu, J. Ge, F. Meng, F. Wang, Facile synthesis of hierarchically porous rGO/MnZn ferrite composites for enhanced microwave absorption performance, Synthetic Metals, 265 (2020) 116407, https://doi.org/10.1016/j.synthmet.2020.116407.

[56] Y. Zhang, C. Liu, X. Zhao, M. Yao, X. Miao, F. Xu, Enhanced microwave absorption properties of barium ferrites by Zr4+-Ni2+ doping and oxygen-deficient sintering, J. Magn. Magn. Mater. 494 (2020) 165828, https://doi.org/10.1016/j.jmmm.2019.165828.

[57] Z. Jiao, Z. Yao, J. Zhou, K. Qian, Y. Lei, B. Wei, W. Chen, Enhanced microwave absorption properties of Nd-doped NiZn ferrite/polyaniline nanocomposites, Ceram. Int. 46 (2020) 25405-25414, https://doi.org/10.1016/j.ceramint.2020.07.010.

[58] Y. Tang, P. Yin, L. Zhang, J. Wang, X. Feng, K. Wang, J. Dai, Novel carbon encapsulated zinc ferrite/MWCNTs composite: Preparation and low-frequency microwave absorption investigation, Ceram. Int. 46 (2020) 28250-28261, https://doi.org/10.1016/j.ceramint.2020.07.326.

[59] R. Shu, J. Zhang, C. Guo, Y. Wu, Z. Wan, J. Shi, Y. Liu, M. Zheng, Facile synthesis of nitrogen-doped reduced graphene oxide/nickel-zinc ferrite composites as high-performance microwave absorbers in the X-band, Chem. Eng. J. 384 (2020) 123266, https://doi.org/10.1016/j.cej.2019.123266.

[60] M. Khadour, Y. Atassi, M. Abdallah, Preparation and characterization of a flexible microwave absorber based on MnNiZn ferrite ($Mn_{0.1}Ni_{0.45}Zn_{0.45}Fe_2O_4$) in a thermoset polyurethane matrix, SN Appl. Sci. vol. 2, 2020. https://doi.org/10.1007/s42452-020-2004-0.

[61] S. R. Bhongale, H. R. Ingavale, T. J. Shinde, K. Pubby, S. Bindra Narang and P. N. Vasambekar, X-Band Microwave Absorption in Nd^{3+}-Substituted Mg–Cd Spinel Ferrites Synthesized Under Microwave Sintering, IEEE Trans. Magn. 56 (2020) 1-7, 2800607, https://doi.org/10.1109/TMAG.2020.3014057.

[62] M. Moradnia, M. Fathi, M. Mehdipour, H. Shokrollahi, Analyzing the Microwave Absorption Properties of $BaFe_{12}O_{19}$, $Ba_4MnZnFe_{36}O_{60}$ and $NiFe_2O_4$ Particles, J. Elect. Mater. 49 (2020) 5957–5963, https://doi.org/10.1007/s11664-020-08317-1.

[63] Y. He, S. Pan, J. Yu, Research on magnetic and microwave absorbing properties of Co2Y ferrite fabricated by sol-gel process, J. Sol-Gel Sci. Technol. 96 (2020) 521-528, https://doi.org/10.1007/s10971-020-05235-w.

[64] M. Rani, M., K.S. Bhatia, H. Singh, H. Kaur, N. Gupta, Synthesis of suitable material for microwave absorbing properties in X-band, SN Appl. Sci. vol. 2, 2035, 2020. https://doi.org/10.1007/s42452-020-03786-9.

[65] A. Arora, S.B. Narang, K. Pubby, Enhanced Microwave Absorption Properties of Doped M-Type Barium Hexagonal Ferrites in Ka-band Frequencies, J. Supercond. and Nov. Magn. 32 (2019) 2705–2709, https://doi.org/10.1007/s10948-019-5044-1.

[66] J. Luo, L. Yue, H. Ji, K. Zhang, N. Yu, Investigation on the optimization, design and microwave absorption properties of $BaTb_{0.2}Eu_{0.2}Fe_{11.6}O_{19}$/PANI decorated on reduced graphene oxide nanocomposites, J. Mater. Sci. 54 (2019) 6332–6346.

[67] M. Wang, Y. Lin, Y. Liu, H. Yang, Core-shell structure $BaFe_{12}O_{19}$@PANI composites with thin matching thickness and effective microwave absorption properties, J. Mater. Sci.: Mater. Electron. 30 (2019) 14344–14354.

[68] R. Shu, G. Zhang, J. Zhang, X. Wang, M. Wang, Y. Gan, J. Shi, J. He, Synthesis and high performance microwave absorption of reduced graphene oxide/zinc ferrite hybrid nanocomposites, Materials Letters 215 (2018) 229-232.

[69] Jun Li, San He, Kouzhong Shi, You Wu, Han Bai, Yang Hong, Wenjing Wu, Qingxin Meng, Dechang Jia, Zhongxiang Zhou, Coexistence of broad-bandwidth and

strong microwave absorption in Co2+-Zr4+ co-doped barium ferrite ceramics, Ceram. Int. 44 (2018) 6953-6958.

[70] Z. Song, J. Li, K. Shi, S. He, C. Yuan, Z. Zhou, The Microwave Absorbing Performance of Co^{+2} - Ti^{+4} Co-doped Barium Ferrite Ceramics, 12th International Symposium on Antennas, Propagation and EM Theory (ISAPE), (2018) 1-4.

[71] R. Joshi, C. Singh, J. Singh, D. Kauur, S.B. Narang, R.B. Jotania, A study of microwave absorbing properties in Co–Gd doped M-type Ba–Sr hexaferrites prepared using ceramic method, J. Mater. Sci. : Mater. Electron. 28 (2017) 11969–11978.

[72] J. Singh, C. Singh, D. Kaur, S.B. Narang, R.B. Jotania, R. Joshi, Microwave absorbing characteristics in Co^{2+} and Al^{3+} substituted $Ba_{0.5}Sr_{0.5}Co_xAl_xFe_{12-2x}O_{19}$ hexagonal ferrite, J Mater Sci: Mater Electron, 28 (2017) 2377–2384.

[73] M.A. Malana, R.B. Qureshi, M.N. Ashiq, M.F. Ehsan, Synthesis, structural, magnetic and dielectric characterizations of molybdenum doped calcium strontium M-type hexaferrites, Ceram. Int. 42 (2016) 2686-2692, https://doi.org/10.1016/j.ceramint.2015.10.144.

[74] Z. Mosleh, P. Kameli, A. Poorbaferani, M. Ranjbar, H. Salamati, Structural, magnetic and microwave absorption properties of Ce-doped barium hexaferrite, J. Magn. Magn. Mater. 397 (2016) 101-107, https://doi.org/10.1016/j.jmmm.2015.08.078.

[75] A. Baniasadi, A. Ghasemi, M.A. Ghadikolaei, A. Nemati, E. Paimozd, Microwave absorption properties of Ti–Zn substituted strontium hexaferrite, J. Mater. Sci.: Mater. Electron. 27 (2016), 1901-1905.

[76] Z. He, S. Qi, X. Zhong, H. Ma, P. Wang, H. Qiu, Preparation and microwave-absorbing properties of silver-coated strontium ferrite with polyaniline via in situ polymerization, J. Alloys Compd. 621 (2015) 194-200, https://doi.org/10.1016/j.jallcom.2014.09.187.

[77] S.T.A. Naqvi, C. Singh, S.K. Godara, R.B. Jotania, P.K. Maji, C.R. Vaja, Tunable electrical and impedance characteristics of Co–Zn doped M-type Sr Hexaferrites: Role of grain, grain boundaries, electrical transport mechanisms and software/circuit modeling, Ceram. Int. 50 (2024) 7323-7335, https://doi.org/10.1016/j.ceramint.2023.11.353.

[78] A.K. Jonscher, Dielectric Relaxation in Solids, first ed., Chelsea Dielectric Press Ltd., London, 1983.

[79] K. Funke, Jump relaxation in solid electrolytes, Prog. Solid State Chem. 22 (1993) 111-195.

[80] C.G. Koops, Resistivity and dielectric constant: On the Dispersion of Resistivity and Dielectric Constant of Some Semiconductors at Audio frequencies. 83 (1951) 121.

[81] N. Rezlescu, and E. Rezlescu. Dielectric properties of copper containing ferrites. Physica Status Solidi (A) 23 (1974) 575-582.

[82] A. Mishra, S.N. Choudhary, K. Prasad, R.N.P. Choudhary, Complex impedance spectroscopic studies of $Ba(Pr_{1/2}Ta_{1/2})O_3$ ceramic, Physica B: Condensed Matter. 406 (2011) 3279–3284, https://doi.org/10.1016/j.physb.2011.05.040.

[83] J.R. Macdonald, Impedance spectroscopy: Emphasizing Solid State Material and Systems (Wiley New York, 1987).

[84] A. Bagum, M. Belal Hossen, F.-U.-Z. Chowdhury, Complex impedance and electric modulus studies of Al substituted $Co_{0.4}Cu_{0.2}Zn_{0.4}Al_xFe_{2-x}O_4$ ferrites prepared by auto combustion technique, Ferroelectrics 494 (2016) 19-32.

[85] A. Langar, N. Sdiri, H. Elhouichet, M. Ferid, Structure and electrical characterization of ZnO-Ag phosphate glasses, Results Phys. 7 (2017) 1022-1029. https://doi.org/10.1016/j.rinp.2017.02.028.

[86] A.S. Bondarenko, G. Ragoisha, EIS Spectrum Analyzer (Version 1.0), July 16, 2013. http://www.abc.chemistry.bsu.by/vi/analyser/.

[87] M.V. Nikolic, D.L. Sekulic, Z.Z. Vasiljevic, M.D. Lukovic, V.B. Pavlovic, O.S. Aleksic, Dielectric properties, complex impedance and electrical conductivity of Fe2TiO5 nanopowder compacts and bulk samples at elevated temperatures, J. Mater. Sci. 28, (2017) 4796, https://doi.org/10.1007/s10854-016-6125-6.

[88] H.S. Mund, B. L. Ahuja, Structural and magnetic properties of Mg doped cobalt ferrite nano particles prepared by sol-gel method, Mater. Res. Bull. 85 (2017) 228–233, https://doi.org/10.1016/j.materresbull.2016.09.027.

[89] C.C. Chauhan, T. Gupta, A.A. Gor, K.R. Jotania, and R.B. Jotania, Effect of calcination temperature on structural and magnetic properties of lightly lanthanum substituted M-type strontium cobalt hexaferrites, Mater. Today Proc. 47 (2020) 715–718, https://doi.org/10.1016/j.matpr.2020.12.1184.

[90] C. Singh, S.B. Narang, I.S. Hudiara, Y. Bai, K. Marina, Hysteresis analysis of Co-Ti substituted M-type Ba-Sr hexagonal ferrite, Mater. Lett. 63 (2009) 1921–1924, https://doi.org/10.1016/j.matlet.2009.06.002.

[91] L. Phor, S. Chahal, V. Kumar, Zn2+ substituted superparamagnetic MgFe2O4 spinel-ferrites: Investigations on structural and spin-interactions, J. Adv. Ceram. 9 (2020) 576-587, https://doi.org/10.1007/s40145-020-0396-3

[92] R. Grössinger, Correlation between the inhomogeneity and the magnetic anisotropy in polycrystalline ferromagnetic materials, J. Magn. Magn. Mater. 28 (1982) 137–142, https://doi.org/10.1016/0304-8853(82)90037-3.

[93] T. Ben Ghzaiel, W. Dhaoui, A. Pasko, F. Mazaleyrat, Effect of non-magnetic and magnetic trivalent ion substitutions on BaM-ferrite properties synthesized by hydrothermal method, J. Alloys Compd, 671 (2016) 245–253, https://doi.org/10.1016/j.jallcom.2016.02.071.

[94] H. Lv, G. Ji, H. Zhag. M. Li, Z. Zuo, Y. Zhao, B. Zhang, D. Tang, Y. Du, Co_xFe_y@C Composites with Tunable Atomic Ratios for Excellent Electromagnetic Absorption Properties, Sci. Rep. 5 (2015) 1–10.

[95] M. A. Abdeen, Dielectric Behaviour in Co-Zn Ferrites, J. Magn. Magn. Mater. 192 (1999) 121–129.

[96] X. Liu D. Yunchen, L. Wenwen, Q. Rong, W. Ying, H. Xijiang, M. Jun and X. Ping, Shell Thickness-Dependent Microwave Absorption of Core−Shell Fe_3O_4@CComposites, ACS Appl. Mater. Interfaces 6 (2014) 12997−13006.

[97] M. Wu, Y.D. Zhang, S. Hui, T.D. Xiao, S. Ge, W.A. Hines, J.I. Budnick, G.W. Taylor, Microwave magnetic properties of $Co_{50}/(SiO2)_{50}$ nanoparticles, Appl. Phys. Lett. 80 (2002) 4404–4406.

[98] R. Shu, X. Wang, Y. Yang, X. Tang, X. Zhou, and Y. Cheng, Coprecipitation Synthesis of Fe-doped ZnO Powders with Enhanced Microwave Absorption Properties, *Nano* 11 (2016) 1650136.

[99] G. Wei, T. Wang, H. Zhang, X. Liu, Y. Han, Y. Chang, L. Qiao, F. Li, Enhanced microwave absorption of barium cobalt hexaferrite composite with improved bandwidth via c-plane alignment, J. Magn. Magn. Mater. 471 (2019) 267–273.

[100] Z. W. Li, Z. H. Yang, Microwave absorption properties and mechanism for hollow Fe_3O_4 nanosphere composites, J. Magn. Magn. Mater. 387 (2015) 131–138.

[101] C.A. Stergiou, M.Y. Koledintseva, K.N. Rozanov, Hybrid polymer composites for electromagnetic absorption in electronic industry. Elsevier Ltd, 2017.

[102] D. S. Aherrao, C. Singh, V.L. Mathe, P.K Maji, A.K. Srivastava, Investigation of structural, morphological, electric modulus, AC conductivity characteristics, and validation of software-based simulated impedance/material parameters of bicomponent Co-Al doped Ba-Sr ferrites, Physica Scripta, 98, (2023), 015813.https://doi.org/10.1088/1402-4896/aca6b0.

[103] E.V. Ramana, S.V. Suryanarayana, T. Bhima Sankaram, ac impedance studies on ferroelectromagneticSr$Bi_{5-x}La_xTi_4FeO_{18}$ ceramics, Materials Research Bulletin 41 (2006) 1077–1088, https://doi.org/10.1016/j.materresbull.2005.11.013.

[104] S.T.A. Naqvi, C. Singh, S.K. Godara, R.B. Jotania, V. Kaur, A.K. Sood, Functionalization of morphology in optimization of dielectric, electrical/impedance modulus, and relaxation mechanisms of Co-Ni doped M-type Sr nanoferrites, Phys. Scr. 99 (2024) 055558. http://iopscience.iop.org/article/10.1088/1402-4896/ad3aaf.

[105] A. Karim, S.E. Shirsath, S.J. Shukla, K.M. Jadhav, Gamma irradiation induced damage creation on the cation distribution, structural and magnetic properties in Ni–Zn ferrite, Nucl Instrum. Methods Phys. Res. B, 268 (2010) 2706-2711, https://doi.org/10.1016/j.nimb.2010.05.058.

[106] T. Ahamed, A. Ahad, Mithun Kumar Das, M.A. Taher, Mohammad J. Miah, M.N.I. Khan, Synthesis and characterization of dielectric, electric, and magnetic properties of vanadium doped-bismuth europium ferrites for multiferroic applications. Results Phys. 50 (2023) 106571, https://doi.org/10.1016/j.rinp.2023.106571.

[107] M.Z. Ahsan, M.M. Kamal, S.S. Rakhi, S.N. Tanha, G.I. Hasan, Electric modulus of manganese doped cobalt ferrite nanoparticles. Results Phys. 50, (2023) 106593. https://doi.org/10.1016/j.rinp.2023.106593.

[108] I.G. Austin, N.F. Mott, Polarons in crystalline and non-crystalline materials. Adv. Phys. 18, 41 (1969). https://doi.org/10.1080/00018736900101267.

[109] S.K. Godara, V. Kaur, K. Chuchra, S.B. Narang, G. Singh, M. Singh, A. Chawla, S. Verma, G.R. Bhadu, J.C. Chaudhary, P.D. Babu, A.K. Sood, Impact of Zn2+-Zr4+ substitution on M-type barium strontium hexaferrite's structural, surface morphology,

dielectric and magnetic properties. Results Phys. 22, 103892 (2021). https://doi.org/10.1016/j.rinp.2021.103892.

[110] C.S. Kim, H.M. Ko, W.H Lee, C.S. Lee, Site preference for Zn^{2+} and Ge^{4+} in mixed ferrite $Zn_xGe_{1-x}Fe_2O_4$, J. Appl. Phys. 73 (1993) 6298–6300, https://doi.org/10.1063/1.352676.

[111] M. Thakur, C. Singh, A.K. Srivastava, Tunable structural, morphological, and hysteresis characteristics of SrFe12O19/Fe3O4 composites, J Mater Sci: Mater Electron 35, (2024) 653. https://doi.org/10.1007/s10854-024-12395-w.

List of Publication

1. S.T.A. Naqvi, C. Singh, S.K. Godara, R.B. Jotania, P.K. Maji, C.R. Vaja, Tunable electrical and impedance characteristics of Co–Zn doped M-type Sr Hexaferrites: Role of grain, grain boundaries, electrical transport mechanisms and software/circuit modeling, Ceram. Int. 50 (2024) 7323-7335, https://doi.org/10.1016/j.ceramint.2023.11.353.
2. S.T.A. Naqvi, C. Singh, S.K. Godara R.B. Jotania, V. Kaur, A.K. Sood, Functionalization of morphology in optimization of dielectric, electrical/impedance modulus, and relaxation mechanisms of Co-Ni doped M-type Sr nanoferrites, Phys. Scr. 99 (2024) 055558. http://iopscience.iop.org/article/10.1088/1402-4896/ad3aaf.
3. S.T.A. Naqvi, C. Singh, S.K. Godara, Functionalization and synthesis of biomass and its composites as renewable, lightweight and eco-efficient microwave-absorbing materials: A review. J. Alloys Compd. 968, 171991 (2023). https://doi.org/10.1016/j.jallcom.2023.171991.

List of Communicated Research Paper

1. S.T.A. Naqvi, C. Singh, S.K. Godara R.B. Jotania, V. Kaur, A.K. Sood, Tailoring of Structural, Electrical, Optical and Impedance Characteristics of Co2+ and Zr4+ Doped Strontium Hexaferrites, Ceram. Int. (2024). Manuscript ID: CERI-D-24-11094.
2. S.T.A. Naqvi, C. Singh, S.K. Godara, B. Ray, S. Dattar, Investigation of Structural, Hysteresis, and Microwave Dielectric/Magnetic Properties of Co-Zn doped M-type Strontium Hexaferrites for Light-Weight Microwave Absorber Applications: Paradigm of Real/Imaginary Impedance, Wide Bandwidth and Thickness. J. Magn. Magn. Mater. (2024). Manuscript ID: MAGMA-D-24-01708.
3. S.T.A. Naqvi, C. Singh, S.K. Godara, B. Ray, S. Dattar, Tunable Structural, Magnetic, Complex Permittivity/Permeability, and Reflection Loss Parameters of Co2+ and Ni2+ Co-doped M-type Strontium Ferrites for Microwave Absorber Applications, J. Mater. Sci. Mater. Elec. (2024). Manuscript ID: JMSE-D-24-03203.

List of Conferences

1. International Conference on Intelligent Circuits and Systems (ICICS-2023) organized by Lovely Professional University, Phagwara, Punjab.
2. International Conference on Nanotechnology: Opportunities & Challenges (ICNOC-2022) organized by Jamia Millia Islamia, Delhi.
3. 7th International Conference Challenges and Opportunities for Innovation in India (COII-2024) organized by Ambalika Institute of Management and Technology, Lucknow, Uttar Pradesh.